UNIVERSIDAD AUTÓNOMA DE MADRID

Facultad de Ciencias
Departamento de Física de la Materia Condensada

Programa de doctorado de Física de la Materia Condensada

NANOSCOPIC SYSTEMS DRIVEN BY MAGNETIC AND ELECTRIC AC FIELDS

Memoria de la tesis presentada por

Maria Begoña Busl

para optar al grado de Doctor en Ciencias Físicas

Directora:

Gloria Platero Coello

Madrid, Mayo de 2012

Agradecimientos

Son muchas personas las que contribuyen al éxito de una tesis. Entre estas personas, la más importante con diferencia es el director de tesis. Quiero agradecerle a Gloria su dedicación profesional y su preocupación por mí, así como la infinita confianza que me ha depositado y su trato cordial y familiar, que dieron lugar a una relación mucho más allá de la estrictamente profesional entre jefa y doctoranda. Gracias a ella mi tesis ha sido un trabajo muy fructífero.

A Rafa, que ha sido casi como mi segundo director de tesis, sobre todo en los primeros años y otra vez al final, quiero agradecerle su tiempo y dedicación – sin exagerar puedo decir que *siempre* estaba disponible para cualquier duda relacionada con la física, y encima *siempre* con buen humor.

Pasé tres meses de la tesis en Copenhague y Helsinki, donde pude empezar una colaboración con Antti-Pekka Jauho. Gracias a él por darme esta oportunidad. Antti sacrificó mucho tiempo en introducirme en el mundo de la teoría de física de muchos cuerpos, y me embarcó en un proyecto de grafeno. He aprendido un montón gracias a él[1].

Hacia el final de mi tesis se dio la oportunidad de colaborar con un grupo experimental – para un físico teórico probablemente el mejor regalo, máxime si se trata de una persona como Andrew Sachrajda. En Andy se une una combinación de profesionalidad, profundo conocimiento y humor británico que ha hecho de esta colaboración una parte muy importante y entretenida de mi tesis[2].

Quiero agradecerle a mi tutor Juan José Saenz del CIII de la Universidad Autónoma por haberse hecho cargo de la tutela de la tesis. También agradezco a Miguel Ángel Ramos su ayuda para incorporarme al programa de doctorado. Agradezco a Nicolas Agraït, Fernando Sols, Antti-Pekka Jauho, Andrew Sachrajda, Tobias Brandes, Leonor Chico y a Rafa Sánchez su disposición para estar en el tribunal.

Quiero agradecer además a Pedro Serena y a los miembros de su grupo por permitirme utilizar su cluster.

En cuestiones y dudas de física he podido contar con la ayuda de muchas más personas. Entre ellas, gracias sobre todo a Fernando. Gracias también a Carlos, que ha estado en buena medida implicado en esta tesis, y a Sigmund, Álvaro, Tobias Stauber y a Mathias, a quien además le agradezco el haber organizado los seminarios de nuestro grupo.

En mis años en el ICMM he compartido el despacho con varios compañeros. Probablemente los

[1] Thanks to Antti-Pekka Jauho I could spend three months in Helsinki and Copenhagen, where we started a fruitful collaboration. I would like to thank him for the time he sacrificed to introduce me into the world of manybody physics and for giving me the opportunity to work on a project on graphene. I have learned a lot from him.

[2] Towards the end of my thesis the opportunity opened up to collaborate with an experimental group – probably the most gratifying reward for a theoretical physicist, even more so if the person responsible is Andrew Sachrajda. His profound knowledge in combination with professionalism and british humor made this part of my thesis a very important and entertaining one.

que más me animaron en los primeros pasos de la tesis, y por ello les doy las gracias explícitamente, fueron Alberto y Debora. He aprovechado y disfrutado mucho de la compañía de Fito, de las conversaciones con él tanto de física como de música. Gracias también a Eduardo, Oliva y Jan por hacer el día a día en el despacho agradable.

Mis años en el ICMM han estado caracterizados no sólo por la tesis, sino también por la música. Primero como cantante y luego como directora del coro he podido contribuir a la vida musical del instituto. Quiero agradecerle a todo el coro, que ha sido siempre una actividad bienvenida y querida, su confianza en estos años. Gracias a Rosa, por su organización ejemplar, y a Federíco y José Antonio por su confianza en mí. En este contexto (y más allá) también quiero agradecer a Lucía, por su disposición y gran ayuda en todo lo relacionado con la música, y a Samuel.

Me gustaría darle las gracias a Giovanni Cuniberti, mi antiguo director de tesina en Alemania, que a lo largo de toda mi tesis siempre ha sido para mí, de alguna manera, como un supervisor y mentor en la distancia.

Esta tesis ha pasado por muchas manos y muchas correcciones, y está tal y como está gracias también a la ayuda de mis padres y mis hermanas, quienes, lejos de la física, hicieron el trabajo de corregir estructura y forma – absolviéndoles aquí de cualquier culpa de errores que seguro que aún quedan.

Me queda dar las gracias a una persona que ha contribuido en una medida tan grande a esta tesis, que aquí no cabe más que gracias, Javi.

Contents

Abstract

The present thesis belongs to the field of theoretical condensed matter physics. Its main objective is the analysis of electronic properties, electronic transport and spin dynamics in nanoscopic systems which are exposed to either magnetic or electric time-dependent fields.

The thesis is divided into two parts: the first part concentrates on electronic transport and spin dynamics through different configurations of a *triple quantum dot* that is exposed to *time-dependent magnetic fields*. In the second part the influence of a *time-dependent electric field* on the electronic properties of *graphene* is studied.

The experimental and theoretical study of electronic transport through quantum dots and arrays of quantum dots started more than twenty years ago, when the first measurements on mesoscopic semiconductor systems showed single electron charging effects. But not until a few years ago, has the triple quantum dot (TQD) – an array of three tunnel-coupled semiconductor quantum dots, either in triangular or linear arrangement – been fabricated experimentally. This experimental realization has triggered off a plethora of theoretical works exploring the new physics that a TQD offers as compared to the double quantum dot (DQD).

The first part of this thesis starts with an introduction to important properties and features of transport through arrays of quantum dots (chapter 1), which serve as a basis for the following chapters. After a short overview of the most important properties of a quantum dot special attention is paid to spin effects in transport through quantum dot arrays, such as the spin blockade phenomenon. The interaction of the electron spin with its surroundings in a semiconductor quantum dot – the hyperfine interaction – is shortly explained because of its importance in transport in the spin blockade regime and in the field of quantum information. The effect of time-dependent magnetic fields on the single electron spin in quantum dots has been studied experimentally, revealing the possibility to coherently control and manipulate the electron – an intensely persecuted goal in the field of quantum information technology. Several experimental ways have been proposed of inducing such coherent rotations of the electron spin in quantum dots, out of which a few are explained. Finally, the TQD is presented, and an overview of the most important experimental and theoretical works is given.

The following chapter 2 is dedicated to the *technique* that has been used for all calculations throughout the first part of this thesis: the equation of motion for the reduced density matrix. Besides other techniques such as the non-equilibrium Green's function technique, transport through arrays of quantum dots is well described by the equations of motion of the reduced density matrix. The system of interest – in this case a TQD – is connected to a much bigger system – the leads –, whose degrees of freedom are traced out, so that one is left with a system of equations for the elements of the density matrix of the TQD. This technique allows one to calculate both the transport through the quantum

dot array and the dynamics of electron and spin inside the system. The equations of motion for the reduced density matrix are derived, and several example calculations are performed for the occupation probabilities of the closed as well as of the open TQD. The current is calculated for one electron in a triangular and linear TQD, which simultaneously serves as a basis to understand the results of the subsequent chapters.

The next three chapters present the *results* that have been obtained in this thesis regarding *transport through quantum dots in time-dependent magnetic fields*. In chapter 3 the focus of attention is on transport through a triangular TQD exposed to crossed dc and ac magnetic fields. The dc magnetic field introduces an energy difference between the spin-up and spin-down state of the electron, the Zeeman splitting. The ac magnetic field rotates the electron spin, if its frequency is resonant with the Zeeman splitting (electron spin resonance). First we concentrate on transport for only one electron. Tunneling interference due to the triangular arrangement of the TQD leads to an electronic version of the so-called coherent population trapping phenomenon, which is known from atomic optics. The electron in the dot delocalizes over two of the three dots that are not connected to the drain, so that current through the TQD is blocked. The combination of this interference phenomenon together with the coherent rotation of the electron spin due to the ac magnetic field leads to *single-electron spin rotations* that are decoupled from the decoherence introduced by the leads (up to first order in tunneling to the leads). We then introduce a second electron into the TQD in such a way that the system is operated in the spin blockade regime. The second electron therefore induces spin correlations between the two electrons, and new effects can be observed: the combination of coherent trapping, – which also occurs for two electrons –, spin blockade and ac magnetic fields can be used to control spin blockade, i.e. both lift it *and* induce it again.

Chapter 4 exposes the results for spin-polarized currents through both DQDs and linear TQDs induced by dc and ac magnetic fields. This research has been motivated by an experiment, where current in a DQD exposed to a dc magnetic field and with one electron was measured. There it was found that a considerable difference in the Zeeman splittings of the two dots leads to maximal current, when none of the spin-split levels are aligned, but rather symmetrically placed around each other, whereas, when two levels are aligned, the current suffers a *spin bottleneck* situation. In this chapter we show that by additionally applying an ac magnetic field to either a DQD or a TQD strongly spin-polarized current can be achieved, and the quantum dot arrays can work as spin-filter or even spin-inverter.

The first part of this thesis ends with chapter 5, which shows the results that have been obtained in order to explain experiments performed by the group of Prof. A. Sachrajda (NRC, Canada). In a specific configuration of a linear TQD, where both the left and right dot are connected to leads and in each of them an electron is confined electrostatically, current has been measured as a function of two gate voltages applied to the left and right dot, while the center dot is kept at a constant gate voltage. For both bias directions it has been found that the current is blocked by spin blockade, thus exhibiting *bipolar spin blockade*. Furthermore, a detailed analysis of the eigenstates of the system has shown that spin blockade is lifted via eigenstates in which an electron is delocalized between the two extremes, without passing through the center dot.

The second part of the thesis studies the electronic properties of *graphene irradiated by time-dependent electric fields*. Although in the few years since the first ground-breaking experimental results, graphene's electronic, magnetic, optic, thermic and mechanic properties have been investigated to a large extent, its behavior when exposed to time-dependent fields is a relatively new area, and only few experiments have been performed. On the theoretical side several works exist that suggest that time-dependent fields applied to graphene can reveal new and interesting physics. The research done in this part of the present thesis focuses on the calculation of the dynamical polarizability of irradiated graphene, which gives information on the electron-electron interactions and how they change by applying a time-dependent electric field.

The most important aspects about pristine graphene are summarized in the introductory chapter 6. The following chapter 7 is dedicated to the analysis of single and multiparticle properties of irradiated graphene. In order to treat the time-dependence of the ac field, Floquet theory is introduced and, subsequently, applied to the Hamiltonian for graphene in both a linearly and a circularly polarized ac electric field. For both types of polarization we show analytical approximations, which allow to capture the main physics regarding weak field intensity, i.e. when only absorption processes of up to one photon are important. These approximations are then used to calculate the quasienergy spectrum and the generalized density of states for both field polarizations. Finally, the dynamical polarizability is calculated for the case of a circularly polarized field. It is shown that the presence of the ac field modifies both single and multiparticle properties of graphene by inducing dynamical gaps in the density of states on the one hand, and inducing a collective excitation – a plasmon – on the other hand, even for undoped graphene. This is in strong contrast to pristine graphene where a plasmon is only found at finite doping. Thus it becomes clear that by applying a time-dependent electric field to graphene its electronic properties can be manipulated to a great extent, which can be useful for future applications.

Resumen

La presente tesis pertenece al campo de la física teórica de la materia condensada. Su objetivo principal es el análisis de las propiedades electrónicas, el transporte electrónico y la dinámica del espín en sistemas nanoscópicos que están expuestos a campos magnéticos o eléctricos dependientes del tiempo.

La tesis está dividida en dos partes: la primera parte se centra en el transporte electrónico a través de un *triple punto cuántico* bajo la influencia de un *campo magnético dependiente del tiempo*. En la segunda parte se estudian las propiedades electrónicas de *grafeno* irradiado por un *campo eléctrico dependiente del tiempo*.

El estudio experimental y teórico del transporte electrónico a través de puntos cuánticos empezó hace más de veinte años, cuando se midieron por primera vez efectos de una única carga electrónica en sistemas mesoscópicos de semiconductores. Sin embargo, la primera realización experimental de un triple punto cuántico (TQD) data de hace un par de años. Un TQD es una formación de tres puntos cuánticos de semiconductores acoplados por túnel, en configuración triangular o lineal. A la vez que estos experimentos, se han publicado numerosos trabajos teóricos en los que se ha ido explorando la nueva física que ofrece un triple punto cuántico en contraste con la de un doble punto cuántico.

En el capítulo 1 de esta primera parte, se presenta una introducción al transporte electrónico a través de puntos cuánticos, donde se discuten las propiedades más importantes para fundamentar el contenido de los capítulos consecutivos. En particular, se tratan los efectos del espín en el transporte, como por ejemplo el efecto llamado bloqueo de espín. Debido a su importancia en el campo de información cuántica y su papel en el transporte en el régimen de bloqueo de espín, se explica brevemente la interacción del espín electrónico con los espines nucleares en su entorno, la interacción híperfina. El efecto de un campo magnético dependiente del tiempo en el espín electrónico en un punto cuántico se ha estudiado experimentalmente, revelando la posibilidad de controlar y manipular coherentemente el espín – una meta de enorme relevancia dentro del área de la información cuántica. Se han propuesto varios métodos experimentales para inducir tales rotaciones coherentes, de los cuales algunos se analizan en detalle. Finalmente se describen las diferentes configuraciones de un TQD y se comentan los trabajos teóricos y experimentals más relevantes realizados hasta la fecha presente.

El siguiente capítulo 2 está dedicado a la *técnica* que se a utilizado a lo largo de esta primera parte de la tesis para calcular el transporte electrónico en puntos cuánticos: la teoría de la matriz densidad en sistemas abiertos. Esta técnica permite estudiar la dinámica de sistemas cuánticos acoplados a reservorios externos, siendo por lo tanto la herramienta natural para estudiar transporte electrónico en puntos cuánticos. En este capítulo, se muestra la derivación de las ecuaciones de movimiento de

los elementos de la matriz densidad para un array de puntos cuánticos acoplados a contactos, y se desarrollan varios cálculos para un TQD cerrado (es decir, sin contactos) y abierto. Estos cálculos a la vez sirven de base para entender los resultados de los siguientes capítulos.

Los siguientes tres capítulos presentan los resultados obtenidos en relación con el *transporte electrónico en puntos cuánticos en presencia de campos magnéticos dependientes del tiempo*. En el capítulo 3 se calcula el transporte a través de un TQD triangular, que está sometido a campos magnéticos tanto estáticos como dependientes del tiempo. El campo estático induce un desdoblamiento entre los estados spin-up y spin-down del electrón (desdoblamiento Zeeman), entre los cuales el campo dependiente del tiempo induce rotaciones si su frecuencia está en resonancia con la diferencia energética. Primero se trata el caso de un solo electrón dentro del TQD, en el que, debido a un efecto llamado *atrapamiento coherente de población*, el electrón queda atrapado dentro del TQD bajo ciertas condiciones. En esta situación, se inducen rotaciones del espín del electrón que no se ven afectadas por la decoherencia inducida por los contactos (en primer orden de túnel a los contactos). A continuación, se introduce un segundo electrón en el TQD, de manera que la corriente se puede bloquear por medio de bloqueo de espín. El segundo electrón, por lo tanto, introduce correlaciones de espín entre los dos electrónes, y se pueden observar nuevos efectos con respecto al caso de sólo un electrón: la combinación de atrapamiento coherente, – el cual también ocurre con dos electrónes presentes, aunque de forma un poco diferente –, bloqueo de espín y campos magnéticos dependientes del tiempo, se puede utilizar para controlar el bloqueo de espín, es decir, tanto *romperlo* como *inducirlo*.

El siguiente capítulo 4 presenta los resultados para corrientes polarizadas de espín a través de dobles puntos cuánticos (DQD) y TQDs, inducidos por campos magnéticos estáticos y dependientes del tiempo. Este trabajo está motivado por la observación experimental de que la corriente a través de un DQD con sólo un electrón en un campo magnético estático. Experimentalmente se ha encontrado que, debido a la presencia de una diferencia considerable de desdoblamiento Zeeman entre los dos puntos cuánticos, – fabricados a partir de materiales distintos y por lo tanto con factores giromagnéticos distintos –, la corriente es máxima cuando ninguno de los niveles está alineado con el otro, y sufre un "atascamiento" cuando se alinean niveles del mismo espín. Se analiza que en esa situación un campo magnético dependiente del tiempo puede inducir una corriente altamente polarizada de espín, tanto en un DQD como en un TQD. Adicionalmente, se demuestra que un TQD puede funcionar como convertidor del espín.

La primera parte de la tesis termina con el capítulo 5, en el que se presentan los resultados obtenidos para explicar un experimento que se llevó a cabo en el grupo del Profesor A. Sachrajda (NRC, Canada). En este experimento, se midió la corriente a través de un TQD lineal en una configuración específica, en la que los dos puntos extremos están conectados a contactos, habiendo confinado un electrón en cada uno de los puntos cuánticos aplicando un voltaje electrostático. La corriente se bloquea debido a bloqueo de espín en dos direcciones opuestas de un voltaje externo, es decir, el TQD demuestra un bloqueo *bipolar* de espín. Adicionalmente, se muestra que el proceso de romper el bloqueo de espín ocurre a través de unos autoestados en los que un electrón está deslocalizado entre los dos extremos del TQD, sin pasar por el punto central.

La segunda parte de la presente tesis trata del estudio de las propiedades electrónicas de *grafeno*

irradiado por un campo eléctrico dependiente del tiempo. Aunque en los años inmediatamente posteriores a los primeros experimentos las propiedades electrónicas, magnéticas, ópticas, térmicas y mecánicas de grafeno se han estudiado con mucha intensidad, su comportamiento bajo la influencia de campos externos dependientes del tiempo es un campo relativamente nuevo, y pocos experimentos se han hecho hasta ahora. Desde el punto de vista teórico, se han publicado varios trabajos que sugieren que nuevos e interesantes efectos pueden ocurrir debido al efecto de campos dependientes del tiempo. La investigación en esta parte de la presente tesis se centra en el cálculo de la polarizabilidad dinámica de grafeno, y en qué manera cambian las interacciones electrón-electrón al aplicar un campo eléctrico dependiente del tiempo.

Los aspectos más importantes del grafeno libre están resumidos en el capítulo introductorio 6. El siguiente capítulo está dedicado al análisis de las propiedades electrónicas de grafeno irradiado por campos eléctricos dependientes del tiempo. Para tratar la dependencia del tiempo del campo externo, se introduce la teoría de Floquet, con la que se analiza el Hamiltoniano de grafeno para un campo externo tanto circular como linealmente polarizado. A continuación, se desarrollan varias aproximaciones analíticas que permiten captar la física para campos de intensidad débil, es decir los casos en los que sólo procesos de hasta un fotón juegan un papel relevante. Estas aproximaciones se utilizan entonces para calcular el espectro de cuasienergías y la densidad de estados, para ambas polarizaciones. Finalmente, se calcula la polarizabilidad dinámica para el caso de un campo circularmente polarizado. Se demuestra que la presencia de un campo dependiente del tiempo modifica las propiedades electrónicas tanto de excitaciones monopartícula como las colectivas, induciendo bandas prohibidas en la densidad de estados por un lado, y por otro lado induciendo un plasmón incluso para el grafeno sin dopar, donde en ausencia de un campo externo un plasmón de larga vida sólo existe cuando hay un dopaje finito. Así se muestra que con un campo eléctrico dependiente del tiempo se pueden manipular en gran medida las propiedades electrónicas del grafeno, lo cual podría tener un fuerte impacto en futuras aplicaciones electrónicas.

Part I.

Electronic transport and spin dynamics in lateral triple quantum dots

1. Transport through arrays of quantum dots

1.1. Introduction

Quantum dots are the solid state counterpart to real atoms [1, 2]. Due to strong confinement of electrons in all three directions in a solid state material, their energy spectrum is discrete with a level spacing big enough to be observed experimentally under certain conditions. Quantum dots have proven to be an excellent testing ground for atomic physics, owing to the fact that they can quite easily be manipulated by attaching leads or applying gates or external fields [3], in a regime that is not accessible in real atoms [4]. In electronic transport measurements in quantum dots the discrete nature of the electron charge has been displayed beautifully in conductance oscillations and the so-called Coulomb diamonds [5, 6], see Fig. 1.1. The number of free electrons in a quantum dot can routinely

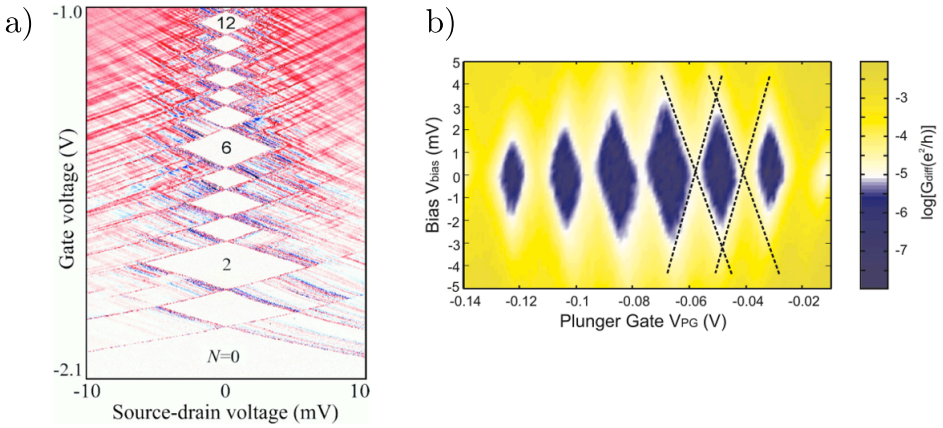

Figure 1.1.: **Coulomb blockade diamonds in quantum dots. a)** One of the first measurements of Coulomb blockade in a vertical few-electron InGaAs quantum dot. The numbers within the white rhombs stand for the number of electrons in the quantum dot. Figure taken from ref. [4]. **b)** Coulomb blockade diamonds in a graphene quantum dot. Figure taken from ref. [7].

be controlled and lowered down to two, one or even zero electrons [8, 9]. Single electron transport on the nanoscale has been extended successfully from semiconductor quantum dots – made of III-V semiconductors such as GaAs [8, 9] or II-VI semiconductors such as CdSe/ZnSe [10, 11] – to other materials: metallic nanoparticles [12, 13], carbon-based structures such as carbon nanotube quantum dots [14–17] or graphene quantum dots [7, 18–20], and organic materials, the last one having opened a whole new branch of research known as molecular electronics [21–23].

By confining single electrons, naturally one defines a two-level system out of the spin-up and spin-down component of the electron spin. It has become a widely pursued and at least partially achieved

goal to individually address and manipulate the single electron spin in a quantum dot [24–26], an effort motivated by the spin's potential role in a quantum computer [27]. However, difficulties arise with this task due to the spin-orbit coupling or the hyperfine interaction, i.e. the coupling of the electron spin to the spin of the nuclei in the host material [28–31]. These spin interactions, however, although they might be considered a disadvantage for perturbing the coherence of the electron spin and destroying its phase, can also be exploited in an advantageous way [32–34].

A natural step towards creating quantum networks for a future application in quantum information processing is to couple two or more quantum dots in an array to get so-called artificial molecules [35–38]. Double quantum dots have been investigated and are still being investigated to a great extent, as they have revealed new intriguing transport phenomena like for instance the spin blockade due to the Pauli exclusion principle, and current rectification due to spin blockade [39, 40]. They can also provide more insight into entanglement between spins and therefore be candidates for realizing a qubit. It seems only natural to extend the double quantum dot to the next level of complexity, the triple quantum dot. This extension is, however, far from being trivial, both from an experimental and theoretical point of view. Fundamentally new physics can occur in a three-level system such as an effect called *coherent population trapping*, – known from atomic optics for a long time [41] –, or spin-busing [42]. Another striking example of the non-triviality of a three-level system are three spins arranged in a triangle, where an antiferromagnetic ground state clearly cannot exist (*frustration*).

The first part of the present thesis is dedicated to the theoretical investigation of a few specific problems concerning electronic transport and spin dynamics in different configurations of a lateral semiconductor triple quantum dot array. In all problems, we take into account external magnetic dc fields that split the electron's degenerate spin-up and spin-down level. In several cases, single spin manipulation is considered by applying an ac magnetic field that rotates the electron spin under resonance conditions. The hyperfine interaction is taken into account in some problems in a phenomenological way in order to mimic its effect on spin dynamics.

In the next sections, basic properties of quantum dots and their fabrication will be summarized, as well as transport features of single and double quantum dot structures. Special emphasis will be placed on the spin blockade regime in transport through quantum dot arrays, in which several of the problems considered are set. Finally, the triple quantum dot array will be presented, with a short summary of former experimental and theoretical achievements in this system.

1.2. Quantum dots

In order to understand the electronic properties of a triple quantum dot, one must naturally first look at its smallest building block, the single quantum dot. In the following paragraphs, we will therefore start with an introduction to the properties of single and subsequently of double quantum dots, which will serve as a basis for the triple quantum dot that is treated later on.

A semiconductor quantum dot is an artificially made nanostructure of only a few tens of nm size. Depending on the way they are fabricated, one can distinguish different types of semiconductor

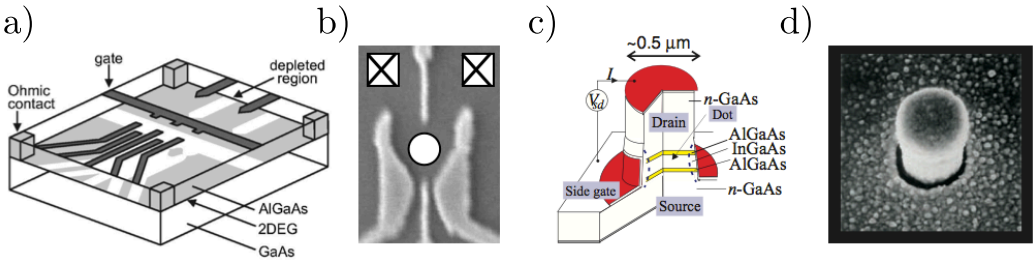

Figure 1.2.: **Lateral and vertical quantum dot. a)** Schematic view of a lateral quantum dot defined in a 2DEG (light gray). Depleted region in white, negative voltages applied to metal gate electrodes in dark gray. Ohmic contacts (light gray columns) to the 2DEG reservoirs. Figure taken from ref. [44]. **b)** Scanning electron micrograph of a lateral few-electron single quantum dot. The white dot indicates the location of the QD, and the white squares display Ohmic contact. Figure taken from ref. [9]. **c)** Schematic diagram of a vertical quantum dot, where the dot is located between the two AlGaAs tunnel barriers. The dashed curves indicate that a negative voltage applied to the side gate effectively reduces the diameter of the dot by squeezing it. Figure taken from ref. [3]. **d)** Scanning electron micrograph of a vertical circular quantum dot pillar, with a width of about 0.5¯m. Figure taken from ref. [3].

quantum dots: lateral, vertical, and self-assembled quantum dots[1]. Lateral semiconductor quantum dots, see Fig. 1.2 a) and b), are fabricated from the two-dimensional electron gas (2DEG) formed at a heterostructure interface of GaAs and AlGaAs. An electric field created by applying negative gate voltages to the heterostructure is used to locally deplete the 2DEG. The depleted regions can then be controlled through gate structures of only tens of nanometers size that are designed by electron beam lithography. Tunnel barriers to the 2DEG outside of the confined region are defined by applying metallic surface gates. With an electron mobility in the 2DEG as large as 1000 m^2/Vs and a relatively low density of $n \approx (1-5) \times 10^{15}$ m^{-2}, the mean free path of the electrons is several orders of magnitude bigger than the system dimensions, 100 ¯m, and the Fermi wavelength $\lambda_F \approx 80 - 30$ nm is roughly two orders of magnitude larger than in metals, due to the low density [45]. The term "lateral" expresses that the current through the quantum dot flows in the 2DEG plane to which the electrons are confined. In contrast, in a vertical quantum dot, the current flows in the direction perpendicular to the plane. The pillar where the vertical quantum dot is confined (see Fig. 1.2 c) and d) is etched from a semiconductor double-barrier heterostructure, typically made of GaAs and AlGaAs, and a metal gate electrode is deposited around the pillar. This double-barrier structure confines the electrons in the vertical direction, whereas the surface potential together with the gate potential provides confinement in the lateral x- and y-directions. In a central well of InGaAs between the double-barrier structure, the dot is formed with a thickness of about 12 nm [3].

A quantum dot contains roughly a million atoms and the same number of electrons [45]. The majority of the electrons, however, is tightly bound to the nuclei in the host material, and the number

[1]Self-assembled quantum dots form spontaneously in the process of epitaxial growth. They have favorable properties for electronic and optoelectronic device applications, are, however, not so well controllable with regard to placing gate electrodes, and we will not describe them in more detail here. For a short introduction, see ref. [43].

of free electrons in a quantum dot can be controlled to as low as zero electrons. This control was achieved quite early in vertical quantum dots [3]. In lateral quantum dots it proved more difficult to reduce the number of electrons without too much affecting the tunnel barriers: by applying more negative voltages that deplete the quantum dot, the current through the current barriers can become unmeasurably small. This disadvantage can, however, be compensated by an appropriate design of the surface gates. The first lateral few-electron quantum dots were fabricated by Ciorga *et al.* in a GaAs/AlGaAs heterostructure [9]. All calculations done in this thesis are assumed to be valid for lateral few-electron quantum dots.

1.3. Transport through quantum dots

Electron transport through quantum dots is governed by the electron charge on the one hand. On the other hand, a quantum dot with a single electron naturally defines a quantum-mechanical two-level system between spin-up and spin-down state of the electron's spin. We will first give an introduction to charging effects in transport through quantum dots, and then include the spin and its consequences for transport.

1.3.1. Coulomb blockade in a single quantum dot

In analogy to the ionization energy of atoms, the charging energy of a quantum dot is the energy cost one has to pay in order to overcome the Coulomb repulsion between the electrons on the dot when adding an extra electron. In a single quantum, as it is shown in Fig. 1.3, the chemical potential of the dot, when the number of electrons is changed by one, is

$$\mu_{N+1} - \mu_N = \Delta E + U, \tag{1.1}$$

where ΔE is the quantum mechanical level spacing and U the charging energy. If for fixed gate voltage the left and right chemical potentials of source (μ_S) and drain (μ_D) are arranged in such a way that the chemical potential of the dot is higher in energy than the source, no electron can tunnel through the dot and current is said to be blocked by *Coulomb blockade*. Increasing the gate voltage *lowers* the energy levels in the dots, therefore the current measured as a function of the gate voltage for fixed source-drain bias oscillates with a peak spacing that is directly proportional to the addition energy $\Delta E + U$, see Fig. 1.3. When adjusting the bias voltage at the same time, the conductance shows the above mentioned Coulomb diamonds, see Fig. 1.1 a) and b). The theory of Coulomb blockade oscillations has been studied in detail by Glazman *et al.* [47], Averin *et al.* [48, 49] and Beenakker [50]. So far, we have not said anything about the conditions under which these charging effects can be observed experimentally. In order for the Coulomb oscillations to be resolved in a transport experiment, two conditions have to be fulfilled [45]. First, the temperature has to be sufficiently low, $k_B T \ll \Delta E$. For a dot of about 100nm, the level spacing can be estimated to be ≈ 0.03 meV. The temperature then has to be lower, which is the case in a typical dilution refrigerator, where $T \approx 100\text{mK} \approx 0.0086$ meV. Second, in order for the number of electrons to be a well defined quantity on the dot, the barriers to the leads have to be sufficiently opaque. Considering the typical discharging time for the dot, $\Delta t = RC$, the

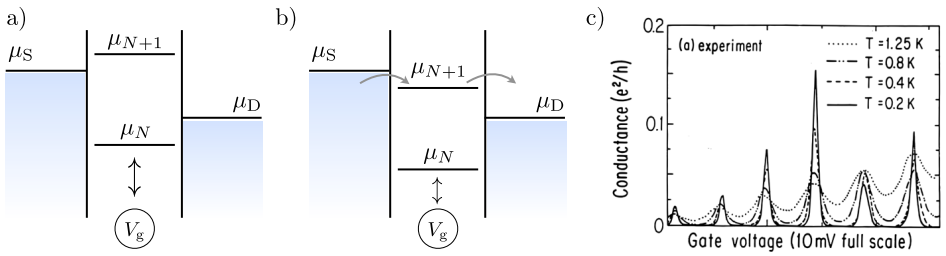

Figure 1.3.: **Coulomb blockade in a single quantum dot. a)** and **b)** The chemical potential of the dot is varied by the gate voltage V_g. If $\mu_{N+1} > \mu_S$, current is blocked. **c)** Measured Coulomb oscillations as a function of gate voltage for different temperatures. Figure taken from ref. [46].

associated energy uncertainty is $\Delta E \Delta t = (e^2/C)RC > h$ which implies that the barrier resistance has to be much larger than the resistance quantum $h/e^2 = 25813\ \mathrm{k}\Omega$. If this condition is met, the electron number fluctuations of the dot are negligible and the coupling to the leads is said to be weak.

1.3.2. Coherent transport through double quantum dots

Quantum dot arrays consist of two or more quantum dots connected in series or in parallel. Although the coupling between the dots can be regarded as classical if it is very weak, the interesting problem is to consider an array where the tunneling between the dots occurs in a phase-coherent way, so that an electron can tunnel many times between the dots before it leaves the array. Much like in a single quantum dot, the energy levels of a double quantum dot can be tuned by near-by gate voltages. Due to the discreteness of the energy spectrum, tunneling from one dot to another will be strong when the energy levels are *in resonance* (resonant tunneling), but is considerably suppressed for off-resonant energy levels. There are two representations of the energy levels in a quantum dot array: If the

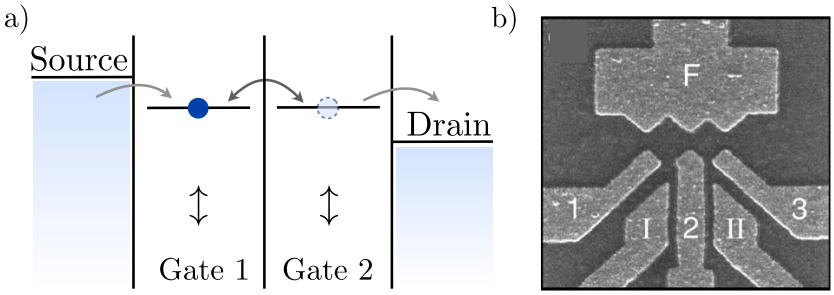

Figure 1.4.: **Lateral double quantum dot. a)** Schematic view of a lateral double quantum dot. If the energy levels are in resonance, an electron can tunnel many times between the dots. **b)** SEM micrograph of a double quantum dot defined by metallic gates (light gray areas). Figure taken from ref. [51].

interdot tunnel coupling is very strong (compared to the energy level detuning between the dots), the electron is delocalized over the whole array, and it is appropriate to speak of bonding and antibonding states, much like in a real molecule. Since a double quantum dot with one energy level per dot constitutes a quantum-mechanical two-level system, one knows that the antibonding and bonding

energy level are separated by $2|t|$, where t is the tunneling amplitude. Consequently, if interdot tunneling is weaker, this separation becomes smaller, and the *molecular* levels more and more resemble the *atomic* levels. Experimentally, precise control of the bonding between dots has been achieved [52]. Transport through single quantum dots has been described traditionally by classical rate equations [47–50] in terms of occupation numbers and tunneling rates to and from the leads. In order to include coherent effects coming from interdot tunneling, however, quantum effects play an important role, and these equations had to be modified, see e.g. ref. [53–55]. In this thesis, a reduced density matrix approach has been used to calculate both the dynamics of the isolated quantum dot system and transport through the open system. The detailed derivation of the corresponding equations of motion is presented in the following chapter.

Let us now continue by describing the stability diagram of a double quantum dot. The stability diagram constitutes a very important way of characterizing the electronic addition spectrum of a given quantum dot sample, and it permits one to get information about the electronic parameters of the dot, such as intradot charging or Coulomb energy U, see e.g. ref. [44]. At very low source-drain bias $V_{\mathrm{sd}} \approx 0$, the differential conductance of a nearby quantum point contact is measured as a function of the two gate voltages applied to each dot. The conductance in the quantum point contact next to the dot changes abruptly due to Coulomb interaction, when by changing the gate voltage an electron enters in one of the dots. These changes in conductance represent the borderlines of regions with a defined number of electrons, see Fig. 1.5. The most important feature in a stability diagram is the slope of the resonance lines, along which the dots are on resonance. In a double quantum dot, there is only the resonance line between the left and right dot (where $V_{g1} = V_{g2}$, see Fig. 1.5 b), in a triple quantum dot, however, three different resonance lines are present. This will be explained in more detail later on.

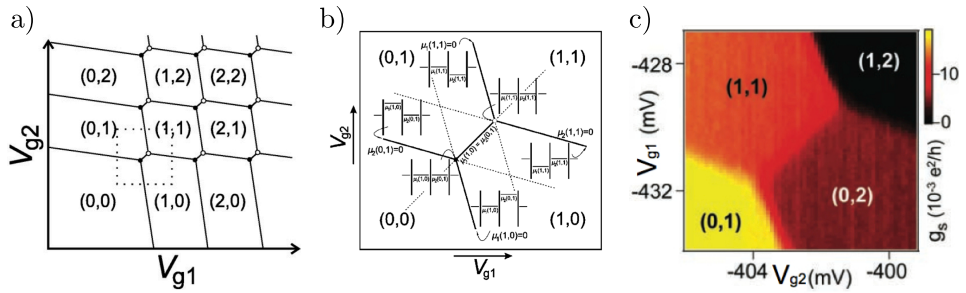

Figure 1.5.: **Stability diagram of a double quantum dot. a)** Schematic stability diagram as a function of two gate voltages. **b)** Zoom into the dotted square region of a). The chemical potentials of the double quantum dot are indicated. Along the diagonal line $V_{g1} = V_{g2}$, the two dots are on resonance. Figure taken from ref. [51]. **c)** Measured stability diagram of a double quantum dot, where the charge states are numbered by (n, m). Figure taken from ref. [31].

When applying a finite bias $V_{\mathrm{sd}} \neq 0$, current will flow only around the so-called triple points, i.e. where three charge configurations are resonant, see Fig. 1.5 b). A typical current measurement looks then like the one shown in Fig. 1.6: the current spots become current *triangles*. Inside the triangle, additional features can be detected, which are attributed to different resonance lines between ground

states and different excited states [51]. The triple points always occur in pairs, where one of the points is due to electron transport, and the other one due to hole transport.

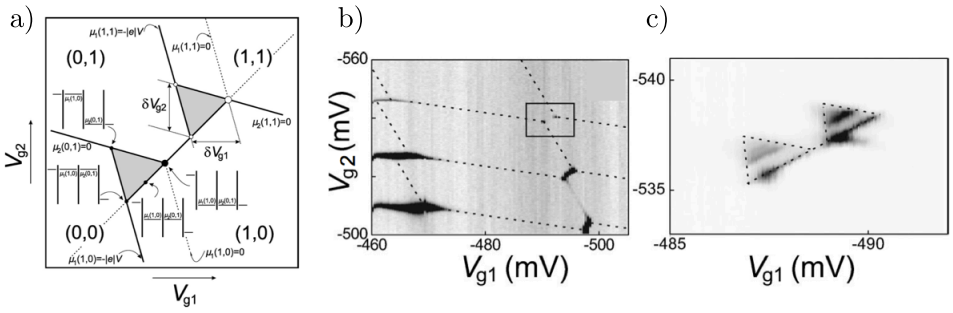

Figure 1.6.: **Current through a double quantum dot. a)** Schematic view of the current triangles at finite bias. **b)** Current through the double quantum dot at zero bias: only black current spots are visible at the triple points where three charge configurations are in resonance. **c)** Current through the double quantum dot at finite bias in the solid square region of b): the spots have increased to triangles with black resonance line features that indicate where the two dots are on resonance. Figures taken from ref. [31].

In a double quantum dot, not only charging effects due to Coulomb blockade are relevant, but also the spin of the electron can play an important role, depending on the electronic configuration of the energy levels in the double quantum dot.

1.3.3. Spin-blockade in double quantum dots

The spin analogue to Coulomb blockade in transport through quantum dots is the so-called *spin blockade*. It occurs when transport is blocked due to Pauli's exclusion principle. Consider a double quantum dot in which one electron is confined electrostatically (by means of a gate voltage) in the dot connected to the drain, see Fig. 1.7 (insets). A finite current is only measured when an electron can tunnel to the right dot onto a level of double occupation and, subsequently, to the drain. Note that this two-electron level has *singlet* character, i.e. only two electrons with different spin ($\uparrow\downarrow$) can occupy it. The two-electron excited level with *triplet* character ($\uparrow\uparrow^*$) is much higher in energy and not accessible at this configuration of gate voltages. For an electron entering from the left lead, a spin selection rule therefore holds for tunneling to the right dot: roughly speaking, if the two electrons have different spin, tunneling is allowed and a finite current flows. However, if both electrons have the same spin (($\uparrow,\uparrow$) or ($\downarrow,\downarrow$)), tunneling to the right dot is suppressed.

Let us consider the properly antisymmetrized eigenstates: Out of the five possible basis states $|\uparrow,\uparrow\rangle$, $|\uparrow,\downarrow\rangle$, $|\downarrow,\uparrow\rangle$, $|\downarrow,\downarrow\rangle$, $|0,\uparrow\downarrow\rangle$ (in the notation $|\mathrm{L},\mathrm{R}\rangle$ for an electron in the left dot L and in the right dot

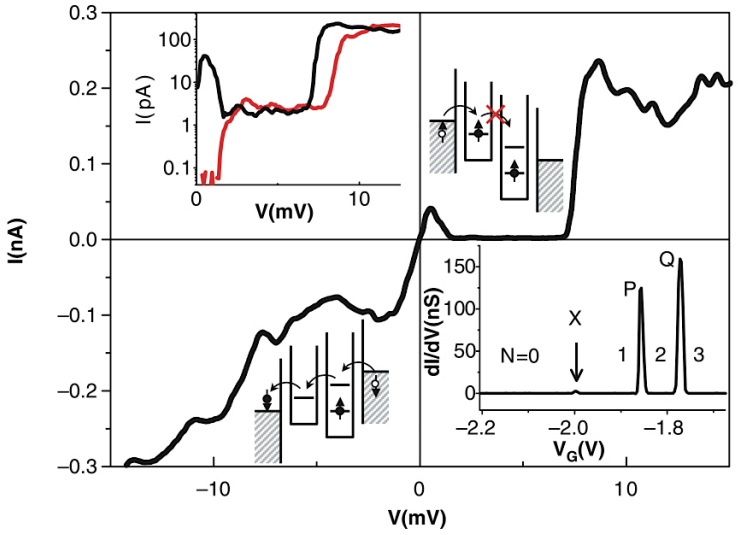

Figure 1.7.: **Spin blockade in a double quantum dot.** Measurement of spin blockade in the current through a double quantum dot. Note that the current drops to zero over a large range, and then suddenly increases. At that point, the excited state in the right quantum dot is accessible for the electron coming from the left and the blockade is lifted. Figure taken from ref. [39].

R) only two *singlet* eigenstates couple to $|0,\uparrow\downarrow\rangle$:

$$
\begin{aligned}
|S_+\rangle &= \frac{1}{\sqrt{2}}(|\uparrow,\downarrow\rangle - |\downarrow,\uparrow\rangle + \sqrt{2}|0,\uparrow\downarrow\rangle) \\
|S_-\rangle &= \frac{1}{\sqrt{2}}(|\uparrow,\downarrow\rangle - |\downarrow,\uparrow\rangle - \sqrt{2}|0,\uparrow\downarrow\rangle) \\
|T_+\rangle &= |\uparrow,\uparrow\rangle \\
|T_0\rangle &= \frac{1}{\sqrt{2}}(|\uparrow,\downarrow\rangle + |\downarrow,\uparrow\rangle) \\
|T_-\rangle &= |\downarrow,\downarrow\rangle
\end{aligned}
\tag{1.2}
$$

Tunneling processes in quantum dot arrays conserve the electron spin. Once an electron enters the double quantum dot and the two electrons form a *triplet* state ($|T_{\pm,0}\rangle$), this state blocks the current which then drops to zero. Spin-blockade in quantum dot arrays was theoretically predicted in 1995 by Weinmann *et al.* [56] and proposed as a spectroscopic tool by Ciorga *et al.* [9]. The first experimental observation of spin blockade in few-electron quantum dots was achieved by Ono *et al.* [39] in a vertical quantum dot, and Johnson *et al.* measured spin blockade in a lateral double quantum dot [40]. Fig. 1.7 shows the current measured by Ono *et al.* [39]: an electron is confined in the right quantum dot. For large enough positive bias, the interdot triplet states $|T_{\pm,0}\rangle$ will sooner or later be occupied, and then a current blockade due to Pauli's exclusion principle occurs, until the bias is again large enough ($\approx$ 7mV) for the triplet intradot level $|0,\uparrow\uparrow^*\rangle$ to enter the bias window. On the other hand, for negative bias, current can always flow: an electron can always tunnel from the singlet level in the right dot to the left dot (see inset in Fig. 1.7), which gives rise to a finite current.

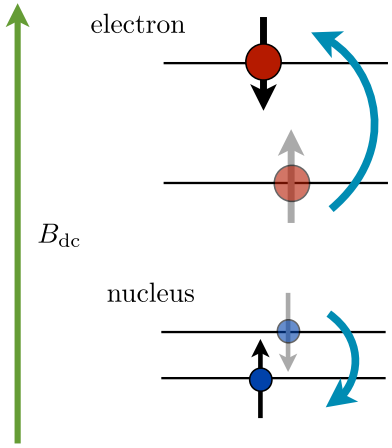

Figure 1.8.: **Spin-flip process between electron and nuclear spin.** Sketch of simultaneous spin-flip processes between electron and nuclear spin. At external magnetic field B_{dc}, the energy mismatch between the electronic and nuclear Zeeman energies is big, and a phonon must be dissipated for the process to occur.

1.3.4. Interactions of the electron spin with the environment

Shortly after the discovery of spin blockade in few-electron quantum dots, Koppens *et al.* measured a strikingly large leakage current in the Pauli blockade region of a double quantum dot [30]. This leakage current has been attributed to the hyperfine interaction between the electron spin and the spin of the nuclei in the surrounding material.

There are three main interactions of the electron spin with its environment in semiconductor quantum dots: the spin-orbit coupling, the hyperfine interaction with the nuclear spins in the host material, and also exchange processes with electrons in the leads. This last interaction process can be neglected, if one considers the tunnel coupling of the dot to the leads only as a weak perturbation [57].

In recent years, great efforts have been made for a deeper understanding of spin interactions in quantum dots, motivated to a large extent by the potential applications of quantum dots in future quantum information processing devices. A spin state can be destroyed by the environment in two different ways: on the one hand, the influence of the environment can lead to relaxation of the spin in form of a spin-flip process that takes place on a timescale T_1. On the other hand, the environment limits the time in which a superposition of spin-up and spin-down state of a single electron stays coherent. This time is referred to as the decoherence time T_2. For a spin ensemble in GaAs quantum wells, the dephasing time, denoted as T_2^*, typically provides a lower bound for the intrinsic decoherence time T_2. At zero magnetic field, energy relaxation is dominated by spin-flip processes involving the flip of a nucleus spin and an electron spin. The spin relaxation time T_1 in this case can be as low as $10 - 100$ns. Relaxation due to spin-orbit interaction is suppressed for zero Zeeman splittings due to Kramer's degeneracy [58]. For increasing external magnetic field B, spin-flip processes induced by hyperfine interaction become less probable since due to the energy mismatch between electronic and nuclei Zeeman splitting (see Fig. 1.8), a phonon must be dissipated. Consequently, T_1 increases fast

with increasing B and has been measured to be $T_1 = 2.58$ ms in a magnetic field $B = 0.02$ T [59]. For fields up to 2 T, T_1 can reach up to 200 ms [60]. The spin ensemble dephasing time T_2^* has been found to be of the order of several 10 ns [30, 31]. In general, the timescale for the loss of phase coherence, T_2, is much shorter than the relaxation time, and results mainly from fluctuations in the nuclear field. If one could suppress the effect of the nuclear field on the phase coherence of the spin, the spin-orbit interaction would still provide the limit $T_2 = 2T_1$ [44], which is, however, very long. According to measurements on quantum dots by Fujisawa *et al.* [57], the spin-flip time $T_1 > 10^{-6}$ s is much longer than the typical tunneling time $T_{\text{tunnel}} = 1 - 100$ ns. This implies that spin-flip processes due to hyperfine interaction play an important role in the spin blockade regime, where tunneling is suppressed due to Pauli's exclusion principle (see before). In the following, we will give a rough overview of the theory of hyperfine interaction in the context of transport through quantum dot arrays in the spin blockade regime. A more profound and general study, however, is beyond the scope of this thesis, and the interested reader shall be referred e.g. to ref. [61–68].

The hyperfine interaction is given by the Hamiltonian

$$H_{\text{HF}} = \sum_{i=1}^{N} A_i \mathbf{I}_i \cdot \mathbf{S}, \tag{1.3}$$

where $\mathbf{I}$ is the nuclear spin, $\mathbf{S}$ the electron spin and A the coupling strength between them. The ensemble of the nuclear spins can be described as a semiclassical magnetic field, the Overhauser field $\mathbf{B}_{\text{N}} \approx \frac{1}{g\mu_B} \sum_{i=1}^{N} A_i \mathbf{I}_i$. The effect of this field is like that of an external magnetic field $\mathbf{B}_0$ and can be added to the Zeeman energy [63, 30], thus giving a total Zeeman splitting

$$\Delta_{\text{Z}} = g\mu_B \mathbf{B}_0 \cdot \mathbf{S} + g\mu_B \mathbf{B}_{\text{N}} \cdot \mathbf{S}. \tag{1.4}$$

The electron g-factor in GaAs is negative $g = -0.44$ [25], hence the ground state of both the nuclei and electrons in GaAs is parallel to the external field, i.e., spin-up (see also Fig. 1.8). In general, the coupling of the electron to the nuclear field is different for each dot, so that an electron in a quantum dot experiences a different splitting Δ_i in different dots. As a consequence, the eigenstates in Eq. (1.2) are not pure singlet and triplet states any more, but are mixed: The off-diagonal coupling due to the nuclear field couples the $|T_0\rangle$ state to the $|S_\pm\rangle$ state (see Eq. (1.2)). If in transport through a quantum dot array in the spin blockade regime a spin-flip process $|T_\pm\rangle \rightsquigarrow |T_0\rangle$ occurs, the coupling between $|T_0\rangle$ and $|S_\pm\rangle$ induced by the hyperfine interaction opens a current channel, which is the cause for the measured leakage current in ref. [30]. It is important to note that the hyperfine-induced spin-flip processes are the more efficient the closer the participating states are in energy. It is therefore crucial to know the eigenenergy spectrum and its (anti)crossings between singlet and triplet states. For a double quantum dot in the spin blockade regime, the spectrum for homogeneous and inhomogeneous Zeeman splittings is shown in Fig. 1.9. The anticrossings due to the coupling between singlet $|S_\pm\rangle$ and triplet $|T_0\rangle$ states are marked by circles, where spin-flip processes become more probable.

In the problems considered in this thesis, spin relaxation processes are mimicked by including a phenomenological spin-flip rate into the equations of motion of the density matrix. This will be explained in the corresponding chapters.

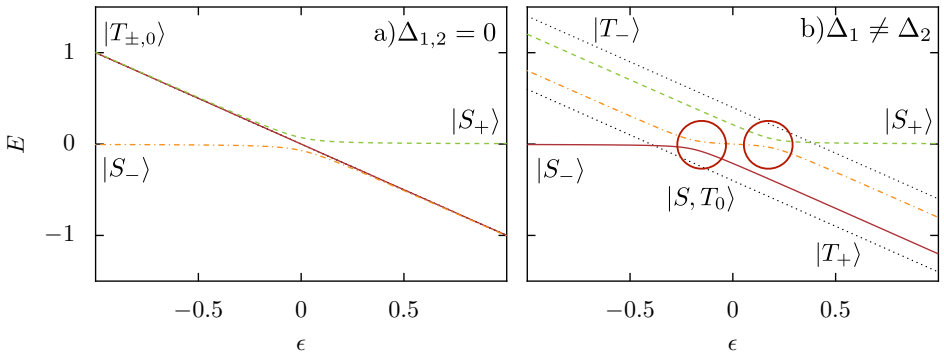

Figure 1.9.: **Eigenenergy spectrum of a double quantum dot with two electrons. a)** Eigenenergies for zero Zeeman splittings. **b)** Eigenenergies for inhomogeneous Zeeman splittings, where the $|T_0\rangle$ state mixes with the $|S_\pm\rangle$ states, see Eq. (1.2).

1.3.5. Electron spin resonance in quantum dots

With regard to the coherent manipulation and control of a single spin in a quantum dot, an important goal to achieve is the ability to drive coherent rotations between the spin-up and spin-down state of a quantum dot. The most direct way of rotating the electron spin is *electron spin resonance* (ESR). There, crossed dc and ac magnetic fields are applied to the system, so that the ac frequency is in resonance with the splitting induced by the dc magnetic field. In quantum dots, electron spin resonance was performed experimentally by Koppens *et al.* [26, 69, 70]. An in-plane dc magnetic field B_{dc} is applied to the 2DEG where the quantum dots are localized. The field B_{dc} creates a Zeeman splitting in z-direction, i.e. the former degenerate spin-levels $\uparrow$ and $\downarrow$ are now split by an amount $\Delta_{\mathrm{Z}} = g\mu_{\mathrm{B}}B_{\mathrm{dc}}$, see Fig. 1.10. Here g is the electron g-factor (that depends on the dot geometry and the material it is

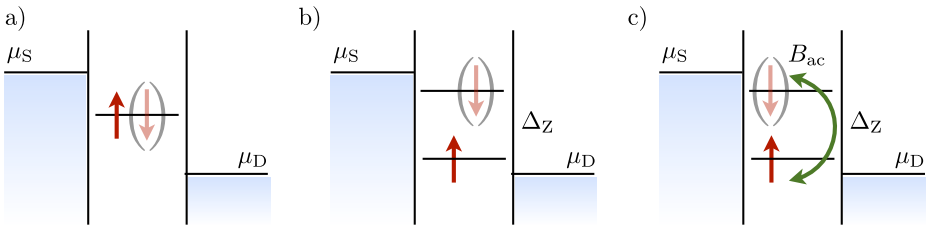

Figure 1.10.: **Crossed dc and ac magnetic fields applied to a quantum dot. a)** Zero fields. Both spin states are degenerate. **b)** A dc field splits the spin-up and spin-down state by Δ_{Z}. **c)** An additional ac field rotates the spin for $\omega_{\mathrm{ac}} = \Delta_{\mathrm{Z}}$.

made of), and μ_{B} is the Bohr magneton. In this thesis, a g-factor of GaAs quantum dots of $g \approx -0.44$ is assumed [25]. For a typical value of $B_{\mathrm{dc}} = 1\mathrm{T}$, the Zeeman splitting is $\Delta_{\mathrm{Z}} \approx 0.025$ meV. An ac magnetic field B_{ac} is applied perpendicularly to the dc field, so that it rotates the electron spin if its frequency is resonant with the Zeeman splitting

$$\hbar\omega_{\mathrm{ac}} = \Delta_{\mathrm{Z}}. \tag{1.5}$$

The Hamiltonian for a dc magnetic field in z-direction and a circularly polarized ac magnetic field in xy-direction reads

$$H_{\mathrm{B}}(t) = \Delta_{\mathrm{Z}} S_z + B_{\mathrm{ac}} \left[\cos(\omega t) S_x + \sin(\omega t) S_y\right], \tag{1.6}$$

with the spin operator $S = \frac{1}{2}\sum_{\sigma\sigma'} \hat{c}^{\dagger}_{\sigma}\sigma_{\sigma\sigma'}\hat{c}_{\sigma'}$ and the Pauli spin matrices $\sigma_{\sigma\sigma'}$. From the theoretical point of view, a circularly polarized field has the advantage that it can be transformed into the rotating reference frame by a unitary transformation

$$U(t) = \exp\left(-i\omega_{\mathrm{ac}} t S_z\right), \tag{1.7}$$

which yields a time-independent Hamiltonian

$$H_{\mathrm{B}} = (\Delta_{\mathrm{Z}} - \omega_{\mathrm{ac}}) S_z + B_{\mathrm{ac}} S_x. \tag{1.8}$$

The time-independent Hamiltonian can be useful for the interpretation of certain transport features, as will become clear in chapters 3 and 4.

It is of particular importance here to explain the effect of the time-dependent magnetic field on spin blockade. It can be shown that the time-dependent magnetic field B_{ac} has no effect on spin blockade as long as the Zeeman splittings in the different dots are homogeneous. The ac field does not mix the singlet $|S_{\pm}\rangle$ and triplet $|T_{\pm,0}\rangle$ subspace (see Eq. (1.2)) for homogeneous Zeeman splittings, so if the electrons occupy a triplet state, the ac field only induces rotations among the triplet states and spin blockade is not lifted. If, however, the Zeeman splittings are different, the triplet state $|T_0\rangle$ is mixed with the singlet states $|S_{\pm}\rangle$. The ac magnetic field therefore *breaks spin blockade* by rotating the electron e.g. from a state $|T_+\rangle$ to $|T_0\rangle$ which is now coupled to $|S_{\pm}\rangle$. As it has been mentioned before, the Zeeman splittings in quantum dot arrays are typically slightly inhomogeneous due to the different Overhauser splittings induced by the hyperfine interaction, and a time-dependent field B_{ac} therefore breaks spin blockade.

In the original experiment by Koppens *et al.* [26], electron spin resonance was detected in a double quantum dot in the spin blockade regime. There the current through the double quantum dot showed peaks that occur when one Zeeman splitting is resonant with the frequency of the applied ac field. The detection scheme is as follows: Due to a confined electron in the right dot, current through the double dot can be blocked by spin blockade. By applying an ac magnetic field with a fixed frequency ω_{ac} and simultaneously varying the dc magnetic field, which changes the Zeeman splittings, there will be a moment when e.g. the left Zeeman splitting of the double quantum dot is in resonance with the ac frequency. Then, an electron in the left dot is rotated and can tunnel to the two-electron singlet level in the right dot, see Fig. 1.11 a) (upper panel). This explains the two current peaks at ± 100 mT in Fig. 1.11 a) (lower panel), that are absent if the ac field is turned off. The large current peak at zero dc magnetic field is traced back to the hyperfine interaction, which is particularly strong for zero field, where the singlet and triplet states are very close in energy. In addition to the current measurement as a function of the dc magnetic field, the authors were also able to detect coherent spin oscillations induced by the ac field. This is shown in Fig. 1.11 b). A gate pulse prepares the double quantum dot in Coulomb blockade in such a way that the electron in the left dot stays there, because the two-electron level in the right dot is energetically inaccessible. In this stage the magnetic ac field induces

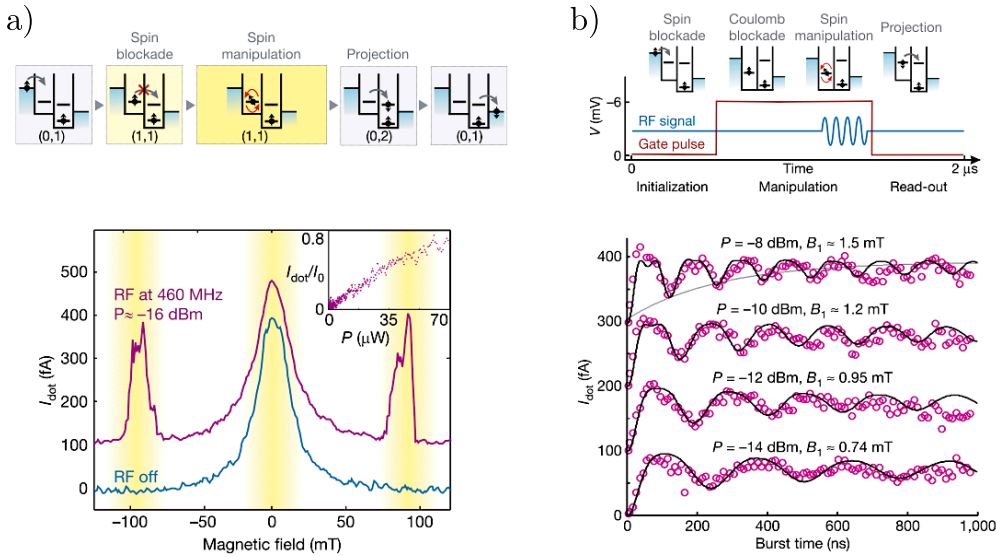

Figure 1.11.: **Electron spin resonance in a double quantum dot in the spin blockade regime. a)** Schematic view of the transport sequence through the double quantum dot (upper panel) and measured current through the double quantum dot as a function of the external magnetic field for fixed frequency ω_{ac} (lower panel). ESR peaks occur around $\pm$100mT, where the Zeeman splittings are resonant with the ac frequency. At zero field, hyperfine-induced spin-flip processes make way for a large leakage current. **b)** Schematic view of the pulse sequence for the measurement of coherent spin oscillations (upper panel) and measured oscillations for different field strength B_{ac} (lower panel). Figures taken from ref. [26].

rotations of the electron spin in the left dot. After a certain rotation time, the gate pushes back the right dot's level so that the doubly occupied energy level is energetically accessible. Then, depending on the spin state of the rotated electron in the left dot, tunneling to the right dot and subsequently to the right lead takes place, if the two electrons have antiparallel spins, but does not occur, if they have parallel spins, see Fig. 1.11 b) (upper panel). As a consequence, the current oscillates as a function of different burst times, see Fig. 1.11 b) (lower panel). These rotations are so-called Rabi oscillations, whose frequency is linearly proportional to the ac field intensity B_{ac} [26, 71]. We will encounter Rabi oscillations, on the one hand spatial, due to tunneling [51], and on the other hand within one dot, due to an ac magnetic field, in a later chapter of the present thesis (see chapter 3).

Although theoretically fairly easily described, electron spin resonance induced by crossed dc and ac magnetic fields is experimentally challenging. The electric fields that inevitably accompany the magnetic ac fields have to be minimized in order not to induce photon-assisted tunneling [73–75]. Therefore, several other techniques have been proposed for driving coherent electron spin oscillations. The main idea behind those other techniques is to actually use an electrical ac field and couple it to the spin degree of freedom via mediating mechanisms. These mechanisms can be hyperfine interaction [32], spin-orbit interaction [33], g-factor modulation [76] or slanting Zeeman fields [72]. In this last alternative for instance, an effective magnetic field gradient that is imposed by a ferromagnetic strip

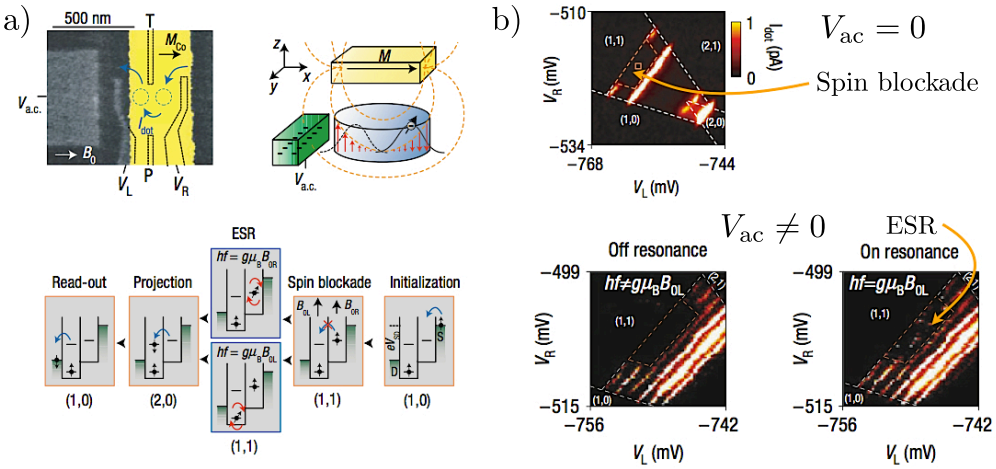

Figure 1.12.: **Electron spin resonance in a double quantum dot in the spin blockade regime, using slanting Zeeman fields. a)** Views of the double quantum dot with a micromagnet placed on top (yellow), which creates a magnetic field gradient along the device. **b)** Charge stability diagrams of the double quantum dot for zero ac electric field (upper panel), off-resonant (lower left) and resonant ac electric field (lower right), where ESR spots appear in the spin blockade region. Figures taken and adapted from ref. [72].

placed on top of the double quantum dot structure and by an additional external in-plane field (see Fig. 1.12 a), yields a different magnetic field in each dot, so that an electron in the left dot feels a field pointing upwards, whereas an electron in the right dot feels a field pointing downwards. The ac electric field is used to periodically displace the electron from one dot to the other, thereby achieving spin rotations of the electron, see Fig. 1.12 b).

1.4. The triple quantum dot

Before the first experimental realization of a few-electron triple quantum dot in 2006 [77], several theoretical proposals existed for triple quantum dots as entanglers [78] or coded qubits [79, 80], and they were predicted to show rectification and ratchet functionalities [81, 82]. Subsequently, a considerable amount of theoretical works on triple quantum dots has accumulated: starting from the fundamental investigation of their electronic filling scheme via topological Hund rules [83], more complex physics has been explored on electronic properties in magnetic [84] and electric fields [85]. A genuine characteristic of a three–level system has been investigated in triple quantum dots: the formation of a *dark state*. This term, which originally stems from atomic optics [86, 87], expresses the fact that in an atom a coherent superposition of two states decouples from the third, which results in the atom becoming *dark*. A solid state analogue has been made for electronic transport through a triangular triple quantum dot both without [88–91] and under an externally applied magnetic field [92, 93]. Ac driven transport in triple quantum dot nanoelectromechanical shuttles has been analyzed by means of Floquet theory [94], and generic interference phenomena have been shown to exist in

triple quantum dot molecules [95]. Furthermore, the role of the electron spin in both linear and triangular triple quantum dots has been investigated in spin-selective Aharonov-Bohm oscillations [96], voltage-controlled spin manipulation [97], entangled GHZ state generation [98, 99], in electron spin resonance in magnetic ac field driven triple quantum dots [93, 100] (see chapter 3), and by proposing spin inversion induced by ac magnetic fields in transport through a linear triple quantum dot [101] (see chapter 4). Very recently, spin blockade has been analyzed in a linear triple quantum dot filled with up to three electrons [102]. Last but not least, triple quantum dots constitute a fruitful testing ground for Kondo physics [103–106].

On the experimental side, after early attempts to fabricate a linear triple quantum dot [107, 108], the charge stability diagram for triangular and linear, lateral and vertical triple quantum dots has been mapped out only quite recently [16, 77, 109–111]. It has been found [112] that in analogy to the triple points in a double quantum dot (see Fig. 1.5), transport through a triple quantum dot occurs around *quadruple points* (QP), where four charge configurations are resonant. Naturally, the stability diagram of a triple quantum dot is more complex than for a double quantum dot, as there are three independent parameters (three gate voltages applied to the three dots), and the full stability diagram is consequently three-dimensional. By measuring the transconductance of a linear triple quantum dot as a function of left and right gate voltages for fixed center gate voltages, and successively varying the center gate voltage, a three-dimensional charge stability diagram has been achieved by Granger *et al.* [113], see Fig. 1.13. The stability diagram shows a unique triple quantum dot feature, – i.e. one

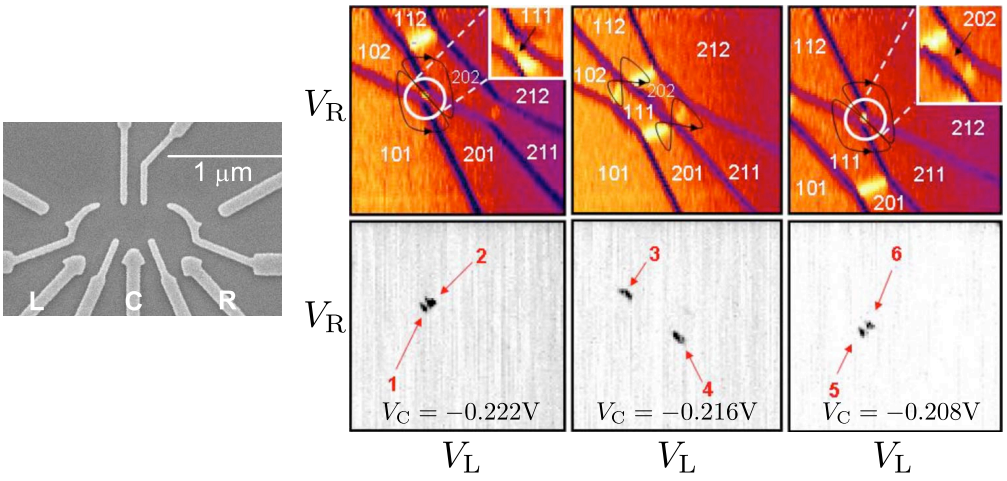

Figure 1.13.: **Charge stability diagram of a linear triple quantum dot.** *Left:* Electron micrograph of a linear triple quantum dot. *Right:* Charge stability diagram as a function of left (V_L) and right (V_R) gate voltage, for three different values of the center gate voltage. The charge configurations are indicated by white numbers in the upper panels. The red numbers in the lower panels indicate the six different quadruple points around which transport is possible for finite bias, see also arrows in the upper panels. Figures taken from ref. [113].

that does not exist in double quantum dots –, commonly referred to as quantum cellular automata process [77]: a charge reconfiguration from the (202) to the (111) region (see upper middle panel in Fig. 1.13) requires a change of the electron number by one in each dot. For four electrons inside the

triple quantum dot, the energy is minimized by placing the electrons in both extremes, but with only three electrons, minimal energy is achieved by their equilibrated repartition in the triple quantum dot. It has been indicated earlier that a particularly important feature of the stability diagram are the resonance lines, i.e. lines along which certain dots are on resonance. Their importance becomes clear when measuring transport for finite bias. The resonance lines in a triple quantum dot can be left-center (LC), center-right (CR) and left-right (LR) resonances. All three of them have different slopes which depend crucially on the electrostatic parameters, i.e. on the cross capacitances between the dots, which, by varying e.g. the left gate voltage, do not only influence the left energy levels, but also to a certain extent the center energy levels and the right energy levels. In Fig. 1.13, the LC line is visible e.g. in the upper rightmost panel as the bright borderline between the (111) and (201) regions, whereas the CR line can be seen in the upper middle panel as the border between (102) and (111). The interpretation of resonance lines in transport experiments will be a topic in chapter 5.

In addition to the stability diagram, coherent control over the three-spin qubit, – a linear triple quantum dot filled with one electron in each dot –, has been reported very recently [114, 115]. In ref. [115], the manipulation of coherent superpositions of quantum states has been achieved by employing the Landau-Zener-Stückelberg method [116]. There, coherence between three spin states has been maintained while decreasing the coupling between two spins and simultaneously increasing the coupling to the other spin.

All in all, both experimental and theoretical advances in understanding the properties of triple quantum dots over the past few years indicate that there is rich and interesting physics to explore in these systems, and yet more is going to come.

2. Density matrix formalism and master equation

In this chapter we describe the theory of the reduced density matrix, one of the theoretical methods that is used to calculate electron transport through quantum dot systems. We first introduce the concept of the density operator of a quantum system and then deduce the master equation for the reduced density matrix. In the following sections we use the master equation in order to calculate the occupation probabilities in a closed linear triple quantum dot (TQD) and the related Rabi frequencies for spatial Rabi oscillations. Finally, as an example, we use the general current formula that is applied to all subsequent problems to calculate the current through a linear and triangular TQD.

2.1. The density matrix

In quantum mechanics the time evolution of a pure state is described by the Schrödinger equation

$$i\hbar\frac{d}{dt}|\psi(t)\rangle = H(t)|\psi(t)\rangle. \tag{2.1}$$

However, one often encounters the problem of finding the time evolution of a physical system whose state is not completely determined, but rather described by a statistical mixture of states. In this case the Schrödinger equation cannot be used and one has to find a formalism that both includes the incomplete information one possesses about the system and gets the maximum use out of it.
The mathematical formalism which fulfills this requirement is the density matrix formalism. In the following we will give a short outline of the theory of the density matrix. A more detailed introduction can be found e.g. in ref. [117].

2.1.1. Basic properties

If a system is described by a statistical mixture of states rather than by a linear superposition of states, there is no state $|\psi\rangle$ that comprises all information about the system. The only thing one can say about the system is that, with a probability of p_n, it can be found in the state $|\psi_n\rangle$, so that

$$\begin{aligned} 0 \leq p_1, p_2, p_3, \ldots, p_n, \ldots \leq 1 \\ \sum_n p_n = 1. \end{aligned} \tag{2.2}$$

The density operator of the system is then defined as

$$\rho = \sum_n p_n |\psi_n\rangle\langle\psi_n|, \tag{2.3}$$

and it fulfills the normalization condition

$$\mathrm{Tr}\rho = \sum_n p_n \mathrm{Tr}\{|\psi_n\rangle\langle\psi_n|\} = 1. \tag{2.4}$$

A system can be described by its density matrix both if it is in a pure state – i.e. if it can be described by a state vector $|\psi\rangle$ – or if it is in a mixed state. Only if the system is in a pure state, then

$$\rho^2 = \rho \quad \text{and} \quad \mathrm{Tr}\rho^2 = 1, \tag{2.5}$$

whereas for a statistical mixture $\rho = \sum_n p_n |\psi_l\rangle\langle\psi_n|$

$$\rho^2 = \sum_{n,l} p_n p_l |\psi_n\rangle\langle\psi_n|\psi_l\rangle\langle\psi_l| \neq \rho \Rightarrow \mathrm{Tr}\rho^2 < 1. \tag{2.6}$$

The expectation value of every observable can be expressed in terms of the density operator

$$\begin{aligned}\langle A\rangle &= \sum_n p_n \langle\psi_n|A|\psi_n\rangle = \sum_{n,l} p_n \langle\psi_n|A|\phi_l\rangle\langle\phi_l|\psi_n\rangle \\ &= \sum_{n,l} \langle\phi_l|p_n|\psi_n\rangle\langle\psi_n|A|\phi_l\rangle \\ &= \mathrm{Tr}\{\rho A\}.\end{aligned} \tag{2.7}$$

Every operator in quantum mechanics can be represented as a matrix by choosing a certain basis of states. The matrix elements of the density operator have, of course, special meanings and they depend on the basis of states one chooses. For a basis $|\phi_l\rangle$ the diagonal elements are

$$\langle\phi_l|\rho|\phi_l\rangle = \sum_n p_n \langle\phi_l|\psi_n\rangle\langle\psi_n|\phi_l\rangle = \sum_n p_n |c_{nl}|^2, \tag{2.8}$$

with $c_{nl} = \langle\psi_n|\phi_l\rangle$. The diagonal elements are therefore positive definite numbers, whose meaning is the *population* of the basis state $|\phi_l\rangle$. The off-diagonal elements

$$\langle\phi_j|\rho|\phi_l\rangle = \sum_n p_n \langle\phi_j|\psi_n\rangle\langle\psi_n|\phi_l\rangle = \sum_n p_n c^*_{nj} c_{nl} \tag{2.9}$$

are cross terms between the basis states $|\phi_l\rangle$ and $|\phi_j\rangle$. If they are non-zero, there is interference between these states, which only exists if $|\psi_n\rangle$ is a *coherent superposition* of $|\phi_l\rangle$ and $|\phi_j\rangle$. The off-diagonal elements are therefore called *coherences*. It is clear that depending on the basis in which the density matrix is written the off-diagonal elements can be zero or non-zero.

2.1.2. Time evolution of the density matrix

The equation of motion of the density matrix can easily be derived using the Schrödinger equation. We suppose that the system at an initial time t_0 is in state $|\psi_n\rangle$ with a probability p_n. Its time evolution is

$$i\hbar \frac{\partial}{\partial t}|\psi_n(t)\rangle = H(t)|\psi_n(t)\rangle, \tag{2.10}$$

by which the time evolution of the corresponding density operator $\rho_n(t) = |\psi_n(t)\rangle\langle\psi_n(t)|$ becomes

$$\begin{aligned}\frac{\partial}{\partial t}\left(|\psi_n(t)\rangle\langle\psi_n(t)|\right) &= \frac{1}{i\hbar} H(t)|\psi_n(t)\rangle\langle\psi_n(t)| - \frac{1}{i\hbar}|\psi_n(t)\rangle\langle\psi_n(t)|H(t) \\ &= \frac{1}{i\hbar}\left[H(t), \rho_n(t)\right].\end{aligned} \tag{2.11}$$

For $\rho(t) = \sum_n p_n |\psi_n(t)\rangle\langle\psi_n(t)|$ we obtain then

$$\frac{\partial}{\partial t}\rho(t) = \frac{1}{i\hbar}\left[H(t), \rho(t)\right]. \tag{2.12}$$

This is the so-called Liouville equation for the time evolution of the density operator of a quantum system in a mixed state.

This equation is sufficient to describe the time evolution of an isolated system. If there are, however, two or more systems interacting with each other and one is only interested in the behavior of one of them, then one can introduce the *reduced density matrix* that captures the behavior of one of the subsystems.

2.1.3. The reduced density matrix

We consider a system $\mathcal{S}$ which we are interested in and which is in contact with an unobserved system $\mathcal{R}$. $\mathcal{S}$ is described by the basis $|s_l\rangle$, while $\mathcal{R}$ is described by $|r_n\rangle$. The elements of the total density matrix can then be written as

$$\rho(t) = \langle r_{n'} s_{l'} | \rho(t) | r_n s_l \rangle. \tag{2.13}$$

The expectation value of an operator $A_\mathcal{S}$ that only acts on $\mathcal{S}$ can be written as

$$\begin{aligned}
\langle A_\mathcal{S} \rangle &= Tr\{\rho(t) A_\mathcal{S}\} \\
&= \sum_{n'l'} \langle r_{n'} s_{l'} | \rho(t) A_\mathcal{S} | r_{n'} s_{l'} \rangle \\
&= \sum_{nln'l'} \langle r_{n'} s_{l'} | \rho(t) | r_n s_l \rangle \langle r_n s_l | A_\mathcal{S} | r_{n'} s_{l'} \rangle \\
&= \sum_{nll'} \langle r_n s_{l'} | \rho(t) | r_n s_l \rangle \langle s_l | A_\mathcal{S} | s_{l'} \rangle \\
&= \sum_{ll'} \left[\sum_n \langle r_n s_{l'} | \rho(t) | r_n s_l \rangle \right] \langle s_l | A_\mathcal{S} | s_{l'} \rangle,
\end{aligned} \tag{2.14}$$

where the expression in brackets are the elements of a matrix $\rho(s,t)$

$$\langle s_{l'} | \rho(s,t) | s_l \rangle = \sum_n \langle r_n s_{l'} | \rho(t) | r_n s_l \rangle, \tag{2.15}$$

in which the sum over n means *tracing out* the degrees of freedom of the system $\mathcal{R}$. We finally conclude

$$\langle A_\mathcal{S} \rangle = \sum_{ll'} \langle s_{l'} | \rho(s,t) | s_l \rangle \langle s_l | A_\mathcal{S} | s_{l'} \rangle. \tag{2.16}$$

Thus, the expectation value of every operator $A_\mathcal{S}$ acting on $\mathcal{S}$ can be calculated only by knowing the density operator $\rho(s,t)$. This operator is therefore called the *reduced density matrix*.

The system $\mathcal{S}$ is considered to be in non-equilibrium, before it comes in contact with the system $\mathcal{R}$. Due to the interaction with $\mathcal{R}$, however, $\mathcal{S}$ will evolve into an equilibrium state after some time. The process from a non-equilibrium state into equilibrium induced by the coupling to an environment is a relaxation process and therefore *irreversible*. The Liouville equation, however, describes only reversible processes, and one needs to extend it in order to take into account the relaxation due to the coupling to an environment.

2.2. The master equation

We write the total Hamiltonian for a system $\mathcal{S}$ coupled to a reservoir $\mathcal{R}$ as

$$H = H_{\mathcal{S}} + H_{\mathcal{R}} = H_0 + V(t). \tag{2.17}$$

Since H_0 is assumed to be known, it is convenient for our subsequent derivations to change from the Schrödinger picture to the interaction picture. In the interaction picture the time dependence of an operator due to H_0 is extracted, so that an operator A is given by

$$A_I = e^{\frac{i}{\hbar}H_0 t} A e^{-\frac{i}{\hbar}H_0 t}, \tag{2.18}$$

with A being the operator in the Schrödinger picture. The density matrix operator in the interaction picture reads then

$$\rho(t) = e^{-\frac{i}{\hbar}H_0 t} \rho_I(t) e^{\frac{i}{\hbar}H_0 t}, \tag{2.19}$$

and the Liouville equation (2.12) becomes therefore

$$\rho_I(t) = -\frac{i}{\hbar}\left[V_I(t), \rho_I(t)\right]. \tag{2.20}$$

This equation can formally be integrated to

$$\rho_I(t) = \rho_I(0) - \frac{i}{\hbar}\int_0^t dt' \left[V_I(t'), \rho_I(t')\right], \tag{2.21}$$

which in turn inserted back into Eq. (2.20) yields

$$\frac{\partial}{\partial t}\rho_I(t) = -\frac{i}{\hbar}\left[V_I(t), \rho_I(0)\right] - \frac{1}{\hbar^2}\int_0^t dt' \left[V_I(t), \left[V_I(t'), \rho_I(t')\right]\right]. \tag{2.22}$$

In order to write down this equation for the reduced density matrix, we use $\rho_{\mathcal{S}}(t) = \mathrm{Tr}_{\mathcal{R}}\rho(t)$ and get

$$\frac{\partial}{\partial t}\rho_{I,\mathcal{S}}(t) = -\frac{i}{\hbar}\mathrm{Tr}_{\mathcal{R}}\left[V_I(t), \rho_I(0)\right] - \frac{1}{\hbar^2}\int_0^t dt' \mathrm{Tr}_{\mathcal{R}}\left[V_I(t), \left[V_I(t'), \rho_I(t')\right]\right]. \tag{2.23}$$

Assuming that the interaction between the two systems begins at the time $t = 0$, $\mathcal{S}$ and $\mathcal{R}$ are uncorrelated for $t < 0$. Therefore the total density matrix at $t = 0$ can be written as the product of the density matrices of the individual systems:

$$\rho(0) = \rho_{\mathcal{S}}(0)\rho_{\mathcal{R}}(0) = \rho_I(0) \tag{2.24}$$

To proceed further, consider that the system $\mathcal{R}$ is large and can always be described by a thermal equilibrium distribution at constant temperature, $\rho_{\mathcal{R}} = \frac{1}{Z}e^{-\beta H_{\mathcal{R}}}$, where $\beta = 1/k_{\mathrm{B}}T$ with the Boltzmann constant k_{B} and temperature T. The irreversibility of the relaxation process is expressed in the fact that the reactions of $\mathcal{R}$ back on $\mathcal{S}$ are expected to be negligible, by which follows

$$\rho_I(t) \to \rho_I(t) = \rho_{\mathcal{S}}(t)\rho_{\mathcal{R}}(0). \tag{2.25}$$

This important step is called the *Born*–approximation. Inserting into (2.23) yields

$$\frac{\partial}{\partial t}\rho(t)_{I,\mathcal{S}} = -\frac{i}{\hbar}\mathrm{Tr}_{\mathcal{R}}\left[V_I(t), \rho_{\mathcal{S}}(0)\rho_{\mathcal{R}}(0)\right] - \frac{1}{\hbar^2}\int_0^t dt' \mathrm{Tr}_{\mathcal{R}}\left[V_I(t), \left[V_I(t'), \rho_{I,\mathcal{S}}(t')\rho_{\mathcal{R}}(0)\right]\right]. \tag{2.26}$$

A useful approximation that turns out to be valid in a wide range of situations is the so–called *Markov*–approximation: the system $\mathcal{S}$ suffers a damping process due to its interaction with $\mathcal{R}$, which destroys all memory of the past. Consequently, the time derivative of the density matrix only depends on its present value $\rho_{I,\mathcal{S}}(t)$ and not on former times t' in the time intervall $[0,t]$. Mathematically this means

$$\rho_{I,\mathcal{S}}(t') \to \rho_{I,\mathcal{S}}(t). \tag{2.27}$$

The intermediate result for the equation of motion of the density matrix is then

$$\frac{\partial}{\partial t}\rho(t)_{I,\mathcal{S}} = -\frac{i}{\hbar}\mathrm{Tr}_{\mathcal{R}}\left[V_I(t), \rho_{\mathcal{S}}(0)\rho_{\mathcal{R}}(0)\right] - \frac{1}{\hbar^2}\int_0^t dt' \mathrm{Tr}_{\mathcal{R}}\left[V_I(t), \left[V_I(t'), \rho_{I,\mathcal{S}}(t)\rho_{\mathcal{R}}(0)\right]\right]. \tag{2.28}$$

In order to calculate the commutators we write the interaction term as a product of operators $A_{\mathcal{S}}$ and $B_{\mathcal{R}}$ that only act on $\mathcal{S}$ and $\mathcal{R}$ respectively. Since they commute, in the interaction picture they have the form

$$V_I(t) = \sum_i A_{\mathcal{S},i}(t) B_{\mathcal{R},i}(t). \tag{2.29}$$

After inserting this into Eq. (2.28) and making use of the permutation rule $Tr(ABC) = Tr(BCA) = Tr(CAB)$, we get after some algebra

$$\begin{aligned}\frac{\partial}{\partial t}\rho_{I,\mathcal{S}}(t) = -\frac{i}{\hbar}\sum_i \left[A_{\mathcal{S},i}(t), \rho_{\mathcal{S}}(0)\right]\langle B_{\mathcal{R},i}\rangle - \\ \frac{1}{\hbar^2}\sum_{i,j}\int_0^t dt' \Big[\left[A_{\mathcal{S},i}(t), A_{\mathcal{S},j}(t')\rho_{I,\mathcal{S}}(t)\right]\mathrm{Tr}_{\mathcal{R}}\left[B_{\mathcal{R},i}(t)B_{\mathcal{R},j}(t')\rho_{\mathcal{R}}(0)\right] - \\ \left[A_{\mathcal{S},i}(t), \rho_{I,\mathcal{S}}(t)A_{\mathcal{S},j}(t')\right]\mathrm{Tr}_{\mathcal{R}}\left[B_{\mathcal{R},i}(t)\rho_{\mathcal{R}}(0)B_{\mathcal{R},j}(t')\right]\Big].\end{aligned} \tag{2.30}$$

Here we have also used $\langle B_{\mathcal{R},i}\rangle = \mathrm{Tr}_{\mathcal{R}}\left[\rho_{\mathcal{R}}(0)B_{\mathcal{R},i}(t)\right]$. Choosing eigenstates $|N\rangle$ of the Hamiltonian $\mathcal{H}_{\mathcal{R}}$ as a basis, the equilibrium density matrix $\rho_{\mathcal{R}}(0)$ is diagonal, whereas $B_{\mathcal{R},i}$ does not have diagonal elements, since otherwise they could be included in the diagonal elements of the Hamiltonian (which would provide an overall energy shift). Consequently we have $\langle B_{\mathcal{R},i}\rangle = 0$, and the first term in (2.30) cancels out.

The terms $\mathrm{Tr}_{\mathcal{R}}\left[B_{\mathcal{R},i}(t)B_{\mathcal{R},j}(t')\rho_{\mathcal{R}}(0)\right] = \langle B_{\mathcal{R},i}(t)B_{\mathcal{R},j}(t')\rangle$ in (2.30) are time correlation functions, in which the time difference $t-t'$ is the range over which $\langle B_{\mathcal{R},i}(t)B_{\mathcal{R},j}(t')\rangle \neq 0$. The correlation functions in fact only depend on the time difference $t-t'$, since

$$\begin{aligned}\langle B_{\mathcal{R},i}(t)B_{\mathcal{R},j}(t')\rangle &= \mathrm{Tr}\left[B_{\mathcal{R},i}(t)B_{\mathcal{R},j}(t')\rho_{\mathcal{R}}(0)\right] \\ &= \mathrm{Tr}\left[e^{-\frac{i}{\hbar}H_{\mathcal{R}}t}B_{\mathcal{R},i}e^{\frac{i}{\hbar}H_{\mathcal{R}}t}e^{-\frac{i}{\hbar}H_{\mathcal{R}}t'}B_{\mathcal{R},j}e^{\frac{i}{\hbar}H_{\mathcal{R}}t'}\rho_{\mathcal{R}}(0)\right] \\ &= \mathrm{Tr}\left[B_{\mathcal{R},i}(t-t')B_{\mathcal{R},j}\rho_{\mathcal{R}}(0)\right].\end{aligned} \tag{2.31}$$

Let the correlation time of the system be τ, then for $t-t' \gg \tau$

$$\langle B_{\mathcal{R},i}(t)B_{\mathcal{R},j}(t')\rangle \approx \langle B_{\mathcal{R},i}(t)\rangle\langle B_{\mathcal{R},j}(t')\rangle = 0. \tag{2.32}$$

This can be used to change the integration variable $t'' = t - t'$ and $dt' = -dt''$ in (2.30). The upper

integration limit can safely be extended to infinity due to Eq. (2.32), and Eq. (2.30) becomes then

$$\frac{\partial}{\partial t}\rho_{I,\mathcal{S}}(t) = -\frac{1}{\hbar^2}\sum_{i,j}\int_0^\infty dt''\Big[\left[A_{\mathcal{S},i}(t), A_{\mathcal{S},j}(t-t'')\rho_{I,\mathcal{S}}(t)\right]\langle B_{\mathcal{R},i}(t'')B_{\mathcal{R},j}\rangle - \\ - \left[A_{\mathcal{S},i}(t), \rho_{I,\mathcal{S}}(t)A_{\mathcal{S},j}(t-t'')\right]\langle B_{\mathcal{R},j}B_{\mathcal{R},i}(t'')\rangle\Big]. \quad (2.33)$$

In the end we are interested in the matrix elements of $\rho_{I,\mathcal{S}}(t)$. We therefore choose a basis of eigenstates $|m\rangle$ of the Hamiltonian $H_\mathcal{S}$. Taking matrix elements of $A_{\mathcal{S},i}(t)$ yields

$$\langle m'|A_{\mathcal{S},i}(t)|m\rangle = \langle m'|e^{\frac{i}{\hbar}H_0 t}A_{\mathcal{S},i}e^{-\frac{i}{\hbar}H_0 t}|m\rangle = e^{i\omega_{m'm}t}\langle m'|A_{\mathcal{S},i}|m\rangle, \quad (2.34)$$

with $\omega_{m'm} = E_{m'} - E_m$ being the difference of eigenenergies $E_{m',m}$ of the Hamiltonian H_0. Inserting the completeness condition $\sum_n |n\rangle\langle n|$ at appropriate positions, the first commutator in Eq. (2.33) becomes

$$\langle m'|\left[A_{\mathcal{S},i}(t), A_{\mathcal{S},j}(t-t'')\rho_{I,\mathcal{S}}(t)\right]|m\rangle = \\ \sum_{nn'}\Big[e^{i\omega_{m'n'}t - i\omega_{nn'}t''}\langle m'|A_{\mathcal{S},i}|n\rangle\langle n|A_{\mathcal{S},j}|n'\rangle\langle n'|\rho_{I,\mathcal{S}}(t)|m\rangle - \\ e^{i\omega_{m'n'}(t-t'')+i\omega_{nm}t}\langle m'|A_{\mathcal{S},j}|n'\rangle\langle n'|\rho_{I,\mathcal{S}}(t)|n\rangle\langle n|A_{\mathcal{S},i}|m\rangle\Big] \quad (2.35)$$

and the second commutator

$$\langle m'|\left[A_{\mathcal{S},i}(t), \rho_{I,\mathcal{S}}(t)A_{\mathcal{S},j}(t-t'')\right]|m\rangle = \\ \sum_{nn'}\Big[e^{i\omega_{m'n}t - i\omega_{n'm}(t-t'')}\langle m'|A_{\mathcal{S},i}|n\rangle\langle n|\rho_{I,\mathcal{S}}(t)|n'\rangle\langle n'|A_{\mathcal{S},j}|m\rangle - \\ e^{i\omega_{nm}t + i\omega_{n'n}t''}\langle m'|\rho_{I,\mathcal{S}}(t)|n\rangle\langle n|A_{\mathcal{S},j}|n'\rangle\langle n'|A_{\mathcal{S},i}|m\rangle\Big]. \quad (2.36)$$

Therefore we get for the matrix element of $\langle m'|\dot{\rho}_{I,\mathcal{S}}(t)|m\rangle$

$$\langle m'|\dot{\rho}_{I,\mathcal{S}}(t)|m\rangle = -\frac{1}{\hbar^2}\sum_{ij}\sum_{nn'}\langle n'|\rho_{I,\mathcal{S}}(t)|n\rangle\times \\ \Big[e^{i\omega_{m'n'}t}\sum_\alpha\langle m'|A_{\mathcal{S},i}|\alpha\rangle\langle\alpha|A_{\mathcal{S},j}|n'\rangle\int_0^\infty dt'' e^{-i\omega_{\alpha n'}t''}\langle B_{\mathcal{R},i}(t'')B_{\mathcal{R},j}\rangle\delta_{nm} - \\ -e^{i(\omega_{m'n'}+\omega_{nm})t}\langle m'|A_{\mathcal{S},j}|n'\rangle\langle n|A_{\mathcal{S},i}|m\rangle\int_0^\infty dt'' e^{-i\omega_{m'n'}t''}\langle B_{\mathcal{R},i}(t'')B_{\mathcal{R},j}\rangle - \\ -e^{i(\omega_{m'n'}+\omega_{nm})t}\langle m'|A_{\mathcal{S},i}|n'\rangle\langle n|A_{\mathcal{S},j}|m\rangle\int_0^\infty dt'' e^{-i\omega_{nm}t''}\langle B_{\mathcal{R},j}B_{\mathcal{R},i}(t'')\rangle + \\ +e^{i\omega_{nm}t}\sum_\alpha\langle n|A_{\mathcal{S},j}|\alpha\rangle\langle\alpha|A_{\mathcal{S},i}|m\rangle\int_0^\infty dt'' e^{-i\omega_{n\alpha}t''}\langle B_{\mathcal{R},j}B_{\mathcal{R},i}(t'')\rangle\delta_{n'm'}\Big]. \quad (2.37)$$

By defining

$$\Gamma^+_{mkln} = \frac{1}{\hbar^2}\sum_{ij}\langle m|A_{\mathcal{S},i}|k\rangle\langle l|A_{\mathcal{S},j}|n\rangle\int_0^\infty dt'' e^{-i\omega_{ln}t''}\langle B_{\mathcal{R},i}(t'')B_{\mathcal{R},j}\rangle \\ \Gamma^-_{mkln} = \frac{1}{\hbar^2}\sum_{ij}\langle m|A_{\mathcal{S},j}|k\rangle\langle l|A_{\mathcal{S},i}|n\rangle\int_0^\infty dt'' e^{-i\omega_{mk}t''}\langle B_{\mathcal{R},j}B_{\mathcal{R},i}(t'')\rangle, \quad (2.38)$$

which fulfill

$$\Gamma^\pm_{mmkl} = \Gamma^\pm_{klmm} = 0 \\ \Gamma^{-*}_{mnkl} = \Gamma^+_{mnkl}, \quad (2.39)$$

and by defining the *Redfield-Tensor* $\mathcal{R}_{m'mn'k}$

$$\mathcal{R}_{m'mn'n} = -\delta_{nm}\sum_{\alpha}\Gamma^{+}_{m'\alpha\alpha n'} + \Gamma^{+}_{nmm'n'} + \Gamma^{-}_{nmm'n'} - \delta_{n'm'}\sum_{\alpha}\Gamma^{-}_{n\alpha\alpha m} \tag{2.40}$$

we can write Eq. (2.37) in a much more compact way:

$$\langle m'|\dot{\rho}_{I,\mathcal{S}}|m\rangle = \sum_{nn'}\langle n'|\rho_{I,\mathcal{S}}(t)|n\rangle\mathcal{R}_{m'mn'n}e^{i(\omega_{m'n'}+\omega_{nm})t} \tag{2.41}$$

One argues now that the typical period of variation of the system, $\frac{\hbar}{\omega_{mn}}$, is much smaller than the integration step dt, i. e. the system $\mathcal{S}$ performs many cycles in the intervall dt. Therefore only the terms with $(\omega_{m'n'} + \omega_{nm}) \approx 0$ will contribute to Eq. (2.41) [118, 119]. This condition,

$$E_{m'} - E_{n'} + E_n - E_m = 0, \tag{2.42}$$

is fulfilled in the following three cases

1. $m' = n'$ and $m = n$, but $m' \neq m$
2. $m' = m$ and $n' = n$, but $m' \neq n'$
3. $m' = n' = n = m$,

which reduce Eq. (2.41) to

$$\begin{aligned}\langle m'|\dot{\rho}_{I,\mathcal{S}}(t)|m\rangle = (1-\delta_{m'm})\langle m'|\rho_{I,\mathcal{S}}(t)|m\rangle\mathcal{R}_{m'mm'm} + \\ \delta_{m'm}\sum_{n\neq m}\langle n|\rho_{I,\mathcal{S}}(t)|n\rangle\mathcal{R}_{mmnn} + \\ \delta_{m'm}\langle m'|\rho_{I,\mathcal{S}}(t)|m'\rangle\mathcal{R}_{m'm'm'm'}.\end{aligned} \tag{2.43}$$

The first and third term with $\mathcal{R}_{m'mm'm}$ and $\mathcal{R}_{m'm'm'm'}$ can be grouped together because the first one contains the second one when the condition $m \neq m'$ is omitted. We define

$$\mathcal{R}_{m'mm'm} = \Lambda_{m'm} = \sum_{\alpha\neq m'}\Gamma^{+}_{m'\alpha\alpha m'} + \sum_{\alpha\neq m}\Gamma^{-}_{m\alpha\alpha m}. \tag{2.44}$$

The Redfield-Tensor in the second term in Eq. (2.43) written out explicitely only contains two summands, which are

$$\mathcal{R}_{mmnn} = \Gamma^{+}_{nmmn} + \Gamma^{-}_{nmmn}, \tag{2.45}$$

as the parts including the δ's drop out. Thus, for

$$\Gamma_{mn} = \Gamma^{+}_{nmmn} + \Gamma^{-}_{nmmn} = 2\mathrm{Re}\Gamma^{+}_{nmmn}, \tag{2.46}$$

we finally obtain the master equation

$$\langle m'|\dot{\rho}_{I,\mathcal{S}}(t)|m\rangle = \delta_{m'm}\sum_{n\neq m}\langle n|\rho_{I,\mathcal{S}}(t)|n\rangle\Gamma_{mn} - \Lambda_{m'm}\langle m'|\rho_{I,\mathcal{S}}(t)|m\rangle. \tag{2.47}$$

Let us now distinguish between diagonal and off-diagonal elements. The diagonal elements read

$$\langle m|\dot{\rho}_{I,\mathcal{S}}(t)|m\rangle = \sum_{n\neq m}\langle n|\rho_{I,\mathcal{S}}(t)|n\rangle\Gamma_{mn} - \langle m|\rho_{I,\mathcal{S}}(t)|m\rangle\Gamma_{nm}. \tag{2.48}$$

They coincide with the classical rate equations for a *loss and gain* process, where due to a detailed balance condition the loss in some states is related to the population of other states. The coefficients Γ_{mn} are the rates for a transition from a state $|n\rangle$ to a state $|m\rangle$ that is induced by the coupling of system $\mathcal{S}$ to the unobserved system $\mathcal{R}$.

For the off-diagonal terms or coherences we get

$$\langle m'|\dot{\rho}_{I,\mathcal{S}}(t)|m\rangle = -\Lambda_{m'm}\langle m'|\rho_{I,\mathcal{S}}(t)|m\rangle, \tag{2.49}$$

with $\Lambda^*_{m'm} = \Lambda_{mm'}$ due to the Hermiticity of the density matrix. These elements describe how coherence in the system is damped by the coupling to the environment. The real part of the coherences is related to the transition rates Γ_{mn} through

$$\begin{aligned}\mathrm{Re}\Lambda_{m'm} &= \frac{1}{2}\left(\Lambda_{m'm} + \Lambda^*_{m'm}\right) = \frac{1}{2}\left(\Lambda_{m'm} + \Lambda_{mm'}\right) \\ &= \frac{1}{2}\left(\sum_{\alpha\neq m}\Gamma_{\alpha m'} + \sum_{\alpha\neq m}\Gamma_{\alpha m}\right).\end{aligned} \tag{2.50}$$

Let us now return to the Schrödinger picture by applying

$$\rho_{\mathcal{S}}(t) = e^{-\frac{i}{\hbar}H_{\mathcal{S}}t}\rho_{I,\mathcal{S}}(t)e^{\frac{i}{\hbar}H_{\mathcal{S}}t}, \tag{2.51}$$

which yields for the equation of motion

$$\dot{\rho}_{\mathcal{S}}(t) = -\frac{i}{\hbar}[H_{\mathcal{S}}, \rho_{\mathcal{S}}(t)] + e^{-\frac{i}{\hbar}H_{\mathcal{S}}t}\dot{\rho}_{I,\mathcal{S}}(t)e^{\frac{i}{\hbar}H_{\mathcal{S}}t}. \tag{2.52}$$

The matrix elements are then

$$\langle m|\dot{\rho}_{\mathcal{S}}(t)|m\rangle = \sum_{n\neq m}\Gamma_{mn}\langle n|\rho_{\mathcal{S}}(t)|n\rangle - \Gamma_{nm}\langle m|\rho_{\mathcal{S}}(t)|m\rangle \qquad \text{for } m = m' \tag{2.53}$$

$$\langle m'|\dot{\rho}_{\mathcal{S}}(t)|m\rangle = -\frac{i}{\hbar}\langle m'|[H_{\mathcal{S}}, \rho_{\mathcal{S}}(t)]|m\rangle - \Lambda_{m'm}\langle m'|\rho_{\mathcal{S}}(t)|m\rangle \qquad \text{for } m \neq m', \tag{2.54}$$

where in the off-diagonal elements we can neglect the imaginary part of $\Lambda_{m'm}$, since it only introduces a small energy shift. In practice this set of differential equations can either be integrated to give $\rho_{mm}(t)$, i.e. the time evolution of the occupation probabilities, or, – if one is primarily interested in the asymptotic limit $\rho(\infty)$, i.e. the stationary solution –, one can set $\dot{\rho}(t) = 0$ and solve the set of equations algebraically. The latter is faster, but only applicable if the Hamiltonian is time-independent.

In the next sections, we will derive the formula for the transition rates Γ_{mn} and finally for the current.

2.2.1. Transition rates

The transition rates Γ_{mn} describe the probability per unit time that the system undergoes a transition between the state $|k\rangle$ and $|m\rangle$ caused by interaction with the reservoir. Starting with

$$\begin{aligned}\Gamma_{mn} &= \Gamma^+_{mnnm} + \Gamma^-_{mnnm} \\ &= \frac{1}{\hbar^2}\sum_{ij}\langle m|A_{\mathcal{S},i}|n\rangle\langle n|A_{\mathcal{S},j}|m\rangle\int_0^\infty dt'' e^{-i\omega_{nm}t''}\langle B_{\mathcal{R},i}(t'')B_{\mathcal{R},j}\rangle \\ &+ \frac{1}{\hbar^2}\sum_{ij}\langle m|A_{\mathcal{S},j}|n\rangle\langle n|A_{\mathcal{S},i}|m\rangle\int_0^\infty dt'' e^{-i\omega_{mn}t''}\langle B_{\mathcal{R},j}B_{\mathcal{R},i}(t'')\rangle,\end{aligned} \tag{2.55}$$

we continue by evaluating the expectation values $\langle B_{\mathcal{R},i}(t'')B_{\mathcal{R},j}\rangle$. Using eigenstates $|N\rangle$ of the Hamiltonian $H_\mathcal{R}$ for which $\langle N|H_\mathcal{R}|N\rangle = E_N$, and using the fact that $\rho_\mathcal{R}(0)$ is diagonal in this basis, we get

$$\begin{aligned}\Gamma_{mn} = &\frac{1}{\hbar^2}\sum_{ij}\sum_{NN'}\langle m|A_{\mathcal{S},i}|n\rangle\langle n|A_{\mathcal{S},j}|m\rangle \\ &\int_0^\infty dt'' e^{\frac{i}{\hbar}(E_N-E_{N'})t''}e^{-i\omega_{nm}t''}\langle N|\rho_\mathcal{R}(0)|N\rangle\langle N|B_{\mathcal{R},i}|N'\rangle\langle N'|B_{\mathcal{R},j}|N\rangle \\ &+\frac{1}{\hbar^2}\sum_{ij}\sum_{NN'}\langle m|A_{\mathcal{S},j}|n\rangle\langle n|A_{\mathcal{S},i}|m\rangle \\ &\int_0^\infty dt'' e^{\frac{i}{\hbar}(E_{N'}-E_N)t''}e^{-i\omega_{nm}t''}\langle N|\rho_\mathcal{R}(0)|N\rangle\langle N|B_{\mathcal{R},j}|N'\rangle\langle N'|B_{\mathcal{R},i}|N\rangle. \end{aligned} \tag{2.56}$$

This can now be simplified by changing the integration variable from t'' to $-t''$

$$\begin{aligned}\Gamma_{mn} = &\frac{1}{\hbar^2}\sum_{ij}\sum_{NN'}\langle N|\rho_\mathcal{R}(0)|N\rangle\times \\ &\Big[\langle mN|A_{\mathcal{S},i}B_{\mathcal{R},i}|nN'\rangle\langle nN'|A_{\mathcal{S},j}B_{\mathcal{R},j}|mN\rangle\int_0^\infty dt'' e^{\frac{i}{\hbar}(E_N-E_{N'}-\hbar\omega_{nm})t''}+ \\ &\langle mN|A_{\mathcal{S},j}B_{\mathcal{R},j}|nN'\rangle\langle nN'|A_{\mathcal{S},i}B_{\mathcal{R},i}|mN\rangle\int_{-\infty}^0 dt'' e^{\frac{i}{\hbar}(E_N-E_{N'}-\hbar\omega_{nm})t''}\Big]. \end{aligned} \tag{2.57}$$

Substituting $V = \sum_i A_{\mathcal{S},i}B_{\mathcal{R},i}$ yields then

$$\frac{1}{\hbar^2}\sum_{NN'}\langle N|\rho_\mathcal{R}(0)|N\rangle|\langle mN|V|nN'\rangle|^2\int_{-\infty}^\infty dt'' e^{\frac{i}{\hbar}(E_N-E_{N'}-\hbar\omega_{nm})t''}, \tag{2.58}$$

which by using $\int_{-\infty}^\infty dk e^{\pm ik(x-a)} = 2\pi\delta(x-a)$ finally becomes

$$\Gamma_{mn} = \frac{2\pi}{\hbar}\sum_{NN'}\langle N|\rho_\mathcal{R}(0)|N\rangle|\langle mN|V|nN'\rangle|^2\delta(E_N - E_{N'} - \hbar\omega_{nm}). \tag{2.59}$$

The transition rates therefore adopt the form of the well-known Fermi golden rule expression of first order time-dependent perturbation theory.

Tunneling rates

In this thesis the master equation is used to calculate transport through arrays of quantum dots. The system $\mathcal{S}$ is the quantum dot array, whereas the unobserved system $\mathcal{R}$ are the leads that are coupled by tunneling to the quantum dot system. The coupling is modeled by the Hamiltonian

$$V = H_\mathrm{T} = \sum_{l,k}\gamma_l(\hat{d}_{lk}^\dagger\hat{c} + \hat{c}^\dagger\hat{d}_{lk}), \tag{2.60}$$

where $\hat{d}_{lk}^\dagger, \hat{d}_{lk}$ are the creation and annihilation operators for an electron in lead l, and $\hat{c}^\dagger, \hat{c}$ are the ones for electrons in the dot closest to the lead. The coupling γ_l is assumed to be weak. The interaction with the reservoir $\mathcal{R}$ consists in the tunneling of an electron from the system to a lead or vice versa. There are therefore two different processes to be considered, to which we will refer as "+", if an electron is transferred from the system to a lead (for increasing number of electrons in the lead) or as

"−" if an electron enters from the lead into the system. In both processes, the number of electrons in the system differs by one. With $\rho_{lN} = \langle N|\rho_{\mathcal{R}}(0)|N\rangle$ the transition rates are

$$\Gamma_{mn} = \frac{2\pi}{\hbar}\sum_{NN'}\rho_{lN}|\langle mN|V|nN'\rangle|^2\delta(E_N - E_{N'} - \hbar\omega_{nm}). \tag{2.61}$$

If an electron is extracted from a dot to one of the leads, only the term $\hat{d}_{lk}^\dagger\hat{c}$ contributes and the transition probability becomes

$$\begin{aligned}\sum_{NN'}\rho_{lN}|\langle mN|V|nN'\rangle|^2 &= \sum_{NN'k}\rho_{lN}|\gamma_l|^2|\langle mN|\hat{d}_{lk}^\dagger\hat{c}|nN'\rangle|^2\\ &= \sum_{NN'k}\rho_{lN}|\gamma_l|^2\langle mN|\hat{d}_{lk}^\dagger\hat{c}|nN'\rangle\langle nN'|\hat{c}^\dagger\hat{d}_{lk}|mN\rangle\\ &= \sum_{NN'k}\rho_{lN}|\gamma_l|^2\langle N|\hat{d}_{lk}^\dagger|N'\rangle\langle N'|\hat{d}_{lk}|N\rangle\\ &= \sum_{Nk}\rho_{lN}|\gamma_l|^2\langle N|\hat{d}_{lk}\hat{d}_{lk}^\dagger|N\rangle\\ &= \sum_{Nk}\rho_{lN}|\gamma_l|^2\left(1 - \langle N|\hat{d}_{lk}^\dagger\hat{d}_{lk}|N\rangle\right).\end{aligned} \tag{2.62}$$

For the last line holds

$$f_l(\epsilon_k) = \sum_N \rho_{lN}\langle N|\hat{d}_{lk}^\dagger\hat{d}_{lk}|N\rangle \tag{2.63}$$

and $\sum_N \rho_{lN} = 1$ due to the normalization of the density matrix. Since the electronic spectrum in the leads forms a continuum of states, one can change the sum over k into an integral $\int \mathcal{D}_l(\epsilon_k)d\epsilon_k$ with $\mathcal{D}_l(\epsilon_k)$ being the density of states in lead l. One obtains then for the transition rate for electrons tunneling from the system to the lead l

$$\begin{aligned}\Gamma_{mn}^+ &= \frac{2\pi}{\hbar}\sum_l|\gamma_l|^2\int d\epsilon_k\mathcal{D}_l(\epsilon_k)(1 - f_l(\epsilon_k))\delta(\epsilon_k - \hbar\omega_{nm})\\ &= \frac{2\pi}{\hbar}\sum_l|\gamma_l|^2\mathcal{D}_l(\hbar\omega_{nm})(1 - f_l(\hbar\omega_{nm})),\end{aligned} \tag{2.64}$$

and analogously for electrons coming from the lead l into the system

$$\Gamma_{mn}^- = \frac{2\pi}{\hbar}\sum_l|\gamma_l|^2\mathcal{D}_l(\hbar\omega_{nm})f_l(\hbar\omega_{nm}). \tag{2.65}$$

The Fermi distribution function is given by

$$f(\epsilon) = \frac{1}{e^{\beta(\epsilon-\mu_l)}+1}, \tag{2.66}$$

where $\beta = 1/k_\mathrm{B}T$ and μ_l is the chemical potential of lead l.

2.2.2. Current formula

Having calculated the transition rates for tunneling processes between system and leads, we will now continue to derive the current formula. As has been said above, every observable can be expressed by

means of the density matrix. The current through a quantum dot or an array of quantum dots can be defined as the time derivative of the number of charged particles accumulated in the collector [53],

$$I(t) = e\frac{d}{dt}\langle N_{\mathcal{R}}(t)\rangle = e\frac{d}{dt}\mathrm{Tr}_{\mathcal{S}+\mathcal{R}}\left(\rho(t)N_{\mathcal{R}}(t)\right). \tag{2.67}$$

If we decompose the reduced density matrix into terms with different numbers N of electrons in the collector, $\rho(t) = \sum_N \rho_N(t)$, the current can be written as

$$I(t) = e\mathrm{Tr}_{\mathcal{S}}\sum_N N\dot{\rho}_N(t). \tag{2.68}$$

The diagonal matrix elements for the N-resolved density matrix are then

$$\langle m|\dot{\rho}_N|m\rangle = \sum_{N'}\sum_{n\neq m}\Gamma_{mn}^{NN'}\langle n|\rho_{N'}|n\rangle - \Gamma_{nm}^{N'N}\langle m|\rho_N|m\rangle, \tag{2.69}$$

with

$$\Gamma_{mn}^{NN'} = \frac{2\pi}{\hbar}|\langle mN|H_{\mathrm{T}}|nN'\rangle|^2\delta(E_N - E_{N'} - \hbar\omega_{mn}). \tag{2.70}$$

The off-diagonal elements do not contribute to the current, since $N_{\mathcal{R}}$ is diagonal in this basis. Therefore we obtain for the current

$$\begin{aligned} I(t) &= e\mathrm{Tr}_{\mathcal{S}}\sum_N N\dot{\rho}_N(t) \\ &= e\sum_{NN'}N\sum_{n\neq m}\left(\Gamma_{mn}^{NN'}\langle n|\rho_{N'}|n\rangle - \Gamma_{nm}^{N'N}\langle m|\rho_N|m\rangle\right). \end{aligned} \tag{2.71}$$

The number N refers to the number of electrons in the collector. Assuming only first order tunneling processes (*sequential tunneling*) while neglecting higher order processes such as cotunneling (see e.g. ref. [120]), N is either decreased or increased by one. Also considering that $\Gamma_{mm} = 0$ we can then drop the condition $k \neq m$:

$$\begin{aligned} I(t) = e\sum_N\sum_{nm}N\Big(&\Gamma_{mn}^{NN+1}\langle n|\rho_{N+1}|n\rangle + \Gamma_{mn}^{NN-1}\langle n|\rho_{N-1}|n\rangle - \\ &-\Gamma_{nm}^{N+1N}\langle m|\rho_N|m\rangle - \Gamma_{nm}^{N-1N}\langle m|\rho_N|m\rangle\Big) \end{aligned} \tag{2.72}$$

By some straightforward index manipulation in the third and fourth term this can be simplified to

$$I(t) = e\sum_N\sum_{nm}\Gamma_{mn}^{NN-1}\langle n|\rho_{N-1}|n\rangle - \Gamma_{mn}^{NN+1}\langle n|\rho_{N+1}|n\rangle. \tag{2.73}$$

In the first term, Γ_{mn}^{NN-1} describes the rate of an electron tunneling from the system to the collector, so that the number of particles in the collector rises from $N-1$ to N. Likewise, in the second term the number of particles in the collector decreases from $N+1$ to N. We can write these rates as $\Gamma_{mn}^{\pm 1}$ and extract them from the sum, so that the formula for the current finally becomes

$$\begin{aligned} I(t) &= e\sum_{nm}\left(\Gamma_{mn}^{+}\sum_N\langle n|\rho_{N-1}|n\rangle - \Gamma_{mn}^{-}\sum_N\langle n|\rho_{N+1}|n\rangle\right) \\ &= e\sum_{nm}\left(\Gamma_{mn}^{+} - \Gamma_{mn}^{-}\right)\langle n|\rho(t)|n\rangle. \end{aligned} \tag{2.74}$$

2.3. Electron dynamics in an isolated triple quantum dot array

We will now proceed to apply the theory derived in the foregoing section to a triple quantum dot (TQD) array. The off-diagonal elements of the density matrix contain information about the coherence between states. A two–level system – e.g. a double quantum dot with one energy level in each dot, where the dots are connected by a coherent tunneling amplitude τ and an electron can thus tunnel between the dots – can be described either by its *atomic* or its *molecular* basis. The latter is the diagonal basis consisting of bonding $|\psi^-\rangle$ and antibonding $|\psi^+\rangle$ states separated by $2|\tau|$ (for resonant single levels), and the former is the set of basis states describing an electron being in the left dot $|\phi_\mathrm{L}\rangle$ or in the right dot $|\phi_\mathrm{R}\rangle$. An important difference between the two descriptions is the fact that the density matrix written in the molecular basis is *diagonal*, because the coherence between the states is already stored in the basis states and therefore the off-diagonal elements are zero. For the atomic basis, however, both Hamiltonian and density matrix are non-diagonal and the coherence between the states is expressed by the non-zero off-diagonal elements. It is a typical problem of atomic physics to calculate the probability of a certain state of a two-level system to be occupied after a certain time t, see e.g. ref. [117]. The occupation probability oscillates as a function of time with a frequency that is proportional to the coupling between the levels. These oscillations are the so-called *Rabi oscillations*. In a double quantum dot as described above with one energy level per dot and tunneling amplitude τ the *Rabi frequency* for oscillations of an electron between the left and right dot is $\Omega = 2\tau$ [117].

The logic extension from a two-level system is the three-level system, which we will encounter in this thesis in form of a TQD either in linear or triangular arrangement. We will now calculate the occupation probabilities and Rabi frequencies for one electron in a three-level system, which will first be given by a linear TQD array and then by a triangular TQD.

2.3.1. Rabi oscillations in an isolated linear TQD

As has been pointed out in the foregoing section, the equation of motion for the density matrix of a closed system is given by the Liouville equation (Eq. (2.12)). Considering a single spinless electron in a closed TQD that can tunnel from left (1) to center (2) and from center to right (3) dot (see Fig. 2.1 a), the Hamiltonian is given by

$$H_S = H_\mathrm{TQD}^\mathrm{lin} = \sum_{i=1,2,3} \epsilon_i \hat{c}_i^\dagger \hat{c}_i - \tau_{12}(\hat{c}_1^\dagger \hat{c}_2 + \hat{c}_2^\dagger \hat{c}_1) - \tau_{23}(\hat{c}_2^\dagger \hat{c}_3 + \hat{c}_3^\dagger \hat{c}_2). \tag{2.75}$$

In the basis

$$\begin{aligned} |\phi_1\rangle &= c_1^\dagger |0,0,0\rangle = |1,0,0\rangle \\ |\phi_2\rangle &= c_2^\dagger |0,0,0\rangle = |0,1,0\rangle \\ |\phi_3\rangle &= c_3^\dagger |0,0,0\rangle = |0,0,1\rangle, \end{aligned} \tag{2.76}$$

the Hamiltonian reads in matrix form

$$H_\mathrm{TQD}^\mathrm{lin} = \begin{pmatrix} \epsilon_1 & -\tau_{12} & 0 \\ -\tau_{12} & \epsilon_2 & -\tau_{23} \\ 0 & -\tau_{23} & \epsilon_3 \end{pmatrix}. \tag{2.77}$$

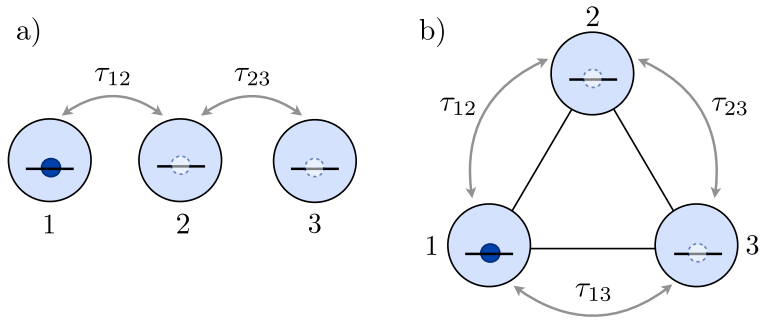

Figure 2.1.: **Sketch of a TQD with one energy level per dot. a)** A linear TQD, in which a spinless electron tunnels coherently between the three dots coupled by $\tau_{12,23}$. **b)** A triangular TQD, in which additionally dot 1 and dot 3 are coupled by τ_{13}.

The density matrix is then also a (3×3) matrix with elements ρ_{ij} $(i, j = 1, 2, 3)$, where the diagonal elements (the occupations) are $\rho_{11}, \rho_{22}, \rho_{33}$. We solve the equation of motion for the density matrix elements, $\dot{\rho}(t) = -\frac{i}{\hbar}\left[H^{\text{lin}}_{\text{TQD}}, \rho(t)\right]$, analytically for the case $\tau_{12} = \tau_{23} = \tau$ and resonant energy levels $\epsilon_{1,2,3} = \epsilon$. In contrast to the two-level system, the Rabi frequency in the three-level system is different

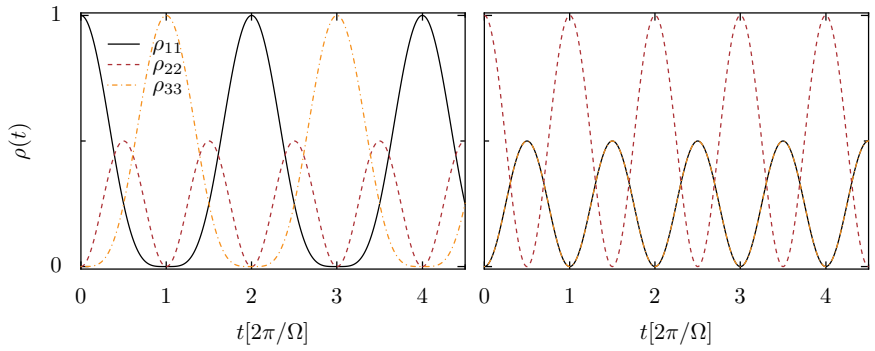

Figure 2.2.: **Occupation probabilities as a function of time of an electron tunneling in a resonant isolated linear TQD.** *Left panel:* The electron is initially placed in dot 1. *Right panel:* The electron starts off from dot 2. $\Omega = 2\sqrt{2}\tau$.

for the different occupations, and also depends on the initial condition we set for the differential equation. For the electron initially placed in dot 1, the occupations as a function of time are

$$\begin{aligned}
\rho_{11}(t) &= \left[\cos\left(\frac{1}{2}\sqrt{2}\tau t\right)\right]^4 \\
\rho_{22}(t) &= \frac{1}{2}\left[\sin\left(\sqrt{2}\tau t\right)\right]^2 \\
\rho_{33}(t) &= \left[\sin\left(\frac{1}{2}\sqrt{2}\tau t\right)\right]^4 .
\end{aligned} \tag{2.78}$$

Since in order to hop to dot 3 the electron has to pass by dot 2, the occupation of dot 2 varies twice as fast as the occupation of dots 1 and 3, $\Omega_1 = \Omega_3 = \sqrt{2}\tau$ and $\Omega_2 = 2\sqrt{2}\tau$, see also Fig. 2.2 (left panel). However, the electron never *fully* resides in the center dot, since the occupation probability

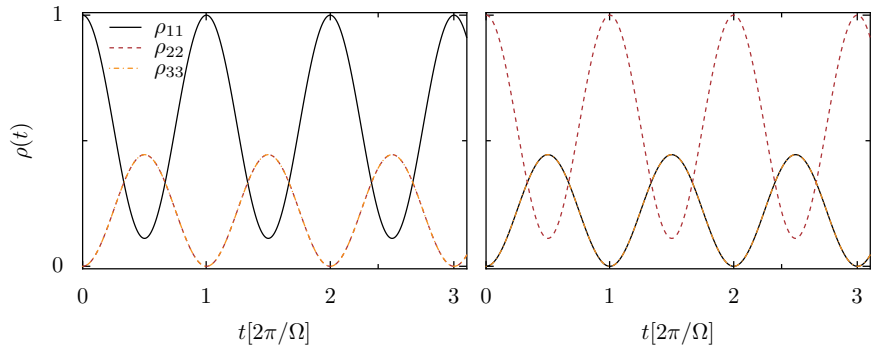

Figure 2.3.: **Occupation probabilities as a function of time of an electron tunneling in a resonant isolated triangular TQD.** *Left panel:* The electron is initially placed in dot 1. *Right panel:* The electron starts off from dot 2. The Rabi frequency is the same for all ρ_{ii}, $\Omega = 3\tau$.

$\rho_{22}(t) \leqq 0.5$. If we let the electron start to hop from dot 2, the situation is different, because it will tunnel with the same probability to the left as to the right dot, whose occupation probabilities consequently coincide, see Fig. 2.2 (right panel). In this case also the Rabi frequencies are the same for all three occupations, $\Omega = 2\sqrt{2}\tau$, as can be seen through

$$\begin{aligned}\rho_{11}(t) &= \frac{1}{2}\left[\sin\left(\sqrt{2}\tau t\right)\right]^2 \\ \rho_{22}(t) &= \left[\cos\left(\sqrt{2}\tau t\right)\right]^2 \\ \rho_{33}(t) &= \frac{1}{2}\left[\sin\left(\sqrt{2}\tau t\right)\right]^2 .\end{aligned} \tag{2.79}$$

2.3.2. Rabi oscillations in an isolated triangular TQD

It is to expect that for a TQD in triangular configuration the Rabi frequencies and occupation probabilities show higher symmetry due to the additional coupling between dot 1 and 3, see Fig. 2.1 b). The Hamiltonian reads now

$$H_{\mathrm{TQD}}^{\mathrm{tri}} = \sum_{i=1,2,3} \epsilon_i \hat{c}_i^\dagger \hat{c}_i - \tau_{12}(\hat{c}_1^\dagger \hat{c}_2 + \hat{c}_2^\dagger \hat{c}_1) - \tau_{23}(\hat{c}_2^\dagger \hat{c}_3 + \hat{c}_3^\dagger \hat{c}_2) - \tau_{13}(\hat{c}_1^\dagger \hat{c}_3 + \hat{c}_3^\dagger \hat{c}_1), \tag{2.80}$$

or in matrix form

$$H_{\mathrm{TQD}}^{\mathrm{tri}} = \begin{pmatrix} \epsilon_1 & -\tau_{12} & -\tau_{13} \\ -\tau_{12} & \epsilon_2 & -\tau_{23} \\ -\tau_{13} & -\tau_{23} & \epsilon_3 \end{pmatrix}. \tag{2.81}$$

We set again $\epsilon_{1,2,3} = \epsilon$ and $\tau_{12,23,13} = \tau$ and obtain with the initial condition $\rho_{11}(0) = 1, \rho_{22,33}(0) = 0$ the occupation probabilities

$$\begin{aligned}\rho_{11}(t) &= \frac{1}{9}\left[5 + 4\cos(3\tau t)\right] \\ \rho_{22}(t) &= \frac{4}{9}\left[\sin\left(\frac{3}{2}\tau t\right)\right]^2 \\ \rho_{33}(t) &= \frac{4}{9}\left[\sin\left(\frac{3}{2}\tau t\right)\right]^2 .\end{aligned} \tag{2.82}$$

Thus, in fact, the Rabi frequencies are the same for all three occupation probabilities, $\Omega = 3\tau$, and $\rho_{22}(t) = \rho_{33}(t)$. Note in Fig. 2.3 (left panel) that the occupation ρ_{11} never goes down to zero. The electron is therefore always delocalized in the TQD, and the electronic density in dot 1 is finite. The same applies to dot 2, when the electron starts from dot 2, see Fig. 2.3 (right panel).

2.4. Electron dynamics and current through a TQD

In the foregoing sections we have seen that an electron in a closed TQD performs Rabi oscillations with a Rabi frequency Ω. These oscillations are undamped as long as the system is isolated from an environment that can introduce decoherence into the system, but they decay once the electron can leave the TQD through a lead. Then, in the stationary limit, a stationary current will flow through the system. In this section we calculate the current through a TQD making use of the master equation derived before, both for a TQD in linear and triangular configuration. These examples will serve as a basis for the subsequent chapters, in which the same master equation is used for the analysis of several specific transport problems.

In general, the Hamiltonian of the quantum dot system coupled to leads will be given as

$$H = H_{\mathcal{S}} + H_{\text{Leads}} + H_{\text{T}}, \tag{2.83}$$

where $H_{\mathcal{S}} = H_{\text{Dots}} + H_{\text{tun}}$ includes the single–particle energies $\epsilon_{i\sigma}$ for an electron in dot i with spin σ, the intradot Coulomb interaction U_i, the interdot Coulomb interaction V_{ij} and the coherent tunneling τ_{ij},

$$H_{\mathcal{S}} = \sum_{i\sigma} \epsilon_{i\sigma} \hat{c}^{\dagger}_{i\sigma} \hat{c}_{i\sigma} + \sum_{i} U_i \hat{n}_{i\uparrow} \hat{n}_{i\downarrow} + \frac{1}{2} \sum_{i \neq j} V_{ij} \hat{n}_i \hat{n}_j - \sum_{ij, i\neq j, \sigma} \tau_{ij} (\hat{c}^{\dagger}_{i\sigma} \hat{c}_{j\sigma} + \hat{c}^{\dagger}_{j\sigma} \hat{c}_{i\sigma}), \tag{2.84}$$

with $\hat{n}_{i\sigma}\hat{n}_{i\sigma'} = \hat{c}^{\dagger}_{i\sigma}\hat{c}_{i\sigma}\hat{c}^{\dagger}_{i\sigma'}\hat{c}_{i\sigma'}$. The Hamiltonians H_{Leads} and H_{T} describe the leads and the tunneling between leads and dots,

$$\begin{aligned} H_{\text{Leads}} &= \sum_{lk} \varepsilon_{lk} \hat{d}^{\dagger}_{lk} \hat{d}_{lk} \\ H_{\text{T}} &= \sum_{lk} \gamma_l \hat{d}^{\dagger}_{lk} \hat{c}_l + \gamma^*_l \hat{c}^{\dagger}_l \hat{d}_{lk}, \end{aligned} \tag{2.85}$$

where $l = \text{L}, \text{R}$ is the index for the left (L) and right (R) lead, and $\hat{d}^{\dagger}_{lk}(\hat{d}_{lk})$ creates (annihilates) an electron in lead l and $\hat{c}^{\dagger}_l(\hat{c}_l)$ creates (annihilates) an electron in the dot close to lead l.

The master equation for the elements of the density matrix is, as derived in the foregoing sections,

$$\dot{\rho}_{mn}(t) = -i\langle m|[H_{\mathcal{S}}, \rho(t)]|n\rangle + \sum_{k\neq n} (\Gamma_{nk}\rho_{kk} - \Gamma_{kn}\rho_{nn})\delta_{mn} - \Lambda_{mn}\rho_{mn}(1-\delta_{mn}). \tag{2.86}$$

The commutator accounts for the coherent dynamics in the quantum dot array (in this case only coherent tunneling), tunneling to and from the leads is governed by the transition rates Γ_{mn} from state $|n\rangle$ to state $|m\rangle$, and decoherence due to interaction with the reservoir is considered in the term $\Lambda_{mn} = \frac{1}{2}\sum_{k\neq m,m'}(\Gamma_{km} + \Gamma_{kn})$, see Eq. (2.50). The transition rates are calculated using Fermi's golden rule (see Eqs. (2.64),(2.65))

$$\Gamma_{mn} = \sum_{l=\text{L,R}} \Gamma_l \{ f(E_m - E_n - \mu_l)\delta_{N_m, N_n+1} + [1 - f(E_n - E_m - \mu_l)]\delta_{N_m, N_n-1} \}, \tag{2.87}$$

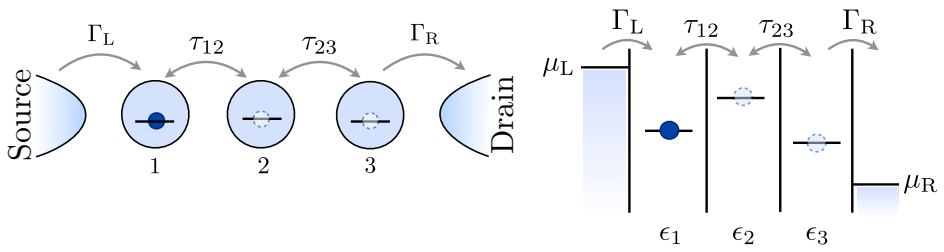

Figure 2.4.: **Sketch of a linear TQD connected to leads at the left and right dot.** The dots are coupled by coherent tunneling τ_{ij} and incoherently to leads by $\Gamma_{L,R}$. Only one electron can be inside the TQD, and the single electron energy levels in each dot are within in the transport window $\mu_L \gg \mu_R$.

where $E_m - E_n$ is the energy difference between states $|m\rangle$ and $|n\rangle$ of the isolated quantum dot array and $\Gamma_{L,R} = 2\pi\mathcal{D}_{L,R}|\gamma_{L,R}|^2$ are the tunneling rates for each lead. The density of states $\mathcal{D}_{L,R}$ and the tunnel couplings $\gamma_{L,R}$ are assumed to be energy independent.

2.4.1. Current through a linear TQD

We start with the analysis of the electron dynamics and current through a linear TQD, see Fig. 2.4. We assume strong Coulomb interaction, so that at most one electron can be inside the dot, and we neglect for now the spin σ of the electron. The Hamiltonian H_S is then given by Eq. (2.75) and reads as a matrix, written in the atomic basis Eq. (2.76)

$$H_{\mathrm{TQD}}^{\mathrm{lin}} = \begin{pmatrix} \epsilon_1 & -\tau & 0 \\ -\tau & \epsilon_2 & -\tau \\ 0 & -\tau & \epsilon_3 \end{pmatrix}, \tag{2.88}$$

where we have set the tunneling amplitudes $\tau_{12,23} = \tau$.

For a TQD biased in left-right direction such that $\mu_L \gg \epsilon_{1,2,3} \gg \mu_R$, an electron can enter from the left lead to the left dot but cannot tunnel back, see Fig. 2.4. Likewise, when an electron exits through the right lead, it will relax into the continuum of states in the lead and not come back. The only nonzero tunneling rates are then $\Gamma_{10} = \frac{2\pi}{\hbar}|\gamma_L|^2 = \Gamma_L$ from the vacuum state $|\phi_0\rangle = |0,0,0\rangle$ to $|1,0,0\rangle$ and $\Gamma_{03} = \frac{2\pi}{\hbar}|\gamma_R|^2 = \Gamma_R$ from $|0,0,1\rangle$ to $|0,0,0\rangle$. Applying the master equation (2.86) we get a set of differential equations for the density matrix elements, out of which the diagonal elements read

$$\begin{aligned}
\dot{\rho}_{00}(t) &= -\Gamma_L\rho_{00}(t) + \Gamma_R\rho_{33}(t) \\
\dot{\rho}_{11}(t) &= \Gamma_L\rho_{00}(t) - i\tau\left[\rho_{12}(t) - \rho_{21}(t)\right] \\
\dot{\rho}_{22}(t) &= -i\tau\left[\rho_{21}(t) - \rho_{12}(t) + \rho_{23}(t) - \rho_{32}(t)\right] \\
\dot{\rho}_{33}(t) &= -\Gamma_R\rho_{33}(t) - i\tau\left[\rho_{32}(t) - \rho_{23}(t)\right].
\end{aligned} \tag{2.89}$$

Let us first look at the Rabi oscillations in the TQD, by integrating the set of differential equations in time to obtain the occupation probabilities $\rho_{ii}(t)$. Depending on the coherent tunneling amplitude as compared to the tunneling rates $\Gamma_{L,R}$ to the leads, an electron in the TQD performs several coherent

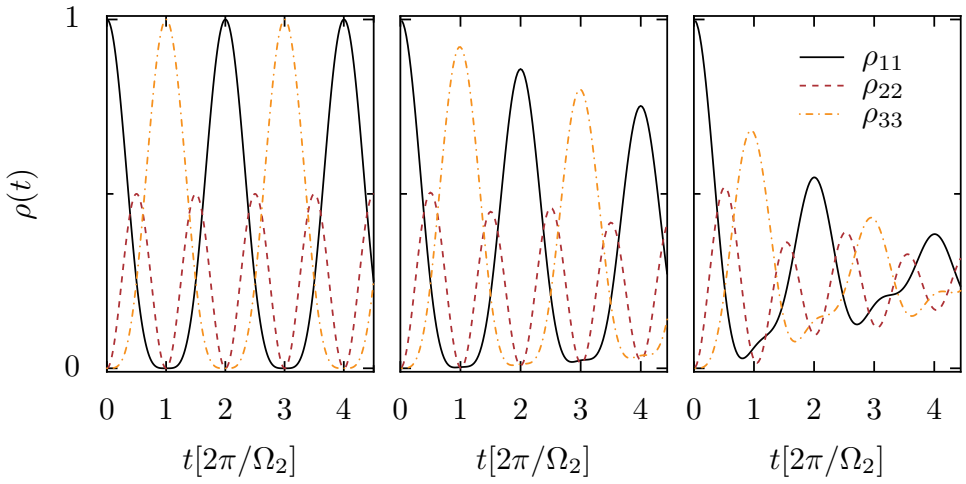

Figure 2.5.: **Occupations probabilities as a function of time for an open linear TQD.** *Left panel:* Occupations for the closed TQD, see also Fig. 2.2. *Middle panel:* Occupations for the open TQD with $\Gamma_{L,R} = \Gamma = 0.1\tau$. *Right panel:* The higher Γ compared to τ, the faster the oscillations decay. $\Gamma = 0.5\tau$, $\Omega_2 = 2\sqrt{2}\tau$.

oscillations before it tunnels out to the right lead. How fast the oscillations decay depends on the ratio $\tau/\Gamma_{L,R}$: the bigger $\Gamma_{L,R}$ compared to τ, the faster the system will reach the stationary state, see Fig. 2.5.

In order to calculate the stationary current, the equations of motion for the elements of the density matrix can be solved algebraically by setting $\dot{\rho}_{ij}(t) = 0$. The current is then proportional to the occupation of the dot next to the drain, in the present case dot 3, see Fig. 2.4:

$$I = \Gamma_R \rho_{33}. \tag{2.90}$$

In contrast to a double quantum dot, here an additional degree of freedom exists concerning the detuning between the dots. With $\epsilon_{ij} = \epsilon_i - \epsilon_j, i < j$, being the difference between energy levels, the current through the TQD is

$$I = \frac{4\Gamma_L\Gamma_R\tau^4}{4\Gamma_L\epsilon_{12}^2\epsilon_{13}^2 + \Gamma_L\Gamma_R^2\epsilon_{12}^2 + \left(8\Gamma_L\epsilon_{13}^2 + 2\Gamma_L\Gamma_R^2\right)\tau^2 + (12\Gamma_L + 4\Gamma_R)\tau^4}, \tag{2.91}$$

see also ref. [121]. We plot the current in Fig. 2.6, in a) as a function of ϵ_{12} for three different detunings ϵ_{13}, and in b) as a function of ϵ_{13} for three different detunings ϵ_{12}. We encounter here a peculiar property of a linear TQD which will be a topic in a later chapter (5): the current through the linear TQD is nearly independent of the position of the central energy level ϵ_2 for $\epsilon_{13} = 0$ over a wide range of detunings (see Fig. 2.6 a). This behavior can be understood by looking at the eigenstates of the isolated Hamiltonian, Eq. (2.88).

Setting $\epsilon_1 = \epsilon_3$, $\epsilon_2 \neq \epsilon_{1,3}$, one of the Hamiltonian's eigenstates is

$$|\psi\rangle = \frac{1}{\sqrt{2}}\left(-|1,0,0\rangle + |0,0,1\rangle\right). \tag{2.92}$$

Note that in this state the electronic density in the center dot (dot 2) is zero, independently of the position of ϵ_2 with respect to the resonant levels $\epsilon_1 = \epsilon_3$. Therefore, an electron that occupies this

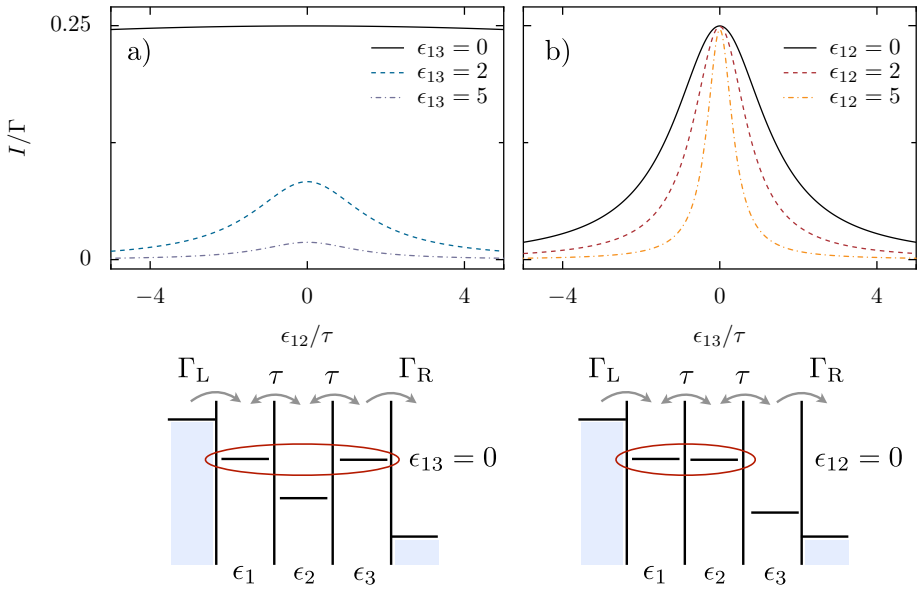

Figure 2.6.: **Current through a linear TQD. a)** Current as given in Eq. (2.91), for three different values of ϵ_{13} as a function of ϵ_{12}. Note that the current for $\epsilon_{13} = 0$ is nearly independent of the detuning ϵ_{12} over a large range. **b)** Current as a function of ϵ_{13} for three different ϵ_{12}. At $\epsilon_{13} = 0$, the maximal current is almost unaffected by the detuning ϵ_{12}, i.e. the position of the energy level in dot 2 is not decisive for the current to be maximal. Parameters: $\tau = 1$, $\Gamma_{L,R} = \Gamma = 0.1$.

state contributes to current through the TQD by a tunneling process from left to right that omits the center dot and that does not depend on the detuning with respect to the center dot. As has been said, in chapter 5, a similar state and its consequences for transport are going to be analyzed in the context of a TQD in the spin blockade regime.

2.4.2. Current through a triangular TQD

We consider now a triangular TQD as shown in Fig. 2.7. There is one single electron energy level per dot and in total only one electron can be inside the TQD. Each dot is coupled to its nearest neighbor by a tunneling amplitude τ_{ij}, with $i \neq j = 1, 2, 3$. Again by choosing the atomic basis Eq. (2.76), the Hamiltonian is written in matrix form as

$$H_{\mathrm{TQD}}^{\mathrm{tri}} = \begin{pmatrix} \epsilon_1 & -\tau_{12} & -\tau_{13} \\ -\tau_{12} & \epsilon_2 & -\tau_{23} \\ -\tau_{13} & -\tau_{23} & \epsilon_3 \end{pmatrix}. \tag{2.93}$$

Before calculating the current, let us analyze the eigenstates of this Hamiltonian.

Without further assumptions about the energy levels and tunneling amplitudes, this Hamiltonian cannot be diagonalized analytically. We choose, only for simplicity, the easiest configuration with equal tunneling amplitudes $\tau_{ij} = \tau$ and resonant energy levels $\epsilon_1 = \epsilon_2 = \epsilon_3 = \epsilon$. One eigenstate of

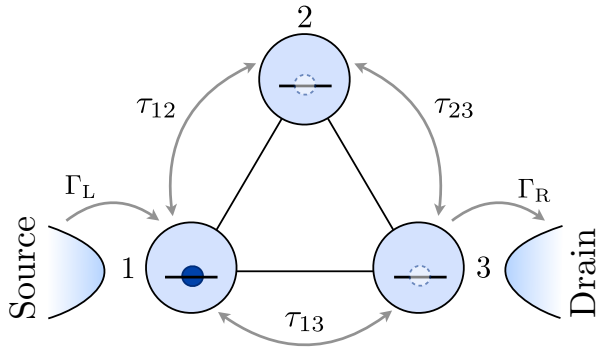

Figure 2.7.: **Schematic view of a triangular TQD.** Each dot is connected to its nearest neighbor by a tunneling amplitudes τ_{ij}, $i \neq j = 1,2,3$, and dot 1 and dot 3 are coupled to leads by tunneling rates $\Gamma_{L,R}$.

the Hamiltonian reads

$$|\psi\rangle = \frac{1}{\sqrt{2}}\left(-|1,0,0\rangle + |0,1,0\rangle\right), \tag{2.94}$$

in which no electronic density can be found in the drain dot, dot 3. As a side note, it should be said that the assumptions $\tau_{ij} = \tau$ and $\epsilon_i = \epsilon$ are not necessary in order to obtain an eigenstate with zero density in dot 3 in this system. It has been shown in ref. [92] that assuming $\epsilon_1 = -\frac{\tau_{12}}{2\tau_{13}\tau_{23}}\left(\tau_{13}^2 - \tau_{23}^2\right) = -\epsilon_2$, the state

$$|\psi'\rangle = \frac{1}{\sqrt{\tau_{13}^2 + \tau_{23}^2}}\left(-\tau_{23}|1,0,0\rangle + \tau_{13}|0,1,0\rangle\right) \tag{2.95}$$

is an eigenstate of the Hamiltonian (2.93). It is clear that in this eigenstate, the two paths τ_{23} and τ_{13} interfere destructively at dot 3 so that no electronic density can be found in dot 3, and instead the electron is delocalized between dots 1 and 2. For the following, the eigenstate $|\psi\rangle$ will be of crucial importance.

Let us now connect the TQD to leads attached to dots 1 and dot 3 and apply a bias from left to right, see Fig. 2.7. In the equation of motion for the density matrix, Eq. (2.86), we set now $H_S = H_{\text{TQD}}^{\text{tri}}$ (Eq. (2.93)). Since we are interested in the stationary current, we solve again the master equation for $\dot{\rho}_{ij}(t) = 0$ in order to obtain the stationary occupations ρ_{ii}. At zero temperature and for a finite bias from left to right the only non-zero rates for tunneling through the source and drain contacts are $\Gamma_{10} = \Gamma_L$, where an electron enters from the left lead to the left dot (dot 1), and $\Gamma_{03} = \Gamma_R$, where an electron exits from the right dot (dot 3) to the right lead. The current through the TQD is then simply proportional to the occupation of the drain dot, i.e. $I = \Gamma_R \rho_{33}$. The result for the current, setting $\tau_{ij} = \tau$, $\epsilon_2 = 0$ and $\Gamma_{L,R} = \Gamma$, is

$$I = \frac{4\Gamma\epsilon_1^2\tau^2}{(4\epsilon_1^2\epsilon_{13}^2 + \Gamma^2\epsilon_1^2) + (8\epsilon_1\epsilon_{13}^2 + 2\Gamma^2\epsilon_1)\tau + (24\epsilon_1^2 - 24\epsilon_1\epsilon_3 + 16\epsilon_3^2 + 4\Gamma^2)\tau^2}. \tag{2.96}$$

It can easily be seen that at $\epsilon_1 = 0$, – i.e. where dot 1 and dot 2 are on resonance –, the current drops to zero, and therefore exhibits a strong antiresonance, as can be seen in Fig. 2.8. This antiresonance occurs due to the fact that the electron inside the TQD occupies the eigenstate $|\psi\rangle$ (2.94). Since in

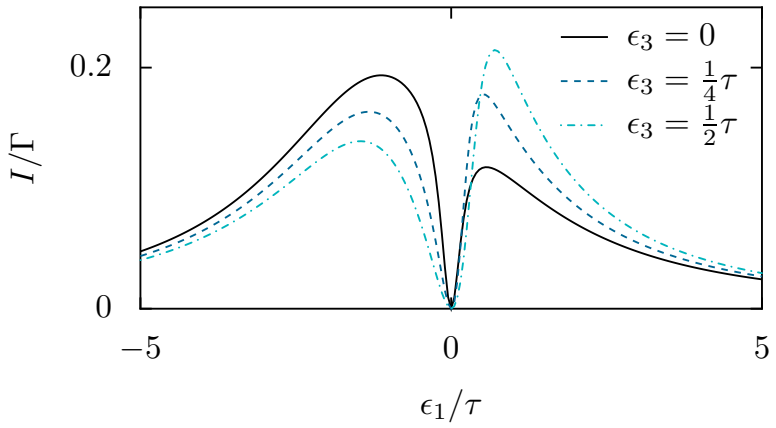

Figure 2.8.: **Current through a triangular TQD.** The current is shown for equal tunneling amplitudes $\tau_{ij} = \tau$, and $\epsilon_2 = 0$, for three different values of ϵ_3. $\Gamma = \tau/2$.

this eigenstate, as has been said above, the electronic density in dot 3 – the drain dot – vanishes and this state therefore does not contribute to transport, it is also called a *dark state*. The term *dark state* makes reference to its atomic counterpart: in a three-level atom that is excited by two resonant laser fields, the electronic wave function evolves towards a coherent superposition that is decoupled from the laser fields and therefore manifests as an antiresonance in the emission spectrum [86, 87, 41]. This phenomenon, also called *coherent population trapping*, has been found to have an all-electronic analog in transport through a triangular TQD as we have seen here [88], and it has also been shown to exist in a double quantum dot with three levels that is excited by bichromatic laser field [122].

In the following chapter, electronic transport through a magnetic-field driven triangular TQD will be treated, in which the dark state will play an important role.

3. Electron spin resonance in magnetic field driven triangular triple quantum dots

Electronic transport through mesoscopic systems can become correlated not only by charge interaction but also by the spin degree of freedom. A dramatic combination of both can be found in systems where strong Coulomb interaction limits the population to a small number of electrons (Coulomb blockade) and where Pauli's exclusion principle avoids certain internal transitions – spin blockade (SB). This was first observed as a rectification effect in the current through a double quantum dot (DQD) [39].

Recent experiments have taken advantage of spin blockade to achieve qubit operations in a double dot by electric gate control [31] or by electron spin resonance (ESR) [26, 70]. The latter consists in inducing transitions between the electron's spin-up and spin-down states, which are split by the Zeeman energy coming from a dc magnetic field, B_{dc}. In quantum dots, different mechanisms for ESR have been considered experimentally and theoretically: crossed dc and ac magnetic fields (B_{ac}), where the ac frequency is resonant with the Zeeman splitting [26, 62, 71], an effective ac magnetic field B_{ac} induced by ac electric fields in the presence of spin-orbit interaction [33], slanting Zeeman fields [72] or hyperfine interaction [32] (see also chapter 1).

In chapter 1, we have introduced the next extension to a DQD, the few-electron triple quantum dot (TQD). Both in linear and triangular arrangement, the first few-electron measurements have been performed quite recently [77, 109, 110], concentrating at first on its stability diagram (see also chapter 1), lately also on coherent control of spin states [114, 115]. With regard to the subsequent analysis, it is important to mention a particular property intrinsic to three-level systems, called coherent population trapping: this is a well-known effect in quantum optics and has been observed in three-level atoms excited by two resonant laser fields [86, 87, 41]. In these systems, the electronic wave function evolves towards an eigenstate superposition, a so-called *dark state*, which is decoupled from the laser fields and therefore manifests itself as an antiresonance in the emission spectrum. An analogy in transport has been made when coherent superpositions avoid transport by interference between tunneling events. These dark states can be achieved by driving three-level double dots with bichromatic ac electric fields [122] or by the interference of tunneling processes in TQDs [88, 90, 100]. It has been shown [92] how coherent trapping can be lifted in closed-loop TQDs by means of the Aharonov-Bohm (AB) effect [123].

In this chapter, the electron spin dynamics and transport for a triangular TQD exposed to crossed dc and ac magnetic fields will be analyzed, and dark states will play a crucial role. We consider at first the case of only one electron within the TQD. In order to analyze spin correlations between electron, we then introduce a second electron into the TQD. We will show that at certain ac field frequencies

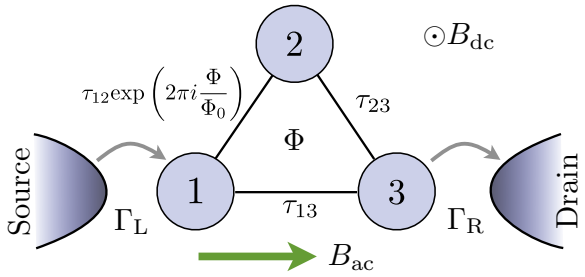

Figure 3.1.: **Schematic diagram of a triangular TQD in crossed dc and ac magnetic fields.** The dots are coupled coherently to each other by a tunneling amplitude $\tau_{12,23,13}$ and incoherently to leads by $\Gamma_{\mathrm{L,R}}$. Due to the perpendicular dc field B_{dc}, the structure encloses a flux Φ which is picked up by a tunneling electron and thereby modifies the tunneling $\tau_{12,23,13}$ by a phase $\phi = \Phi/\Phi_0$. Here we chose to accumulate the phase at τ_{12}.

the magnetic field brings the electronic wave function into a superposition of parallel spins states, unexpectedly bringing the system back to SB.

3.1. Single electron spin rotations in a triple quantum dot interferometer

3.1.1. Model

In this section we treat the case of a triangular TQD filled with at most one electron and exposed to both dc and ac magnetic fields. The system is depicted schematically in Fig.3.1. It consists of a triangular dot structure exposed to crossed dc and ac magnetic fields, in which the three dots are coupled through tunnel barriers and dots 1 and 3 are weakly connected to source and drain contacts respectively. Due to the magnetic fields, a new term has to be included into the Hamiltonian (2.84). It reads now

$$\mathcal{H}_{\mathcal{S}} = \mathcal{H}_{\mathrm{Dots}} + \mathcal{H}_{\mathrm{tun}} + \mathcal{H}_{\mathrm{B}}(t). \tag{3.1}$$

With the single electron energy levels $\epsilon_{i\sigma}$ and tunneling amplitude τ_{ij} the first two terms are

$$\begin{aligned}\mathcal{H}_{\mathrm{Dots}} &= \sum_{i\sigma} \epsilon_{i\sigma}\hat{c}^{\dagger}_{i\sigma}\hat{c}_{i\sigma} \\ \mathcal{H}_{\mathrm{tun}} &= -\sum_{ij,i\neq j,\sigma} \tau_{ij}(\hat{c}^{\dagger}_{i\sigma}\hat{c}_{j\sigma} + \hat{c}^{\dagger}_{j\sigma}\hat{c}_{i\sigma}).\end{aligned} \tag{3.2}$$

The Hamiltonian for the dc and circularly polarized ac magnetic field is (see chapter 1)

$$\mathcal{H}_{\mathrm{B}}(t) = \sum_{i=1}^{3} \left\{\Delta_i S_{z,i} + B_{\mathrm{ac}}\left[\cos(\omega t)S_{x,i} + \sin(\omega t)S_{y,i}\right]\right\}, \tag{3.3}$$

with $S_i = \frac{1}{2}\sum_{\sigma\sigma'} \hat{c}^{\dagger}_{i\sigma}\sigma_{\sigma\sigma'}\hat{c}_{i\sigma'}$ being the spin operators of each dot, $\sigma_{\sigma\sigma'}$ the Pauli spin matrices and Δ_i the Zeeman splitting produced by the dc magnetic field.

We describe the system by the basis $|0,0,0\rangle$, $|\sigma,0,0\rangle$, $|0,\sigma,0\rangle$, $|0,0,\sigma\rangle$, where $\sigma = \{\uparrow,\downarrow\}$. The dynamics of the system is calculated by making use of Eq. (2.86), where the commutator includes now $\mathcal{H}_{\text{Dots}} + \mathcal{H}_{\text{tun}} + \mathcal{H}_{\text{B}}(t)$,

$$\dot{\rho}_{mn}(t) = -i\langle m|[\mathcal{H}_{\text{Dots}} + \mathcal{H}_{\text{tun}} + \mathcal{H}_{\text{B}}(t), \rho]|n\rangle + \sum_{k\neq n}(\Gamma_{nk}\rho_{kk} - \Gamma_{kn}\rho_{nn})\delta_{mn} - \Lambda_{mn}\rho_{mn}(1-\delta_{mn}). \quad (3.4)$$

Eventual spin scattering processes coming from spin-orbit or hyperfine interaction destroy coherence and will thereby influence the transport features, especially when coherent phenomena such as population trapping or spin rotations induced by ESR are important. We include these spin-flip processes *phenomenologically* into the master equation [124]. The spin relaxation time T_1 is given by $W_{\uparrow\downarrow} + W_{\downarrow\uparrow}$, where $W_{\uparrow\downarrow}$ and $W_{\downarrow\uparrow}$ are spin-flip rates that fulfill a detailed balance equation

$$W_{\downarrow\uparrow} = \exp\left(\frac{-\Delta_z}{k_B T}\right) W_{\uparrow\downarrow}.$$

T_2 is the spin decoherence time – i.e. the time over which a superposition of opposite spin states of a single electron remains coherent. This time can be affected by spin relaxation and by the spin dephasing time T_2^*, i.e. the spin decoherence time for an ensemble of spins. We will only consider $T_2^* = 0.1T_1$. T_2^* is included in the decoherence term in Eq. (3.4) via $\Lambda_{mn} = \frac{1}{2}\sum_k(\Gamma_{km} + \Gamma_{kn}) + T_2^{-1}$.

The dc magnetic field B_{dc} applied perpendicularly to the plane of the triangular dot structure (see Fig. 3.1) encloses a magnetic flux Φ in such a way that electron tunneling acquires an additional phase $\phi = \Phi/\Phi_0$, with $\Phi_0 = h/e$ being the flux quantum [123]. Here the phase is accumulated in the tunneling amplitude $\tau_{12\phi} = \tau_{12}e^{-2\pi i\phi}$. We consider a bias high enough to have unidirectional transport (from left to right), so that the current is proportional to the occupation of dot 3,

$$I = \Gamma\left(\rho_{|0,0,\uparrow\rangle} + \rho_{|0,0,\downarrow\rangle}\right), \quad (3.5)$$

with $\Gamma = \Gamma_{\text{L,R}}$ being the tunneling rate to the leads.

3.1.2. Undriven case: $B_{\text{ac}} = 0$

Let us first look at the undriven case, i.e. $B_{\text{ac}} = 0$, but $B_{\text{dc}} \neq 0$. Magnetotransport through a triangular TQD – i.e. a dc magnetic field perpendicular to the TQD plane – has been analyzed by Emary [92] in a slightly different configuration where the left lead was connected both to dot 1 and dot 2. This difference, as we will see later, is expressed in a double periodicity of the current profile. Without any ac field applied to the system, there is no mixing between different spin channels, and the Hamiltonian of the system can be written as

$$\mathcal{H}_\sigma = \begin{pmatrix} \epsilon_{1\sigma} & -\tau_{12}\mathrm{e}^{-i2\pi\phi} & -\tau_{13} \\ -\tau_{21}\mathrm{e}^{i2\pi\phi} & \epsilon_{2\sigma} & -\tau_{23} \\ -\tau_{31} & -\tau_{32} & \epsilon_{3\sigma} \end{pmatrix}, \quad (3.6)$$

where $\epsilon_{i\sigma}$ is the energy of an electron in dot $i = 1,2,3$ with spin σ. In the following we will, for simplicity, consider uniform interdot couplings $\tau_{ij} = \tau$, and $\epsilon_{1\sigma} = \epsilon_{3\sigma}$. The eigenstates of the Hamiltonian can be found analytically and they depend on the phase ϕ. It turns out that for $\Phi/\Phi_0 = n/2, n = 0,1,2,\ldots$

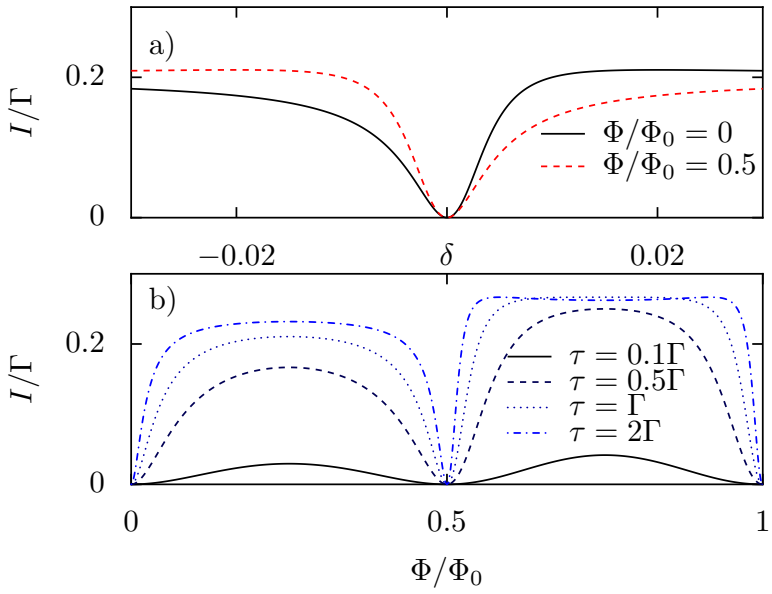

Figure 3.2.: **Current through a triangular TQD in a perpendicular magnetic field** B_{dc}**. a)** Current I vs. detuning δ for $\phi = n/2$. At zero detuning, the electron is trapped in a dark state and transport is cancelled. **b)** Current I vs. magnetic flux ϕ at zero detuning ($\delta = 0$) and for different tunnel couplings τ compared to the rate Γ for the tunneling to and from the leads. The magnetic flux destroys the electron trapping at $\phi = (2n+1)/4$ and current vanishes with a periodicity of $\Phi_0/2$. Parameters: $\Gamma = 0.01$, $\tau = 0.005$ in a), all units in meV.

and resonant transport conditions, – i.e. $\epsilon_{1\sigma} = \epsilon_{2\sigma} = \epsilon_{3\sigma}$ –, the already mentioned dark states (see chapter 2)

$$|\psi_\sigma\rangle = \frac{1}{\sqrt{2}}(|0,\sigma,0\rangle - |\sigma,0,0\rangle) \tag{3.7}$$

are eigenstates of the Hamiltonian (3.6). They do not contribute to current through the right lead due to destructive interference of the tunneling processes that transfer the electron to dot 3. However, a finite detuning $\delta = \epsilon_{1\sigma} - \epsilon_{2\sigma}$ leads to a finite current through the TQD:

$$I(\delta) = \frac{4\Gamma\tau^2\delta^2}{16\tau^2\delta^2 + \Gamma^2(4\tau^2 - (-1)^n 2\tau\delta + \delta^2)}, \quad n = 0,1,2,\ldots \tag{3.8}$$

The number n of flux quanta threading the TQD results in a sign change $(-1)^n$ in the denominator of Eq. (3.8), and is reflected in an asymmetric behavior of the current (see Fig. 3.2 a). It is a consequence of the specific arrangement of the TQD and the leads (cf. Fig. 3.1). Out of these ϕ values, a phase accumulation in the interdot tunneling due to the magnetic flux avoids interference, and a finite current flows, which shows AB-like oscillations. For $\delta = 0$ we find:

$$I(\phi) = \frac{4\Gamma\tau^2 \sin[2\phi\pi]^2}{\Gamma^2 + 8\tau^2 - 8\tau^2\cos[4\phi\pi] + 2\Gamma\tau\sin[2\phi\pi]}. \tag{3.9}$$

Note the double periodicity in the denominator of Eq. (3.9): current vanishes for $\phi = n/2$, but the specific configuration between the TQD and the leads results in non-uniform AB oscillations, see

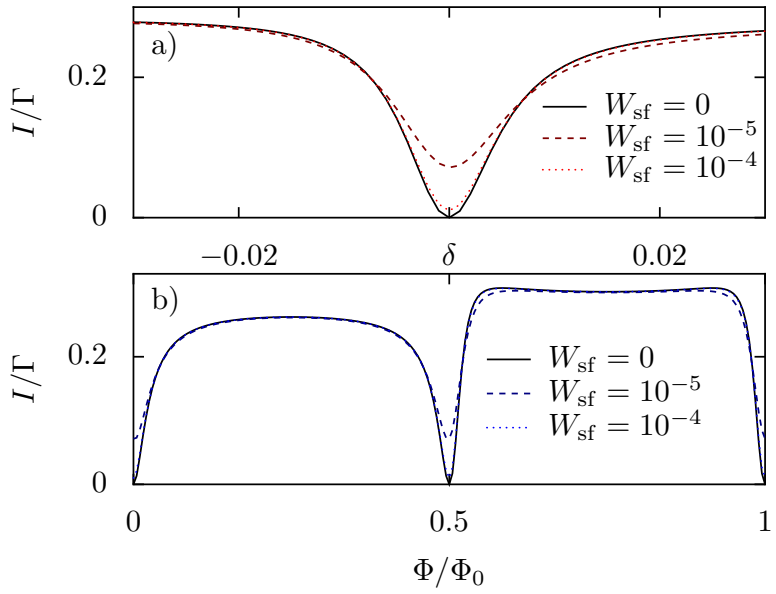

Figure 3.3.: **Current through the triangular TQD for finite spin-flip rate. a)** Current I vs. detuning δ for different spin-flip relaxation rates and $\phi = 1/2$. **b)** Current I vs. magnetic flux ϕ for zero and finite spin-flip probability and $\delta = 0$. Parameters: $\Gamma = 0.01$, $\tau = 0.02$, $W_{\uparrow\downarrow} = T_1^{-1}$, all units in meV.

Fig. 3.2 b). The shape of the interference pattern of the current depends on n, as obtained from the maximal value of the AB oscillations at $\phi = (2n+1)/4$

$$I_{\max,n}(\delta) = \frac{4\Gamma\tau^2(4\tau^2+\delta^2)}{4\tau^2(\Gamma^2-(-1)^n 2\Gamma\tau+16\tau^2)+(\Gamma^2+16\tau^2)\delta^2}. \tag{3.10}$$

The consequence of finite spin relaxation and decoherence times is shown in Fig. 3.3 for the current as a function of both the detuning and the magnetic flux: the spin scattering processes, as one can expect, allow for a finite current to flow at $\delta = 0$ and $\phi = n/2$ by destroying the coherence of the electronic wavefunction.

3.1.3. Driven case: $B_{\rm ac} \neq 0$

Let us now additionally apply a time-dependent magnetic field $B_{\rm ac}$ whose frequency is resonant with the Zeeman splitting induced by $B_{\rm dc}$, i.e. $\omega = \Delta_i$, and $\Delta_1 = \Delta_2 = \Delta_3$. The time-dependent field $B_{\rm ac}$ induces the rotation of the electron spin, however, it does not affect the AB oscillations: For $\phi = n/2$ an electron is trapped in the dark subspace $\{|\psi_\sigma\rangle\}$, as discussed in the previous section, while $B_{\rm ac}$ acts as a coherent coupling between the two dark states. This can be seen in the time evolution of the occupation probabilities shown in Fig. 3.4 for both zero and finite spin relaxation.

In Fig. 3.4 a), one can see that the dark states are being formed and the system behaves as a two-level system oscillating with a Rabi frequency given by $B_{\rm ac}$. Since the dark states are decoupled from tunneling to the leads (in the sequential tunneling regime), these oscillations can only be affected by decoherence coming from spin scattering processes. As seen before, spin scattering processes destroy the dark states, so that there is a finite probability of state $|0,0,\sigma\rangle$ to be occupied, and they introduce

decoherence that suppresses the Rabi oscillations between the dark states, cf. Fig. 3.4 b). Thus, in the stationary limit, current flows through the system.

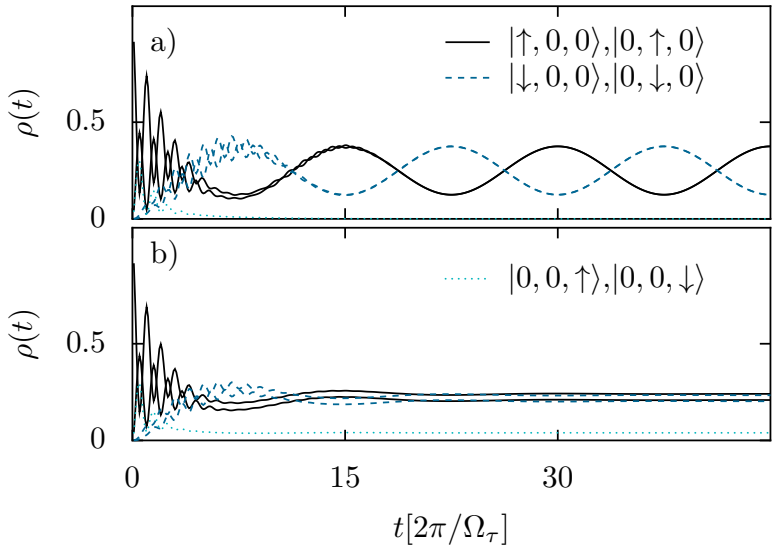

Figure 3.4.: **Occupation probabilities as a function of time for the TQD driven by B_{ac}, $\phi = 1/2$. a)** $W_{\uparrow\downarrow} = 0$. Due to the Aharonov-Bohm phase the electron delocalizes between dot 1 and 2, forming two dark states $|\psi_\sigma\rangle = \frac{1}{\sqrt{2}}(|0,\sigma,0\rangle - |\sigma,0,0\rangle)$, $\sigma = \uparrow,\downarrow$. The ac field now induces single spin rotations between these two dark states, see black solid and blue dashed lines. **b)** $W_{\uparrow\downarrow} = 10^{-4}$ meV: due to the finite spin-flip probability the coherence of the electron wavefunction is destroyed and finite current flows through the TQD, see lightblue dotted line. Parameters: $\Gamma = 0.001$, $\tau = 0.013$, $B_{ac} = 0.0026$, $\Omega_\tau = 3\tau$, $\Omega_{ac} = B_{ac}$.

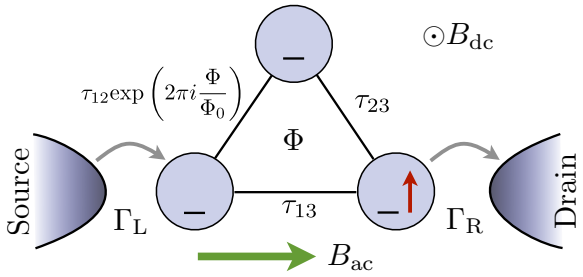

Figure 3.5.: **Schematic view of a triangular TQD exposed to crossed dc and ac magnetic fields.** Up to two electrons can be in the TQD at the same time, and one of them is always confined in the dot connected to the drain, indicated by a red arrow. The three dots are coupled coherently by tunneling amplitudes τ_{ij}, where due to the magnetic flux piercing the TQD a phase $\phi = \Phi/\Phi_0$ is accumulated, which we attribute to τ_{12}. Dot 1 and dot 3 are weakly coupled to leads by rates $\Gamma_{\mathrm{L,R}}$, and the chemical potentials are such that transport is possible only from left to right.

3.2. Control of spin blockade by crossed dc and ac magnetic fields in triple quantum dots

So far we have treated transport through a triangular TQD for only one electron inside the TQD. In order to analyze the effect of spin-spin correlations we include now a second electron in the TQD.

3.2.1. Model

The Hamiltonian for this system reads (see Eq. (3.1))

$$\mathcal{H}_{\mathcal{S}} = \mathcal{H}_{\mathrm{Dots}} + \mathcal{H}_{\mathrm{tun}} + \mathcal{H}_{\mathrm{B}}(t), \tag{3.11}$$

with

$$\begin{aligned}
\mathcal{H}_{\mathrm{Dots}} &= \sum_{i\sigma} \epsilon_{i\sigma} \hat{c}^{\dagger}_{i\sigma}\hat{c}_{i\sigma} + \sum_{i} U_i \hat{n}_{i\uparrow}\hat{n}_{i\downarrow} + \frac{1}{2}\sum_{i\neq j} V_{ij}\hat{n}_i\hat{n}_j \\
\mathcal{H}_{\mathrm{tun}} &= -\sum_{ij\sigma} t_{ij}(\hat{c}^{\dagger}_{i\sigma}\hat{c}_{j\sigma} + \hat{c}^{\dagger}_{j\sigma}\hat{c}_{i\sigma}) \\
\mathcal{H}_{\mathrm{B}}(t) &= \sum_{i=1}^{3} \left\{ \Delta_i S_{z,i} + B_{\mathrm{ac}} \left[\cos(\omega t) S_{x,i} + \sin(\omega t) S_{y,i} \right] \right\},
\end{aligned} \tag{3.12}$$

where $\epsilon_{i\sigma}$ is the energy of an electron with spin σ located in dot i, U_i the intra-dot and $V_{ij} = V$ the inter-dot Coulomb repulsion. We consider a configuration where the dot coupled to the drain is permanently occupied by one electron (see Fig. 3.5) and where only up to two electrons can be in the system.

Double occupancy is only allowed in the drain dot. This is the case when the chemical potentials in the leads satisfy $\epsilon_3 + V < \mu_{\mathrm{R}} < \epsilon_3 + U_3$ and $\mu_{\mathrm{L}} < \epsilon_1 + 2V$. We are only interested in one specific detuning of the energy levels, namely the resonant tunneling condition, where $\epsilon_1 = \epsilon_2$ and $\epsilon_{1,2} + V =$

$\epsilon_3 + U_3$. Out of the full TQD basis with up to two electrons, there are then eleven one- and two-electron states that dominate the dynamics:

$$\begin{aligned}
&|1\rangle = |0,0,\uparrow\rangle, |2\rangle = |0,0,\downarrow\rangle \\
&|3\rangle = |\uparrow,0,\uparrow\rangle, |4\rangle = |\downarrow,0,\uparrow\rangle, |5\rangle = |\uparrow,0,\downarrow\rangle, |6\rangle = |\downarrow,0,\downarrow\rangle \\
&|7\rangle = |0,\uparrow,\uparrow\rangle, |8\rangle = |0,\downarrow,\uparrow\rangle, |9\rangle = |0,\uparrow,\downarrow\rangle, |10\rangle = |0,\downarrow,\downarrow\rangle \\
&|S_3\rangle = |0,0,\uparrow\downarrow\rangle
\end{aligned} \tag{3.13}$$

The magnetic field B_{dc} is perpendicular to the plane of the triangular dot structure (Fig. 3.6) and therefore encloses a magnetic flux Φ, so that electron tunneling acquires an additional phase $\phi = 2\pi\Phi/\Phi_0$, with $\Phi_0 = h/e$ being the flux quantum, see foregoing section. We accumulate the phase between dot 1 and dot 2, $\tau_{12} = \tau e^{-i\phi}$. If not stated otherwise, we set $|\tau_{ij}| = \tau$.

Due to the confined electron in dot 3, transport will be governed by spin blockade (SB) [39]. It has been shown in ref. [71] that the ac magnetic field has no effect on SB unless the Zeeman splitting is inhomogeneous in the sample (see also chapter 1). At first we will consider the simplest configuration that allows us to analyze the relevant mechanisms: $\Delta_1 = \Delta_2 \neq \Delta_3$. Very recently, it has been demonstrated experimentally that tayloring the Zeeman splittings in arrays of quantum dots is possible either due to different g-factors of the dots [125], or also by placing micromagnets above the samples that induce a magnetic field gradient [72] and thus inhomogeneous Zeeman splittings.

We calculate the current through the TQD by integrating numerically the equations of motion of the reduced density matrix, see e.g. Eq. (3.4). Transport is biased from left to right and only state $|S_3\rangle$ contributes to tunneling through to the drain, acting thus as a bottleneck for the current,

$$I(t) = \sum_n \Gamma_{nS_3} \rho_{|S_3\rangle}(t), \tag{3.14}$$

with Γ_{nS_3} being the tunneling rate to the drain from state $|S_3\rangle$ to state $|n\rangle$ with only one electron in the drain dot. For simplicity, we set $\Gamma_{nS_3} = \Gamma$. Though being confined, the electron in dot 3 is essential to induce spin correlated transport.

3.2.2. Undriven case: $B_{\mathbf{ac}} = 0$

We have already seen that in a TQD with up to one extra electron, the current oscillates, due to interference, with Φ (AB oscillations) and periodically drops to zero with a periodicity of $\Phi_0/2$[1]. For an understanding of the two-electron spin dynamics it is crucial to look at the eigenstates of this system, which change, depending on the flux Φ, but also due to the presence of a second electron. We have to distinguish between the phases $\Phi/\Phi_0 = \frac{n}{2}$ and $\Phi/\Phi_0 \neq \frac{n}{2}$ for $n = 0, 1, 2 \ldots$. For $\Phi/\Phi_0 = \frac{n}{2}$

[1] Different periodicities can also occur; this depends on the tunneling amplitudes τ_{ij}, see [92]; for the present choice of parameters, the periodicity is as given.

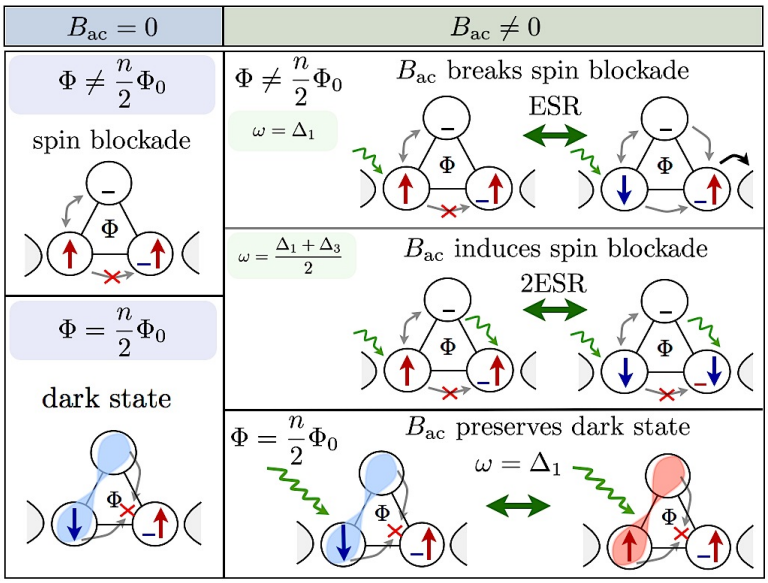

Figure 3.6.: **Coherent processes in a triangular TQD with one electron confined in the dot connected to the drain.** $\Delta_1 = \Delta_2 \neq \Delta_3$, where Δ_i is the Zeeman splitting in dot i. Transport through the system depends on the magnetic flux Φ penetrating the system and on the frequency ω of the time-dependent magnetic field B_{ac}. The shaded regions indicate the existence of a dark state.

the following eigenstates of the TQD Hamiltonian are of interest:

$$|\psi^-_{\sigma\sigma'}\rangle = \frac{1}{\sqrt{2}}(|0,\sigma,\sigma'\rangle - |\sigma,0,\sigma'\rangle) \qquad \sigma,\sigma' = \{\uparrow,\downarrow\} \tag{3.15}$$

$$|\psi^+_{\sigma\sigma}\rangle = \frac{1}{\sqrt{2}}(|0,\sigma,\sigma\rangle + |\sigma,0,\sigma\rangle) \qquad \sigma = \{\uparrow,\downarrow\} \tag{3.16}$$

$$|\psi^-_{\sigma\sigma}\rangle = \frac{1}{\sqrt{2}}(|0,\sigma,\sigma\rangle - |\sigma,0,\sigma\rangle) \qquad \sigma = \{\uparrow,\downarrow\} \tag{3.17}$$

Out of these, the states (3.15), although the two electrons have different spins, avoid tunneling to $|S_3\rangle$:

$$\langle\psi^-_{\sigma\sigma'}|\mathcal{H}_{\text{tun}}|S_3\rangle = 0. \tag{3.18}$$

In the present configuration current only flows when the state $|S_3\rangle$ is occupied. Therefore, once one of the states (3.15) is occupied, tunneling to $|S_3\rangle$ is suppressed, and in the transitory current regime the occupation of $|S_3\rangle$ and therefore the current decays due to the coupling to the drain, see purple dashed-dotted line in Fig. 3.7 b). The states in (3.15) remind of the dark states found in the single electron case, see section 3.1, Eq. (3.7). A significant difference is that *for two electrons the spin degree of freedom plays a role*: Pauli exclusion principle introduces spin correlation, so that the electrons are being trapped in combinations of dark states $|\psi^-_{\sigma\sigma'}\rangle$ and $|\psi^-_{\sigma\sigma}\rangle$ and spin-blockaded states $|\psi^+_{\sigma\sigma}\rangle$. Thus SB competes with coherent population trapping in the blocking of the current, and the relative occupation of $|\psi^-_{\sigma\sigma'}\rangle$ and $|\psi^\pm_{\sigma\sigma}\rangle$ depends on the initial condition. The current blocking mechanism, however, is different if the magnetic flux is $\Phi = \Phi_0/4$. In this case, the AB phase removes the dark

state $|\psi^{-}_{\sigma\sigma'}\rangle$, and only eigenstates with parallel spins are decoupled from $|S_3\rangle$:

$$|\xi^{\pm}_{\sigma\sigma}\rangle = \frac{1}{\sqrt{2}}(|0,\sigma,\sigma\rangle \pm i|\sigma,0,\sigma\rangle) \quad \sigma = \{\uparrow,\downarrow\} \tag{3.19}$$

Transport keeps being cancelled, however, now only by SB (Figs. 3.6, 3.7 a). In summary, one can understand that the undriven system is always blocked for transport – the stationary current is insensitive to AB effect due to SB.

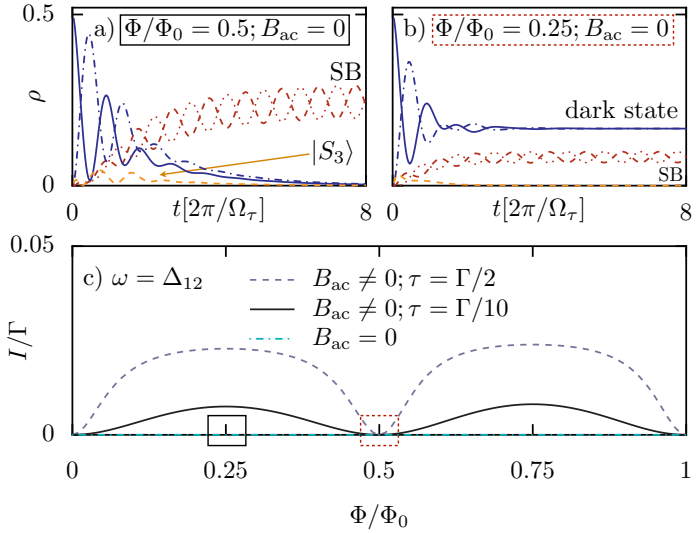

Figure 3.7.: **Occupation probabilities and current in a triangular TQD with up to two electrons, exposed to crossed dc and ac magnetic fields. a)** Occupation probabilities ρ_{ii} as a function of time t for $\Phi/\Phi_0 = 0.25$, $B_{ac} = 0$. Current is proportional to the occupation of $|S_3\rangle$ (dashed-dotted orange line), therefore transport is blocked due to SB, once the parallel spin states (dashed and dotted red lines) are occupied. **b)** Occupation probabilities ρ_{ii} as a function of time t for $\Phi/\Phi_0 = 0.5$, $B_{ac} = 0$. The electrons form a coherent state of the form (3.15). However, due to SB, there is a finite occupation of parallel spin states $|\psi^{\pm}_{\sigma\sigma}\rangle$ (dashed and dotted red lines), while electrons with antiparallel spin form dark states as in (3.15) (solid and dashed-dotted blue lines), all of them contributing to quench the current (see dashed-dotted orange line). **c)** Current I vs. magnetic flux Φ: for $B_{ac} = 0$, $I = 0$ due to SB (dashed turquoise line); $B_{ac} \neq 0$: for $\omega = \Delta_{1,2}$, SB is removed and the current shows AB-like oscillations (solid black and dashed gray lines for different τ). Rabi frequency: $\Omega_\tau = 2\tau$. $\tau = 0.0025$, $\Gamma = 0.01$, $\Delta_3 = 0.77\Delta_1$, $\Delta_1 = \Delta_2$, in meV.

3.2.3. Driven case: $B_{ac} \neq 0$

In order to remove SB we apply a time-dependent magnetic field B_{ac} with frequency $\omega = \Delta_{1,2} \neq \Delta_3$. Figure 3.7 c) shows the current as a function of the magnetic flux Φ through the TQD excited by B_{ac} for fixed ω. For $\Phi/\Phi_0 \neq n/2$, dark states are avoided by AB effect, and the ac field B_{ac} enables transitions of the form $|\sigma,0,\sigma\rangle \to |\sigma',0,\sigma\rangle \to |S_3\rangle$ ($|0,\sigma,\sigma\rangle \to |0,\sigma',\sigma\rangle \to |S_3\rangle$) that produce a finite current.

The magnetic ac field B_{ac} does not affect the destructive tunneling interference of the superpositions

(3.15) for $\Phi/\Phi_0 = n/2$. Instead, the system evolves towards a state that is only composed of dark states performing spin rotations, e.g.:

$$\begin{aligned}
&\mathcal{H}_{\mathrm{B}}(t)\left[\frac{1}{\sqrt{2}}\left(|0,\downarrow,\uparrow\rangle - |\downarrow,0,\uparrow\rangle\right)\right] \\
&= \frac{B_{\mathrm{ac}}}{2}\left[\cos(\omega t)\frac{1}{\sqrt{2}}\left(|0,\uparrow,\uparrow\rangle - |\uparrow,0,\uparrow\rangle\right) + \cos(\omega t)\frac{1}{\sqrt{2}}\left(|0,\downarrow,\downarrow\rangle - |\downarrow,0,\downarrow\rangle\right)\right] + \\
&\quad \frac{B_{\mathrm{ac}}}{2}\left[i\sin(\omega t)\frac{1}{\sqrt{2}}\left(|0,\uparrow,\uparrow\rangle - |\uparrow,0,\uparrow\rangle\right) - i\sin(\omega t)\frac{1}{\sqrt{2}}\left(|0,\downarrow,\downarrow\rangle - |\downarrow,0,\downarrow\rangle\right)\right] \\
&= \frac{B_{\mathrm{ac}}}{2}\left[\exp(i\omega t)|\psi^{-}_{\uparrow\uparrow}\rangle + \exp(-i\omega t)|\psi^{-}_{\downarrow\downarrow}\rangle\right], \qquad (3.20)
\end{aligned}$$

also shown schematically in Fig. 3.6. Since the dark states are decoupled from transport, the current oscillations can only be affected by decoherence due to spin scattering processes, which are not considered here. As a consequence, a magnetic ac field B_{ac} induces current through the system only when assisted by the AB lifting of dark states – i.e. for $\Phi/\Phi_0 \neq n/2$ – and the current shows the familiar AB oscillations (Fig. 3.7 c).

Remarkably, not imposing the resonance condition $\omega = \Delta_i$, one can find a novel kind of SB induced by the B_{ac}, which quenches the current even in the presence of AB effect. This is the main result of this work. As can be seen in Fig. 3.8 a), the current shows a resonant behavior as the frequency of B_{ac} approaches the ESR condition (i.e. $\omega \sim \Delta_1, \Delta_3$). Surprisingly, though, an antiresonance appears for $\omega_0 = (\Delta_1 + \Delta_3)/2$, i.e. when the two electrons are equally far from the resonance condition. Note that the two peaks around the antiresonance are not Lorentzian-like and cannot be identified as two different resonance peaks centered at the conditions $\omega = \Delta_1 = \Delta_2$ and $\omega = \Delta_3$, but as a collective effect due to the simultaneous rotation of the *two* electron spins (2ESR) [71], see also Fig 3.6.
We want to stress that the *appearance* of the antiresonance does not depend on the field intensity B_{ac} or tunnel couplings τ_{ij} (see Fig. 3.8 a, b): it occurs for different τ_{ij} as well as for linear TQD configurations (setting $\tau_{13} = 0$) and DQDs in series (setting $\tau_{12} = \tau_{23} = 0$), see Fig. 3.8 b). The *width* of the antiresonance scales with the Rabi frequency of the coherent processes involved [126]: spin rotation ($\propto B_{\mathrm{ac}}$) and interdot tunneling ($\propto \tau_{ij}$) (Figs. 3.8 a) and 3.8 b), respectively); it also depends on the tunneling rates Γ through the contact barriers, which induce decoherence, see Fig. 3.8 c).

The quenching of the current can be understood analytically by transforming the Hamiltonian $\mathcal{H}_{\mathrm{B}}(t)$ into the rotating frame [93]. This transformation yields a time-independent Hamiltonian

$$\mathcal{H}'_{\mathrm{B}} = \sum_{i=1}^{3}[(\Delta_i - \omega)S_{zi} + B_{\mathrm{ac}}S_{xi}].$$

Since tunneling conserves the spin, this transformation commutes with the tunneling Hamiltonian

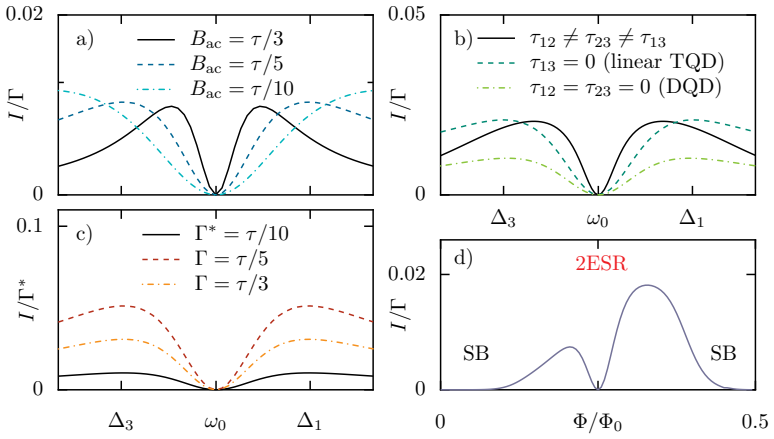

Figure 3.8.: **2ESR in a TQD by tuning ω, for $\Phi/\Phi_0 = 0.25$, is manifested in the current as an antiresonance at $\omega_0 = (\Delta_1 + \Delta_3)/2$. a)** For different B_{ac} and fixed $\tau_{ij} = \tau$: the width of the antiresonance depends on the Rabi frequencies associated with τ and B_{ac}. **b)** For different τ_{ij} and fixed $B_{ac} = \tau/5$. The antiresonance appears for any configuration of the τ_{ij}. Black solid line: $\tau_{12} = 2\tau$, $\tau_{23} = 0.1\tau$, $\tau_{13} = 0.5\tau$. **c)** For different Γ and $\tau_{ij} = \tau$. **d)** Current I vs. magnetic flux Φ for fixed ω while tuning B_{dc}, so both Φ and Δ_i are modified. AB oscillations are suppressed by SB except when the Zeeman splittings are close to resonance with ω. At $\Phi/\Phi_0 = 0.25$, where current vanishes, the Zeeman splittings have values, so that $\omega = 1/2(\Delta_1 + \Delta_3)$. Parameters: $\tau = 0.01$, $\Gamma = \Gamma^* = 0.001$.

$\mathcal{H}_{tun}$. In matrix notation, the two-electron Hamiltonian $\mathcal{H}' = \mathcal{H}_{tun} + \mathcal{H}'_B$ can be written as

$$
\begin{array}{c|ccccccccc}
 & |\uparrow,0,\uparrow\rangle & |\downarrow,0,\uparrow\rangle & |\uparrow,0,\downarrow\rangle & |\downarrow,0,\downarrow\rangle & |0,\uparrow,\uparrow\rangle & |0,\downarrow,\uparrow\rangle & |0,\uparrow,\downarrow\rangle & |0,\downarrow,\downarrow\rangle & |0,0,\uparrow\downarrow\rangle \\
\hline
 & -\frac{\Delta_1+\Delta_3}{2}+\omega & \frac{B_{ac}}{2} & \frac{B_{ac}}{2} & 0 & i\tau & 0 & 0 & 0 & 0 \\
 & \frac{B_{ac}}{2} & \frac{\Delta_1-\Delta_3}{2} & 0 & \frac{B_{ac}}{2} & 0 & i\tau & 0 & 0 & \tau \\
 & \frac{B_{ac}}{2} & 0 & \frac{\Delta_3-\Delta_1}{2} & \frac{B_{ac}}{2} & 0 & 0 & i\tau & 0 & -\tau \\
 & 0 & \frac{B_{ac}}{2} & \frac{B_{ac}}{2} & \frac{\Delta_1+\Delta_3}{2}-\omega & 0 & 0 & 0 & i\tau & 0 \\
 & -i\tau & 0 & 0 & 0 & -\frac{\Delta_2+\Delta_3}{2}+\omega & \frac{B_{ac}}{2} & \frac{B_{ac}}{2} & 0 & 0 \\
 & 0 & -i\tau & 0 & 0 & \frac{B_{ac}}{2} & \frac{\Delta_2-\Delta_3}{2} & 0 & \frac{B_{ac}}{2} & \tau \\
 & 0 & 0 & -i\tau & 0 & \frac{B_{ac}}{2} & 0 & \frac{\Delta_3-\Delta_2}{2} & \frac{B_{ac}}{2} & -\tau \\
 & 0 & 0 & 0 & -i\tau & 0 & \frac{B_{ac}}{2} & \frac{B_{ac}}{2} & \frac{\Delta_2+\Delta_3}{2}-\omega & 0 \\
 & 0 & \tau & -\tau & 0 & 0 & \tau & -\tau & 0 & 0
\end{array}
. \tag{3.21}
$$

One can easily verify that for $\Delta_1 = \Delta_2$ and at $\omega_0 = (\Delta_1 + \Delta_3)/2$ the coherent superpositions

$$
\begin{aligned}
|\Psi_1\rangle &= \frac{1}{2}\left(i|\uparrow,0,\uparrow\rangle - i|\downarrow,0,\downarrow\rangle + |0,\uparrow,\uparrow\rangle - |0,\downarrow,\downarrow\rangle\right) \\
|\Psi_2\rangle &= \frac{1}{2}\left(i|\uparrow,0,\uparrow\rangle - i|\downarrow,0,\downarrow\rangle - |0,\uparrow,\uparrow\rangle + |0,\downarrow,\downarrow\rangle\right)
\end{aligned} \tag{3.22}
$$

are eigenstates of this Hamiltonian. At ω_0 the single electrons in each dot are equally far away from resonance with the ac magnetic field. However, the two-electron states $|\uparrow,0,\uparrow\rangle$ and $|\downarrow,0,\downarrow\rangle$, $|0,\uparrow,\uparrow\rangle$ and $|0,\downarrow,\downarrow\rangle$ are brought into resonance when $\omega = 1/2(\Delta_1 + \Delta_3)$, i.e. their corresponding energies are equal (see diagonal elements of (3.21)). The electrons in (3.22) have parallel spins and are decoupled from the transport state $|S_3\rangle$. Once states (3.22) are occupied, the tunneling to dot 3 is therefore

suppressed and the current is quenched due to SB. Note that the electron spins in (3.22) are maximally entangled [127]. By evaluating the off-diagonal elements of the density matrix Eq. (3.4) at $\omega_0 = (\Delta_1 + \Delta_3)/2$ we can unambiguously show that in fact these states are responsible for the current quenching: the off-diagonal elements of the density matrix represent the coherences between the basis states, and, as we can see in Fig. 3.9, the only important coherence exists between states $|3\rangle = |\uparrow, 0, \uparrow\rangle$, $|6\rangle = |\downarrow, 0, \downarrow\rangle$, $|7\rangle = |0, \uparrow, \uparrow\rangle$, and $|10\rangle = |0, \downarrow, \downarrow\rangle$ which hence form the superpositions (3.22), see purple columns and purple dashed curve in Fig. 3.9.

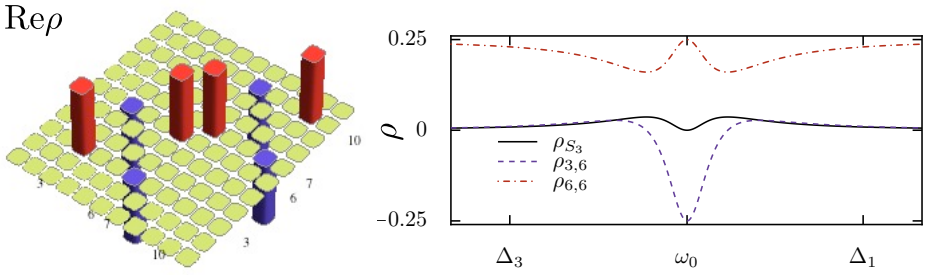

Figure 3.9.: **Analysis of the density matrix of a triangular TQD exposed to crossed dc and ac magnetic fields.** *Left plot:* Bar chart of the real part of the density matrix at $\omega_0 = (\Delta_1 + \Delta_3)/2$. Red positive columns represent the diagonal elements, i.e the occupations, of the states $|3\rangle, |6\rangle, |7\rangle, |10\rangle$ of the density matrix, purple negative columns the real part of the off-diagonal elements – i.e. coherences – between states $|3\rangle$ and $|6\rangle$, $|7\rangle$ and $|10\rangle$, see text. At frequency ω_0 the electrons occupy only parallel spin states (red columns) and form a coherent superposition given by state (3.22), which is decoupled from the driving field $B_{\rm ac}$. *Right plot:* Occupations and coherences of the density matrix as a function of ω for a few selected elements. Black solid line: occupation of $|S_3\rangle$, the transport state ($\propto$ current). Red dashed-dotted line: occupation of state $|6\rangle = |\downarrow, 0, \downarrow\rangle$, one of the basis states which forms part of (3.22). Its occupation is $1/4$ as expected at ω_0. Purple dashed line: $\rho_{3,6}$, i.e. the coherence between states $|3\rangle$ and $|6\rangle$ is highest at ω_0.

We want to emphasize that SB can be *switched* on and off by tuning the frequency of $B_{\rm ac}$, which is usually introduced to lift it, or also by changing the flux Φ at a fixed frequency ω, see Fig. 3.8 d).

In a TQD, a necessary condition for (3.22) to be eigenstates of $\mathcal{H}'$ is the equal coupling of dots 1 and 2 to $B_{\rm dc}$, i.e. $\Delta_1 = \Delta_2$ ($\neq \Delta_3$). If $\Delta_1 \neq \Delta_2$, though, this symmetry is broken and $\mathcal{H}'_{\rm B}$ couples all parallel to antiparallel spin states and thus to the transport state $|S_3\rangle$. However, numerical results show that even in the asymmetric case a pronounced antiresonance still appears in the current, although at a different frequency, see Fig. 3.10. An analysis of the density matrix elements reveals that at the antiresonance the electrons still drop into an eigenstate $|\Psi'\rangle$ of the Hamiltonian (3.21), similar to (3.22), which includes a finite but very small contribution of antiparallel spin states. We can determine where the antiresonance occurs by analyzing the Hamiltonian (3.21). Setting $B_{\rm ac} = 0$ but keeping ω finite, we diagonalize this Hamiltonian analytically. Four of its eigenenergies are

$$\begin{aligned} E_{a,b} &= \frac{1}{4}\left(\Delta_1 + \Delta_2 + 2\Delta_3 \pm \sqrt{\delta^2 + 16\tau^2} - 4\omega\right) \\ E_{c,d} &= -\frac{1}{4}\left(\Delta_1 + \Delta_2 + 2\Delta_3 \pm \sqrt{\delta^2 + 16\tau^2} - 4\omega\right), \end{aligned} \tag{3.23}$$

where $\delta = \Delta_1 - \Delta_2$. These eigenenergies correspond to eigenstates of the type $|\downarrow,0,\downarrow\rangle \pm |0,\downarrow,\downarrow\rangle$ and $|\uparrow,0,\uparrow\rangle \pm |0,\uparrow,\uparrow\rangle$ (where we omit the normalization for simplicity). It is easy to see that at $\omega_1 = \frac{1}{4}(\Delta_1 + \Delta_2 + 2\Delta_3)$, $E_a = E_d$ and $E_b = E_c$, i.e. the eigenenergies cross as a function of ω. For finite but small $B_{\rm ac} \ll \Delta_i$, the crossing becomes an anticrossing, and the energies are split by an amount $\propto B_{\rm ac}$, see Fig. 3.10 c). It is therefore at ω_1 where the corresponding eigenstates $|\downarrow,0,\downarrow\rangle \pm |0,\downarrow,\downarrow\rangle$ and $|\uparrow,0,\uparrow\rangle \pm |0,\uparrow,\uparrow\rangle$ have almost the same energy, and form, induced by the field $B_{\rm ac}$, a coherent superposition $|\Psi'\rangle \approx |\Psi\rangle$ that does not contribute to current and is ultimately responsible for the antiresonance in the current profile. It should be noted that for three different Zeeman splittings the position of the antiresonance as shown in Fig. 3.10 is valid only for a certain parameter range. The interplay between $B_{\rm ac}$, τ, Δ_i and ω can become very complicated, and it is a task for future works to analyze transport in these cases in more detail. In the plots in Fig. 3.10 we set $\tau \approx \Delta_i$, $B_{\rm ac} \ll \tau, \Delta_i$, and $\Delta_i - \Delta_j < \tau$ $(i,j = 1,2,3)$.

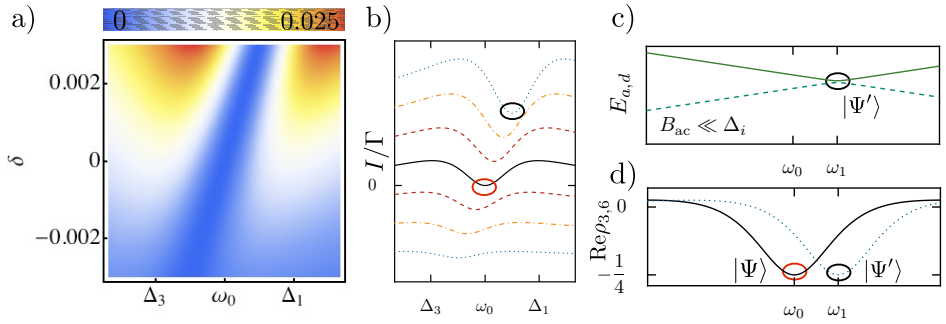

Figure 3.10.: **Current, eigenenergies, and off-diagonal element $\rho_{3,6}$ of the density matrix of the triangular TQD for different $\Delta_1 \neq \Delta_2 \neq \Delta_3$. a)** Density plot of the current as a function of ω and $\delta = \Delta_1 - \Delta_2$. At $\delta = 0$, $\Delta_1 = \Delta_2$ and the antiresonance occurs at ω_0 (see red circle in panel b). For $\delta \neq 0$, however, the antiresonance is shifted, which can also be seen in panel **b)**, where the current is plotted vs. ω for specific values of δ, with a certain offset in order to better visualize the different curves. **c)** Two eigenenergies of $\mathcal{H}_{\rm tun} + \mathcal{H}'_{\rm B}$ (3.21) for $\delta \neq 0$ and $B_{\rm ac} \ll \Delta_i, \tau$ (see Eq. 3.23): an anticrossing occurs at $\omega_1 = 1/4(\Delta_1 + \Delta_2 + 2\Delta_3)$ (black circle) between eigenstates of the form $|\downarrow,0,\downarrow\rangle \pm |0,\downarrow,\downarrow\rangle$ and $|\uparrow,0,\uparrow\rangle \pm |0,\uparrow,\uparrow\rangle$, which form a coherent superposition $|\Psi'\rangle$ similar to (3.22) whose occupation gives rise to the antiresonance in the current. **d)** Coherence $\rho_{3,6}$ between the basis states $|\uparrow,0,\uparrow\rangle$ and $|\downarrow,0,\downarrow\rangle$ as a function of ω for $\delta = 0$ (black solid line) and $\delta \neq 0$ (blue dotted line): note that for $\delta \neq 0$, i.e. three different Zeeman splittings, coherence between parallel spin states is as high as for $\delta = 0$, cf. also Fig. 3.9. Parameters: $\tau = 0.01, \Gamma = 0.001$, $B_{\rm ac} = \tau/5$, $\Delta_1 = 0.013$, $\Delta_3 = 0.01001$, en meV.

3.3. Conclusions

In summary, in this chapter we have presented results for electron transport through a specific configuration of a triangular TQD driven by crossed dc and ac magnetic fields. For the case of only one electron within the TQD we have analyzed the current and electron dynamics of the undriven and

the driven system. In the undriven case we have calculated the current as a function of both detuning and magnetic flux analytically, showing the formation of a dark state as well as Aharonov–Bohm oscillations. The configuration considered here leads to asymmetric current characteristics. Electron spin resonance conditions allow one to consider the TQD as a qubit where Rabi oscillations between two dark states can be controlled. Both in the undriven and driven case we have shown that finite spin scattering destroys the coherent electron trapping and allows for a finite current to flow through the TQD. It has become clear by our analysis that TQDs in triangular configuration under dc and ac magnetic fields exhibit rich dynamics due to the interplay of different coherent phenomena induced by the magnetic fields.

For two extra electrons in the system the interplay of the Pauli exclusion principle and coherent trapping is discussed in terms of the magnetic flux piercing the TQD. We have shown that, in contrast to the one-electron case, electrons remain trapped even for $\Phi/\Phi_0 \neq n/2$ due to spin blockade. We have demonstrated that it is a generic property of magnetic ac fields to induce spin blockade at certain frequencies in both DQDs and TQDs. Furthermore, the coherent superposition induced by the magnetic ac field B_{ac} constitutes a novel spin blockade state, which decouples from the field. Its experimental realization will make it possible to infer properties of the system such as Zeeman inhomogeneities and to manipulate spin qubits in DQDs and TQDs. It opens new perspectives for manipulating spin transport properties, thereby providing possibilities for designing spintronic devices.

4. Spin-polarized currents through double and triple quantum dots induced by ac magnetic fields

A key aim in spintronics is the realization of spin-based quantum information devices, where coherent electron-spin manipulation is a fundamental issue [27, 128, 124]. In semiconductor quantum dots coherent electron-spin manipulation can be realized by electron spin resonance (ESR), where an oscillating magnetic field is applied to the sample in order to rotate the electron spin [26, 129, 71, 62, 64] (see chapter 1). Together with ESR, electron-dipole spin-resonance techniques – which combine ac electric fields with spin-orbit interaction [33] or with a dc magnetic field gradient [32, 72] – have been implemented in order to measure coherent rotations of one single electron spin in double quantum dots (DQDs) [26, 33]. Coherent spin rotations of one single spin have also been proposed theoretically in triple quantum dots (TQDs) under crossed ac and dc magnetic fields [100].

In ESR experiments in quantum dot arrays, an important issue is to individually address the electron spin in each quantum dot. To this end, it has been proposed to tune the Zeeman splitting in order to manipulate the electron spin independently in each dot [130]. The Zeeman splitting in a quantum dot is determined by the intensity of the applied dc magnetic field and the electron g-factor, $\Delta_Z = g\mu_B B_{\rm dc}$. Different Zeeman splittings can occur in quantum dot arrays either when the dots have different g-factors or by applying different magnetic fields to each quantum dot. Both alternatives have been realized experimentally very recently: vertical DQDs made out of different materials – e.g., GaAs and InGaAs – show different g-factors [125]. On the other hand, in a sample with a spatially homogeneous g-factor, an additional microferromagnet placed near the quantum dot array creates a different external magnetic field $B_{\rm dc}$ in each dot [72].

In this chapter we are interested in single electron manipulation, and we theoretically study transport both through DQDs and TQDs. We calculate the current and current spin polarization through a DQD and a linear TQD array exposed to crossed dc and ac magnetic fields. We consider an inhomogeneous dc magnetic field that produces different Zeeman splittings in the dots while the g- factor is the same in both dots. For DQDs a regime is considered where the system is occupied either by zero or one electron. For TQDs the corresponding features are discussed for one or two electrons in the system. With the single electron-spin levels resolved in each quantum dot, interdot tunneling is governed by definite spin-selection rules, i.e. tunneling from one dot to the other is only possible when two equal spin levels are aligned. However, when an ac magnetic field is applied, it rotates the spin and allows spin-flip processes along the tunneling, which can lead to new features in the

current. This effect of an ac magnetic field has been explored previously in a DQD [26], where the authors report on single electron-spin rotations by using a combination of an ac magnetic field and sharp electric pulses. Here, as will be discussed in more detail below, we will focus our attention on the polarizing effect of an ac field, i.e. we will show that the combination of inhomogeneous dc and ac magnetic fields in DQDs and TQDs allows the creation of spin-polarized currents and thus the design of spin-filters and spin-inverters.

4.1. Model

We consider quantum dot arrays as shown schematically in Fig. 4.1. The dots are coupled to each

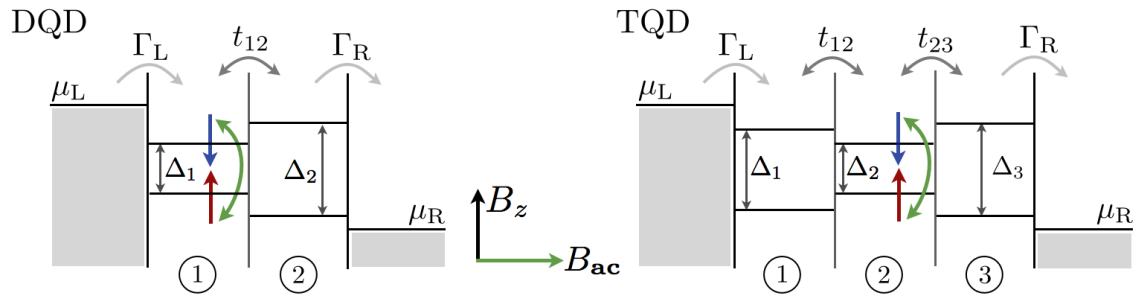

Figure 4.1.: **Schematic diagram of a DQD and TQD exposed to crossed dc (B_{dc}) and ac (B_{ac}) magnetic fields.** The electron spin is rotated once the ac frequency matches the Zeeman splitting in one of the dots. In the TQD, one electron is confined in the left dot, so that only an electron with opposite spin can enter the TQD. The dots are coupled coherently by tunneling amplitudes t_{ij} and incoherently to leads by rates Γ_L and Γ_R.

other coherently by a tunneling amplitude t_{ij} and are weakly connected to source and drain contacts by rates Γ_L and Γ_R.

The total Hamiltonian reads

$$\mathcal{H} = \mathcal{H}_{\text{Dots}} + \mathcal{H}_{\text{tun}} + \mathcal{H}_{\text{B}}(t) + \mathcal{H}_{\text{T}} + \mathcal{H}_{\text{Leads}}, \tag{4.1}$$

where the individual terms are

$$\begin{aligned}
\mathcal{H}_{\text{Dots}} &= \sum_{i\sigma} \xi_i \hat{c}^\dagger_{i\sigma}\hat{c}_{i\sigma} + \sum_i U_i \hat{n}_{i\uparrow}\hat{n}_{i\downarrow} + \frac{1}{2}\sum_{i\neq j} V \hat{n}_i \hat{n}_j \\
\mathcal{H}_{\text{tun}} &= -\sum_{ij\sigma} t_{ij}(\hat{c}^\dagger_{i\sigma}\hat{c}_{j\sigma} + \hat{c}^\dagger_{j\sigma}\hat{c}_{i\sigma}) \\
\mathcal{H}_{\text{Leads}} &= \sum_{l\in \text{L,R},k\sigma} \epsilon_{lk}\hat{d}^\dagger_{lk\sigma}\hat{d}_{lk\sigma} \\
\mathcal{H}_{\text{T}} &= \sum_{l\in \text{L,R},k\sigma} \gamma_l(\hat{d}^\dagger_{lk\sigma}\hat{c}_{l\sigma} + \hat{c}^\dagger_{l\sigma}\hat{d}_{lk\sigma}).
\end{aligned} \tag{4.2}$$

The first term, $\mathcal{H}_{\text{Dots}}$, describes an isolated array of quantum dots with electrons coupled electrostatically. Here, $\xi_{i\sigma}$ stands for the single electron energy level located in dot i, and U_i and V are the

intradot and the interdot Coulomb repulsion, respectively. $\mathcal{H}_{\text{tun}}$ describes the coherent tunneling between the dots, which in the case of a DQD is given by t_{12} and in a TQD by t_{12} and t_{23}. The quantum dot array is coupled to leads, which are described by $\mathcal{H}_{\text{Leads}}$, and the coupling of the array to the leads is given by $\mathcal{H}_{\text{T}}$. The magnetic field Hamiltonian consists of two parts coming from a dc field B_{dc} in z-direction and an ac field B_{ac} applied in xy-direction

$$\mathcal{H}_{\text{B}}(t) = \sum_i \left\{ \Delta_i S_{zi} + B_{\text{ac}}[\cos(\omega t) S_{xi} + \sin(\omega t) S_{yi}] \right\}, \tag{4.3}$$

being $\mathbf{S}_i = \frac{1}{2} \sum_{\sigma\sigma'} \hat{c}^\dagger_{i\sigma} \sigma_{\sigma\sigma'} \hat{c}_{i\sigma'}$ the spin operator of the ith dot, σ_σ the Pauli spin matrices, and the sum running over $i = 1, 2$ for the DQD and $i = 1, 2, 3$ for the TQD.

B_{dc} has a different intensity in each dot and thus produces different Zeeman splittings $\Delta_i = g\mu B_{\text{dc},i}$, whereas we consider the dots to have equal g-factor. B_{ac} induces spin rotations when its frequency fulfills the resonance condition $\omega = \Delta_i$. The time-dependent Hamiltonian can be transformed by means of a unitary transformation $U(t) = e^{-i\omega t \sum_i S_{zi}}$ into the rotating reference frame [71, 93]. The resulting time-independent Hamiltonian is then

$$\mathcal{H}_{\text{B}} = \sum_i \left[(\Delta_i - \omega) S_{zi} + B_{\text{ac}} S_{xi} \right]. \tag{4.4}$$

In order to calculate the current through the system, we make use of the density matrix formalism and solve the equations of motion for the reduced density matrix, see Eq. (2.86) (chapter 2),

$$\dot{\rho}_{mn}(t) = -i\langle m|[\mathcal{H}_{\text{Dots}} + \mathcal{H}_{\text{tun}} + \mathcal{H}_{\text{B}}(t), \rho]|n\rangle + \sum_{k \neq n} (\Gamma_{nk}\rho_{kk} - \Gamma_{kn}\rho_{nn})\delta_{mn} - \Lambda_{mn}\rho_{mn}(1 - \delta_{mn}). \tag{4.5}$$

We consider strong Coulomb repulsion, so that the DQD can be occupied with at most one extra electron. It is then described by a basis of five states, namely: $|0,0\rangle$, $|\uparrow,0\rangle$, $|\downarrow,0\rangle$, $|0,\uparrow\rangle$, $|0,\downarrow\rangle$. With a bias applied from left to right, current I flows whenever dot 2 is occupied,

$$I_{\text{DQD}} = \Gamma(\rho_{|0,\uparrow\rangle} + \rho_{|0,\downarrow\rangle}), \tag{4.6}$$

where $\Gamma = \Gamma_{\text{L,R}}$ is the tunneling rate to the right lead. The spin-resolved currents are then $I_\uparrow = \Gamma\rho_{|0,\uparrow\rangle}$ and $I_\downarrow = \Gamma\rho_{|0,\downarrow\rangle}$. In the TQD, one electron is confined in the left dot (dot 1, see Fig. 4.1), and the chemical potential of the left lead is arranged in such a way that only an electron with the opposite spin can enter the TQD. Considering here strong Coulomb repulsion as well, we allow only one additional electron to enter the TQD. The full two-electron basis for the TQD contains 15 two-electron states and one zero- and six one-electron states. For the scope of this work it is sufficient to look at transport around the transitions $(2,0,0) \leftrightarrow (1,1,0) \leftrightarrow (1,0,1) \rightarrow (1,0,0)$. The number of relevant basis states is then reduced to 11, which are (a) one-electron states: $|\uparrow,0,0\rangle$, $|\downarrow,0,0\rangle$, (b) two-electron states: $|\uparrow,\uparrow,0\rangle$, $|\downarrow,\uparrow,0\rangle$, $|\uparrow,\downarrow,0\rangle$, $|\downarrow,\downarrow,0\rangle$, $|\uparrow,0,\uparrow\rangle$, $|\downarrow,0,\uparrow\rangle$, $|\uparrow,0,\downarrow\rangle$, $|\downarrow,0,\downarrow\rangle$, and $|\uparrow\downarrow,0,0\rangle$. The current from left to right through the TQD is calculated summing over all states that include an electron in the right dot (dot 3)

$$I_{\text{TQD}} = \Gamma(\rho_{|\uparrow,0,\uparrow\rangle} + \rho_{|\downarrow,0,\uparrow\rangle} + \rho_{|\uparrow,0,\downarrow\rangle} + \rho_{|\downarrow,0,\downarrow\rangle}). \tag{4.7}$$

The spin-resolved currents are then

$$\begin{aligned} I_\uparrow &= \Gamma(\rho_{|\uparrow,0,\uparrow\rangle} + \rho_{|\downarrow,0,\uparrow\rangle}) \\ I_\downarrow &= \Gamma(\rho_{|\uparrow,0,\downarrow\rangle} + \rho_{|\downarrow,0,\downarrow\rangle}). \end{aligned} \tag{4.8}$$

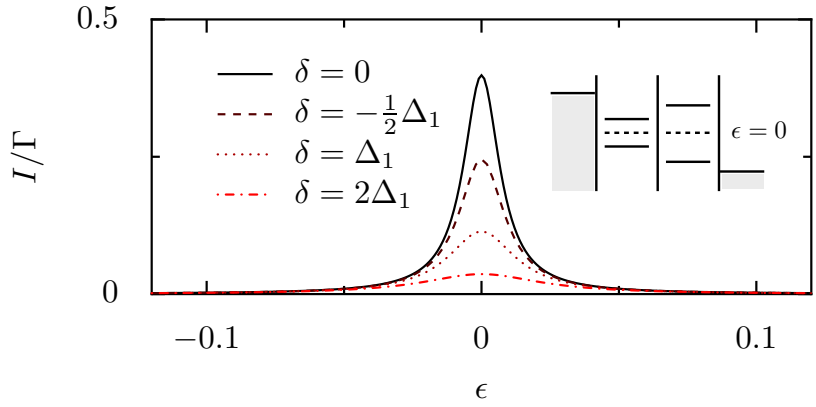

Figure 4.2.: **Current versus detuning in an undriven DQD with different Zeeman splittings.** Maximal current I flows when the detuning $\epsilon = 0$, and this central current decreases for increasing δ, since parallel spin levels are then more separate. Parameters ($e = \hbar = 1$, in meV): $t_{12} = 0.005$, $\Gamma = 0.001$, $\Delta_1 = 0.025$ ($B_{\rm dc} \approx 1$T), and the current I is normalized in units of the hopping Γ to the leads.

The spin polarization of the current is defined as

$$P = \frac{I_\uparrow - I_\downarrow}{I_\uparrow + I_\downarrow}, \tag{4.9}$$

where $I_\uparrow(I_\downarrow)$ is the $\uparrow(\downarrow)$-current.

4.2. Undriven case: $B_{\rm ac} = 0$

Let us now start by describing transport through a DQD (see Fig. 4.1, upper panel). In this section, within our theoretical framework, we reproduce the results recently reported by Huang *et al.* [125]. The authors have shown that in transport through DQDs with different Zeeman splittings a so-called spin bottleneck situation can occur. When either $\uparrow$- or $\downarrow$-levels are aligned, transport is suppressed, whereas the current is largest in the configuration where the interdot level detuning ϵ is set to half the Zeeman energy difference. Applying a dc magnetic field in z direction produces a Zeeman splitting Δ_Z, which we consider inhomogeneous: $\Delta_1 \neq \Delta_2$ and $\delta = \Delta_2 - \Delta_1$. If an electron tunnels onto the $\uparrow(\downarrow)$-level in dot 1 that is far from resonance from the corresponding spin level in dot 2, a spin-blockade or bottleneck situation arises. Spin is conserved at tunneling, so the electron remains in dot 1 without being able to tunnel to dot 2. This blockade is only relieved by a finite level broadening and by coupling to the leads. The maximal current occurs then for the most symmetric level arrangement, that is when neither $\uparrow$- nor $\downarrow$-levels are in resonance, but when they are symmetrically placed around each other (see Fig. 4.2). Increasing the Zeeman splitting difference δ maintains the bottleneck situation, but the central current decreases, since it is a consequence of the level hybridization of the same spin levels due to tunneling. Hence, the further separated they are, the less current will flow. Notice that the current only depends on the Zeeman splitting difference δ and not on the absolute values.

Interdot tunneling conserves spin, and the current through the sample is completely unpolarized. In ac magnetic fields, however, the electron spin undergoes rotations, and the spin- selection rules

thus do not apply any more. For certain detunings this will lead to spin-polarized currents, as we will see in the next section.

4.3. Driven case: $B_{\mathrm{ac}} \neq 0$

4.3.1. Resonance condition: $\omega = \Delta_1$

With a circularly polarized ac magnetic field B_{ac} applied to the DQD, the transformed Hamiltonian $\mathcal{H}^0 = \mathcal{H}_{\mathrm{Dots}} + \mathcal{H}_{\mathrm{tun}} + \mathcal{H}_{\mathrm{B}}$ reads

$$\mathcal{H}^0 = \begin{pmatrix} -\frac{\Delta_1}{2} + \frac{\omega}{2} & \frac{B_{\mathrm{ac}}}{2} & -t_{12} & 0 \\ \frac{B_{\mathrm{ac}}}{2} & \frac{\Delta_1}{2} - \frac{\omega}{2} & 0 & -t_{12} \\ -t_{12} & 0 & -\frac{\Delta_2}{2} + \frac{\omega}{2} - \epsilon & \frac{B_{\mathrm{ac}}}{2} \\ 0 & -t_{12} & \frac{B_{\mathrm{ac}}}{2} & \frac{\Delta_2}{2} - \frac{\omega}{2} - \epsilon \end{pmatrix}, \tag{4.10}$$

where ϵ is the detuning between dot 1 and dot 2.

For the ease of its analysis, the Hamiltonian Eq. (4.10) can be seen as a pair of two-level systems coupled by t_{12}. In a two-level system the important physical quantities are the energy difference (*detuning*) of the two levels and the coupling between them. In the present case, note that t_{12} couples only levels with the same spin, which are detuned by $\pm\delta/2 + \epsilon$, where $\delta = \Delta_2 - \Delta_1$. Moreover, within each dot the different spin levels are coupled by $B_{\mathrm{ac}}/2$ and *detuned* by $\omega - \Delta_{1,2}$, see diagonal elements in Eq. (4.10). Therefore, depending on the ac frequency ω, the energy levels in either left or right dot are renormalized to the same energy. In the other dot, however, since there $\omega \gtrless \Delta_i$, the renormalized splitting between the spin levels becomes smaller compared to the field-free splitting Δ_i, when $\omega < 2\Delta_i$ or bigger for $\omega > 2\Delta_i$. We will focus first on the resonance condition $\omega = \Delta_1$, as it is the most relevant here.

In order to understand the effect of B_{ac} on the system, let us look at the eigenstates of the isolated dots 1 and 2. In dot 1, since $\omega = \Delta_1$, the eigenstates are $|\psi_1\rangle^{\pm} = \frac{1}{\sqrt{2}}(|\uparrow_1\rangle \pm |\downarrow_1\rangle)$ and their eigenenergies differ by B_{ac}. In dot 2, however, since it is out of resonance, the eigenstates depend both on δ and B_{ac}:

$$\begin{aligned} |\psi_2\rangle^{+} &= \frac{1}{N}\left[B_{\mathrm{ac}}|\uparrow_2\rangle + \left(\delta + \sqrt{B_{\mathrm{ac}}^2 + \delta^2}\right)|\downarrow_2\rangle\right] \\ |\psi_2\rangle^{-} &= \frac{1}{N}\left[\left(\delta + \sqrt{B_{\mathrm{ac}}^2 + \delta^2}\right)|\uparrow_2\rangle - B_{\mathrm{ac}}|\downarrow_2\rangle\right] \end{aligned} \tag{4.11}$$

Here $N = \sqrt{2}\sqrt{B_{\mathrm{ac}}^2 + \delta^2 + \delta\sqrt{B_{\mathrm{ac}}^2 + \delta^2}}$ is the normalization factor. The eigenenergies associated to these states are separated by $\sqrt{B_{\mathrm{ac}}^2 + \delta^2}$. One can straightforwardly show that for $B_{\mathrm{ac}} \ll \delta$ the eigenstates in dot 2 are almost pure $\uparrow(\downarrow)$ states, i.e. the spin-mixing is weak. Regarding the detuning ϵ, we distinguish three different level arrangements, see Fig. 4.3, upper panel: In case I, the $\uparrow$- and $\downarrow$-levels in dot 1 are aligned with the $\uparrow$-level in dot 2, case II is the *symmetric* situation, and in case III the levels in dot 1 are in resonance with the $\downarrow$-level in dot 2.

In Fig. 4.3, lower panels, we plot the current I through the driven DQD as a function of the level detuning ϵ. It shows two peaks at $\epsilon \approx \pm\frac{\delta}{2}$. At these lateral peaks, – corresponding to case I and III

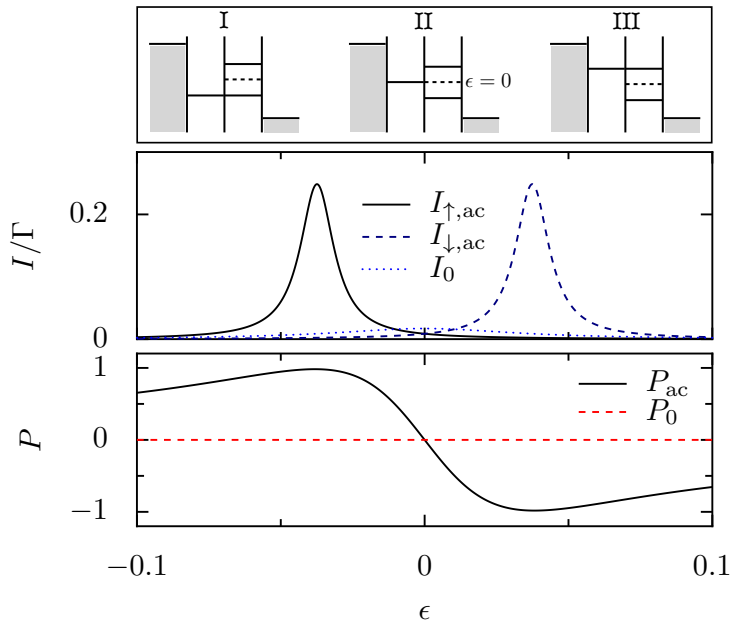

Figure 4.3.: **Current as a function of detuning through a DQD driven by an ac magnetic field B_{ac}.** *Upper panel:* Energy level distribution for different detunings ϵ. When $\omega = \Delta_1$, the levels in dot 1 renormalize to the same energy (their eigenenergies are split by B_{ac}, see text), and the levels in dot 2 get closer or farther apart than in the undriven case. *Middle panel:* Spin-resolved currents $I_\uparrow$ and $I_\downarrow$ vs. detuning ϵ. At $\epsilon \approx \pm\frac{\delta}{2}$, the current is strongly $\uparrow(\downarrow)$-polarized, compared to the undriven current I_0. *Lower panel:* Polarization P versus the detuning ϵ. Note the strong polarization ($P \approx \pm 1$) around $\epsilon \approx \pm\frac{\delta}{2}$. Parameters in meV ($e = \hbar = 1$): $\Gamma = 0.001$, $t_{12} = 0.005$, $B_{\mathrm{ac}} = 0.005$ (≈ 0.2T), $\Delta_1 = 0.025$ ($B_{z1} \approx 1$T), $\Delta_2 = 0.1$.

–, the current is strongly *spin-polarized*: an electron in dot 1 is rotated by the ac field, which breaks the spin bottleneck, and the electron can thus tunnel to dot 2 where the spin levels are almost pure. Speaking in terms of the rotating field, the ac frequency in dot 2 is far off resonance and cannot rotate the electron there. We thus arrive at one of the main results of this chapter: under the condition $\omega = \Delta_1$, dot 2 acts as a spin-filter, and it depends on ϵ, whether it filters $\uparrow$- or $\downarrow$-electrons. Notice that the current I only depends on δ and not on the absolute values $\Delta_{1,2}$.

For the purpose of a spin-filter, one has to answer the question as to how reliable the mechanism is and how it depends on the different system parameters. Both strong polarization and measurable currents are desirable. Here we discuss the sensibility of the spin-filtering mechanism towards the interplay between tunneling t_{12}, ac field intensity B_{ac} and Zeeman splitting difference δ. In order to get more insight into the problem, we obtain the current I analytically for certain limits: at symmetric detuning $\epsilon = 0$ (case II), the current is unpolarized and reads

$$\frac{I_0}{\Gamma} = \frac{4t_{12}^2(4B_{\mathrm{ac}}^2 + \Gamma^2 + \delta^2)}{4B_{\mathrm{ac}}^2(\Gamma^2 + 10t_{12}^2) + (\Gamma^2 + \delta^2)(\Gamma^2 + 10t_{12}^2 + \delta^2)}. \tag{4.12}$$

I_0 decreases for large δ and increases with growing B_{ac}. In the limit of very large t_{12} the total current

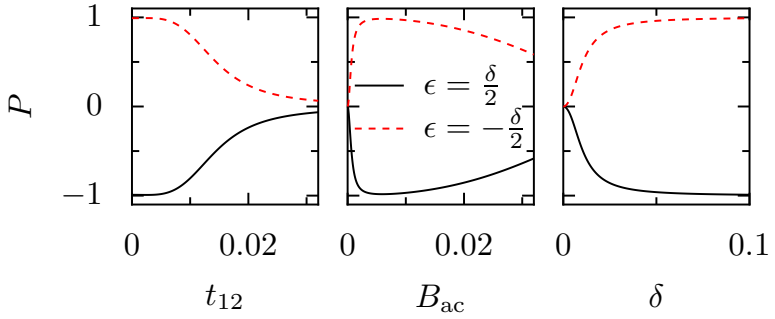

Figure 4.4.: **Current polarization P as a function of different system parameters.** Polarization P versus t_{12} (left), $B_{\rm ac}$ (middle) and δ (right) in ac-driven DQD at detuning $\epsilon = \pm\frac{\delta}{2}$ for $\omega = \Delta_1$: *Left and middle panel:* For both small t_{12} and $B_{\rm ac}$, spin-polarized current flows. $|P|$ becomes smaller as $B_{\rm ac}$ and t_{12} grow. *Right panel:* P is zero at $\delta = 0$ and increases with δ. Parameters see Fig. 4.3.

I saturates to $\frac{I}{\Gamma}(t_{12} \to \infty) = \frac{2}{5}$. For the limiting cases of $B_{\rm ac}$ we get

$$\lim_{B_{\rm ac}\to 0} \frac{I_{\uparrow,\downarrow}}{e\Gamma} = \frac{2t_{12}^2}{\Gamma^2 + 10t_{12}^2 + 4\epsilon^2 + \delta^2} \tag{4.13}$$

$$\lim_{B_{\rm ac}\to \infty} \frac{I_{\uparrow,\downarrow}}{e\Gamma} = \frac{2t_{12}^2}{\Gamma^2 + 10t_{12}^2 + 4\epsilon^2}. \tag{4.14}$$

For $B_{\rm ac} \to 0$, i.e. in the undriven case, the current is unpolarized and maximal at $\epsilon = 0$ and decreases for growing δ, see Eq. (4.13). Notice that in the opposite limit, i.e. for large $B_{\rm ac}$ (Eq. (4.14)), the current is the same as in the undriven case for $\delta = 0$. In this case, the difference of the eigenenergies in each isolated dot becomes $B_{\rm ac}$ in *both* dots, and the spins are mixed almost equally strongly. The polarized side-peaks therefore disappear in favor of the unpolarized central current peak, see also Eq. (4.12). Already with t_{12} and $B_{\rm ac}$ of the order of δ, we find that the current is practically unpolarized. Hence both t_{12} and $B_{\rm ac}$ have to be sufficiently small to ensure strong current spin polarization.

It can be shown numerically that for small t_{12} and $B_{\rm ac}$ the position ϵ of the side-peaks is $\epsilon \approx \pm\frac{\delta}{2}$. The larger δ is, the further separated will be the peaks corresponding to $I_\uparrow$ and $I_\downarrow$. As a consequence also the polarization is stronger for large δ, since the overlap of the spin-resolved currents tends to zero.

In order to illustrate the effect of tunneling t_{12}, of ac field intensity $B_{\rm ac}$ and of Zeeman splitting difference δ on the polarization P, we calculate P at $\epsilon = \pm\frac{\delta}{2}$ (Fig. 4.4). In the left and middle panel one can appreciate that for both small t_{12} and $B_{\rm ac}$, $P \approx \pm 1$, and it becomes smaller as t_{12} and $B_{\rm ac}$ increase. The right panel in Fig. 4.4 shows P for increasing δ: the larger δ, the stronger P.

4.3.2. Resonance condition: $\omega = \Delta_2$

When the ac field, however, fulfills the resonance condition $\omega = \Delta_2$, the energy renormalization due to ω is reversed in the two dots as compared to $\omega = \Delta_1$, and now the energy levels in dot 2 become degenerate. The analytical limits described for $\omega = \Delta_1$ hold here as well: for large t_{12} and $B_{\rm ac}$ the current becomes unpolarized, and at $\epsilon = 0$ it follows Eq. (4.12). However, out of these limits, transport

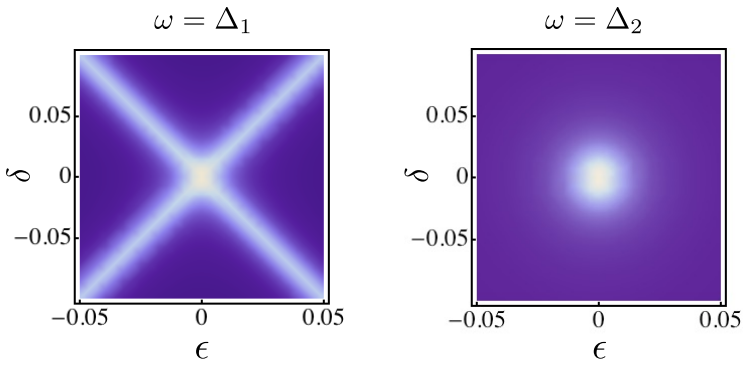

Figure 4.5.: **Density plots of the current I versus detuning ϵ and Zeeman splitting difference δ.** *Left panel:* $\omega = \Delta_1$. For growing δ and ϵ, the current I splits off in two branches (light-colored regions), which are spin-polarized in opposite direction (cf. previous section). *Right panel:* $\omega = \Delta_2$. Current flows only around $\delta = \epsilon = 0$ (light-colored region); $P = 0$. Parameters see Fig. 4.3.

behavior here is very different from the case $\omega = \Delta_1$. At detunings $\epsilon \approx \pm\frac{\delta}{2}$, spin bottleneck occurs similar as has been shown in the undriven case. Since dot 1 is out of resonance, the ac field cannot rotate the electron there, hence tunneling to dot 2 is strongly suppressed. The maximal (unpolarized) current then flows for $\epsilon = 0$, and no side-peaks appear.

In summary, at $\omega \approx \Delta_1$, dot 2 can always act as a spin-filter. The mixing of $\uparrow$- and $\downarrow$-states due to the ac field is always stronger in dot 1 than in dot 2, no matter if $\Delta_1 \gtrless \Delta_2$. The ac field mixes $\uparrow$- and $\downarrow$-states in dot 1, so that at $\epsilon \approx \pm\frac{\delta}{2}$ the electron tunnels onto the almost pure $\uparrow$- or $\downarrow$-levels in dot 2, which thus filters the spin and gives rise to spin-polarized currents. This is opposed to the case $\omega = \Delta_2$: here, due to spin bottleneck, tunneling to dot 2 is only possible around $\epsilon = 0$ where the current is totally unpolarized. This behavior is shown in Fig. 4.5 in two density plots of the current I versus detuning ϵ and $\delta = \Delta_2 - \Delta_1$, for the two cases $\omega = \Delta_1$ (left) and $\omega = \Delta_2$ (right). In the left plot one can clearly see the formation of the two spin-polarized current branches which move far apart as δ and ϵ grow. In contrast to that, the right plot shows that current only flows for both $\epsilon = 0$ and $\delta = 0$, and no spin-polarized side-peaks arise.

4.3.3. Non-resonant driving

If the ac frequency does not match any of the Zeeman splittings $\Delta_{1,2}$, the effective finite Zeeman splittings are $\Delta^*_{1,2} = \Delta_{1,2} - \omega$. It is easy to prove that for $\omega = \frac{\Delta_1+\Delta_2}{2} = \Delta_s$ there is a "symmetric" situation, namely $\Delta^*_1 = \frac{\Delta_1-\Delta_2}{2}$, and $\Delta^*_2 = -\Delta^*_1$. In this case, the mixing of the spin-states within each dot is equal in both dots, or in other words, both dots are equally far from resonance with the ac field. Regarding interdot tunneling, the levels are resonant at $\epsilon = 0$, giving rise to one unpolarized current-peak. At all other detunings ϵ, spin bottleneck avoids the formation of polarized side-peaks. In Fig. 4.6 we show the total current I (upper left) and spin-resolved currents (upper middle, upper right) vs. detuning ϵ and frequency ω, for $\Delta_2 > \Delta_1$. In order to appreciate the different current intensities we plot in the lower panel the current versus the detuning ϵ for the three relevant frequencies $\omega =$

$\Delta_1, \Delta_2, \Delta_s$. Note the regimes for ω as discussed in the previous sections: for $\omega = \Delta_2$, spin bottleneck only allows for a very weak and unpolarized current to flow around $\epsilon = 0$. When the frequency matches the symmetric value Δ_s, at $\epsilon = 0$ one sharp and unpolarized current peak arises as predicted. Further decreasing of the frequency splits the current into two branches, which are enhanced and broadened as $\omega \approx \Delta_1$. The sidearms correspond to either $\uparrow$ (middle panel) or $\downarrow$ (right panel) electrons. For any off-resonant frequency, the current depends not only on δ as in the resonant case, but also on the absolute values $\Delta_{1,2}$. Hence the position of the side-peaks is not $\epsilon \approx \pm\frac{\delta}{2}$, but follows a different behavior. This explains the kink in Fig. 4.6 (upper panel) around $\omega = \Delta_1$. We want to stress that

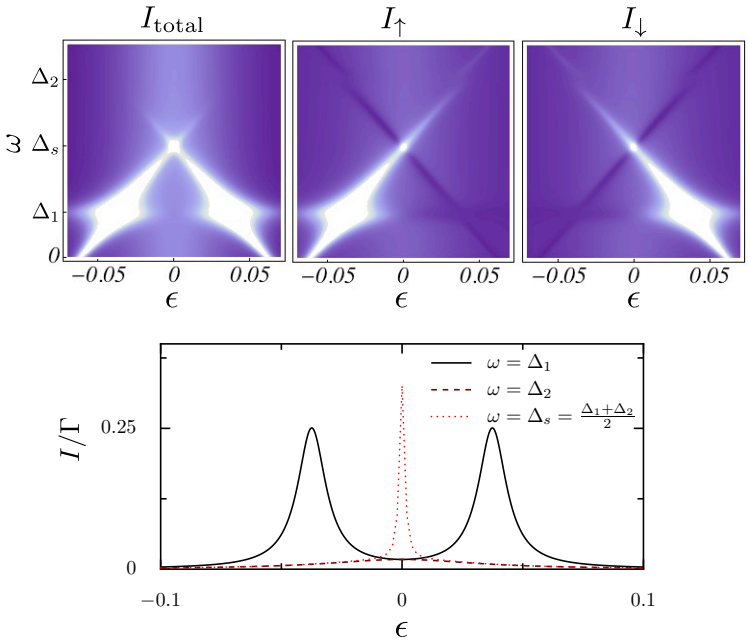

Figure 4.6.: **Plots of the total current and spin-resolved currents in a DQD for different resonance conditions.** *Upper panel:* Density plots of the total current I (left) and spin-resolved currents $I_\uparrow$ (middle) and $I_\downarrow$ (right) as a function of detuning ϵ and ac frequency ω for $\Delta_1 < \Delta_2$. The lighter the color, the higher the current. Note that only very low current flows in the frequency range $\omega > \Delta_s$ around $\epsilon = 0$. At $\omega = \Delta_s$ and $\epsilon = 0$, one sharp unpolarized peak arises. Lowering ω further, the current splits into two arms and successively grows, until around $\omega = \Delta_1$ current is strongly enhanced and polarized, since the sidearms stem from either $\uparrow$- or $\downarrow$-electrons, see middle and right upper panels. *Lower panel:* Current versus ϵ for the three different situations $\omega = \Delta_1$, $\omega = \Delta_2$, and $\omega = \Delta_s$. One can appreciate the big difference in the current intensities: only for $\omega = \Delta_1$, polarized sidepeaks arise. For $\omega = \Delta_2$ current flows weakly around $\epsilon = 0$ and for Δ_s, only at $\epsilon = 0$ a sharp current peak appears. Parameters see Fig. 4.3.

in the ac-driven DQD spin-polarized currents can be achieved both for $\Delta_1 > \Delta_2$ or $\Delta_1 < \Delta_2$, since by varying the frequency ω one can always tune one Zeeman splitting to be smaller than the other, as schematically indicated by the renormalization of the energy levels due to ω (see Fig. 4.3, upper panel). In contrast to that, a static magnetic field set-up – for example, considering dc magnetic fields in x-direction [125] – would only produce polarized currents for $\Delta_1 < \Delta_2$.

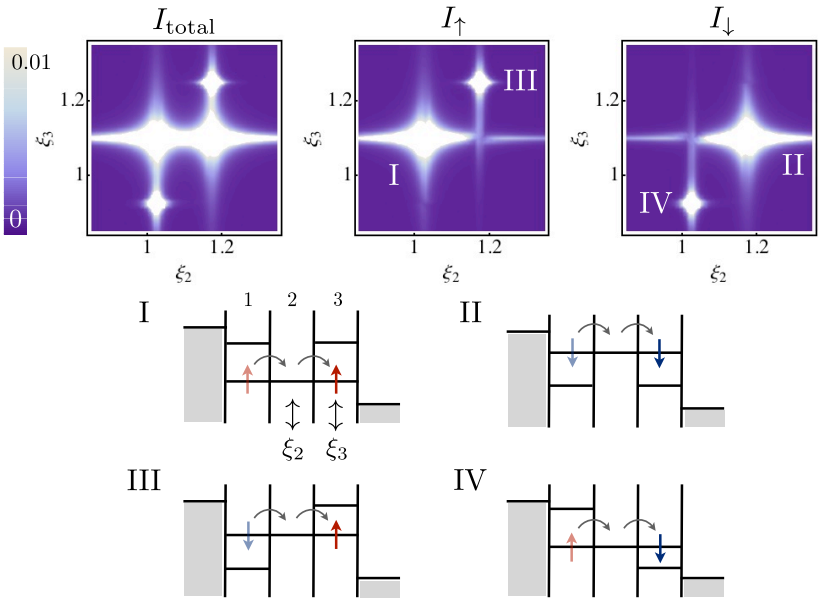

Figure 4.7.: **Total current and spin-resolved currents vs. two energy levels in a TQD exposed to crossed B_{dc} and B_{ac}.** In all plots: $\omega = \Delta_2$ and $\Delta_1 = \Delta_3 > \Delta_2$. Four relevant level configurations can occur when varying ξ_2 and ξ_3: in cases I and II, current through the TQD is polarized in one spin-direction, and in cases III and IV, the electron spin is inverted. In order not to overload the figure, we indicate only the spins of the incoming and outgoing electrons, but note that always one electron is confined in dot 1, cf. Fig. 4.1. Parameters: $\Gamma = 0.01$, $t_{12,\,23} = 0.01$, $B_{\text{ac}} = 0.01$ (≈ 0.4T), $\Delta_1 = \Delta_3 = 7\Delta_2$, $\Delta_2 = 0.025$ ($B_{\text{dc}} \approx 1$T), $U = 1.0$, $\xi_1 = 0.1$, all units in meV.

4.3.4. A triple quantum dot as spin-inverter

Now we want to implement the spintronic functionality of the spin-filter device towards a *spin-inverter*, and to this end we consider a TQD. Our goal is to produce spin-polarized incoming current I_{in} and oppositely spin-polarized outgoing current I_{out}.

We consider the TQD in a regime where only 2 electrons can be in the TQD at a time, and one electron is confined electrostatically in dot 1 (cf. Fig. 4.1, lower panel). This confinement is necessary to introduce spin correlations in the dot, so that only an electron with opposite spin can enter the TQD. The incoming current is then either $\uparrow$- or $\downarrow$-polarized, depending on the position of the energy levels in the adjacent dot. The ac field frequency ω is in resonance with the central dot (dot 2), $\omega = \Delta_2$, in order for the right dot (dot 3) to act as the filter dot. The TQD is here operated around the resonances $(2,0,0) \leftrightarrow (1,1,0) \leftrightarrow (1,0,1)$. For simplicity, we restrict the discussion to the case where the Zeeman splittings are $\Delta_1 = \Delta_3 > \Delta_2$, although this condition is not necessary, as long as $\Delta_{1,3} \neq \Delta_2$.

From the previous sections we already know that, depending on the detuning, the dot connected to the drain can act as $\uparrow$- or $\downarrow$-filter. In a TQD there is one more degree of freedom compared to the DQD, regarding the detuning between the dot levels. Without loss of general validity, we can fix the energy level of dot 1 and move the energy levels of dot 2 and 3 (which is experimentally realized by applying

gate voltages to the corresponding dots). Under these conditions, there are then four relevant energy level configurations, which are shown in Fig. 4.7, lower panel. In two of the configurations (I and II), the TQD acts as a *spin-polarizer*, and in the other two (III and IV) the electron spin is *inverted*. We hereby arrive at another important result of our work: a TQD can be tuned as both spin-polarizer and spin-inverter by confining one electron in the left dot and adjusting the gate voltages at two of the three dots. Then electrons coming from the left lead can only enter with a distinct spin-polarization that depends on the level position of the central dot. As the magnetic field B_{ac} is turned on with frequency $\omega = \Delta_2$, the electron spin coming from dot 1 is rotated in dot 2, whereas dot 1 and dot 3 due to their different Zeeman splittings are far off resonance from the ac field. Dot 3 then acts as spin-filter and, depending on the relative position ϵ of its energy levels with respect to dot 2, a $\uparrow$- or $\downarrow$-polarized current is produced, similar as it happens in the DQD described in the previous sections.

We plot the total I_{total} and spin-resolved currents $I_\uparrow$ and $I_\downarrow$ as functions of the energy levels $\xi_{2,3}$ of dot 2 and dot 3 in Fig. 4.7, together with sketches of the corresponding energy level distribution. In situations I and IV, dot 2 is energetically in resonance with the $\uparrow$-level in dot 1. Therefore only $\uparrow$-electrons coming from the left lead will be able to tunnel to dot 2. Here they are inverted due to $\omega = \Delta_2$, where the renormalized energy levels have been depicted schematically in the same way as has been done for the DQD. It depends then on the level position of dot 3, whether the outgoing current is spin-up (case I) or spin-down (case IV) polarized. An analogous situation occurs for cases II and III: the energy level of dot 2 is positioned in such a way that only $\downarrow$-electrons can tunnel from dot 1 to dot 2. Again, after rotation due to the ac field in dot 2, in dot 3 the spin is filtered without inversion (case II) or inverted (case III).

4.4. Conclusions

In this chapter we have analyzed spin current polarization in transport, both through a DQD with one extra electron and through a TQD with two extra electrons in the system. The quantum dot arrays are subject to two different external magnetic fields: an inhomogeneous dc field which produces different Zeeman splittings Δ_Z in the dots, and a time-dependent ac field that rotates the electron spin in one dot, if the resonance condition $\omega = \Delta_Z$ is fulfilled. For the DQD we have analyzed both off-resonance and resonance conditions of the ac field with each of the Zeeman splittings. Our results show that ac magnetic fields produce strongly spin-polarized current through a DQD, depending on the detuning of the energy levels in the dots and on the resonance conditions.

Finally, we have proposed a TQD in series as both spin-polarizer and spin-inverter. As in a DQD, in a TQD different Zeeman splittings in the sample combined with a resonant ac frequency give way to spin-polarized currents. In addition, spin-polarized incoming current can be achieved, and thus the spin-polarizing mechanism can be extended to a spin-inversion mechanism. Our results show that dc and ac magnetic fields combined with gate voltages allow one to manipulate the current spin polarization through DQDs and TQDs, which are then able to work as a spin-filter and spin-inverter.

In spintronic devices at the nanometer scale an environment of nuclei introduces additional spin-flip processes that can lower the efficiency of the desired mechanism. In our setup, we do not expect

spin-flip processes due to hyperfine interaction to influence drastically on the results because hyperfine spin-flip times are usually much longer than typical tunneling times in quantum-dot arrays, especially in finite magnetic fields where the hyperfine interaction is an inelastic process. Therefore the systems presented in this work are promising candidates for spintronic devices.

5. Bipolar spin blockade in triple quantum dots

Transport experiments in double quantum dots (DQD) have revealed a phenomenon called *spin blockade* (see also chapter 1) [9, 39]: it occurs when, due to the confinement of an electron in the dot closest to the drain, another electron with the same spin cannot pass through this dot as a consequence of Pauli's exclusion principle. To operate a quantum dot array in the spin blockade regime is a basis for spin readout of a qubit state due to spin-to-charge conversion. The archetypal spin blockade transport signature in DQDs takes the form of a rectified current. Spin qubits based on interacting spins in DQDs have been demonstrated [131, 31, 132], and currently more complex spin qubit circuits such as triple quantum dots (TQDs) are being developed [77, 109, 110]. There the coherent control of three-spin qubit has been achieved [114, 115]. In a spin blockade situation in DQDs, leakage currents have been observed and attributed to hyperfine interaction, i.e. to the interaction between the spin of conduction electrons and nuclei spins in the host material [30] (see chapter 1). Spin-flip processes can occur between one electron and one nuclear spin, thus contributing to remove the occupation of spin blockaded states. Hyperfine interaction induces Overhauser fields that give rise to an inhomogeneous magnetic field $B_{z,\mathrm{nucl}}$. The inhomogeneous nuclear field $B_{z,\mathrm{nucl}}$ mixes the singlet and triplet states of spins in neighboring dots. Once an external magnetic field bigger than the difference between Overhauser fields $B_{z,\mathrm{nucl}}$ and exchange coupling is applied, triplet states $\uparrow\uparrow$ and $\downarrow\downarrow$ are no longer mixed with singlet states, and therefore leakage current is suppressed as well by spin blockade.

In this chapter we show both experimental results (obtained by Sachrajda *et al.*) and theoretical results for spin blockade in transport through a linear TQD. The spin blockade becomes *bipolar* with current suppressed in both bias directions. The blockade is lifted by the hyperfine interaction via the formation of coherent superpositions of states. The responsible coherent state transfers charge non-intuitively from one end of the triple dot circuit to the other without involving the intermediate site, which suggests that new quantum coherent mechanisms are relevant in TQDs as compared to DQDs.

5.1. Model

The TQD is prepared in a similar way as a DQD in the spin blockade regime: an electron is confined electrostatically both in the dot connected to the source and in the dot close to the drain, see Fig. 5.1. The charge stability diagram of a TQD prepared in such a way has been measured by Granger *et al.* [113]. There six quadruple points, – i.e. six different points with four resonant charge configurations –, have been found, around which transport is possible. Out of these six points, we are interested here

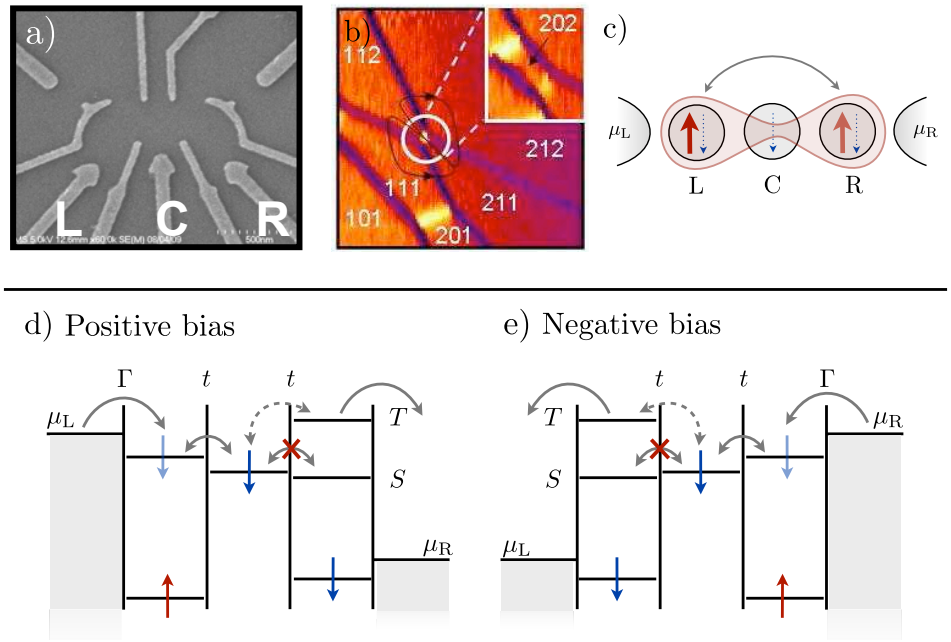

Figure 5.1.: **Bipolar spin blockade in a linear TQD. a)** Scanning electron micrograph of the sample structure. **b)** Stability diagram of the TQD measured for fixed center gate voltage and varying left (horizontal) and right (vertical) gate voltages. The tunneling sequence at quadruple points 5 and 6 (see Eq. (5.1)) is marked by arrows, and the (202) region is zoomed in the upper right corner. **c)** Schematic picture of the TQD indicating a coherent state forming between a spin-up electron in the left and in the right dot (the same situation would occur for a spin-down electron), under the condition that left and right dot energy levels align. **d)** Schematic description of spin blockade in positive bias direction. In the left and right dot one electron is confined electrostatically, so that only doubly occupied levels in left and right dot contribute to transport. The central dot can only accept one electron. If the two electrons in the center and right dot have the same spin, current is blocked due to spin blockade. **e)** Spin blockade in negative bias direction. Figures a) and b) taken from ref. [113].

in transport around two of them, which in the original work were labelled as points 5 and 6

$$\begin{aligned} \text{QP5} &: (1,1,1)\ (1,1,2)\ (2,1,1)\ (2,0,2) \\ \text{QP6} &: (1,1,2)\ (2,1,1)\ (2,0,2)\ (2,1,2). \end{aligned} \tag{5.1}$$

We are modeling the TQD, the leads and the coupling between them with an Anderson-like Hamiltonian that reads

$$\mathcal{H} = \mathcal{H}_{\text{TQD}} + \mathcal{H}_{\text{tun}} + \mathcal{H}_{\text{B}} + \mathcal{H}_{\text{T}} + \mathcal{H}_{\text{Leads}}, \tag{5.2}$$

where the individual terms are

$$\begin{aligned}
\mathcal{H}_{\mathrm{TQD}} &= \sum_{i\sigma} \epsilon_{i\sigma} \hat{c}^{\dagger}_{i\sigma} \hat{c}_{i\sigma} + \sum_{i} U_i \hat{n}_{i\uparrow} \hat{n}_{i\downarrow} + \frac{1}{2} \sum_{i \neq j} V_{ij} \hat{n}_i \hat{n}_j \\
\mathcal{H}_{\mathrm{tun}} &= -\sum_{ij\sigma} t_{ij} (\hat{c}^{\dagger}_{i\sigma} \hat{c}_{j\sigma} + \hat{c}^{\dagger}_{j\sigma} \hat{c}_{i\sigma}) \\
\mathcal{H}_{\mathrm{B}} &= \sum_{i=1}^{3} g \mu_B (B_z + B_{i,\mathrm{nucl}}) S_{z,i} = \sum_{i=1}^{3} \Delta_i S_{z,i} \\
\mathcal{H}_{\mathrm{T}} &= \sum_{l \in \mathrm{L,R}, k\sigma} \gamma_l (\hat{d}^{\dagger}_{lk\sigma} \hat{c}_{l\sigma} + \hat{c}^{\dagger}_{l\sigma} \hat{d}_{lk\sigma}) \\
\mathcal{H}_{\mathrm{Leads}} &= \sum_{l \in \mathrm{L,R}, k\sigma} \epsilon_{lk} \hat{d}^{\dagger}_{lk\sigma} \hat{d}_{lk\sigma}.
\end{aligned} \tag{5.3}$$

The first term represents the TQD itself, with $\epsilon_{i\sigma}$ being the energy of an electron with spin σ, U_i the on-site Coulomb interaction energy, $V_{12,23,13}$ the interdot Coulomb interaction energies; we set $V_{12} = V_{23} = V \neq V_{13}$. The second term describes the coherent tunneling between the dots where we set $t_{ij} = t$; the third term is the magnetic field Hamiltonian with different Zeeman splittings Δ_i in each dot; the fourth term describes the tunneling between dot 1 and the left lead, and between dot 3 and the right lead; finally, the last term describes the leads themselves. The creation and annihilation operators for an electron on dot i with spin σ are given by $\hat{c}^{\dagger}_{i\sigma}, \hat{c}_{i\sigma}$, and for an electron in lead l by $\hat{d}^{\dagger}_{l\sigma}$, $\hat{d}_{l\sigma}$.

The experimentally measured quadruple points include electronic configurations for three, four and five electrons (see Eq. (5.1)), with the restriction that the center dot can only host one single electron, whereas both left and right dot contain one confined electron and can accept one more electron, see Fig. 5.1. In positive bias (negative bias), the left (right) dot – i.e. the dot connected to the electron source – accepts an additional incoming electron, so that the two electrons occupy a *singlet* state $|\uparrow\downarrow\rangle_{\mathrm{s}}$. The higher levels, such as excited triplets $|\uparrow\uparrow^*\rangle_{\mathrm{s}}$, $|\downarrow\downarrow^*\rangle_{\mathrm{s}}$ and $1/\sqrt{2}(|\uparrow\downarrow^*\rangle + |\downarrow\uparrow^*\rangle)_{\mathrm{s}}$ or excited singlet $1/\sqrt{2}(|\uparrow\downarrow^*\rangle - |\downarrow\uparrow^*\rangle)_{\mathrm{s}}$ states, are not accessible for an incoming electron (the index s stands for *source*). In contrast, the right (left) dot in positive (negative) bias is modeled in such a way that not only the singlet state $|\uparrow\downarrow\rangle_{\mathrm{d}}$, but also the energetically higher excited states $|\uparrow\uparrow^*\rangle_{\mathrm{d}}$, $|\downarrow\downarrow^*\rangle_{\mathrm{d}}$, $1/\sqrt{2}(|\uparrow\downarrow^*\rangle + |\downarrow\uparrow^*\rangle)_{\mathrm{d}}$ and $1/\sqrt{2}(|\uparrow\downarrow^*\rangle - |\downarrow\uparrow^*\rangle)_{\mathrm{d}}$ (where d expresses *drain*) can participate in transport, depending on their alignment with the adjacent central dot.

This confinement of electrons in the dot close to the drain introduces spin correlations between the electrons, so that double occupation in the drain dot undergoes a selection rule due to Pauli exclusion principle: the TQD is thus operated in the so-called *spin blockade regime* [39]. The full basis of states for the present problem contains 58 states. In the forward bias direction these states are

$$\begin{aligned}
|1,1,1\rangle &= |\sigma'', \sigma', \sigma\rangle & |1,1,1^*\rangle &= |\sigma'', \sigma', \sigma^*\rangle \\
|2,1,1\rangle &= |S, \sigma', \sigma\rangle & |2,1,1^*\rangle &= |S, \sigma', \sigma^*\rangle \\
|2,0,2\rangle &= |S, 0, S\rangle & |2,0,2^*\rangle &= |S, 0, T^*(S^*)\rangle \\
|1,1,2\rangle &= |\sigma, \sigma', S\rangle & |1,1,2^*\rangle &= |\sigma, \sigma', T^*(S^*)\rangle \\
|2,1,2\rangle &= |S, \sigma, S\rangle & |2,1,2^*\rangle &= |S, \sigma, T^*(S^*)\rangle
\end{aligned} \tag{5.4}$$

with $\{\sigma,\sigma',\sigma''\} = \{\uparrow,\downarrow\}$. For the calculation of the current we make use of the density matrix formalism and write the equation of motion for the elements of the reduced density matrix as presented in chapter 2 (Eq. (2.86))

$$\dot{\rho}_{mn}(t) = -i\langle m|[\mathcal{H}_{\mathrm{TQD}} + \mathcal{H}_{\mathrm{tun}} + \mathcal{H}_{\mathrm{B}}, \rho]|n\rangle + \sum_{k\neq n}(\Gamma_{nk}\rho_{kk} - \Gamma_{kn}\rho_{nn})\delta_{mn} - \Lambda_{mn}\rho_{mn}(1-\delta_{mn}). \tag{5.5}$$

For an approximate modeling of the spin-flip processes induced by hyperfine interaction we include a *phenomenological* spin-flip rate into the equations for the reduced density matrix [124] and a finite inhomogeneous Overhauser field. The spin relaxation time T_1 is given by $W_{\uparrow\downarrow} + W_{\downarrow\uparrow}$, where $W_{\uparrow\downarrow}$ and $W_{\downarrow\uparrow}$ are spin-flip rates that fulfill a detailed balance equation

$$W_{\downarrow\uparrow} = \exp\left(\frac{-\Delta_i}{k_B T}\right) W_{\uparrow\downarrow}.$$

T_2 is the spin decoherence time – i.e. the time over which a superposition of opposite spin states of a single electron remains coherent. This time can be affected by spin relaxation and by the spin dephasing time T_2^*, i.e. the spin decoherence time for an ensemble of spins (see also chapter 1). We set the spin relaxation rate $T_1 \approx 1$ s and the spin decoherence time $T_2^* \approx 10$ ns. The spin decoherence time is included in the master equation (5.5) via $\Lambda_{mn} = \frac{1}{2}\sum_k(\Gamma_{km} + \Gamma_{kn}) + T_2^{-1}$. As we are interested in the stationary current through the TQD, we solve the set of equations of the reduced density matrix algebraically and then calculate the current, which e.g. in positive bias direction (i.e. from left to right) is given by

$$I_{\mathrm{R}} = e\sum_{mn}\left(\Gamma^+_{mn} - \Gamma^-_{mn}\right)\rho_{nn}, \tag{5.6}$$

where Γ^+_{mn} expresses the rate of tunneling of an electron to the drain from the TQD and Γ^-_{mn} the tunneling of an electron from the drain to the TQD.

In the experiment the current is measured for a fixed center gate voltage while varying the left and right gate voltages. A change in the left gate voltage, however, does not only affect the energy levels in the left dot, but also affects, due to cross capacitances, – albeit slightly weaker – the energy levels of the neighboring dots. It has been stated in ref. [77] that the energy levels of the dots can be written as linear functions of the affecting gate voltages. Following therefore the scheme in ref. [77] and considering cross capacitances as proposed by the experiment, we write the energy levels ϵ_i of the dots $i = 1,2,3$ as

$$\epsilon_i = \mathcal{C}_i - \alpha_i V_{\mathrm{L}} - \beta_i V_{\mathrm{R}}, \tag{5.7}$$

where $\mathcal{C}_{1,2,3}$ are constants that provide an overall energy shift. The conversion parameters are given in eV/V. In the appendix A.1 we provide more details on how the conversion parameters influence the current profile.

5.2. Current through the TQD

In contrast to spin blockade measurements in DQDs [39, 40] the current profile of the TQD looks very similar *for both bias directions*. The most prominent features in the transport triangles are, as can

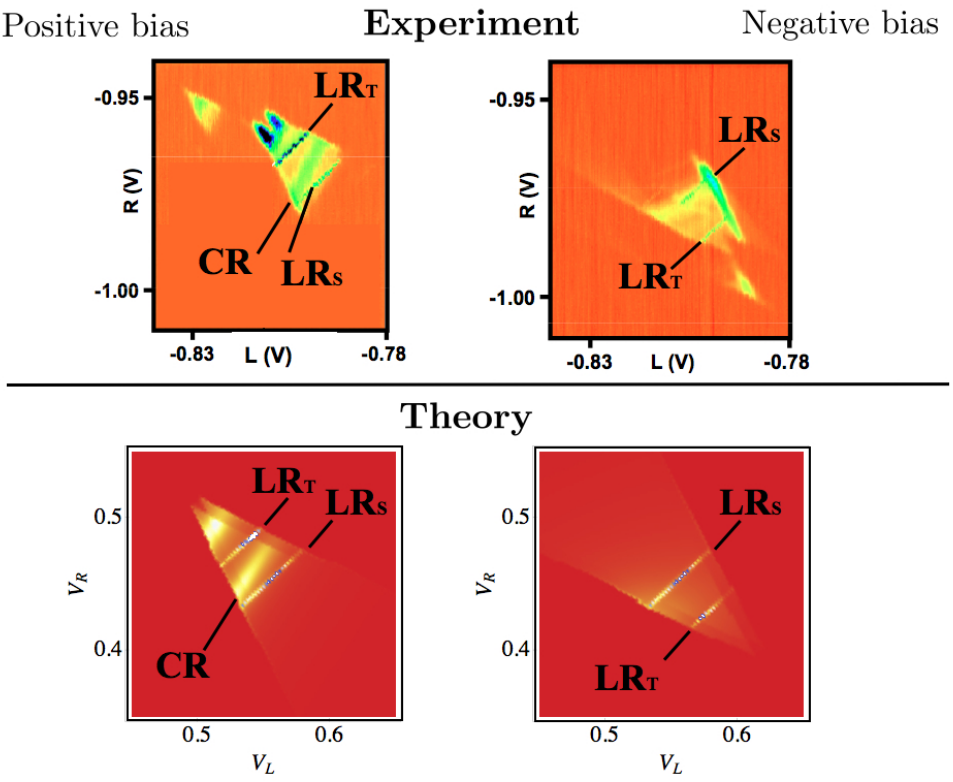

Figure 5.2.: **Current through the TQD for zero magnetic field.** Both for positive (left column) and negative (right column) bias and for the experimental (upper panels) and theoretical results (lower panel), one can clearly distinguish resonance lines with two different slopes: the LR resonance lines where left and right dot are on resonance and the steeper CR resonance lines that occur when center and right dot levels are aligned. Parameters: $t = 0.005$, $U_1 = 3.1$, $U_3 = 2.2$, $V = 0.5$, $V_{13} = 0.25$, $\varepsilon = 0.6$, $J = -0.02$, $\Gamma_{\mathrm{L,R}} = 0.001$, $W_{\uparrow\downarrow} = 5 \cdot 10^{-7}$, $W_{\downarrow\uparrow,i} = \exp[-\Delta_i/T]W_{\uparrow\downarrow}$, $W_{\mathrm{dec}} = 100(W_{\uparrow\downarrow} + W_{\downarrow\uparrow})$, $W_{\mathrm{rel}} = 2 \cdot 10^{-5}$, $\Delta_1 = 0.15 \cdot 10^{-3}$, $\Delta_2 = 0.2 \cdot 10^{-3}$, $\Delta_3 = 0.1 \cdot 10^{-3}$, $B_{\mathrm{dc}} = 0$T. All parameters in meV.

be seen in Fig. 5.2, several relatively sharp lines: out of these lines, it is clear that parallel ones are due to similar resonance processes within the dot. We have indicated the LR lines, i.e. the lines along which the left and right dots are on resonance, by black lines, see Fig. 5.2. The two parallel LR lines correspond to resonances of $|2,1,1\rangle$ and $|1,1,2\rangle$ states which involve different orbital states in the side quantum dots: for positive bias, in the lower one only the ground (singlet) state participates ($\mathrm{LR_S}$), while in the upper one transport takes place through the occupation of an excited state in the drain dot ($\mathrm{LR_T}$). Another resonance line, steeper than the LR line, is clearly visible: the CR resonance line (in positive bias), where tunneling of an electron from the center to the right dot, i.e. $|2,1,1\rangle \rightarrow |2,0,2\rangle$, is resonant. It is also indicated by a black line in Fig. 5.2, left panels. At the top of the transport triangle we can see blue spots whose basis line is parallel to the CR line and thus indicates that along this line the states $|2,1,1\rangle$ are on resonance with those $|2,0,2^*\rangle$ states that contain an electron in the excited orbital.

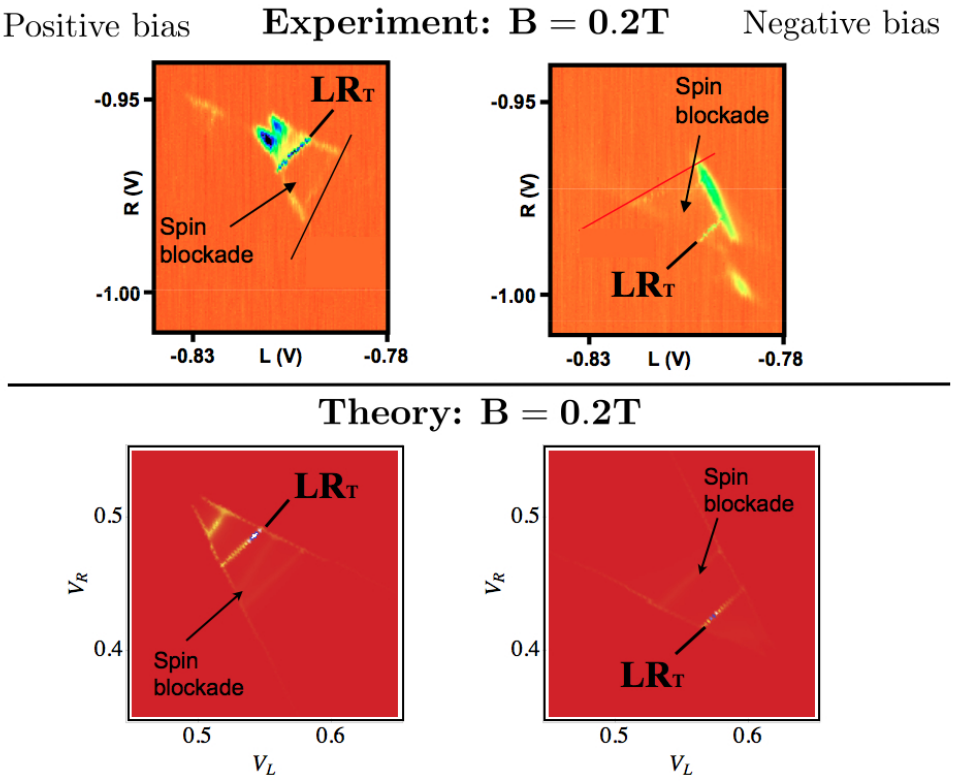

Figure 5.3.: **Current through the TQD for finite magnetic field.** For positive (left column) and negative (right column) bias, both the experimental (upper panels) and theoretical results (lower panel) are shown. In a finite magnetic field, spin-flip processes are less effective and spin blockade occurs. Parameters as in Fig. 5.2, but $B_{\mathrm{dc}} = 0.2$ T.

Let us now switch on a static magnetic field B_{dc}. In Fig. 5.3 we show the measured and calculated current for finite magnetic field in positive and negative bias direction. In the following, we concentrate on the LR resonance lines. Note that from the aforementioned LR resonance lines only one survives when turning on the magnetic field. This lets us deduce that the disappearing line now suffers spin blockade, whereas the surviving one does not. Remembering the origin of the LR lines it is clear what happens: the lower resonance line (the one that disappears) occurs for a resonance of the type $|\uparrow\downarrow,\uparrow,\downarrow\rangle \rightarrow |\downarrow,\uparrow,\uparrow\downarrow\rangle$. However, when two electrons with the same spin occupy the center and right dot (or the center and left dot in negative bias), a tunneling process from center to right (center to left in negative bias) is forbidden once a state of the type $|\uparrow\downarrow,\uparrow,\uparrow\rangle$ ($|\uparrow,\uparrow,\uparrow\downarrow\rangle$) is occupied, since two electrons with the same spin cannot occupy the singlet level in the right dot (in the left dot). This intermediate channel from center to right (to left), although not resonant along the LR resonance lines, has to be open in order for a finite current to flow. The excited triplet level in the right dot (left dot), which would open such a channel, is energetically not accessible at this voltage configuration. It is, however, accessible at different voltages $V_{\mathrm{L,R}}$, where the surviving LR line ($\mathrm{LR_T}$) is visible in Fig. 5.3. It is not affected by spin blockade, since it arises due to the alignment of a singlet level in the left dot (right dot) with the excited triplet levels $|\uparrow\uparrow^*\rangle$, $|\downarrow\downarrow^*\rangle$, $1/\sqrt{2}(|\uparrow\downarrow^*\rangle + |\downarrow\uparrow^*\rangle)$ in the right dot (in

the left dot in negative bias).

5.3. Coherent transport features

Coherent coupling of quantum states can lead to molecular-like superpositions where the electronic wave function has no weight in a spatial region of the system. In an array of states coupled in series, superpositions can be formed, which are localized at the two extremes of the chain, avoiding the occupation of the intermediate states. These kinds of orbitals have been revealed to be responsible for dark resonances in the fluorescence of sodium atoms [133]. In an electronic device, transport through arrays of quantum dots has been predicted to be similarly affected by dark states [122, 88] (see also chapter 3). If the intermediate quantum dot is connected to a drain terminal, the occupation of a dark state switches off the flow of current. In contrast, in a linear chain of three or more quantum dots with contacts at both extremes, the resonance of the two side dots favors transport regardless of the configuration of the intermediate sites [134].

Transport through the TQD presented here is governed by coherent processes that are not trivial and quite distinct from the DQD case. A definite signature for coherence are the LR resonance lines in the current (see Figs. 5.2,5.3). Note that no direct tunneling is possible from the left to the right dot. For the following analysis we will concentrate on the LR singlet line (in positive bias), i.e. the one that disappears due to spin blockade when a magnetic field is turned on. The LR triplet line is somewhat more complicated, and it is a task for future works to analyze its coherence properties.

The LR singlet resonance line is suppressed by spin blockade when spin-flip processes become less probable, as happens in the presence of a magnetic field. Spin-flip processes are the more efficient the closer the participating states are in energy, i.e. in the energy spectrum close to crossings. For a reduced Hamiltonian of the closed system, we have analyzed the eigenstates and eigenenergy spectrum, see appendix A.2. We have observed that in the case where the difference of effective Zeeman splittings, – i.e. the Zeeman splittings induced by the external field plus the splittings induced by the Overhauser field –, is negligible, one eigenstate is of particular importance for the interpretation of the LR resonance line, which is

$$|\Sigma_2\rangle = \frac{1}{2}\left(|\uparrow\downarrow,\uparrow,\downarrow\rangle - |\uparrow\downarrow,\downarrow,\uparrow\rangle - |\downarrow,\uparrow,\uparrow\downarrow\rangle + |\uparrow,\downarrow,\uparrow\downarrow\rangle\right) \tag{5.8}$$

Remarkably, this state is a swapped superposition of singlets with a different charge distribution: double occupation equally affects the source and drain dots. Such a charge transfer would require a sequence $|2,1,1\rangle \rightarrow |S,0,S\rangle \rightarrow |1,1,2\rangle$. Note, however, that the intermediate state $|S,0,S\rangle = |\uparrow\downarrow,0,\uparrow\downarrow\rangle$ is not involved in the superposition $|\Sigma_2\rangle$. We emphasize the similarity of such a superposition with dark resonances observed in multilevel atoms. If a small difference between the effective Zeeman splittings Δ_i (see Hamiltonian Eq. (5.3)) appears due to the hyperfine interaction, the superposition given by $|\Sigma_2\rangle$ acquires a perturbative mixing with triplet states, still, however, without participation of the $|\uparrow\downarrow,0,\uparrow\downarrow\rangle$ state, see appendix A.2.

By analyzing the occupation probabilities and coherences of the density matrix ρ, we can determine the electron dynamics at the LR line. In Fig. 5.4 b) we plot the occupation of the state $|\uparrow\downarrow,0,\uparrow\downarrow\rangle = |S,0,S\rangle$ for fixed V_R as a function of V_L, i.e. along a horizontal line indicated in the current plot in

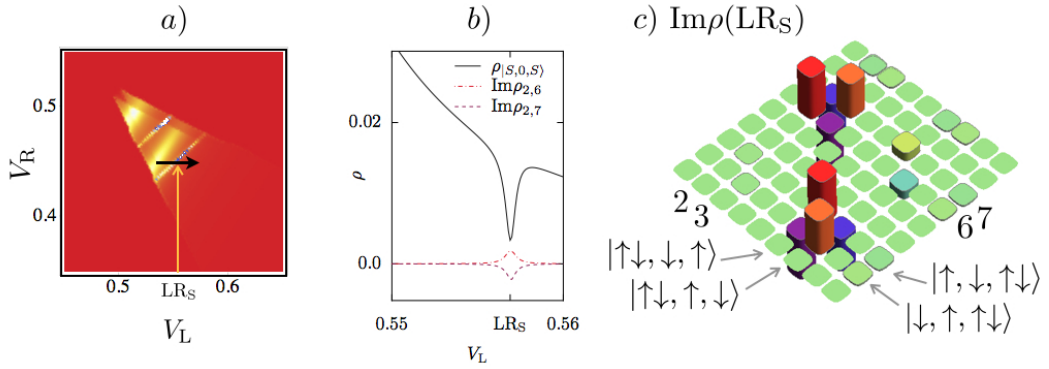

Figure 5.4.: **Density matrix analysis at LR singlet resonance line. a)** Current in positive bias for zero external magnetic field (remember, however, that inhomogeneous Zeeman splittings are present due to hyperfine interaction). **b)** Selected elements of the density matrix along the black horizontal arrow indicated in a). The occupation of $|S,0,S\rangle$ decreases significantly at LR$_S$, i.e. at the LR singlet resonance line. At the same time, the coherence between the states $|2\rangle = |\downarrow,\uparrow,S\rangle$, $|3\rangle = |\uparrow,\downarrow,S\rangle$, $|6\rangle = |S,\downarrow,\uparrow\rangle$, $|7\rangle = |S,\uparrow,\downarrow\rangle$ increases. **c)** Histogramm of the imaginary part of the density matrix for a part of the basis of states at the point LR$_S$, see b). The highest columns indicate the coherence between the states $|2\rangle$, $|3\rangle$, $|6\rangle$ and $|7\rangle$.

Fig. 5.4 a) by a black arrow. Once the left and right dots are on resonance (LR$_S$), the coherence between states $|2\rangle = |\downarrow,\uparrow,S\rangle$, $|3\rangle = |\uparrow,\downarrow,S\rangle$, $|6\rangle = |S,\downarrow,\uparrow\rangle$, $|7\rangle = |S,\uparrow,\downarrow\rangle$ increases, while simultaneously the occupation of state $|S,0,S\rangle$ decreases significantly. This antiresonance corresponds to an increased tunneling process directly from left to right dot, through coherent superpositions of the form $|\Sigma_2\rangle$. This in turn results in an increased current along the whole LR resonance line. Note also in Fig. 5.4 c), – where we show the imaginary part of the system's density matrix at the point LR$_S$ –, the coherences (given by the off-diagonal elements, see chapter 2) between the states $|2,1,1\rangle$ and $|1,1,2\rangle$. These also indicate the formation of a coherent superposition of the type $|\Sigma_2\rangle$ (Eq. (A.5)).

On top of the states which participate in the transport from left to right there are other eigenstates with a finite contribution of the state $|S,0,S\rangle$. Consequently, the occupation of this state will never go to zero and several states contribute to the total current along the LR line. We want to emphasize, however, that the coherent superpositions that transfer an electron directly from left to right are responsible for removing spin blockade and for opening the current channels along this resonance line. This is due to the fact that in the eigenenergy spectrum the superpositions of the type $|\Sigma_2\rangle$ are close in energy to spin blockade states and are thus the most probable states for eventual spin-flip processes induced by hyperfine interaction (see appendix A.2).

5.4. Conclusions

In summary, in this chapter we have presented theoretical results for current through a linear TQD array in a certain electronic configuration. These results have been used to explain corresponding experimental results obtained by the group of A. Sachrajda. The current profile of the TQD shows

spin blockade in positive and negative bias direction, which we therefore call *bipolar spin blockade*. Within the current profile we could interpret certain distinct lines as resonances between the left (L) and right (R) dot that occur without a direct coupling between these dots. By applying an external magnetic field, their origin has been attributed to tunneling processes from a singlet state in the source dot to *singlet* or *excited triplet* states in the drain dot, the latter surviving the external magnetic field, the former, however, disappearing in an external magnetic field due to spin blockade.

The LR resonance lines are a unique feature of the TQD, which do not have a counterpart in the DQD. We have found that, along the singlet LR line, spin blockade is broken through a spin-flip process involving coherent superpositions of states that do not include an electron passing through the central dot. Therefore our results are related to suggested schemes for spin busing and quantum rectification and will have implications in future complex nano-spintronic circuits.

Part II.

Electronic properties of graphene irradiated by ac electric fields

6. A general introduction to graphene

Since its experimental discovery in 2004 [135, 136], graphene – a single layer of carbon atoms arranged in a hexagonal lattice and the first known stable two-dimensional crystal – has shown outstanding properties in a large variety of fields. Theoretically known for almost a century [137], it was its fabrication, isolation *and* subsequent experimental achievements that culminated in the Nobel prize awarded to two of its discoverers, A. Geim and K. Novoselov, in 2010. Graphene is the strongest and thinnest material ever isolated – it is only one atom thick, and nevertheless "a sheet of it as thin as clingfilm could support an elephant" [138]. The high mobility of its charge carriers makes them move 10-100 times faster than in silicon chips [139], the thermal conductivity in graphene is much better than in carbon nanotubes [140], and graphene can sustain a very high current density. It has peculiar optical properties, which make it very suitable for applications in optoelectronic devices [141]. Remarkably, although only one atom thick, graphene can be visualized optically, being its transmittance a multiple of the fine structure constant [142], see Fig. 6.1. Due to these outstanding properties, graphene, after not even 10 years of experimental research, has already entered the stage of being fabricated at an industrial scale – samples of graphene as large as 30 inches are being produced for transparent electrodes [143] – and it has found its way into a plethora of applications, and more are to come for sure. In the field of electrical engineering, graphene is starting to replace traditional materials in high-frequency transistors [144] and it is used as frequency generator in the THz regime [145]. As electronic components are getting smaller and smaller, and single molecules can be the building blocks of electronic circuits, it becomes increasingly difficult to detect their mass, and graphene has

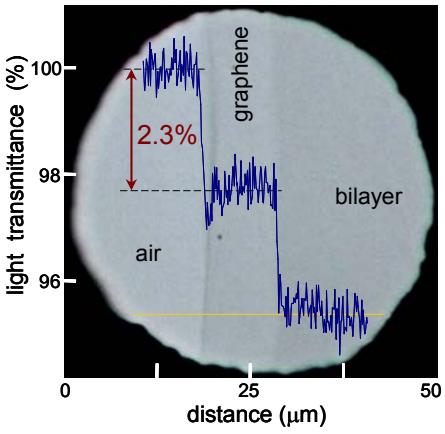

Figure 6.1.: **Absorption of light by mono- and bilayer graphene.** Figure taken from ref. [142].

qualified to be an ideal candidate for highly sensitive mass detectors [146]. Moreover, in the last few years, graphene has become an important ingredient in the field of *plasmonics* [147]: in nanoelectronics, transmission of information by light is strongly limited due to the fact that light breaks free when the confinement length is shorter than its wavelength. However, light couples to the free electrons of metals in form of a plasmon whose wavelength is at the nanometer scale. Plasmonics is hence dedicated to efficiently connect photonics and nanoelectronics. Plasmons bound to the surface of doped graphene, due to their large confinement and long propagation distances, make graphene a suitable alternative to traditional metal plasmonics [148].

In the next sections, we will give a review of how graphene is fabricated and what are its most important electronic properties, with a special emphasis on plasmons, as they constitute an important part of the research done in this thesis.

6.1. Experimental fabrication and characterization of graphene layers

Naturally, the discovery of graphene's outstanding electronic, mechanical and optical properties has entailed an intense work on its fabrication, both with regard to fundamental research as well as for production on a large scale. Single layers of carbon were actually known to be produced by epitaxial growth many years before the breakthrough in 2004. These graphene layers, however, were too strongly coupled to the substrate as to show the characteristic properties observed later on. The achievement of the Manchester group was therefore not so much the discovery of single graphene layers, but rather the isolation of these layers and their characterization that henceforth showed the intrinsic features expected from a 2D crystal, e.g. the presence of massless Dirac fermions. Very recently, graphene has actually been designed artificially [149]: a conventional two-dimensional electron gas at a copper surface was used for assembling carbon monoxide molecules by atomic manipulation into a structure called *molecular graphene*.

In the following sections we will shortly summarize the most important ways of fabricating graphene.

6.1.1. Mechanical exfoliation and suspended graphene

The first successful isolation of graphene by the Manchester group was achieved in a rather unsophisticated way that is commonly referred to as the scotch-tape method: atomically thin carbon films are prepared by repeatedly peeling off highly orientated graphite samples (mechanical exfoliation). In order to identify 2D samples, they are primarily analyzed in an optical microscope, and furtheron by an atomic force microscope [150]. However, as has been said before, graphene is almost completely transparent, and it is not at all sure that one can see it in an optical microscope. The substrate the flakes are placed on and its thickness are a crucial issue: the graphene flakes are transferred to a 300nm thick SiO_2 layer, which, due to interference effects, makes the flakes visible in an optical microscope. Monolayer graphene flakes prepared by mechanical exfoliation can nowadays be as large as 100 μm. They were used in the pioneering experiments in 2004 and 2005 (see Fig. 6.2), and still

are the leading ones in fundamental research on graphene, after considerable improvement regarding e.g. their purity. In addition, later experimental research has achieved the removal of part of the SiO_2 substrate, yielding *suspended* graphene. The procedure to produce suspended graphene starts with

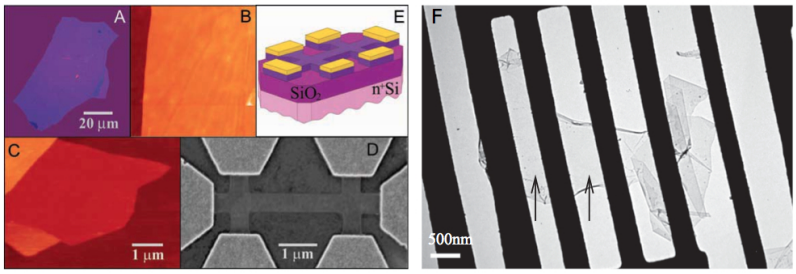

Figure 6.2.: **Graphene samples produced by mechanical exfoliation (left) and suspended graphene (right).** *Left:* Multilayer graphene (A,B) and monolayer graphene (C) on top of SiO_2 substrate and incorporated into electronic device (D,E). Figure taken from ref. [135]. *Right:* TEM image of suspended graphene membrane. The area indicated by arrows is monolayer graphene. Figure taken from ref. [151].

mechanically exfoliating graphene and then with placing it on top of a 300nm SiO_2 substrate [151]. After identifying the films as single-atom layers by optical and atomic force microscopes, electron beam lithography is then used to deposit a metal grid out of Cr and Au on top of one of the flakes. The bulk *Si* is etched away afterwards by putting the samples in tetramethylammonium hydroxide, and the remaining SiO_2 layer is removed by hydrofluoric acid. In the final samples graphene flakes are attached to a metallic scaffold. Important optical experiments have been performed in samples of suspended graphene, which led to the discovery of graphene's optical transparency determined by the fine structure constant α [142], see also Fig. 6.1. Additionally, these samples show ultrahigh mobility of charge carriers of around $\mu = 200.000\ \mathrm{cm}^2/\mathrm{Vs}$ [152].

6.1.2. Epitaxially grown graphene

Epitaxial growth means the deposition of a crystalline layer onto another crystalline substrate in an ordered manner, i.e. in a preferred crystalline direction. For epitaxial graphene, various subtrates have been used, among them Ru [153] and SiC [154–156]. In the latter, graphene layers are produced by heating the SiC to high temperatures ($1000 - 1500°\mathrm{C}$) in order to desorb the Si from the top layers, so that just a few layers of graphene are left on the surface [154]. Of these graphene layers, the first one is strongly bound to the substrate, and only the second one is less coupled. Thus, intrinsic graphene properties have been detected, as e.g. the linear dispersion of massless Dirac electrons [157] or the half-integer quantum Hall effect [158]. The coupling to the substrate, however, leads to considerable doping of the graphene layers, which makes it difficult to access experimentally the Dirac point, where the valence and conduction band touch each other. The coupling to the substrate is also responsible for the appearance of gaps in the energy spectrum of graphene [159].

6.1.3. Chemical vapor deposition

The formerly described methods of fabricating graphene are in general not suitable for the production of larger samples on an industrial scale desirable for many of the applications graphene is supposed to provide. In the case of mechanical exfoliation, even if the sample quality is very good, it is not clear how to extend the production to graphene layers larger than μm size. Epitaxial growth requires ultrahigh vacuum conditions and is therefore expensive. An alternative method has been proposed three years ago by different groups [160, 161]: Chemical Vapor Deposition (CVD). There, carbon is dissolved on a Ni substrate, and then forced to precipitate out by cooling the Ni. The precipitated carbon atoms form graphene on the Ni surface. The graphene layer is then separated from the Ni substrate by chemical etching, and is subsequently transferred onto another appropriate substrate [162]. The graphene films produced by CVD show inferior results as compared to suspended graphene or mechanically exfoliated probes in terms of carrier mobility (3700 cm^2/Vs [160]) and optical transparency (90%, [160, 161]). They are, however, still attractive for applications such as solar cells or high-frequency electronic and optoelectronic devices [162].

6.2. Electronic properties of graphene

It has been known already since 1947, when P. R. Wallace published his paper about the band theory of graphite [137], that electrons in graphene behave as massless Dirac fermions, i.e. they have a linear dispersion relation. The carbon atoms in graphene form a honeycomb lattice, as is shown in Fig. 6.3. Since the honeycomb lattice is not a Bravais lattice, it is formally described as two triagonal lattices with two inequivalent atoms a and b per unit cell (see blue and white circles and light blue rhomb in Fig. 6.3). The basis vectors for this lattice are

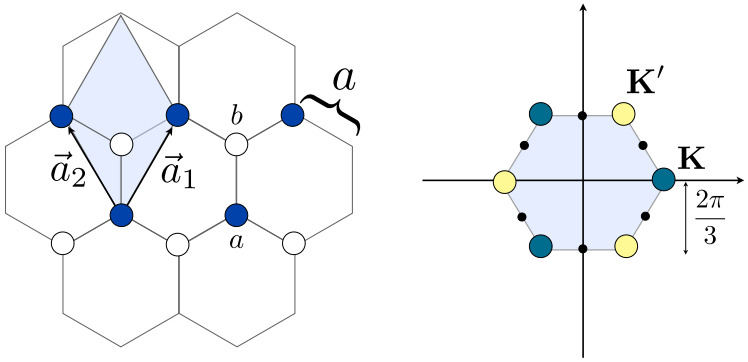

Figure 6.3.: **Sketch of the graphene honeycomb lattice and its first Brillouin zone.**

$$\mathbf{a_1} = \sqrt{3}a\left(\frac{1}{2}, \frac{\sqrt{3}}{2}\right)$$
$$\mathbf{a_2} = \sqrt{3}a\left(-\frac{1}{2}, \frac{\sqrt{3}}{2}\right). \tag{6.1}$$

The distance a between next neighbors is $a = 1.42$Å and the hopping element between them $t = 2.7$ eV. It is much bigger than the next-nearest neighbor hopping t_2 [163], so that it can safely be neglected as a first approximation in the analysis of the electronic structure of graphene. The unit cell of the reciprocal lattice, the first Brillouin zone, is also a hexagon, and as it happens in the direct lattice, it has two inequivalent points called the Dirac points, $\mathbf{K}$ and $\mathbf{K}'$, see Fig. 6.3,

$$\mathbf{K} = \frac{4\pi}{3\sqrt{3}a}(1, 0)$$
$$\mathbf{K}' = \frac{4\pi}{3\sqrt{3}a}\left(\frac{1}{2}, \frac{\sqrt{3}}{2}\right). \tag{6.2}$$

The Hamiltonian for graphene reads, in second quantization,

$$H = -\frac{t}{2}\sum_{\mathbf{n}} a^\dagger_{\mathbf{n}}(b_{\mathbf{n}-\mathbf{a_1}} + b_{\mathbf{n}-\mathbf{a_1}} + b_{\mathbf{n}}) - b^\dagger_{\mathbf{n}}(a_{\mathbf{n}+\mathbf{a_1}} + a_{\mathbf{n}+\mathbf{a_1}} + a_{\mathbf{n}}) + \text{h.c.}, \tag{6.3}$$

where $\mathbf{n} = n_1\mathbf{a_1} + n_2\mathbf{a_2}$ is a lattice vector and $\mathbf{a_i}$ are the basis lattice vectors, and $a^\dagger_{\mathbf{n}}(b^\dagger_{\mathbf{n}})$ are operators that create an electron at site $a(b)$. The Hamiltonian can be simplified by using Bloch's theorem for periodic crystal potentials:

$$a_{\mathbf{n}} = \sum_{\mathbf{k}} e^{i\mathbf{k}\cdot\mathbf{n}} a_{\mathbf{k}}$$
$$b_{\mathbf{n}} = \sum_{\mathbf{k}} e^{i\mathbf{k}\cdot\mathbf{n}} b_{\mathbf{k}}$$

Inserting this into the Hamiltonian (6.3) yields

$$H = -t\sum_{\mathbf{k}} \begin{pmatrix} a^\dagger_{\mathbf{k}} & b^\dagger_{\mathbf{k}} \end{pmatrix} \begin{pmatrix} 0 & \phi^*(\mathbf{k}) \\ \phi(\mathbf{k}) & 0 \end{pmatrix} \begin{pmatrix} a_{\mathbf{k}} \\ b_{\mathbf{k}} \end{pmatrix}, \tag{6.4}$$

where $\phi(\mathbf{k}) = 1 + e^{-i\mathbf{k}\cdot\mathbf{a_1}} + e^{-i\mathbf{k}\cdot\mathbf{a_2}}$. By diagonalizing this Hamiltonian one obtains the dispersion relation $E(\mathbf{k}) = \pm t|\phi(\mathbf{k})|$, which is shown in Fig. 6.4 (middle panel). For the low energy regime, one can expand $\phi(\mathbf{k})$ for small $\mathbf{q}$ around one of the Dirac points, $\mathbf{K}$, which yields

$$\phi(\mathbf{K} + \mathbf{q}) \approx \phi(\mathbf{K}) + \frac{d}{d\mathbf{k}}\phi(\mathbf{K}) \cdot \mathbf{q} = \frac{3}{2}ta(q_x - iq_y). \tag{6.5}$$

Setting $\mathbf{q} \to \mathbf{k}$ for the ease of notation, the low-energy Hamiltonian becomes

$$H = \hbar v_{\mathrm{F}} \boldsymbol{\sigma} \cdot \mathbf{k}, \tag{6.6}$$

with the Fermi velocity $v_{\mathrm{F}} = \frac{3}{2}\frac{ta}{\hbar} \approx 10^6$ m/s and the Pauli matrices

$$\sigma_x = \begin{pmatrix} 0 & 1 \\ 1 & 0 \end{pmatrix} \quad \text{and} \quad \sigma_y = \begin{pmatrix} 0 & -i \\ i & 0 \end{pmatrix}. \tag{6.7}$$

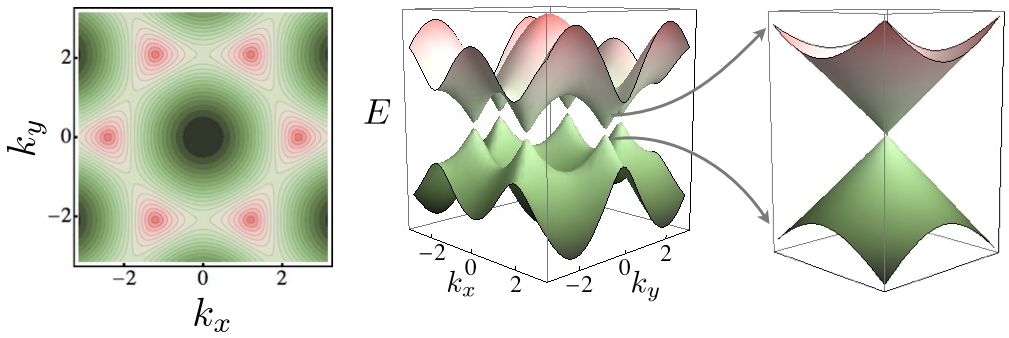

Figure 6.4.: **Plots of the dispersion relation of graphene.** *Left and middle panel:* Dispersion around the whole Brillouin zone. *Right panel:* Low-energy approximation around one of the Dirac points.

This Hamiltonian is in fact the famous Dirac Hamiltonian. After diagonalization one obtains the eigenenergies and eigenstates

$$E(\mathbf{k}) = \pm\hbar v_{\mathrm{F}}|\mathbf{k}| \quad |\phi^{\pm}\rangle = \frac{1}{\sqrt{2}}\begin{pmatrix} e^{-i\frac{\Theta}{2}} \\ \pm e^{i\frac{\Theta}{2}} \end{pmatrix}, \tag{6.8}$$

where $\Theta = \arctan\frac{k_y}{k_x}$. The dispersion relation is shown in Fig. 6.4 (right panel). It has the structure of two opposing (Dirac) cones that touch each other at the Dirac point $\mathbf{K}$, leaving no gap between them. At the other Dirac point $\mathbf{K}'$, a similar result is obtained. The cones at $\mathbf{K}$ and $\mathbf{K}'$ are also called the two valleys of graphene, and the full low-energy Hamiltonian would actually be a (4×4)-matrix with the Hamiltonians (6.6) as (2×2) building blocks. If, however, there are no mechanisms that couple the two valleys (like external magnetic fields or spin-orbit coupling), it is sufficient to treat only one valley and treat the other one as an additional degeneracy to the usual spin degeneracy. For the problem treated in this thesis, no intervalley couplings are present, and we will henceforth continue with the description of only one valley.

The existence of the two sublattices brings along an additional quantum number, which is usually called the *pseudospin* and arises from the fact that an electron can live either in sublattice a or b. In the diagonal basis (6.8), it is clear that the pseudospin refers to either the upper or the lower cone. Closely related with the pseudospin of the electrons is their *chirality*: the Dirac Hamiltonian (6.6) introduces a coupling between the motion of an electron ($\mathbf{k}$) and its pseudospin, so that they are aligned either parallel (in the upper cone) or antiparallel (in the lower cone). The consequence of this extra quantum number is the fact that it has to be conserved in many processes, an example being the *Klein* paradox for relativistic particles [164]: the transmission probability for an electron approaching a potential barrier reaches perfect transparency for an infinitely high potential, as opposed to non-relativistic particles, whose transmission probability decays exponentially with increasing potential barrier. This phenomenon can be explained by taking into account that a very strong potential, repulsive for electrons, can be attractive for positrons, and results in positron states inside the barrier [165]. It was, however, never observed experimentally, due to the fact that very high potential drops are necessary.

In graphene, where the electrons behave as effective relativistic particles, this phenomenon was first predicted to occur [166] and then actually measured [167].

The pseudospin gives rise to another peculiarity of graphene, namely the half-integer quantum Hall effect. Owing to its two-dimensionality, graphene is usually compared with a benchmark of solid state physics, the two-dimensional electron gas (2DEG). In strong contrast to the result obtained in the 2DEG, graphene shows conductivity plateaus at half-integer filling factors, that are ultimately traced back to the pseudospin. The half-integer quantum Hall effect was predicted theoretically [168, 169] and henceforth measured in the first experiments [136, 170], see Fig. 6.5. The Landau levels are given

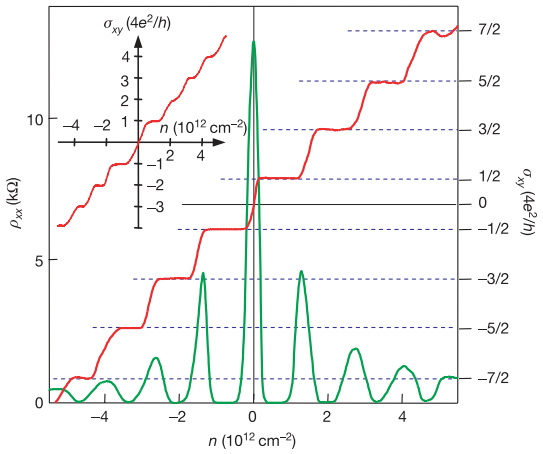

Figure 6.5.: **The half-integer quantum Hall effect in graphene.** Hall conductivity σ_{xy} and longitudinal resistivity ρ_{xx} of graphene as a function of carrier concentration n. Figure taken from ref. [170].

by [171]

$$E_\nu = \sqrt{2|e|Bv_\mathrm{F}\left(\nu + \frac{1}{2} \pm \frac{1}{2}\right)}, \tag{6.9}$$

with $\nu = 0, 1, 2\ldots$ being the filling factor and $\pm 1/2$ stemming from the pseudospin. Most remarkably and in contrast to the 2DEG, the quantum Hall effect in graphene can also be observed at room temperature [172], due to the fact that the implied energy scales are different in graphene [163].

The first proof of really dealing with a single sheet of graphene was accomplished by measuring the electric field effect [135], which means the control of the density of electrons in the sample by adjusting a gate voltage V_g (see device in Fig. 6.2). By using this effect, it has been shown that the electronic carriers have a linear energy spectrum, and that there are two bands touching at a single point, where the conductivity has a quantized minimum, see Fig. 6.6. The minimum conductivity is $\propto e^2/h$ and seems to be an intrinsic property of Dirac electrons [173, 174]. There is, however, controversy about its exact value [175, 176].

It should finally be noted that the existence of a 2D crystal is in fact something very unexpected, according to the classical result obtained by Landau and Peierls [177, 178] and to the Mermin-Wagner-Hohenberg theorem [179, 180]. The latter states that in two dimensions any crystal would be ther-

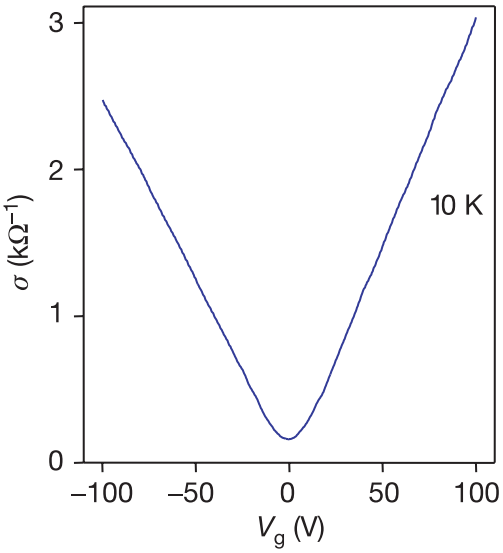

Figure 6.6.: **Conductivity of graphene.** Figure taken from ref. [170].

modynamically unstable due to phonons, which effectively try to reinstall the broken translational symmetry. There are several arguments as to why graphene nevertheless exists. First, the Mermin-Wagner-Hohenberg theorem is, strictly speaking, only true for infinite crystals, and the graphene samples are finite. Additionally, the σ-bonds between the carbon atoms are sufficiently strong as not to be destroyed up to high temperatures [181]. Finally, it was both experimentally and theoretically confirmed that graphene is not completely flat, but has *ripples* [182, 183], and the coupling to out-of-plane bending modes can provide a stabilizing mechanism against in-plane stretching modes.

6.3. Electron-electron interactions in graphene monolayers

Most of the physics of graphene at the neutrality point (undoped) or close to it (slightly doped) can be explained by the simple low-energy single-electron picture. The vanishing density of states at the Dirac point,

$$\rho(E) = \frac{N_s N_v}{2\pi} \frac{|E|}{v_F^2}, \tag{6.10}$$

is responsible for many of the exotic phenomena observed in undoped and slightly doped graphene. The singularity at $E = 0$, however, constitutes a complicated issue when analyzing electron-electron interactions in graphene. Traditionally, electron-electron interactions in solid state physics have been treated successfully by applying the Fermi liquid theory. The concept of the Fermi liquid, derived originally by Landau to explain the behavior of ^{3}He [184] but applicable to a much broader range of interacting fermion systems at low temperatures, comprises a simple and yet crucially important statement: the low-energy excitations of strongly interacting electrons behave as a system of weakly interacting *quasiparticles*, which are described by the same quantum numbers as the particles in the

absence of interaction. The Fermi liquid theory owes much of its success in explaining solid state physics to the fact that electrons in metals tend to *screen* electric fields, so that the long-range Coulomb interaction becomes effectively short-ranged. The different role of electron-electron interaction in a conventional 2D system and graphene becomes clear when estimating its strength: The kinetic energy in a 2D system scales with the inverse of the quadratic inter particle distance l, $E_{\text{kin}} \propto 1/l^2$, which in turn is proportional to the density n, $E_{\text{kin}} \propto n$. The Coulomb energy is $E_{\text{C}} \propto 1/l = \sqrt{n}$, their ratio is hence

$$g = \frac{E_{\text{C}}}{E_{\text{kin}}} \propto \frac{1}{\sqrt{n}}. \tag{6.11}$$

At high densities, the kinetic energy predominates over the Coulomb energy, and the Fermi liquid picture can safely be applied. For lower densities, however, the Fermi liquid description breaks down, and new phenomena emerge and can become stable, such as the Wigner crystal, the formation of an electron lattice. Other phenomena where the Fermi liquid picture does not apply include superconductivity, which emerges due to additional interaction of electrons with phonons, or Mott insulators in which strong local electron-electron interaction leads to unexpected insulating behavior.

Graphene, due to its linear dispersion relation $E_{\text{kin}} = \hbar v_{\text{F}}|k| \propto \hbar v_{\text{F}}/l$, scales with the square root of the particle density, $E_{\text{kin}} = \hbar v_{\text{F}}\sqrt{n}$, and the ratio $E_{\text{C}}/E_{\text{kin}}$ is therefore independent of the density,

$$g = \frac{E_{\text{C}}}{E_{\text{kin}}} = \frac{e^2}{4\pi\epsilon_0\kappa\hbar v_{\text{F}}}. \tag{6.12}$$

Hence, the strength of the Coulomb interaction depends only on the material parameter κ, and in vacuum, where $\kappa = 1$, $g \approx 2.2$. For doped graphene, i.e. away from the neutrality point, where a well-defined Fermi surface exists and screening renormalizes the electron-electron interactions, Fermi liquid theory still holds true. In fact, for heavy doping, graphene resembles more and more its two-dimensional counterpart, the 2DEG. The vanishing density of states at the neutrality point, however, makes undoped or slightly doped graphene a unique material as compared to traditional metals or semiconductors: since no states are available at the Dirac point, interactions are poorly screened, and the theory of the Fermi liquid breaks down [185, 186]. The reason why, nevertheless, the single electron picture often suffices to explain the experiments may be related to the fact that the neutrality point is somewhat elusive, one possibility for it being the formation of electron and hole puddles due to disorder [187]. It could also happen that interactions are screened due to the presence of agents living in the environment that graphene is coupled to – be it in the form of phonons from the substrate, of charge impurities or of water molecules [188].

The graphene Hamiltonian including electron-electron interactions reads

$$H = \sum_{\mathbf{k}} \begin{pmatrix} a_{\mathbf{k}}^\dagger & b_{\mathbf{k}}^\dagger \end{pmatrix} \begin{pmatrix} 0 & k_x - ik_y \\ k_x + ik_y & 0 \end{pmatrix} \begin{pmatrix} a_{\mathbf{k}} \\ b_{\mathbf{k}} \end{pmatrix} + \frac{1}{2}\sum_{\mathbf{q}} v_{\mathbf{q}} n_{\mathbf{q}} n_{-\mathbf{q}}, \tag{6.13}$$

with $n_{\mathbf{q}} = a_{\mathbf{k}+\mathbf{q}}^\dagger a_{\mathbf{k}} + b_{\mathbf{k}+\mathbf{q}}^\dagger b_{\mathbf{k}}$ and $v_{\mathbf{q}} = 2\pi e^2/\epsilon q$ being the unscreened Coulomb interaction in 2D, and $\epsilon = \epsilon_0\kappa$. A large set of tools has been employed to study this Hamiltonian, both in strong and weak coupling regimes (i.e. for $g \gg 1$ and $g \ll 1$) (for a review, see ref. [189]). Due to the singular nature of the Dirac point where graphene does not behave as a Fermi liquid, one has to distinguish between the analysis for undoped and for doped graphene. For undoped graphene, mostly renormalization group techniques have been employed to analyze the role of interactions, as e.g. in the first

calculations in the nineties by González *et al.* [185, 190]. In these articles, starting from the hypothesis that the low-energy limit of undoped graphene is that of weak interactions, they found that electrons behave as a *marginal Fermi liquid*, whose quasiparticles have an anomalous lifetime with respect to the conventional Fermi liquid. More recent research points out to the possibility of the existence of strong coupling phases in undoped graphene, where an excitonic condensate is created [191–193]. One of the most important approximation techniques for electron-electron interactions, the so-called random phase approximation (RPA), has been applied successfully to doped graphene. It was first derived by Bohm and Pines in the 1950s in a series of seminal papers [194–196]. We will not go into details about the derivation of the RPA, an excellent explanation can be found e.g. in ref. [197]. However, a sort of handwaiving demonstration of the RPA will be given below. Before that, let us first introduce another very important physical quantity of charged systems, the electric polarizability.

6.3.1. Electric polarizability

The polarizability $\Pi(\mathbf{r}, \mathbf{r}', t, t')$ (or also susceptibility $\chi(\mathbf{r}, \mathbf{r}', t, t')$) of a medium describes its tendency to polarize under the influence of a weak external probe potential. In metals and semiconductors, this is closely related to the aforementioned screening of electric fields by electrons. The polarizability is the *response* of a charge distribution to a weak external probe potential (just as the conductivity is the response to an electric field, or the spin susceptibility the response to a magnetic field). The response of a system to a weak external agent is described mathematically by linear response theory (for an introduction to linear response theory see e.g. ref. [198, 197, 199]). There, the polarizability or charge-charge correlation function of non-interacting particles is defined in momentum space as

$$\Pi(\mathbf{q}, t - t') = -i\Theta(t - t')\langle[\rho(\mathbf{q}, t), \rho(-\mathbf{q}, t')]\rangle, \tag{6.14}$$

where the Heaviside function expresses the fact that the external perturbation is turned on at a time t', before which the response is naturally zero, and the charge operator for electrons with spin σ is given by

$$\rho(\mathbf{q}) = \sum_{\mathbf{q}\sigma} c^{\dagger}_{\mathbf{k}\sigma} c_{\mathbf{k}+\mathbf{q}\sigma}. \tag{6.15}$$

The commutator in (6.14) can easily be performed for non-interacting electrons described by the diagonal Hamiltonian

$$H = \sum_{\mathbf{k}\sigma} \epsilon_{\mathbf{k}\sigma} c^{\dagger}_{\mathbf{k}\sigma} c_{\mathbf{k}\sigma}, \tag{6.16}$$

and the polarizability of free electrons is [197]

$$\Pi^0(\mathbf{q}, \omega) = \sum_{\mathbf{k}\sigma} \frac{f_{\mathbf{k}\sigma} - f_{\mathbf{k}+\mathbf{q}\sigma}}{\epsilon_{\mathbf{k}\sigma} - \epsilon_{\mathbf{k}+\mathbf{q}\sigma} + \omega + i\eta}, \tag{6.17}$$

with the Fermi distribution $f_{\mathbf{k}\sigma} = [1 + \exp(\epsilon_{\mathbf{k}\sigma}\beta)]^{-1}$ at temperature $\beta = k_B T$. This function is known as the Lindhard function [200].

The relationship between the polarizability and the dielectric function, which gives information about the dielectric properties of the medium, can be derived in the following way, where, for the

sake of simplicity, we will treat all quantities now in the momentum and frequency space $(\mathbf{q}, \omega)$. The external probe potential $\phi_{\text{ext}}(\mathbf{q}, \omega)$ is related to the total potential $\phi_{\text{tot}}(\mathbf{q}, \omega) = \phi_{\text{ext}}(\mathbf{q}, \omega) + \phi_{\text{ind}}(\mathbf{q}, \omega)$ by the dielectric function $\varepsilon(\mathbf{q}, \omega)$

$$\varepsilon(\mathbf{q}, \omega) = \frac{\phi_{\text{ext}}(\mathbf{q}, \omega)}{\phi_{\text{tot}}(\mathbf{q}, \omega)}. \tag{6.18}$$

The polarizability connects the induced charge distribution to the external potential,

$$\rho_{\text{ind}}(\mathbf{q}, \omega) = \Pi(\mathbf{q}, \omega)\phi_{\text{ext}}(\mathbf{q}, \omega), \tag{6.19}$$

so that the induced potential becomes

$$\phi_{\text{ind}} = v_{\mathbf{q}}\Pi(\mathbf{q}, \omega)\phi_{\text{ext}}(\mathbf{q}, \omega). \tag{6.20}$$

The dielectric function is then easily shown to be

$$\varepsilon(\mathbf{q}, \omega) = \frac{1}{1 + v_{\text{q}}\Pi(\mathbf{q}, \omega)}. \tag{6.21}$$

The most important achievement of linear response theory is that the response functions are completely governed by the properties of the system itself and not the externally applied force. This means that by evaluating e.g. the polarizability of a system, although making use of an external agent, the information gained is inherent to the system *if the external force is weak*. In this context, the *fluctuation-dissipation theorem* should be mentioned [201]: it states that the response of a system to an applied force is the same as its response to fluctuations about equilibrium. Fluctuations about equilibrium are expressed by the correlation function $S(\mathbf{q}, \omega)$, which is related to the dissipative part of the system's polarizability $\Pi(\mathbf{q}, \omega)$ via

$$S(\mathbf{q}, \omega) = 2\hbar(1 + n_{\text{B}}(\hbar\omega))\text{Im}\Pi(\mathbf{q}, \omega), \tag{6.22}$$

with $n_{\text{B}}(\hbar\omega)$ being the Bose-Einstein distribution. In order to find out the possible dissipative processes, and subsequently the dielectric properties given by the dielectric function Eq. (6.21), one has to calculate the imaginary part of the polarizability of a system. Note, however, that Eq. (6.21) is the dielectric function of a system of charged *non-interacting* particles. The Coulomb interaction $v_{\mathbf{q}}$ merely enters due to the definition of the electrostatic potential of a charged system given by the Poisson equation. We have not considered interactions between the particles that respond to the external potential. If these are included via the Hamiltonian

$$H_{\text{int}} = \frac{1}{2}\sum_{\mathbf{k},\mathbf{k}',\mathbf{q}\neq\mathbf{0}\sigma} v_{\mathbf{q}} c^{\dagger}_{\mathbf{k}+\mathbf{q}\sigma} c^{\dagger}_{\mathbf{k}-\mathbf{q}\sigma} c_{\mathbf{k}'\sigma} c_{\mathbf{k}\sigma}, \tag{6.23}$$

the calculation of the commutator in Eq. (6.14) becomes much more complicated, and one has to apply approximations, one of which is the already mentioned RPA. In the RPA, the interacting polarizability can be written as a geometrical series

$$\begin{aligned}\Pi(\mathbf{q}, \omega)^{\text{RPA}} &= \Pi^0(\mathbf{q}, \omega) + \Pi^0(\mathbf{q}, \omega)v_{\mathbf{q}}\Pi(\mathbf{q}, \omega) = \Pi^0(\mathbf{q}, \omega)(1 + v_{\mathbf{q}}\Pi(\mathbf{q}, \omega)) \\ &= \frac{\Pi^0(\mathbf{q}, \omega)}{1 - v_{\mathbf{q}}\Pi^0(\mathbf{q}, \omega)},\end{aligned} \tag{6.24}$$

by which the dielectric function becomes

$$\varepsilon^{\mathrm{RPA}}(\mathbf{q},\omega) = 1 - v_{\mathbf{q}} \Pi^0(\mathbf{q},\omega). \tag{6.25}$$

This surprisingly easy result can also be justified in a more physical, albeit not very rigorous way: for interacting particles, the potential induced by an external probe should depend not only on the external potential (see Eq. (6.20)) but on the *total* potential ϕ_{tot}

$$\phi_{\mathrm{ind}} = v_{\mathbf{q}} \Pi(\mathbf{q},\omega) \phi_{\mathrm{tot}}(\mathbf{q},\omega). \tag{6.26}$$

The dielectric function becomes then directly

$$\varepsilon(\mathbf{q},\omega) = 1 - v_{\mathbf{q}} \Pi(\mathbf{q},\omega) \tag{6.27}$$

as derived in the RPA.

A very important feature of the RPA is that it predicts the existence of a plasmon. Note that if $\varepsilon(\mathbf{q},\omega) = 0$, one can encounter the situation that the total potential $\phi_{\mathrm{tot}}(\mathbf{q},\omega) \neq 0$, i.e. it varies in space and time, while $\phi_{\mathrm{ext}}(\mathbf{q},\omega) = 0$ (Eq. (6.18)). Since $\varepsilon(\mathbf{q},\omega) = 0$ in the RPA means (see Eq. (6.27))

$$1 = v_{\mathbf{q}} \Pi(\mathbf{q},\omega), \tag{6.28}$$

this equation has real solutions if $\mathrm{Im}\Pi(\mathbf{q},\omega) = 0$. The imaginary part of the polarizability describes the possible dissipative processes, i.e. particle-hole excitations. Hence, if $\mathrm{Im}\Pi(\mathbf{q},\omega) = 0$, then no single-particle excitations exist, and the electrons oscillate collectively in an eigenmode $\omega_p(\mathbf{q})$, that is called the plasma mode or plasmon frequency. If on the contrary $\mathrm{Im}\Pi(\mathbf{q},\omega) \neq 0$, the plasmon is said to be damped, as it can decay into single-particle excitations.

The plasma oscillation can be understood by using a simple classical picture [198]. Although being somewhat rough, it gives the correct result for the plasma frequency and provides physical intuition. On average, a metal is neutral, i.e. the free moving electrons compensate the positive charge background of the ions. When electrons try to screen a local charge disturbance, they will move by a distance x and leave behind a positively charged area. An electric field is established that attracts the electrons again, so that they follow the equation of motion

$$m\ddot{x} = -eE = -ne^2 x, \tag{6.29}$$

with n being the electron density. This is the equation for a harmonic oscillator with eigenfrequency or plasma frequency

$$\omega_p \propto \sqrt{\frac{e^2 n}{m}}. \tag{6.30}$$

In a 2DEG, the polarizability was first calculated by Stern [202], where the plasmon frequency in RPA was found to be $\omega(q) \propto \sqrt{q}$. In Fig. 6.7, the imaginary part $\mathrm{Im}\Pi(\mathbf{q},\omega)$ of the 2DEG is shown together with the plasmon dispersion relation for the long wavelength limit.

It has already been mentioned that the screening behavior of graphene is somewhat peculiar, since at zero doping in fact no screening can exist, due to the lack of states at the Dirac point. The RPA

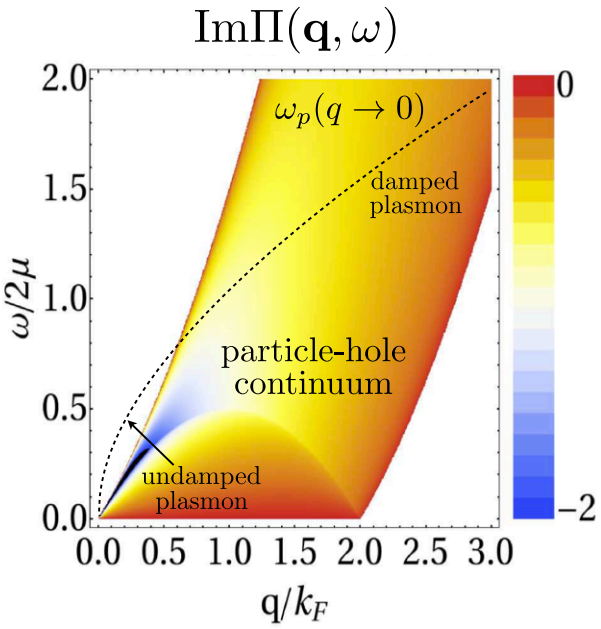

Figure 6.7.: **Imaginary part of the polarizability of the 2DEG.** Density plot of $\mathrm{Im}\Pi(q,\omega)$ with plasmon dispersion relation for the long wavelength limit. Figure adapted from ref. [189].

is known to break down at zero doping [203]; nevertheless, a plasmon mode was found for zero doping in a different approximation [204]. In this thesis, interactions will only be introduced either for gapped or doped graphene, in which the RPA is assumed to hold [189], and we will hence not enter into more detail about the different approximation methods for electron-electron interactions in graphene. We will now continue by summarizing known results on the dynamical polarizability of undoped and doped graphene.

6.3.2. Polarizability of graphene

In graphene, the dynamical polarizability for the non-interacting and interacting system has been calculated by various authors [205–207]. It is given by the Lindhard function

$$\Pi(\omega,\mathbf{q}) = \sum_{\mathbf{k},\sigma,\sigma'} \frac{f_{\mathbf{k}+\mathbf{q}\sigma'} - f_{\mathbf{k}\sigma}}{\omega - \epsilon_{\mathbf{k}+\mathbf{q}\sigma'} + \epsilon_{\mathbf{k}\sigma} + i\eta} F_{\sigma\sigma'}(\mathbf{k}+\mathbf{q},\mathbf{k}), \tag{6.31}$$

with the wavefunction overlap

$$F_{\sigma\sigma'}(\mathbf{k}+\mathbf{q},\mathbf{k}) = \frac{1}{2}(1+\sigma\sigma'\cos(\theta_{\mathbf{k},\mathbf{k}+\mathbf{q}})). \tag{6.32}$$

Here $\sigma,\sigma' = \pm 1$ for the two cones, and $\theta_{\mathbf{k},\mathbf{k}+\mathbf{q}}$ is the angle between $\mathbf{k}$ and $\mathbf{k}+\mathbf{q}$. As compared to the polarizability for the 2DEG, in graphene one has to take into account the two sublattices a,b, which introduces the overlap function $F_{\sigma\sigma'}(\mathbf{k}+\mathbf{q},\mathbf{k})$ [208]. For zero temperature and undoped graphene,

the imaginary part of the polarizability reads [205]

$$\mathrm{Im}\Pi(\omega, \mathbf{q}) = -\frac{gq^2}{16\sqrt{\omega^2 - q^2}}\Theta(\omega - q), \tag{6.33}$$

where $g = 4$ expresses the degeneracy due to valley and spin, and $q = |\mathbf{q}|$. The imaginary part of the polarizability, as has been discussed above, is related to the dissipation in the system. Considering a non-interacting system, the only possible excitations are particle-hole excitations. In undoped graphene, the lower cone is full whereas the upper cone is empty, and excitations from the electrons in the lower cone to the upper cone are possible only for $\omega \geqq q$, due the Heaviside function in Eq. (6.33), which constitutes a threshold for excitations for $\omega < q$. A density plot of the imaginary part of the polarizability is shown in Fig. 6.8, together with constant-momentum cuts $\mathrm{Im}\Pi(\omega)$.

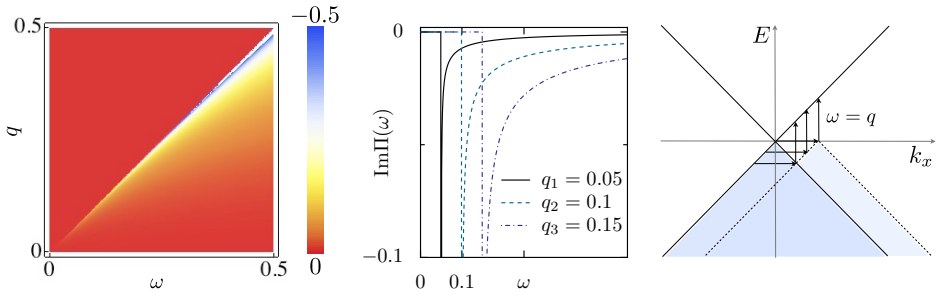

Figure 6.8.: **Imaginary part of the polarizability of undoped graphene at zero temperature.** *Left panel*: Density plots of $\mathrm{Im}\Pi(\omega, q)$, see Eq. (6.33). Particle-hole continuum for $\omega \geqq q$, i.e. in the lower triangle. *Middle panel*: Constant-momentum cuts of $\mathrm{Im}\Pi(\omega)$ for $q = 0.05, 0.1.0.15$. *Right panel*: Sketch of the possible excitations from the lower to the upper Dirac cone.

In doped graphene, the chemical potential μ is placed either in the lower cone ($\mu < 0$) away from the Dirac point or in the upper cone ($\mu > 0$). Here, we will describe the behavior for positive doping, i.e. $\mu > 0$. In addition to interband transitions that are already possible for zero doping (see Fig. 6.8), in doped graphene there also exist intraband transitions (see Fig. 6.9, right panel). Most importantly, these intraband transitions exist for arbitrarily small ω but *finite* momentum $\mathbf{q}$. It was found [206, 205, 207] that in the RPA, doped graphene sustains an undamped plasmon with dispersion relation in the long wavelength limit $q \to 0$

$$\omega_p = \omega_0\sqrt{q} = \sqrt{\frac{2e^2\mu q}{\epsilon_0}}. \tag{6.34}$$

The plasmon resonance can be seen in Fig. 6.9 (left panel). An undamped plasmon exists when $\mathrm{Im}\Pi(\omega, q)^{\mathrm{RPA}} = 0$, cf. middle panel in Fig. 6.9. The $\sqrt{q}$-behavior of the plasmon is the same as for the 2DEG, however, the density dependence in graphene is different: $\omega_0 \propto n^{1/4}$, instead of $\propto n^{1/2}$ as in the 2DEG [209].

We conclude here the introduction to graphene and continue in the next section with electronic properties of graphene irradiated by ac electric fields.

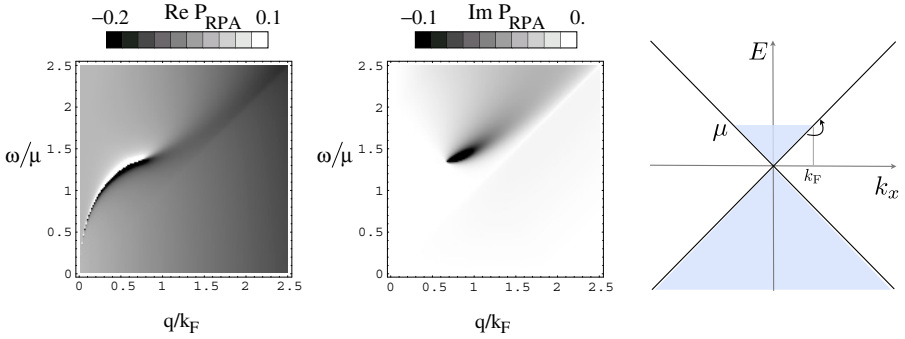

Figure 6.9.: **Imaginary and real part of the polarizability in RPA of doped graphene at zero temperature.** *Left and middle panel*: Density plots of $\Pi(\omega, q)^{\mathrm{RPA}}$. Note in the real part the resonance that shows the existence of a plasmon. Figure taken from ref. [205]. *Right panel*: Sketch of the possible intraband excitations due to finite doping.

7. Electronic single and many particle properties of graphene irradiated by ac electric fields

The effect of external fields in the low energy properties of the electric carriers in graphene has been a topic of extensive research since early days, an example being the discovery of the anomalous Quantum Hall effect [170, 136] (see previous chapter). Understanding the behavior of graphene in the presence of electrical and magnetic fields is of major relevance both from a fundamental and an applied point of view. From a fundamental point of view, since new exotic behavior may arise in the presence of external fields; name for instance the recent discovery of the fractional Hall effect in graphene [210, 211]. From an applied point of view, because external fields can be used to manipulate its properties, for instance by opening gaps in the electronic spectrum, which is essential for applications in the semiconductor industry.

The effect of radiation on both monolayer and bilayer graphene has been analyzed only recently, and has led to the prediction of a variety of phenomena, such as the photovoltaic Hall effect [212], metal-insulator transition of graphene [213], valley-polarized currents in both monolayer and bilayer graphene [214, 215], and photoinduced quantum Hall effect in the absence of magnetic fields [216]. Other theoretical works include the analysis of ac transport properties through graphene ribbons [217], graphene-based *pn*-junctions [218], graphene-based Fabry-Pérot devices [219] and the recent proposal of quantum pumping in graphene by an external ac field [220]. Experimentally it has been found that a circularly polarized ac field induces a dynamic Hall effect in graphene [221]. Several studies have been devoted to the theoretical analysis of the quasienergy spectrum of graphene and graphene dots under ac fields [222–225], and the optical properties of graphene have been studied by calculating the optical conductivity [226]. One of the earliest and yet most important findings in all these studies is that a circularly polarized field induces a band-gap at the Dirac point, along with dynamical gaps at other momenta, all of which are tunable by the field intensity. This is, however, not the case for a linearly polarized field: there the *anisotropic* quasienergy spectrum shows dynamical gaps at non-zero momentum only in certain directions, and especially no gap is induced at the Dirac point [222, 226].

In this chapter we will study theoretically the effect of a circularly polarized ac electric field in the terahertz regime on the electron excitation spectrum and on the electron-electron interaction. The interactions are found to be affected qualitatively by the external field, altering the nature of the single particle excitations as well as the many-particle excitations, both in doped and undoped graphene.

Special attention is paid to the existence of a plasmon in *undoped* graphene, which is not present in its field-free counterpart. In order to perform this investigation, the natural object to study is the dynamical polarizability that we introduced in the previous chapter for graphene without external ac fields (see also ref. [205, 186, 206, 207, 227–229]).

The structure of this chapter is the following: In Sect. 7.1, we briefly introduce the Hamiltonian of graphene in the presence of a linearly and circularly polarized electric field, emphasizing the role of Floquet theory in Sect. 7.1.1. In the following sections, we present several approximations to the single electron Hamiltonian valid for weak fields; for the linearly polarized field see Sect. 7.1.2, and for the circularly polarized field see Sect. 7.1.3. Single-particle properties for the analytical approximations are then shown in Sect. 7.1.4 and Sect. 7.1.5. Section 7.2 is dedicated to the analysis of the dynamical polarizability: we derive a general expression for the polarizability of graphene in a circularly polarized ac electric field in Sect. 7.2.1, and compare it with the corresponding expression for the two dimensional electron gas [230]. Finally in section 7.2.2, the general formula is combined with the analytical approximations in order to work it out both for the non-interacting system and for the interacting system in the Random Phase Approximation (RPA).

7.1. Single electron properties of graphene irradiated by an ac electric field

7.1.1. Model and technique

As mentioned already, in the low-energy regime, the Hamiltonian for single electron excitations in graphene is the Dirac Hamiltonian, $H = \boldsymbol{\sigma} \cdot \mathbf{k}$. In order to introduce a time-dependent electric field we choose a gauge in which the latter is represented via a gauge potential $\mathbf{A}(t)$, whose time dependence is that of a single monochromatic wave of frequency Ω:

$$\mathbf{A}(t) = -\frac{E_0}{\Omega\sqrt{2}}[\hat{x}\sin(\Omega t) - \hat{y}\cos(\Omega t)], \qquad \text{for a circularly polarized field} \tag{7.1}$$

$$\mathbf{A}(t) = -\frac{E_0}{\Omega}\hat{x}\sin(\Omega t), \qquad \text{for a field linearly polarized in } \hat{x}\text{–direction} \tag{7.2}$$

By using a minimal coupling scheme, the Hamiltonian for graphene irradiated by a circularly electric field reads:

$$H(t)_{\text{circ}} = \begin{pmatrix} 0 & k_x - ik_y + iAe^{-i\Omega t} \\ k_x + ik_y - iAe^{i\Omega t} & 0 \end{pmatrix}, \tag{7.3}$$

with $A = eE_0/(\sqrt{2}\Omega)$ and $v_{\text{F}} = \hbar = 1$. Analogously we get for the linearly polarized field

$$H(t)_{\text{lin}} = \begin{pmatrix} 0 & k_x - ik_y + A\sin(\Omega t) \\ k_x + ik_y + A\sin(\Omega t) & 0 \end{pmatrix}, \tag{7.4}$$

with $A = eE_0/\Omega$. The Hamiltonian is expressed in terms of Bloch states of momentum $\mathbf{k}$, which is defined with respect to one of the valleys. Note that the electric field does not couple the spin and valley degrees of freedom in graphene, which remain as an extra degeneracy $N_{\text{s}}N_{\text{v}} = 4$. As we discussed

extensively in the introduction, the eigenstates of graphene in the absence of the external field are two-dimensional spinors representing the two components of the unit cell of the honeycomb lattice in graphene, that once diagonalized give rise to two bands (or Dirac cones). In the Dirac Hamiltonian, the pseudospin has a scalar coupling with the momentum, and its eigenstates are those whose pseudospin is either parallel or antiparallel to its momentum. It is remarkable that the mathematical structure of the Hamiltonian is very similar to that of an electronic spin coupled through Rashba interaction to a magnetic field. In this analogy, the momentum in graphene plays the role of the magnetic field, and the pseudospin operator is analogous to the ordinary spin, both having the same representation in terms of Pauli matrices. This allows one to write the Hamiltonian $H = \boldsymbol{\sigma} \cdot \mathbf{k}$. In the presence of an external electric field an extra term of the same nature arises in the Hamiltonian, now coupling the pseudospin and the electric field, and inducing transitions between the eigenstates for the isolated system. In a sense the momentum and the electric field are competing dynamically for the direction of the pseudospin, but no compromise can be reached due to the time-dependence of the field, which no longer allows for an analysis of the problem in terms of stationary eigenstates.

To proceed, we apply the Floquet theorem, which is the most suitable way to address time periodic Hamiltonians (detailed accounts can be found in Refs. [231, 75, 232]). Floquet theory states that for a Hamiltonian that is periodic in time – $H(t + 2\pi/\Omega) = H(t)$ – a complete set of solutions of the time-dependent Schrödinger equation

$$H(t)|\psi(t)\rangle = i\frac{d}{dt}|\psi(t)\rangle \tag{7.5}$$

can be written as

$$\begin{aligned} |\psi_\alpha(t)\rangle &= e^{-i\epsilon_\alpha t}|\phi_\alpha(t)\rangle \\ |\phi_\alpha(t)\rangle &= |\phi_\alpha(t+T)\rangle, \end{aligned} \tag{7.6}$$

where α contains the quantum numbers of the problem and the so-called Floquet index that we will label as l. The role of this index is to classify the different *sidebands*, since ϵ_α, the quasienergies, are defined $\mod \hbar\Omega$ and are related by the simple transformation

$$\epsilon_{\alpha(l)} = \epsilon_{\alpha(0)} + l\Omega. \tag{7.7}$$

In analogy to the Bloch theorem, the quasienergies can be mapped into a first time Brillouin zone, which is $[-\Omega/2, \Omega/2]$, and therefore corresponds to $l = 0$.

The Floquet states $|\phi_\alpha(t)\rangle$ have the same periodicity as the driving field (see Eq. (7.6)) and can therefore be expanded into a Fourier series

$$|\phi_\alpha(t)\rangle = \sum_{n=-\infty}^{\infty} e^{in\Omega t}|\phi_\alpha^n\rangle. \tag{7.8}$$

The Floquet states are also defined in different branches of solutions, related to one another by the transformation

$$|\phi^n_{\alpha(l)}\rangle = |\phi^{l+n}_{\alpha(0)}\rangle. \tag{7.9}$$

Substituting Eq. (7.6) into Eq. (7.5) and using Eq. (7.8) yields a static eigenvalue equation of the form

$$\sum_m (H^{nm} - n\Omega\delta_{mn})|\phi_\alpha^m\rangle = \epsilon_\alpha |\phi_\alpha^n\rangle. \tag{7.10}$$

If we now define the Floquet Hamiltonian as $H_{\mathrm{F}}^{nm} = H^{nm} - m\Omega\delta_{mn}$, we see that a significant simplification has been achieved: the time-dependent problem has been transformed to a static problem, and, consequently, one can apply the intuition about equilibrium problems to make statements about a dynamical problem. The resulting equilibrium-like observables derived within this framework have to be understood as time averages over a period of the external field.

Let us now apply the Floquet formalism to the Hamiltonian of irradiated graphene (7.3) and (7.4). In both cases, the solutions are characterized by indices $\alpha = (\mathbf{k}, \sigma, l)$, being $\sigma = \pm$ the pseudospin index. For the circularly polarized field, we obtain

$$\begin{aligned} n\Omega\phi_\alpha^{n,a} + (k_x - ik_y)\phi_\alpha^{n,b} + iA\phi_\alpha^{n+1,b} &= \epsilon_\alpha\phi_\alpha^{n,a} \\ n\Omega\phi_\alpha^{n,b} + (k_x + ik_y)\phi_\alpha^{n,a} - iA\phi_\alpha^{n-1,a} &= \epsilon_\alpha\phi_\alpha^{n,b}, \end{aligned} \tag{7.11}$$

and for the field linearly polarized in $\hat{x}$–direction

$$\begin{aligned} (n\Omega)\phi_\alpha^{n,a} + (k_x - ik_y)\phi_\alpha^{n,b} + \frac{A}{2i}(\phi_\alpha^{n-1,b} - \phi_\alpha^{n+1,b}) &= \epsilon_\alpha\phi_\alpha^{n,a} \\ (n\Omega)\phi_\alpha^{n,b} + (k_x + ik_y)\phi_\alpha^{n,a} + \frac{A}{2i}(\phi_\alpha^{n-1,a} - \phi_\alpha^{n+1,a}) &= \epsilon_\alpha\phi_\alpha^{n,b}. \end{aligned} \tag{7.12}$$

Notice that a and b are the indices for the sublattices of the honeycomb lattice. These equations can be written in matrix form, where the infinite Floquet Hamiltonian for the circular field reads

$$H_{\mathrm{F,circ}} = \left(\begin{array}{c|cc|cc|cc|c} \ddots & \vdots & \vdots & \vdots & \vdots & \vdots & \vdots & \iddots \\ \hline \cdots & -\Omega & ke^{-i\Theta} & 0 & iA & 0 & 0 & \cdots \\ \cdots & ke^{i\Theta} & -\Omega & 0 & 0 & 0 & 0 & \cdots \\ \hline \cdots & 0 & 0 & 0 & ke^{-i\Theta} & 0 & iA & \cdots \\ \cdots & -iA & 0 & ke^{i\Theta} & 0 & 0 & 0 & \cdots \\ \hline \cdots & 0 & 0 & 0 & 0 & \Omega & ke^{-i\Theta} & \cdots \\ \cdots & 0 & 0 & -iA & 0 & ke^{i\Theta} & \Omega & \cdots \\ \hline \iddots & \vdots & \vdots & \vdots & \vdots & \vdots & \vdots & \ddots \end{array}\right), \tag{7.13}$$

and $k = \sqrt{k_x^2 + k_y^2}$, $\Theta = \arctan k_y/k_x$.

Analogously, we write the Floquet Hamiltonian for the linearly polarized field as

$$H_{\mathrm{F,lin}} = \left(\begin{array}{c|cc|cc|cc|c} \ddots & \vdots & \vdots & \vdots & \vdots & \vdots & \vdots & \iddots \\ \hline \cdots & -\Omega & ke^{-i\Theta} & 0 & \frac{i}{2}A & 0 & 0 & \cdots \\ \cdots & ke^{i\Theta} & -\Omega & \frac{i}{2}A & 0 & 0 & 0 & \cdots \\ \hline \cdots & 0 & -\frac{i}{2}A & 0 & ke^{-i\Theta} & 0 & \frac{i}{2}A & \cdots \\ \cdots & -\frac{i}{2}A & 0 & ke^{i\Theta} & 0 & \frac{i}{2}A & 0 & \cdots \\ \hline \cdots & 0 & 0 & 0 & -\frac{i}{2}A & \Omega & ke^{-i\Theta} & \cdots \\ \cdots & 0 & 0 & -\frac{i}{2}A & 0 & ke^{i\Theta} & \Omega & \cdots \\ \hline \iddots & \vdots & \vdots & \vdots & \vdots & \vdots & \vdots & \ddots \end{array}\right). \tag{7.14}$$

The structure of these Hamiltonians deserves a few comments. Note that the ac field A connects (2×2) graphene Hamiltonians with energies $n\Omega$ and $(n+1)\Omega$ and so on. Each of these building blocks contributes with its own dispersion relation (that of a Dirac cone) to the energy spectrum, and the field introduces transitions between these cones. These transitions are expressed as anticrossings in the spectrum, and become exact crossings for $A \to 0$. It can easily be seen that the anticrossings occur at $|\mathbf{k}| \approx n\Omega/2$, with $n = 0,1,2,\ldots$. At $|\mathbf{k}| \approx \Omega/2$ e.g., the $(+,0)$ and the $(-,1)$ sideband anticross, which would be a so-called *one-photon resonance*. In contrast to the circularly polarized field (Eq. (7.13)), in the Hamiltonian for the linearly polarized field (7.14) the component $\phi_\alpha^{n,a}$ is coupled to both $\phi_\alpha^{n-1,b}$ and $\phi_\alpha^{n+1,b}$, see also Eq. (7.12).

The Floquet Hamiltonians, Eqs. (7.14,7.13) can be diagonalized numerically in order to analyze the energy spectrum and its features. However, in order to simplify the calculations and to illuminate the main physics, here we resort to analytical approximations which capture the main features whenever the electric field intensity is sufficiently weak. We will show in Sect. 7.1.4 and 7.1.5 the full numerical results for the quasienergy spectrum in order to compare it with the analytical approximations.

7.1.2. Analytical approximations to the single particle Hamiltonian: Linearly polarized field

Let us start by analyzing the case of a linearly polarized field. Before introducing the analytical approximations, it is convenient to project the Hamiltonian (7.14) into another basis. It can be seen in Fig. 7.1, that for $\mathbf{k} = 0$ the Hamiltonian for the linearly polarized field breaks up into two degenerate chains of the form "abab" and "baba". These types of Hamiltonians are well known as so-called *Wannier-Stark ladders* [233], and appear in tight-binding models in static electric fields. As compared to the present case, the frequency Ω plays the role of the electric potential in a Wannier-Stark ladder, and the field intensity A represents the hopping between neighboring sites. The Wannier-Stark ladder is solved by Bessel functions (see appendix B.1 for some important properties). Now the Hamiltonian for $\mathbf{k} = 0$, as drawn in Fig. 7.1, is

$$H_{\mathrm{F,lin}}^{\mathbf{k}=0} = \sum_n n\Omega |\phi_{\mathbf{k}=0}^n\rangle\langle\phi_{\mathbf{k}=0}^n| + \frac{iA}{2}\sum_n |\phi_{\mathbf{k}=0}^n\rangle\langle\phi_{\mathbf{k}=0}^{n+1}| - \frac{iA}{2}\sum_n |\phi_{\mathbf{k}=0}^{n+1}\rangle\langle\phi_{\mathbf{k}=0}^n|, \tag{7.15}$$

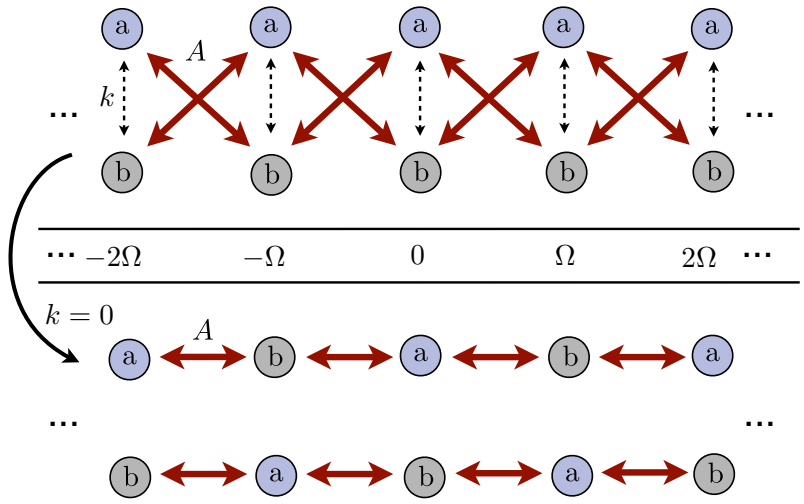

Figure 7.1.: **Sketch of Floquet Hamiltonian for linearly polarized electric field.** Upper half for $\mathbf{k} \neq 0$ and lower half for $\mathbf{k} = 0$.

or in matrix form

$$H_{\mathrm{F,lin}}^{\mathbf{k}=0} = \begin{pmatrix} \ddots & \vdots & \vdots & \vdots & \iddots \\ \cdots & (n-1)\Omega & \frac{iA}{2} & 0 & \cdots \\ \cdots & -\frac{iA}{2} & n\Omega & \frac{iA}{2} & \cdots \\ \cdots & 0 & -\frac{iA}{2} & (n+1)\Omega & \cdots \\ \iddots & \vdots & \vdots & \vdots & \ddots \end{pmatrix}. \tag{7.16}$$

For coefficients c_n of the corresponding eigenvectors, this can be written as a recurrence relation

$$-\frac{iA}{2}c_{n-1} + n\Omega c_n + \frac{iA}{2}c_{n+1} = Ec_n. \tag{7.17}$$

With the ansatz $E = l\Omega$, we rewrite

$$(n\Omega - l\Omega)c_n = \frac{iA}{2}(c_{n-1} - c_{n+1}), \tag{7.18}$$

and recognize the recurrence relation of the modified Bessel function, see Eq. (B.1), with

$$I_\nu(z) = I_{n-l}\left(\frac{iA}{\Omega}\right) = c_n^l. \tag{7.19}$$

The index $n = -\infty \ldots \infty$ numbers the Fourier mode of the Floquet Hamiltonian (or also the *site* of the tight-binding chain), and $l = -\infty \ldots \infty$ is the index for the solution of the Floquet Hamiltonian $H_{\mathrm{F,lin}}^{\mathbf{k}=0}$. A solution for $H_{\mathrm{F,lin}}^{\mathbf{k}=0}$ can hence be written as

$$|\psi_l\rangle = \sum_{n=-\infty}^{\infty} I_{n-l}\left(\frac{iA}{\Omega}\right)|\phi_{\mathbf{k}=0}^n\rangle. \tag{7.20}$$

We will now project the Hamiltonian $H_{\mathrm{F,lin}}^{\mathbf{k}=\mathbf{0}}$ into the basis $|\psi_l\rangle$. For the derivation of the matrix elements, see appendix B.2. Using the property $I_n(ix) = i^n J_n(x)$ and $z = 2A/\Omega$, the Hamiltonian can then be written as

$$H_{\mathrm{F,lin}} = \left(\begin{array}{c|cc|cc|cc|c} \ddots & \vdots & \vdots & \vdots & \vdots & \vdots & \vdots & \iddots \\ \hline \dots & -\Omega & \kappa e^{i\theta} & 0 & k_y J_1(z) & 0 & -ik_y J_2(z) & \dots \\ \dots & \kappa e^{-i\theta} & -\Omega & -k_y J_1(z) & 0 & ik_y J_2(z) & 0 & \dots \\ \hline \dots & 0 & -k_y J_1(z) & 0 & \kappa e^{-i\theta} & 0 & -k_y J_1(z) & \dots \\ \dots & k_y J_1(z) & 0 & \kappa e^{i\theta} & 0 & k_y J_1(z) & 0 & \dots \\ \hline \dots & 0 & -ik_y J_2(z) & 0 & k_y J_1(z) & \Omega & \kappa e^{i\theta} & \dots \\ \dots & ik_y J_2(z) & 0 & -k_y J_1(z) & 0 & \kappa e^{-i\theta} & \Omega & \dots \\ \hline \iddots & \vdots & \vdots & \vdots & \vdots & \vdots & \vdots & \ddots \end{array}\right), \tag{7.21}$$

where we introduced

$$\kappa = \sqrt{k_x^2 + k_y^2 J_0^2\left(\frac{2A}{\Omega}\right)} \tag{7.22}$$

$$\theta = \arctan\left[\frac{k_y J_0\left(\frac{2A}{\Omega}\right)}{k_x}\right]. \tag{7.23}$$

Note that the Hamiltonian includes couplings up to infinite order in the Bessel functions (see e.g. ref. [75, 234]), and here we have displayed only part of the infinite Hamiltonian. In the subsequent analysis, we will at first only consider the elements $\propto J_0(z)$, and will afterwards include the couplings $\propto J_1(z)$. Higher order couplings, however, will be neglected. This approach is valid as long as the field strength A is small compared to the frequency Ω, so $z = 2A/\Omega \ll 1$, since then $J_{n\geq 2}(z) \approx 0$.

J_0–approximation

Neglecting therefore $J_{n\geq 1}(z)$, the Hamiltonian (7.21) is block diagonal, and one building block reads

$$H_{J_0}^n = \begin{pmatrix} n\Omega & \kappa e^{-i\theta} \\ \kappa e^{i\theta} & n\Omega \end{pmatrix}. \tag{7.24}$$

It can easily be diagonalized, and its eigenenergies and eigenvectors are

$$\begin{aligned} \epsilon_{l,J_0}^{\pm} &= l\Omega \pm \kappa \\ |\chi_{l,J_0}^{+}\rangle &= \frac{1}{\sqrt{2}}\left(e^{-\frac{i}{2}\theta}|\psi_l^{+}\rangle + e^{\frac{i}{2}\theta}|\psi_l^{-}\rangle\right) \\ |\chi_{l,J_0}^{-}\rangle &= \frac{1}{\sqrt{2}}\left(e^{-\frac{i}{2}\theta}|\psi_l^{+}\rangle - e^{\frac{i}{2}\theta}|\psi_l^{-}\rangle\right). \end{aligned} \tag{7.25}$$

This approximation illustrates very clearly that the linearly polarized field renormalizes the Fermi velocity by $J_0(2A/\Omega)$. Notice, however, that a linearly polarized field has no effect on the system along its polarization axis $\hat{x}$: for $k_y = 0$, we recover the dispersion relation for free graphene.

J_1–approximation

In order to capture higher order photon processes, we take into account the matrix elements $\propto J_1(2A/\Omega)$, but keep $J_{n\geq 2}(2A/\Omega) = 0$. In the Hamiltonian (7.21), one of the (2×2)-matrices including J_1 reads

$$H_{J_1} = \begin{pmatrix} 0 & k_y J_1\left(\frac{2A}{\Omega}\right) \\ -k_y J_1\left(\frac{2A}{\Omega}\right) & 0 \end{pmatrix}. \tag{7.26}$$

We now apply the unitary matrix U that diagonalizes $H^n_{J_0}$ to the Floquet Hamiltonian (7.21). However, one has to be careful here: since the $H^n_{J_0}$ matrices alternate between (7.24) and their hermitian conjugate, the unitary matrix that we have to use is

$$U = \begin{pmatrix} \ddots & \vdots & \vdots & \vdots & \iddots \\ \cdots & U_0^{n*} & 0 & 0 & \cdots \\ \cdots & 0 & U_0^{n} & 0\cdots & \\ \cdots & 0 & 0 & U_0^{n*} & \cdots \\ \iddots & \vdots & \vdots & \vdots & \ddots \end{pmatrix}, \tag{7.27}$$

where

$$U_0^n = \frac{1}{\sqrt{2}} \begin{pmatrix} e^{-\frac{i}{2}\theta} & e^{-\frac{i}{2}\theta} \\ e^{\frac{i}{2}\theta} & -e^{\frac{i}{2}\theta} \end{pmatrix}. \tag{7.28}$$

We apply hence $U^\dagger H_{\mathrm{F,lin}} U$ and pick the relevant couplings to get two effective decoupled Hamiltonians

$$H^{\mathrm{eff},n,1}_{J_1} = \begin{pmatrix} \epsilon^+_{n-1,J_0} & -k_y J_1\left(\frac{2A}{\Omega}\right) \\ -k_y J_1\left(\frac{2A}{\Omega}\right) & \epsilon^-_{n,J_0} \end{pmatrix} \text{ and } H^{\mathrm{eff},n,2}_{J_1} = \begin{pmatrix} \epsilon^+_{n,J_0} & k_y J_1\left(\frac{2A}{\Omega}\right) \\ k_y J_1\left(\frac{2A}{\Omega}\right) & \epsilon^-_{n+1,J_0} \end{pmatrix}. \tag{7.29}$$

Out of the eigenvalues of these effective Hamiltonians we then choose those that become the free graphene eigenvalues for $A \to 0$. They read

$$\epsilon^+_{l,J_1} = \begin{cases} l\Omega + \frac{1}{2}\left(\Omega - \sqrt{(\Omega-2\kappa)^2 + 4k_y^2 J_1^2\left(\frac{2A}{\Omega}\right)}\right) & \text{if } \kappa < k_c \\ (l+1)\Omega - \frac{1}{2}\left(\Omega - \sqrt{(\Omega-2\kappa)^2 + 4k_y^2 J_1^2\left(\frac{2A}{\Omega}\right)}\right) & \text{if } \kappa > k_c \end{cases} \tag{7.30}$$

$$\epsilon^-_{l,J_1} = \begin{cases} l\Omega - \frac{1}{2}\left(\Omega - \sqrt{(\Omega-2\kappa)^2 + 4k_y^2 J_1^2\left(\frac{2A}{\Omega}\right)}\right) & \text{if } \kappa < k_c \\ (l-1)\Omega + \frac{1}{2}\left(\Omega - \sqrt{(\Omega-2\kappa)^2 + 4k_y^2 J_1^2\left(\frac{2A}{\Omega}\right)}\right) & \text{if } \kappa > k_c \end{cases} \tag{7.31}$$

and their corresponding eigenvectors are

$$|\xi^+_{l,J_1}\rangle = \begin{cases} \frac{1}{\sqrt{|\xi_a|^2+|\xi_b|^2}}\left[\xi_a|\chi^+_{l,J_0}\rangle + \xi_b|\chi^-_{l+1,J_0}\rangle\right] & \text{if } \kappa < k_c \\ \frac{1}{\sqrt{|\xi_a|^2+|\xi_b|^2}}\left[\xi_b|\chi^+_{l,J_0}\rangle - \xi_a|\chi^-_{l+1,J_0}\rangle\right] & \text{if } \kappa > k_c \end{cases} \tag{7.32}$$

$$|\xi^-_{l,J_1}\rangle = \begin{cases} \frac{1}{\sqrt{|\xi_a|^2+|\xi_b|^2}}\left[\xi_b|\chi^+_{l-1,J_0}\rangle + \xi_a|\chi^-_{l,J_0}\rangle\right] & \text{if } \kappa < k_c \\ \frac{1}{\sqrt{|\xi_a|^2+|\xi_b|^2}}\left[\xi_a|\chi^+_{l-1,J_0}\rangle - \xi_b|\chi^-_{l,J_0}\rangle\right] & \text{if } \kappa > k_c, \end{cases} \tag{7.33}$$

where

$$\xi_a = \kappa - \frac{1}{2}\left(\Omega + \sqrt{(\Omega - 2\kappa)^2 + 4k_y^2 J_1^2\left(\frac{2A}{\Omega}\right)}\right) \tag{7.34}$$

$$\xi_b = k_y J_1\left(\frac{2A}{\Omega}\right). \tag{7.35}$$

At the critical momentum k_c, where the eigenvalues suffer an anticrossing and both eigenenergies and eigenvectors change their character, the one-photon resonance takes place and a gap opens in the quasienergy spectrum. The size of the gap, however, or even its existence, depend on k_y. It has already been mentioned that for $k_y = 0$, the field is decoupled from the system and cannot induce transitions. Therefore along this line, no gaps open in the energy spectrum, and neither zero- nor multi-photon resonances exist. For this reason, the one-photon gap is zero at $k_y = 0$ and biggest at $k_x = 0, k_y = k_c$. There, the critical momentum is

$$k_c = \pm \frac{\Omega J_0\left(\frac{2A}{\Omega}\right)}{2\left[J_0^2\left(\frac{2A}{\Omega}\right) + J_1^2\left(\frac{2A}{\Omega}\right)\right]}. \tag{7.36}$$

The maximum gap can be found analytically from Eqs. (7.30), (7.31) and (7.36) to be

$$\Delta_{J_1} = \frac{\Omega J_1\left(\frac{2A}{\Omega}\right)}{\sqrt{J_0^2\left(\frac{2A}{\Omega}\right) + J_1^2\left(\frac{2A}{\Omega}\right)}}. \tag{7.37}$$

For a field frequency in the mid-infrared regime, $\Omega \approx 150$ meV, and field intensity $E_0 \approx 3.4 \cdot 10^6$ V/m (so that $A/\Omega = 0.1$), the gap due to one-photon resonances can reach $\Delta_{J_1} \approx 15$ meV.

7.1.3. Analytical approximations to the single particle Hamiltonian: Circularly polarized field

As it happened for the linearly polarized field, for the circularly polarized field it is also advantageous to project the Hamiltonian (7.13) into another basis. Note that for $\mathbf{k} = 0$, the Floquet chain breaks up into a series of disconnected two-level systems, see Fig. 7.2. We therefore diagonalize the Hamiltonian for the two-level-system, and then write the full Hamiltonian in the resulting basis. The Hamiltonian for $\mathbf{k} = 0$ reads

$$H_{\mathrm{F}}^{\mathbf{k}=\mathbf{0}} = \sum_n n\Omega\left[|\phi_{\mathbf{k}=0}^{n,a}\rangle\langle\phi_{\mathbf{k}=0}^{n,a}| + |\phi_{\mathbf{k}=0}^{n,b}\rangle\langle\phi_{\mathbf{k}=0}^{n,b}|\right] + iA\left[|\phi_{\mathbf{k}=0}^{n,a}\rangle\langle\phi_{\mathbf{k}=0}^{n+1,b}| - |\phi_{\mathbf{k}=0}^{n+1,b}\rangle\langle\phi_{\mathbf{k}=0}^{n,a}|\right]. \tag{7.38}$$

An excerpt of the series of (2×2) Hamiltonians is

$$H_{\mathrm{F}}^{\mathbf{k}=0} = \begin{pmatrix} n\Omega & iA & 0 & 0 \\ -iA & (n+1)\Omega & 0 & 0 \\ 0 & 0 & (n-1)\Omega & iA \\ 0 & 0 & -iA & n\Omega \end{pmatrix}. \tag{7.39}$$

Out of the four eigenenergies of this matrix we are interested in

$$\epsilon_l^{\pm} = l\Omega \pm \frac{1}{2}\Delta, \tag{7.40}$$

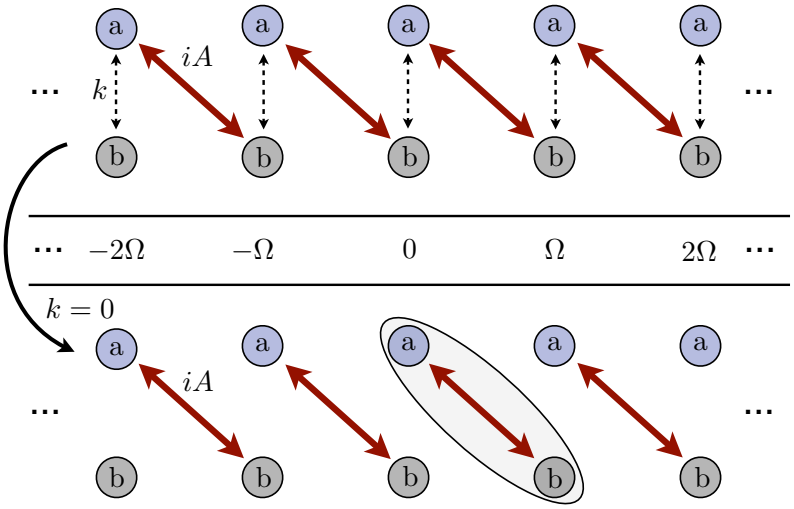

Figure 7.2.: **Sketch of the Hamiltonian for the circularly polarized field**. Note that if $\mathbf{k} = 0$, the Hamiltonian breaks up into disconnected two-level systems, in which site a_n is coupled to site b_{n+1}.

with

$$\Delta = \widetilde{\Omega} - \Omega$$
$$\widetilde{\Omega} = \sqrt{4A^2 + \Omega^2},$$

because these two energies fulfill $\lim_{A\to 0} \epsilon_0^{\pm} = 0$. Thus, we associate the first Brillouin zone, $l = 0$, from the Floquet solutions, with the solutions corresponding to graphene in the absence of an external field. The corresponding eigenvectors are

$$|\phi_l^+\rangle = \frac{1}{N}\left(2iA|\phi_{\mathbf{k}=0}^{l-1,a}\rangle + (\Delta + 2\Omega)|\phi_{\mathbf{k}=0}^{l,b}\rangle\right) \tag{7.41}$$
$$|\phi_l^-\rangle = \frac{1}{N}\left((\Delta + 2\Omega)|\phi_{\mathbf{k}=0}^{l,a}\rangle + 2iA|\phi_{\mathbf{k}=0}^{l+1,b}\rangle\right), \tag{7.42}$$

where $N = \sqrt{4A^2 + (\Delta + 2\Omega)^2}$. From here on and for the rest of this section, we neglect the index $\mathbf{k}$ in the energies and vectors, unless we have to distinguish between $\mathbf{k}$ and $\mathbf{k} + \mathbf{q}$.

Using these eigenvectors as a basis, we rewrite the full Floquet Hamiltonian (7.13)

$$H_{\mathrm{F}} = \left(\begin{array}{c|c|c|c|c|c|c} \ddots & \vdots & \vdots & \vdots & \vdots & \vdots & \iddots \\ \hline \dots & \epsilon^{+}_{n-1} & F_0 k e^{i\Theta} & F_1 k e^{i\Theta} & 0 & 0 & \dots \\ \dots & F_0 k e^{-i\Theta} & \epsilon^{-}_{n-1} & 0 & F_1^* k e^{i\Theta} & F_2 k e^{i\Theta} & \dots \\ \hline \dots & F_1^* k e^{-i\Theta} & 0 & \epsilon^{+}_{n} & F_0 k e^{i\Theta} & F_1 k e^{i\Theta} & \dots \\ \dots & 0 & F_1 k e^{-i\Theta} & F_0 k e^{-i\Theta} & \epsilon^{-}_{n} & 0 & F_1^* k e^{i\Theta} & \dots \\ \hline \dots & 0 & F_2 k e^{-i\Theta} & F_1^* k e^{-i\Theta} & 0 & \epsilon^{+}_{n+1} & F_0 k e^{i\Theta} & \dots \\ \dots & 0 & 0 & 0 & F_1 k e^{-i\Theta} & F_0 k e^{-i\Theta} & \epsilon^{-}_{n+1} & \dots \\ \hline \iddots & \vdots & \vdots & \vdots & \vdots & \vdots & \vdots & \ddots \end{array}\right), \tag{7.43}$$

where $k = |\mathbf{k}|$, $\Theta = \arctan k_y/k_x$. Here we have introduced the three functions F_0, F_1 and F_2 that will form the basis for our approximations:

$$\begin{aligned} F_0 &= \frac{(\Delta + 2\Omega)^2}{4A^2 + (\Delta + 2\Omega)^2} \\ F_1 &= \frac{2iA(\Delta + 2\Omega)}{4A^2 + (\Delta + 2\Omega)^2} \\ F_2 &= \frac{4A^2}{4A^2 + (\Delta + 2\Omega)^2}. \end{aligned} \tag{7.44}$$

All three functions in Eq. (7.44) are functions of A and Ω. For small $A/\Omega \ll 1$, one finds that $F_0 \approx 1$, and $F_{1,2} \approx 0$, however, F_1 increases linearly, whereas F_2 increases quadratically with A. Note that for a two-level system driven by a linearly polarized field, the nth order Bessel function $J_n(A/\Omega)$ plays the role of the function $F_{0,1,2}$ presented here, and for a complete analysis one has to consider Bessel functions up to infinite order, see previous section. Here, however, the complete information lies in $F_{0,1,2}$. In the subsequent analysis, we will at first only consider the couplings given by F_0, and then include also the couplings given by F_1. We will neglect F_2 in general, which is valid for small A/Ω.

F_0–approximation

A first approximation consists in neglecting both F_1 and F_2 and considering only F_0, which connects energies with the same photon number n. This approximation is valid for the calculation of many observables as far as the dimensionless quantity $A/\Omega \ll 1$, – i.e. the field intensity is small compared to the frequency –, and we are interested in excitations in the low energy sector, as we will see below, when we analyze the excitation spectrum and the generalized density of states. The resulting Hamiltonian (7.43) is then block diagonal with building blocks $H^n_{F_0}$, where the matrix $H^n_{F_0}$ reads

$$H^n_{F_0} = \begin{pmatrix} \epsilon^{+}_{n} & F_0 k e^{i\Theta} \\ F_0 k e^{-i\Theta} & \epsilon^{-}_{n} \end{pmatrix}. \tag{7.45}$$

Its eigenvalues and eigenvectors are

$$\epsilon^{\pm}_{l,F_0} = l\Omega \pm \frac{1}{2}\sqrt{4F_0^2 k^2 + \Delta^2} \tag{7.46}$$

$$|\chi^{+}_{l,F_0}\rangle = \frac{1}{\sqrt{|\chi_a|^2+|\chi_b|^2}}\left(\chi_a|\phi^{+}_{l}\rangle + \chi_b|\phi^{-}_{l}\rangle\right)$$
$$|\chi^{-}_{l,F_0}\rangle = \frac{1}{\sqrt{|\chi_a|^2+|\chi_b|^2}}\left(\chi^*_b|\phi^{+}_{l}\rangle - \chi^*_a|\phi^{-}_{l}\rangle\right), \tag{7.47}$$

where

$$\chi_a = 2F_0 k e^{i\frac{\Theta}{2}} \tag{7.48}$$
$$\chi_b = \left(\sqrt{4F_0^2k^2+\Delta^2}-\Delta\right)e^{-i\frac{\Theta}{2}}. \tag{7.49}$$

The main virtue of this approximation consists in the fact that it captures the gap Δ at $\mathbf{k}=0$ produced by the ac electric field, giving an analytical expression for its magnitude, $\Delta = \sqrt{4A^2+\Omega^2}-\Omega$, so that this gap can be tuned by varying the field strength of the applied ac field, see also refs. [212, 222, 226]. We point out that an analogous phenomenon occurs in the optics of semiconductors in a strong THz-field: There, the dynamical Franz-Keldysh effect [235, 236] blue-shifts the conduction band edge (or, equivalently, the optical absorption edge) by the ponderomotive energy, which also depends quadratically on the ac-field amplitude.

The so called F_0–*approximation* neglects the coupling between Hamiltonians with a different number of photons, and is therefore not useful once we are interested in the anticrossings of the Floquet quasienergies for non-zero momentum.

F_1–approximation

In order to analyze higher order processes, we go one step further and take into account the coupling elements F_1, which capture the one-photon resonances, yielding a much more robust approximation for the Hamiltonian $H_{\rm F}$ (7.43). At the resonances the relevant couplings are the ones between ϵ^{+}_{n-1} and ϵ^{-}_{n}, ϵ^{+}_{n} and ϵ^{-}_{n+1} etc., see Eq. (7.43). By applying the unitary matrix that diagonalizes $H^{n}_{F_0}$

$$U_n = \frac{1}{\sqrt{|\chi_a|^2+|\chi_b|^2}}\begin{pmatrix}\chi_a & \chi^*_b\\ \chi_b & -\chi^*_a\end{pmatrix}, \tag{7.50}$$

we can construct a new effective infinite Hamiltonian which includes the features of the one-photon resonance, and which is again block diagonal, now mixing the sectors that differ in one photon in the F_0–approximation:

$$H^{\mathrm{eff},n}_{F_1} = \begin{pmatrix}\epsilon^{+}_{n-1,F_0} & \frac{2}{S_k}F_0F_1k^2e^{i\Theta}\\ \frac{2}{S_k}F_0F_1^*k^2e^{-i\Theta} & \epsilon^{-}_{n,F_0}\end{pmatrix}, \tag{7.51}$$

where $S_k = \sqrt{4F_0^2k^2+\Delta^2}$. The intensity of the coupling is proportional to F_1, as expected. Diagonalizing this Hamiltonian yields the following Floquet quasienergies:

$$\epsilon^{+}_{l,F_1} = \begin{cases} l\Omega + \frac{1}{2}\left(\Omega - \sqrt{(\Omega-S_k)^2+\frac{16}{S_k^2}F_0^2|F_1|^2k^4}\right) & \text{if } k<k_c\\ (l+1)\Omega - \frac{1}{2}\left(\Omega - \sqrt{(\Omega-S_k)^2+\frac{16}{S_k^2}F_0^2|F_1|^2k^4}\right) & \text{if } k>k_c\end{cases} \tag{7.52}$$

$$\epsilon^{-}_{l,F_1} = \begin{cases} l\Omega - \frac{1}{2}\left(\Omega - \sqrt{(\Omega - S_k)^2 + \frac{16}{S_k^2}F_0^2|F_1|^2k^4}\right) & \text{if } k < k_c \\ (l-1)\Omega + \frac{1}{2}\left(\Omega - \sqrt{(\Omega - S_k)^2 + \frac{16}{S_k^2}F_0^2|F_1|^2k^4}\right) & \text{if } k > k_c, \end{cases} \tag{7.53}$$

where k_c is the momentum at which the one-photon resonance takes place. For the Floquet eigenvectors, it is more convenient to write them in the basis that diagonalizes the Hamiltonian for $\mathbf{k} = 0$, reading

$$|\xi^{+}_{l,F_1}\rangle = \begin{cases} \frac{1}{N}\left[\xi_a\chi_a|\phi^{+}_{l}\rangle + \xi_a\chi_b|\phi^{-}_{l}\rangle - \xi_b\chi^*_b|\phi^{+}_{l+1}\rangle + \xi_b\chi^*_a|\phi^{-}_{l+1}\rangle\right] & \text{if } k < k_c \\ \frac{1}{N}\left[\xi^*_b\chi_a|\phi^{+}_{l}\rangle + \xi^*_b\chi_b|\phi^{-}_{l}\rangle + \xi^*_a\chi^*_b|\phi^{+}_{l+1}\rangle - \xi^*_a\chi^*_a|\phi^{-}_{l+1}\rangle\right] & \text{if } k > k_c \end{cases} \tag{7.54}$$

$$|\xi^{-}_{l,F_1}\rangle = \begin{cases} \frac{1}{N}\left[\xi^*_b\chi_a|\phi^{+}_{l-1}\rangle + \xi^*_b\chi_b|\phi^{-}_{l-1}\rangle + \xi^*_a\chi^*_b|\phi^{+}_{l}\rangle - \xi^*_a\chi^*_a|\phi^{-}_{l}\rangle\right] & \text{if } k < k_c \\ \frac{1}{N}\left[\xi_a\chi_a|\phi^{+}_{l-1}\rangle + \xi_a\chi_b|\phi^{-}_{l-1}\rangle - \xi_b\chi^*_b|\phi^{+}_{l}\rangle + \xi_b\chi^*_a|\phi^{-}_{l}\rangle\right] & \text{if } k > k_c, \end{cases} \tag{7.55}$$

where $N = \sqrt{(|\chi_a|^2 + |\chi_b|^2)(|\xi_a|^2 + |\xi_b|^2)}$ and where we have introduced

$$\xi_a = \left[(\Omega - S_k) + \sqrt{(\Omega - S_k)^2 + \frac{16}{S_k^2}F_0^2|F_1|^2k^4}\right] e^{\frac{i}{2}\Theta} \tag{7.56}$$

$$\xi_b = \frac{4}{S_k}F_0F_1^*k^2e^{-\frac{i}{2}\Theta}. \tag{7.57}$$

The F_1–*approximation* captures the gap at $\mathbf{k} = 0$ as well as the first resonance. The latter gives rise to the opening of new gaps, whose expression can be obtained analytically in this approximation, yielding

$$\Delta_{F_1} = \sqrt{(S_{k_c} - \Omega)^2 + \frac{16}{S^2_{k_c}}F_0^2F_1^2k_c^4}. \tag{7.58}$$

For a frequency $\Omega \approx 150$ meV in the mid-infrared regime, and field intensity $E_0 \approx 4.8 \cdot 10^6$ V/m (which is so that $A/\Omega = 0.1$), the sizes of the two gaps would be $\Delta \approx 3$ meV, $\Delta_{F_1} \approx 15$ meV.

7.1.4. Single particle properties derived from the analytical approximations: Linearly polarized field

Let us now plot the quasienergy spectrum as a function of the momentum in the different analytic approximations, both for linearly and circularly polarized field.

For a linearly polarized field, the spectrum is not isotropic, and we choose here to plot the quasienergies as a function of k_y. In Fig. 7.3 we show the full numerical spectrum (upper panel), the spectrum for the J_0–approximation (middle panel) and finally for the J_1–approximation (lower panel). The solid black lines represent the Floquet band $l = 0$, the dashed lines the $l = -1$, and the dashdotted lines the $l = 1$ band. Note that the J_0–approximation captures the renormalized Fermi velocity, but no gaps due to higher order photon processes open. In the J_1–approximation (lower panel), however, the gap at around $k_y \approx \Omega/2$ is well reproduced, as compared to the full numerical result in the upper panel. For the field strength chosen here – $A/\Omega = 0.2$ –, higher order gaps due to processes involving two or more photons are negligible.

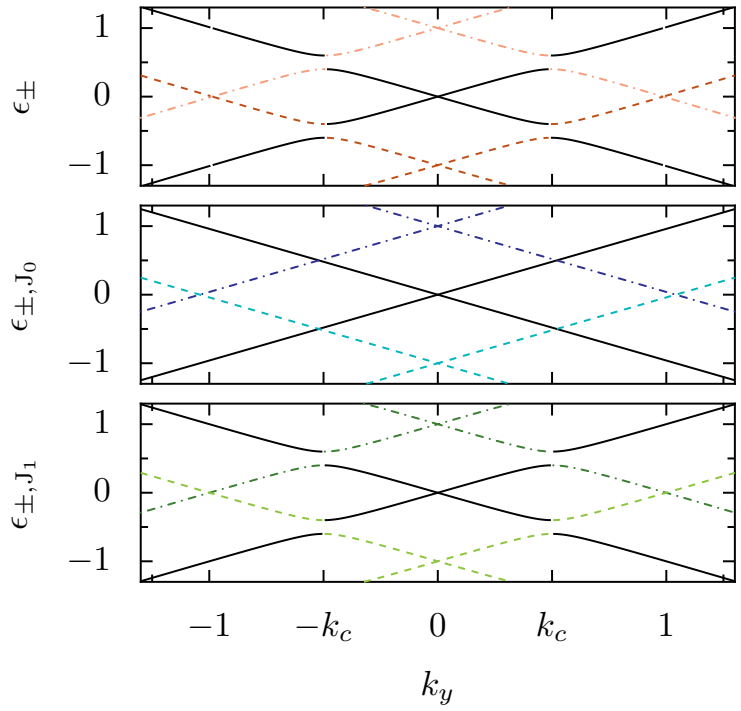

Figure 7.3.: **Quasienergy spectrum for graphene irradiated by a linearly polarized electric field.** The quasienergies are plotted as a function of k_y for $k_x = 0$. The solid lines represent the $l = 0$ band, the dashed lines the $l = -1$, and the dashdotted lines the $l = 1$ sideband. *Upper panel*: The full numerical result of the quasienergies. *Middle panel*: The quasienergies for the zero-photon approximation J_0. *Lower panel*: The quasienergies for the one-photon approximation J_1. Parameters: $k_x = 0$, $A = 0.2$, $\Omega = 1$.

For weak fields, the J_1–approximation constitutes an excellent analytic approach to the real system. We will therefore use it to calculate the density of states (DOS), and compare it henceforth with the full numerical result. The generalized (time averaged) density of states is calculated by

$$D(\omega) = 4 \sum_{\mathbf{k},\sigma} \delta(\omega - \epsilon_{\mathbf{k},\sigma,0}), \tag{7.59}$$

where the quasienergies are those defined in the first Brillouin zone of the Floquet spectrum. In the J_0–approximation, $\epsilon_{\mathbf{k},\sigma,l=0} = \epsilon^{\pm}_{0,J_0}$, see Eq. (7.25), and the density of states can be calculated analytically yielding

$$D_{J_0}(\omega) = \frac{2}{\pi J_0\left(\frac{2A}{\Omega}\right)} |\omega|, \tag{7.60}$$

which differs from the density of states for free graphene only by the factor $1/J_0(2A/\Omega)$. This can be understood as an effective renormalization of the Fermi velocity. The results from both J_0– and J_1–approximations are displayed in Fig. 7.4, together with the full numerical density of states. Note the good agreement of the J_1–approximation with the full numerical one, where only a very narrow additional gap opens at $\omega \approx \Omega$, due to two-photon resonances. The density of states both for circularly and linearly polarized field has already been obtained numerically by Oka *et al.* [212], Calvo

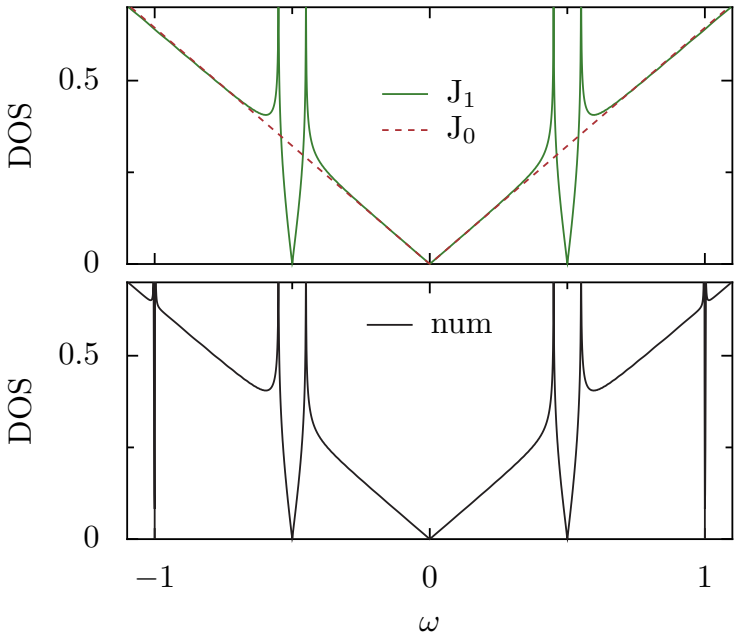

Figure 7.4.: **Generalized density of states of graphene irradiated by a linearly polarized ac electric field.** *Upper panel:* Density of states for the analytical approximations J_0 and J_1. *Lower panel:* Full numerical result for the density of states. Note the good agreement between the full numerical result and the J_1–approximation. The antiresonance at $\omega \approx \pm 1$ due to two-photon processes is very narrow at low field strengths as they have been chosen here. Parameters: $A = 0.1$, $\Omega = 1$.

et al. [222] and Zhou *et al.* [226] using the full Floquet Hamiltonian. The analytical approximations derived here, especially the J_1–approximation, as it coincides very well with the numerical result for low field strength, should, however, be useful for future work concerning graphene irradiated by a linearly polarized ac electric field.

7.1.5. Single particle properties of the Hamiltonian derived from the analytical approximations: Circularly polarized field

We next consider the quasienergy spectrum for circularly polarized field, both the full numerical result and the analytical approximation derived in the previous section. With increasing field strength, zero-photon, one-photon, two-photon and higher order resonances appear. In Fig. 7.5 we compare the numerical (upper panel) and the analytical results (middle and lower panels) for the quasienergy spectrum as a function of the wavevector k_x and for weak fields. In the middle panel we plot the F_0–approximation, which reproduces very well the gap at $k_x = 0$, but no other features induced by the ac field show up. The lower panel shows the results for the F_1–approximation, which, in addition to the F_0 result, nicely captures the one-photon resonance at $k_c \approx \pm 0.5$.

As for the linearly polarized field, the analytical approximations can be tested by computing the

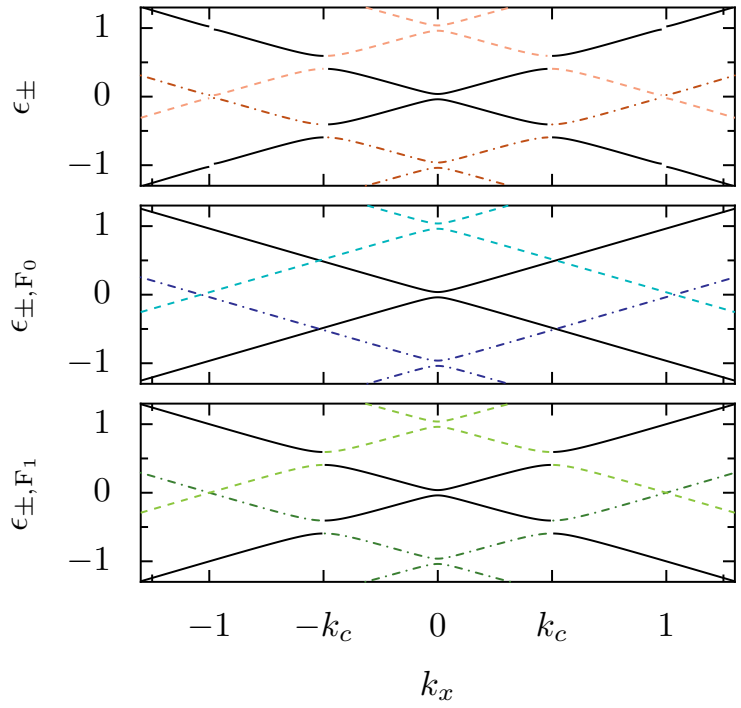

Figure 7.5.: **Quasienergy spectrum of graphene irradiated by a circularly polarized electric field.** The quasienergies are plotted as a function of k_x for $k_y = 0$. The solid lines represent the $l = 0$ band, the dashed lines the $l = 1$, and the dashdotted lines the $l = -1$ sideband. *Upper panel*: The full numerical result of the quasienergies. *Middle panel*: The quasienergies for the zero-photon approximation F_0. *Lower panel*: The quasienergies for the one-photon approximation F_1. Parameters: $k_y = 0$, $A = 0.2$, $\Omega = 1$.

density of states,

$$D(\omega) = 4 \sum_{\mathbf{k},\sigma} \delta(\omega - \epsilon_{\mathbf{k},\sigma,0}). \tag{7.61}$$

In the F_0–approximation the quasienergies are $\epsilon_{\mathbf{k},\sigma,l=0} = \epsilon^{\pm}_{0,F_0}$, see Eq. (7.46), and we obtain the density of states in the F_0–approximation

$$D_{F_0}(\omega) = \frac{2}{\pi F_0^2} |\omega| \Theta \left(|\omega| - \frac{\Delta}{2} \right). \tag{7.62}$$

Notice the presence of the gap at zero energy in the density of states. The simplicity of this zero-photon approximation allows for analytical computations of many physical quantities, something that no longer happens in general in the one-photon approximation, for which we have to resort to numerical calculations in most of the cases. The results for the generalized density of states in both the F_0– and F_1–approximation are plotted in Fig. 7.6 (upper panel), using the analytical quasienergies from Eqs. (7.52) and (7.53). As a comparison, the lower panel of Fig. 7.6 shows the density of states calculated numerically by diagonalizing the full Floquet Hamiltonian (7.13). Once again, notice that the F_0–approximation works very well for energies of the order of the zero-photon gap, whereas in order to study the one-photon resonance the F_1–approximation excels quite well. Higher resonances

– visible in the numerical result for the density of states at around $\omega \approx 1$, are almost negligible for the field strength we are considering here.

The developed approximations are useful in order to obtain analytical results when this is possible or at least simplify the numerical complexity of the problem, as it happens when we use the one-photon approximations. In principle, these approximations are valid for arbitrary $\mathbf{k}$, as long as $A/\Omega \ll 1$. The results for the density of states show that in both the analytical approximations and the full numerical case the gaps remain stable independently of the range of integration in the momentum included in the density of states, i.e., the inclusion of higher momentum states does not close the gaps in our case, contrary to what was found in ref. [226].

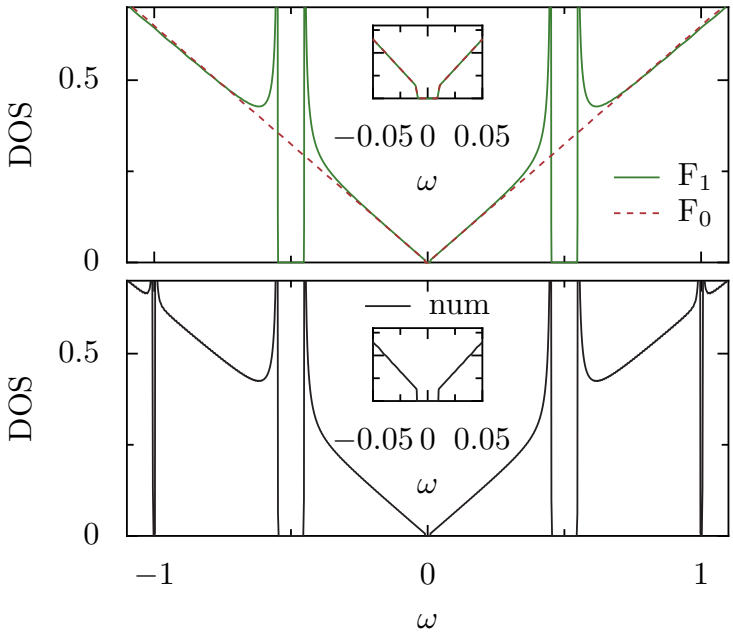

Figure 7.6.: **Generalized density of states of graphene irradiated by a circularly polarized ac electric field.** *Upper panel:* DOS for the analytical approximations F_0 and F_1. *Lower panel:* DOS considering the full Floquet Hamiltonian Eq. (7.13). The F_0–approximation reproduces the gap given by Δ, see text. For the one-photon resonance in the F_1–approximation the gap at $\omega = 0.5$, where the field couples modes with n and $n+1$ photons, is reproduced. For the same field strength as considered in the F_0– and F_1–approximations the full numerical density of states is identical up to an additional very small gap at $\omega \approx 1$, which is due to two-photon processes. In the inset, the region around the gap $\omega = 0$ is blown up for better visibility. Parameters: $A = 0.1$, $\Omega = 1$.

7.2. Single and many-particle excitations in graphene in a circularly polarized ac electric field

7.2.1. Electron interactions and the formula for the dynamical polarizability

So far we have analyzed the single particle properties of the Hamiltonian. However, a full description of electron excitations in graphene requires to understand the role of electron-electron interactions in the system. The Hamiltonian of the interacting system in the presence of an ac field reads now, in second quantization,

$$H(t) = v_{\mathrm{F}} \sum_{\mathbf{k}} \Psi^{\dagger}_{\mathbf{k}} \boldsymbol{\sigma} \cdot (\mathbf{k} - e\mathbf{A}(t)) \Psi_{\mathbf{k}} + \sum_{\mathbf{q}} v_{\mathbf{q}} n^{\dagger}_{\mathbf{q}} n_{\mathbf{q}}, \tag{7.63}$$

where $v_{\mathbf{q}} = 2\pi e^2/\epsilon_0 q$ is the 2D unscreened Coulomb interaction in vacuum. We have already introduced this Hamiltonian in Sect. 6.3. As has been discussed there, for doped graphene, the Coulomb interaction becomes screened, yielding a system whose low-energy excitations around the Fermi surface are barely interacting, i.e., electrons in graphene behave as a Fermi liquid. Moreover, there exists a collective excitation, a plasmon [205, 207]. This is no longer true when the level of doping is zero or very small, where the role of interactions is controversial due to the singular nature of the Dirac point and screening is uneffective [185, 186]. In order to understand the effect of interactions between electrons when an external ac field is applied, we will compute the dynamical polarizability, which tells us about the response of the system to probes that couple to the electric charge. This function will yield information about the full spectrum of electron interactions of the system that contains both single particle and collective excitations. The dynamical polarizability of graphene in the presence of an ac electric field shows particular features that differ from its counterpart, the 2DEG, as well as from the one derived for graphene in the absence of the field [206], see also Sect. 6.3.2. The detailed derivation of the polarizability function is set out in the Appendix B.3, whereas here we only present the final result:

$$\Pi(\mathbf{q},\omega) = \sum_{\sigma,\sigma'} \sum_{\mathbf{k}} \sum_{l} \frac{f_{\mathbf{k},\sigma} - f_{\mathbf{k}+\mathbf{q},\sigma'}}{\omega - \epsilon_{\mathbf{k}+\mathbf{q},\sigma',l} + \epsilon_{\mathbf{k},\sigma,0} + i\eta} \sum_{n} |\phi^{n,a,*}_{\mathbf{k}+\mathbf{q},\sigma',l} \phi^{n,a}_{\mathbf{k},\sigma,0} + \phi^{n,b,*}_{\mathbf{k}+\mathbf{q},\sigma',l} \phi^{n,b}_{\mathbf{k},\sigma,0}|^2 \tag{7.64}$$

The index n stands for the Fourier component of a solution in the sideband l of the infinite Floquet Hamiltonian. The summation over n constitutes the scalar product of the solution $|\phi_{\mathbf{k}+\mathbf{q},\sigma',l}\rangle$ with $|\phi_{\mathbf{k},\sigma,0}\rangle$, where we have made use of the fact that solutions belonging to the lth Brillouin zone in the Floquet spectrum are those of the first Brillouin zone shifted by l units, see Eqs. (7.7) and (7.9). The solution $l = 0$ is the one which fulfills the condition that at $A \to 0$, $\Pi(\mathbf{q},\omega)$ becomes the polarizability for an isolated graphene sheet. Mathematically, it is important to notice that the analytical properties of the dynamical polarizability do not change in the presence of the external ac field. It is a complex function, analytical in the upper half plane, whose real and imaginary parts are not independent, but related via the Kramers-Kronig relations, see e.g. ref. [237]. The latter can also be seen as a consequence of the causality in the response of the system to the external probe.

The polarizability is written in terms of the single particle excitations of the system, as in conventional linear response theory. In the presence of the ac electric field, there is an infinite set of single

particle excitations that differ between them in the relative number of photons. Once the external field is switched on, the system is no longer isolated, and the field can pump or extract energy into the system in the form of photons of frequency Ω. Therefore, the polarizability can be seen as a linear combination of polarizabilities, each describing excitations in which the number of photons in the system changes by a certain integer number l. Or in other words, the response of the system to an external probe of energy ω and momentum q can arise from excitations in which no extra photons are introduced into the system, as it happens in the absence of the field, or in which a given number l of photons is introduced into or extracted from it. Similar results as those shown here have been derived in the context of low-dimensional semiconductors [238] and the 2DEG [230]. The latter is usually the benchmark to compare the results derived for graphene, and therefore we include here the formula for the ease of comparison:

$$\Pi_{ac}^{\mathrm{2DEG}}(\mathbf{q},\omega) = \sum_{\mathbf{k}}\sum_{l} \frac{f_{\mathbf{k}} - f_{\mathbf{k}+\mathbf{q}}}{\omega - \epsilon_{\mathbf{k}+\mathbf{q},l} + \epsilon_{\mathbf{k},0} + i\eta} \tag{7.65}$$

Note in this expression that the effects due to the ac electric field appear in two different places: (i) in the index l of the sideband, reflecting a change in the number of photons, and (ii) as a modification of the single particle excitations in $\epsilon_{\mathbf{k},\sigma,l}$. The situation is more complicated in the case of graphene, Eq. (7.64), where also a momentum dependent overlap term between the excitations with different momentum must be included. This overlap is reflected in the polarizability via the scalar product between quasieigenstates, and it is in turn a consequence of the existence of the pseudospin in graphene. The effect of the electric field on the electronic system can be understood in terms of transfer of spectral weight, as we shall show in the next section. As the electric field is switched on, the spectral weight is reorganized, although in a way that still preserves the conservation rule imposed by the f-sum rule, which was derived and analyzed in the context of low-energy graphene by Sabio *et al.* [227]. As a last remark, since we are dealing with a system in which a polarized ac electric field is already present, one has to ask oneself about the possible influence of the polarization of the external probe to which the system responds. In fact, since we are analyzing the dynamical polarizability, which arises from the coupling between the electronic density and the potential induced by the external probe, the response of the system in the linear regime is insensitive to the polarization of the probe field. In order to see a response that depends on the polarization of the probe, we would have to analyze the response of the electronic current, which couples to the electric field, and whose linear response function is the conductivity. Notice, however, that the response function itself will not be altered due to this polarization, since in linear response it only depends on the properties of the system in the absence of the external probe by virtue of the fluctuation-dissipation theorem (cf. Sect. 6.3.1).

7.2.2. Analytic approximations for the dynamical polarizability

We now evaluate the dynamical polarizability (7.64) using the analytic approximations developed in Sect. 7.1.3. We first consider the imaginary part of (7.64). This yields the response of the non-interacting system to an external probe of energy ω and momentum q, and is a building block for the Random Phase Approximation (RPA). As we mentioned in the introductory chapter 6, RPA is known to work well for doped graphene [189], where Landau's theory of the Fermi liquid provides

a good description of the low energy excitations. In the case of undoped graphene, the issue is more complicated due to the lack of screening near the Dirac point [186]. In our case, due to the opening of a gap at $\mathbf{k} = 0$, we expect RPA to be sufficient to describe the main features of the response of the system once electron-electron interactions are taken into account.

F_0–approximation

In the F_0–approximation a gap opens up at zero momentum, so it can be used for a qualitative description of the response to an external ac probe. We set the temperature $T = 0$, and for the moment we will restrict ourselves to undoped graphene. In this case, the dynamical polarization involves only the term that accounts for transitions between the Floquet bands $(0,-)$ and $(0,+)$, i.e., transitions in which the number of photons is conserved,

$$\Pi_{F_0}(\mathbf{q},\omega) = \sum_{\mathbf{k}} \frac{|\langle \chi^{+}_{\mathbf{k}+\mathbf{q},0}|\chi^{-}_{\mathbf{k},0}\rangle|^2}{\omega - \epsilon^{+}_{\mathbf{k}+\mathbf{q},0} + \epsilon^{-}_{\mathbf{k},0} + i\eta}, \tag{7.66}$$

where $|\chi^{\pm}_{\mathbf{k},0}\rangle$ are the eigenvectors from the F_0–approximation, see Eq. (7.47). We find

$$\mathrm{Im}\,\Pi_{F_0}(\mathbf{q},\omega) = -\frac{1}{4}\frac{F_0^2 q^2}{\sqrt{\omega^2 - F_0^2 q^2}}\left(1 + \frac{\Delta^2}{\omega^2 - F_0^2 q^2}\right)\Theta\left(\omega^2 - F_0^2 q^2 - \Delta^2\right), \tag{7.67}$$

with $\Delta = \sqrt{4A^2 + \Omega^2} - \Omega$ being the gap opened at the first resonance. This is actually the dynamical polarizability for a “gapped graphene"; now the gap is due to the presence of the circularly polarized ac field. Gapped graphene has been studied extensively by Pyatkovskiy [239], who also derived analytical expressions for the real part of the polarization, for both doped and undoped graphene. We show the imaginary part of the polarizability in the F_0–approximation in Fig. 7.7. For a given momentum of the external probe, the energy threshold required to produce single particle excitations is increased due to the existence of the gap, which is now located at $\omega = \sqrt{F_0^2 q^2 + \Delta^2}$. This yields a rearrangement of the spectral weight of the excitations, which might allow for the existence of more complex excitations in the spectrum of the interacting system. We investigate this question within RPA. As shown in Sect. 6.3, the polarizability in the RPA is

$$\Pi_{\mathrm{RPA}}(\mathbf{q},\omega) = \frac{\Pi_0(\mathbf{q},\omega)}{1 - v_q \Pi_0(\mathbf{q},\omega)}, \tag{7.68}$$

where the denominator is the dielectric function in RPA with v_q being the 2D unscreened Coulomb potential. In order to have long-lived collective excitations, i.e. plasmons, the dielectric function must vanish at certain points $\omega_p(q)$, which leads to the conditions $v_q\,\mathrm{Re}\,\Pi_0(\mathbf{q},\omega) = 1$ and $\mathrm{Im}\,\Pi_0(\mathbf{q},\omega) = 0$. In Fig. 7.8 the imaginary and real part of the polarizability in the RPA are plotted, using $\Pi_0(\mathbf{q},\omega) = \Pi_{F_0}(\mathbf{q},\omega)$ (Eq. (7.66)) in Eq. (7.68). It can be seen that the divergence at the threshold of excitations found for the non-interacting polarizability has disappeared, a feature that is also observed in graphene in the absence of ac fields. However, the real part of the polarizability does not develop a resonance, and therefore no plasmons, at least within the RPA of the F_0–approximation. This is not surprising, since in gapped undoped graphene there are no electronic states at the Fermi level that

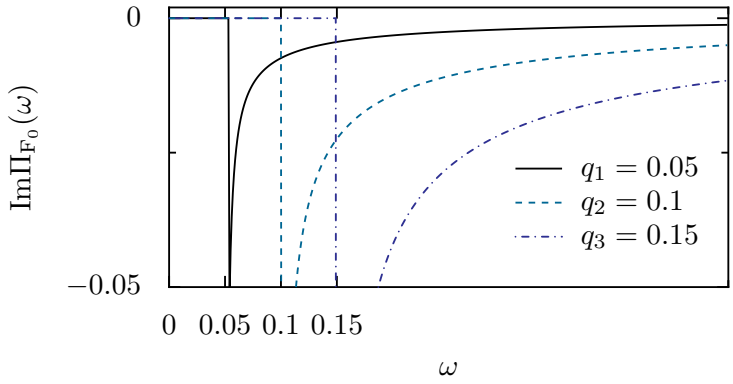

Figure 7.7.: **Imaginary part of the polarizability Π_{F_0} for irradiated graphene**. Imaginary part of the polarizability in the F_0–approximation as a function of ω and for different values of q, Eq. (7.67). For $\omega < \sqrt{F_0^2 q^2 + \Delta^2}$ no excitations are possible, as compared to free graphene, where no excitations are possible for $\omega < q$. Note that only for small $q = 0.05$ the effect of the gap is visible as a shift of the divergence away from $\omega = q$. Parameters: $A = 0.1$, $\Omega = 1$.

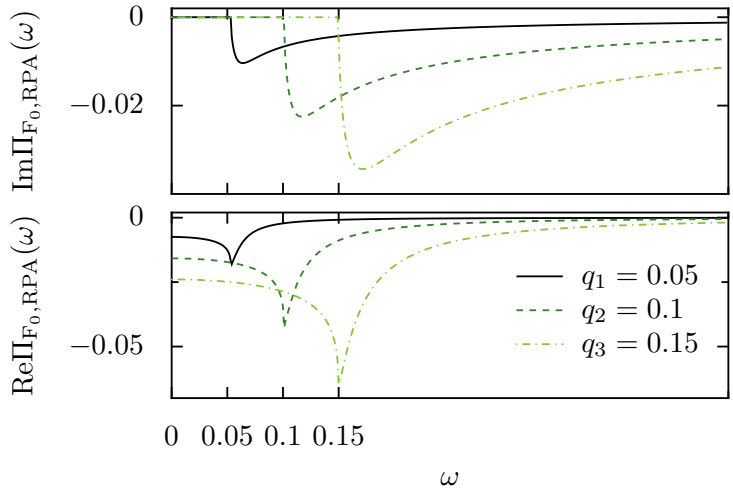

Figure 7.8.: **Imaginary part of the polarizability Π_{F_0} for irradiated graphene in the RPA**. Imaginary and real part of the polarizability in the F_0–approximation as a function of ω for different q in the RPA. The divergence in the imaginary part of the polarizability has disappeared, but the real part has not developed a resonance, which would be the signature of the existence of collective electronic excitations. Parameters: $A = 0.1$, $\Omega = 1$.

provide the support necessary for plasmons. In order to test if this is still true when higher order photon resonances are included, we analyze the F_1–approximation in the next section.

Before that, let us analyze the case of doped graphene. As already shown in Ref. [239] for the case of gapped graphene, the plasmon already present in the system without ac fields is still robust once a

weak field is introduced. The main effect of the external ac field is to modify the plasmon dispersion

$$\omega_p^{F_0}(q) = \sqrt{\frac{gN_sN_vF_0q\mu}{2}\left(1-\frac{\Delta^2}{4\mu^2}\right)}, \tag{7.69}$$

where $g = e^2/v_F\epsilon_0\hbar$ is the fine structure constant of graphene. The correction affects the plasmon frequency $\omega_0 = \sqrt{\frac{gN_sN_vF_0\mu}{2}(1-\frac{\Delta^2}{4\mu^2})}$, but not the dependence on momentum, which still follows the law $\omega_p^{F_0}(q) \propto \sqrt{q}$. The plasmon frequency is diminished due to the effect of the external ac field, since $F_0 < 1$ and $1-\Delta^2/(4\mu^2) < 1$. The correction coming from the factor F_0 is essentially due to the renormalization of the Fermi velocity due to the ac field. The second correction depends on the relation of the chemical potential to the gap at zero momentum, and it is maximal for a chemical potential below $\Delta/2$, where the plasmon is completely suppressed since no electrons are populating the upper Dirac cone. For chemical potentials above this value, the correction tends to be smaller, being almost negligible for $\mu \gg \Delta/2$. We point out that similar results hold in a quite different context, that of graphene anti-dot lattices [240, 241], where it has been found out that in the limit of low doping, gapped graphene models reproduce very well the plasmon dispersion of the anti-dot lattice.

In short, the results from the F_0–approximation yield a similar picture to that of graphene in the absence of an external field, and the main effect of the ac field is a renormalization of the single and many-particle spectrum, with a shift of the threshold for excitations, due to the gap at zero momentum.

F_1–approximation

The F_1–approximation accounts for non-zero-photon processes neglected in the F_0–approximation. It is not fully analytically tractable in the calculation of many observables. In the F_1–approximation using Eqs. (7.52)-(7.55) the polarizability for undoped graphene at $T = 0$ becomes

$$\begin{aligned}\Pi_{F_1}(\mathbf{q},\omega) = &\sum_{\mathbf{k}} \frac{|\langle\xi^+_{\mathbf{k}+\mathbf{q},0}|\xi^-_{\mathbf{k},0}\rangle|^2}{\omega-\epsilon^+_{\mathbf{k}+\mathbf{q},0}+\epsilon^-_{\mathbf{k},0}+i\eta}+\\ &+|\langle\xi^+_{\mathbf{k}+\mathbf{q},-1}|\xi^-_{\mathbf{k},0}\rangle|^2\left(\frac{1}{\omega-\epsilon^+_{\mathbf{k}+\mathbf{q},-1}+\epsilon^-_{\mathbf{k},0}+i\eta}-\frac{1}{\omega-\epsilon^-_{\mathbf{k}+\mathbf{q},1}+\epsilon^+_{\mathbf{k},0}+i\eta}\right)\\ &+|\langle\xi^+_{\mathbf{k}+\mathbf{q},-2}|\xi^-_{\mathbf{k},0}\rangle|^2\left(\frac{1}{\omega-\epsilon^+_{\mathbf{k}+\mathbf{q},-2}+\epsilon^-_{\mathbf{k},0}+i\eta}-\frac{1}{\omega-\epsilon^-_{\mathbf{k}+\mathbf{q},2}+\epsilon^+_{\mathbf{k},0}+i\eta}\right).\end{aligned} \tag{7.70}$$

Here, there are three different contributions to the polarizability, which come from the Floquet bands $l = 0$, $l = \pm1$ and $l = \pm2$, i.e., from excitations that involve the exchange of up to two photons from the external field. However, for the electric fields in which this approximation holds, the contribution from the $l = \pm2$ components is essentially negligible, and therefore only zero- and one-photon processes will be considered. In the following we evaluate (7.70) numerically, first integrating the imaginary part and then computing the real part via the Kramers Kronig relations.

Figure 7.9 shows the imaginary part of the polarizability Π_{F_1} for fixed q as a function of ω. In the upper panel, the components $l = 0$ and $l = \pm1$ and their sum are shown for $q = 0.1$, in order

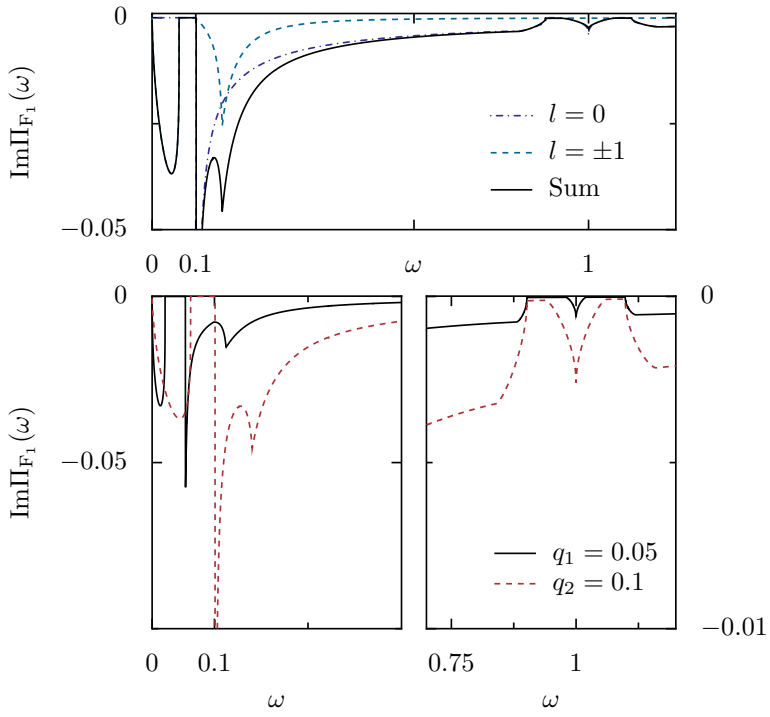

Figure 7.9.: **Imaginary part of the polarizability** Π_{F_1}. *Upper panel*: $q = 0.1$; the components $l = 0, \pm 1$ of the polarizability and their sum are shown, see Eq. (7.70). *Lower panels*: Imaginary part of the total polarizability as a function of ω for two different q, $q_1 = 0.05$, $q_2 = 0.1$. Left plot for $\omega < 0.4$, right plot for $\omega > 0.7$. Parameters: $A = 0.1$, $\Omega = 1$.

to illustrate where its structure comes from. The two lower panels represent the total polarizability for two different wavevectors q, divided into two regions for better visibility of the different features. Several new features emerge from the F_1–approximation. As shown in Fig. 7.9, at the level of zero-photon processes, there is a gap at zero momentum already captured in the F_0–approximation. In addition, gaps appear at higher momenta, where the first anticrossing of Floquet sidebands occurs (see Fig. 7.5). For a sufficiently small q this second gap translates into two small gaps in the single particle excitation spectrum around $\omega \approx 1$, which are eventually closed for higher momenta, as shown in Fig. 7.9 (lower panel, right plot). The first of those gaps, for $0.9 < \omega < 1$, comes from the fact that for electrons from the lower cone of graphene no states are available in the upper band for the corresponding values of q and ω, due to the anticrossing of Floquet sidebands. The second one, at $1 < \omega < 1.1$, is due to the lack of states in the lower cone in the region where this anticrossing occurs with lower Floquet sidebands. The most important new features of the response of the system, however, come from the contribution of one-photon processes, in which transitions from the $l = 0$ to the $l = \pm 1$ sidebands are taken into account. New single particle excitations appear below $\omega = \sqrt{F_0^2 q^2 + \Delta^2}$, leaving only a small region of energies where no excitations are found, a region which, again, closes for sufficiently large q (dashed line for $q = 0.1$).

One-photon processes introduce new single particle excitations into the response of the system, and we next examine the effect of these processes on the collective excitations of the system. The

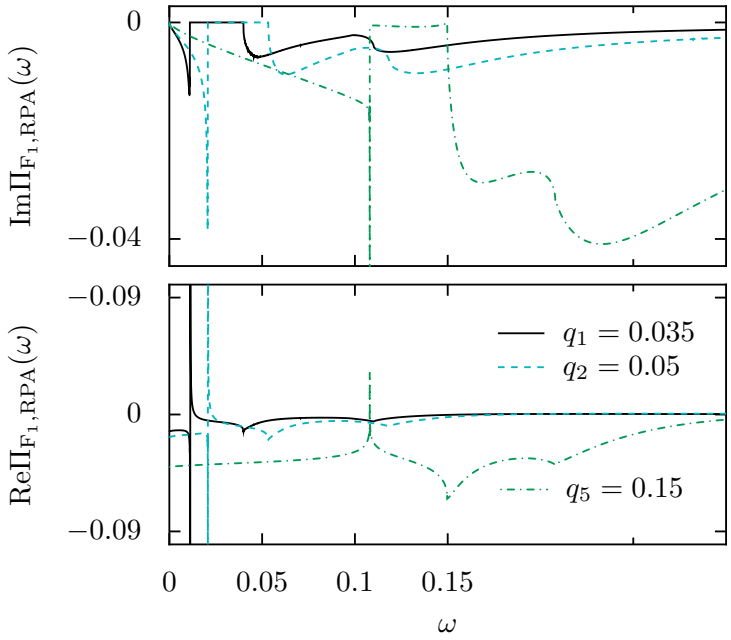

Figure 7.10.: **Imaginary and real part of the polarizability Π_{F_1} in the RPA**. Notice the resonance in the real part for small momenta $q_1 = 0.035$ and $q_2 = 0.05$ (lower panel), where no excitations exist in the imaginary part (upper panel), which points to the existence of collective excitations. Parameters: $A = 0.1$, $\Omega = 1$.

RPA polarizability $\Pi_{F_1,\mathrm{RPA}}$ is shown in Fig. 7.10 for different values of the external momentum q. One-photon processes have an important effect on the response of the interacting system, as they make the existence of collective excitations possible for small enough momentum, see curves for $q_1 = 0.035$, $q_2 = 0.05$ in Fig. 7.10. For these momenta, the plasmon conditions are fulfilled, which is reflected in the development of a resonance in the real part of the RPA polarizability. The important difference here compared to *undoped undriven* graphene is that the driving field induces single-particle excitations at low energy for finite momentum via one-photon absorption or emission processes (see the peak at low ω in the excitation spectrum in the imaginary part of $\Pi_{F_1,\mathrm{RPA}}(\omega)$ in Fig. 7.10). These excitations are necessary in order for an undamped plasmon to exist, as it is also the case for *undriven doped* graphene, see Sect. 6.3. For an external momentum of $q = 0.05$, e.g., the resonance is located at $\omega \simeq 0.021$, which is already in the region where the imaginary part of the polarizability is zero, making the existence of an undamped plasmon possible. It is important to mention that this plasmon becomes unstable in two different scenarios. (i) For large enough momentum of the external probe, where the resonance is weakened and occurs in a region where single particle excitations exist, so that the plasmon can decay into those excitations, see $q_3 = 0.15$ in Fig. 7.10. (ii) When two-photon processes are considered, there is no longer a region where the imaginary part of the polarizability is zero. For weak fields, however, these processes are negligible and their effect on the plasmon should also essentially be irrelevant. However, this suggests that as we increase the intensity of the electric field and higher order photon processes are important, there is no region of momenta q in which the plasmon is stable.

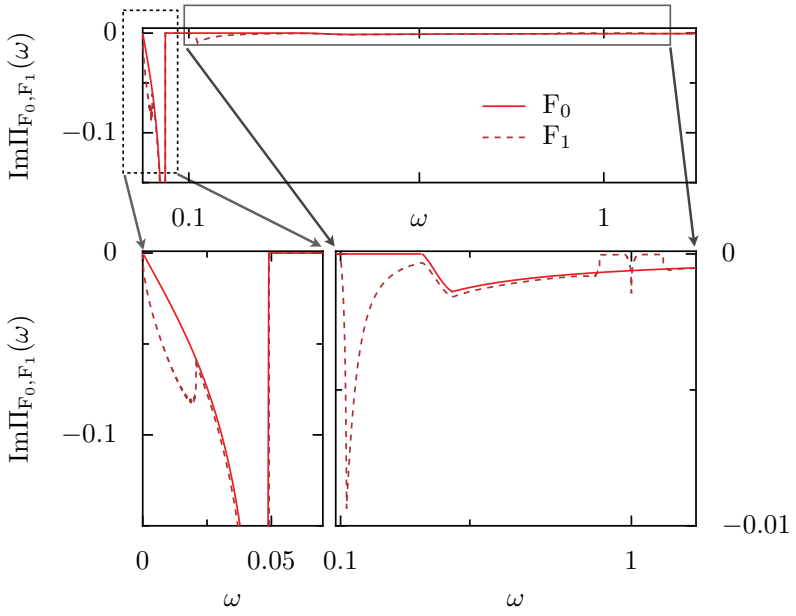

Figure 7.11.: **Imaginary part of the polarizability for doped graphene.** Both the F_0– (solid red) and the F_1–approximation (dashed dark red) are shown as a function of ω for $q = 0.05$. In the lower panels, the upper plot is split in two parts in order to better visualize the different regions of ω. Parameters: $A = 0.1$, $\Omega = 1$, $\mu = 0.2$.

For doped graphene, the F_1–approximation introduces features similar to those described for undoped graphene, see Fig. 7.11. The effect of the anticrossing of Floquet sidebands is to induce gaps in the response of the system for $\omega \sim 1$, and processes including the exchange of one-photon give rise to new excitations for small energies. In order to quantify the effect of these processes, in this figure the polarizability is compared to the one for doped graphene using the F_0–approximation, where only zero-photon processes are considered. The RPA response of the interacting system is shown for a couple of representative external momenta in Fig. 7.12. As it happened in the undoped case, for small external momentum ($q = 0.05$ in Fig. 7.12) there is a resonance in the real part, signaling the existence of a plasmon, which again has a renormalized dispersion relation due to the effect of the external ac field. However, non-zero-photon processes are again responsible for the appearance of low-energy excitations that tend to make the plasmon unstable for large enough momenta q ($q = 0.15$ in Fig. 7.12) and for larger intensities of the field, as discussed for the undoped case. These momenta q for which plasmons become unstable are still lower than those for which the plasmon is damped in graphene without ac field.

Summarizing, the inclusion of non-zero-photon processes is crucial in order to capture the physics of the response of graphene to an external probe in the presence of a weak ac field. This is due to the appearance of excitations in the low-energy spectrum of the system not included in the F_0–approximation, which allow for the existence of collective excitations in undoped graphene, but make those plasmons unstable for smaller momenta than their counterparts in graphene with no ac fields.

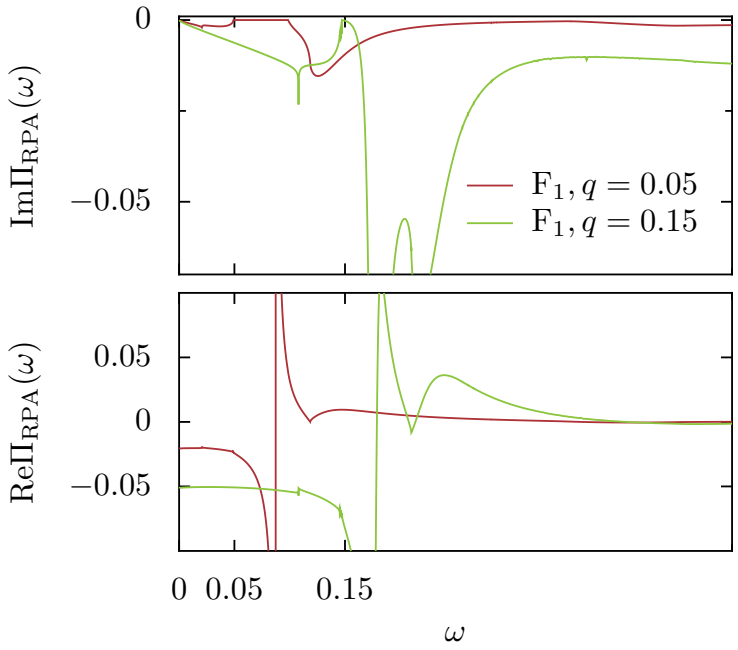

Figure 7.12.: **Polarizability in the RPA for doped graphene in the F_0, F_1–approximation**. *Upper panel*: Imaginary part. *Lower panel*: Real part. The results are shown for two different momenta $q = 0.05$ and $q = 0.15$. In both figures the results are compared with the F_0–approximation. Notice, in both approximations, the existence of the resonance in the real part of the polarizability, signalizing the existence of a collective excitation. For large momentum $q = 0.15$, however, the imaginary part shows no gap and therefore the plasmon can decay into single particle excitations. Parameters: $A = 0.1$, $\Omega = 1$, $\mu = 0.2$.

7.3. Conclusions

In this chapter we have analyzed the properties of graphene under an external ac field in the weak field regime. Both for the case of a linearly and circularly polarized field, we have developed analytical approximations to the Hamiltonian, – the so-called J_0– and J_1–approximations for linearly polarized field (Sect. 7.1.2), and F_0– and F_1–approximations for circularly polarized field (Sect. 7.1.3) –, which allow for a certain analytical tractability of many relevant objects. The J_0– and F_0–approximations include only zero-photon excitations in the system and are useful to calculate certain observables in the low-energy sector. The J_1– and F_1–approximations include higher-order photon processes, thereby making possible the analysis of a wider range of observables and a larger energy sector. However, in many cases they require numerical calculations to extract the observables.

Special emphasis has been put on the calculation of the dynamical polarizability of graphene irradiated by a circularly polarized field, which can be used to analyze the spectra of single and many-particle excitations of the system. We have derived a general expression for the polarizability of graphene in the presence of a circularly polarized ac electric field, which we have afterwards analyzed in the context of the F_0– and F_1–approximations. While the former allows for analytical expressions and captures well the effect of the zero-momentum gap in the system, it misses the non-

zero-photon processes that are captured by the F_1–approximation, and in turn are responsible for the emergence of collective excitations even for undoped graphene, as long as the Random Phase Approximation remains valid. However, it also points out that these collective excitations are less stable when compared to graphene with no external ac field: for large enough external momenta and ac field intensities, these excitations become damped and acquire a finite lifetime.

We have shown that both linearly and circularly polarized ac fields can be used to modify the properties of graphene in several ways: (i) They open up gaps at zero momentum (for circularly polarized field) and finite momenta (for both polarizations) that can be exploited in practical applications. (ii) Circularly polarized ac fields permit the existence of plasmons (in both undoped and doped graphene), (iii) The plasmon frequency is tunable with the external field, and, finally, (iv) For large enough fields the plasmons become unstable. Moreover, we have developed and tested analytical tools to analyze theoretically the behavior of graphene in the presence of ac electric fields, which should be useful in future works in this field.

A. Appendix: Bipolar spin blockade in triple quantum dots

A.1. Conversion parameters and slope of the resonance lines

As has been said in chapter 5, the energy levels ϵ_i of the dots $i = 1, 2, 3$ are written as linear functions of the three gate voltages,

$$\begin{aligned}\epsilon_1 &= \mathcal{C}_1 - \alpha_1 V_\mathrm{L} - \beta_1 V_\mathrm{R} \\ \epsilon_2 &= \mathcal{C}_2 - \beta_{12} V_\mathrm{L} - \beta_{23} V_\mathrm{R} \\ \epsilon_3 &= \mathcal{C}_3 - \beta_3 V_\mathrm{L} - \alpha_3 V_\mathrm{R},\end{aligned} \tag{A.1}$$

where $\mathcal{C}_{1,2,3}$ are constants that provide an overall energy shift. The conversion parameters are given in eV/V.

The stability diagram and the current depend very sensitively on the values of the conversion parameters $\alpha_{1,3}$, $\beta_{1,3}$, and $\beta_{12,23}$. The measurement of the stability diagram of a quantum dot or an array of quantum dots is a fundamental way of determining its filling scheme and serves e.g. to find the electrostatical parameters of the device. In particular, the slopes of resonance lines appearing in the stability diagram indicate unambiguously along which line either the left and center dots (LC), the center and right dots (CR) or the left and right dots (LR) are on resonance. For the theoretical calculation it is therefore of crucial importance to know the conversion factors by which the slopes of the resonance lines become equal to the ones obtained experimentally. In the following, we restrict our discussion to the basis states participating in the positive bias direction. The LC resonance line occurs when the tunneling from a state $|2,0,2\rangle$ to a state $|1,1,2\rangle$ (or from $|2,0,2^*\rangle$ to $|1,1,2^*\rangle$) is resonant. Analogously, for the CR line one must have resonant tunneling from $|2,1,1\rangle$ to $|2,0,2\rangle$ (or $|2,1,1\rangle$ or $|2,1,1^*\rangle$ to $|2,0,2^*\rangle$). Again the same must be true for the LR resonance line which occurs for resonance between $|2,1,1\rangle$ and $|1,1,2\rangle$. One can easily write down the equations for each of the the resonance lines; as an example we show here the equation for the LR resonance line (for non-excited levels in the right dot in positive bias direction). For zero magnetic field we have

$$\epsilon_1 + \epsilon_2 + 2\epsilon_3 + U_3 + 3V + 2V_{13} = 2\epsilon_1 + U_1 + \epsilon_2 + \epsilon_3 + 3V + 2V_{13}, \tag{A.2}$$

which yields, after inserting equations (A.1) and solving for V_R,

$$V_\mathrm{R} = \frac{U_3 - U_1 + \mathcal{C}_3 - \mathcal{C}_1}{\alpha_3 - \beta_1} + \frac{\alpha_1 - \beta_3}{\alpha_3 - \beta_1} V_\mathrm{L}. \tag{A.3}$$

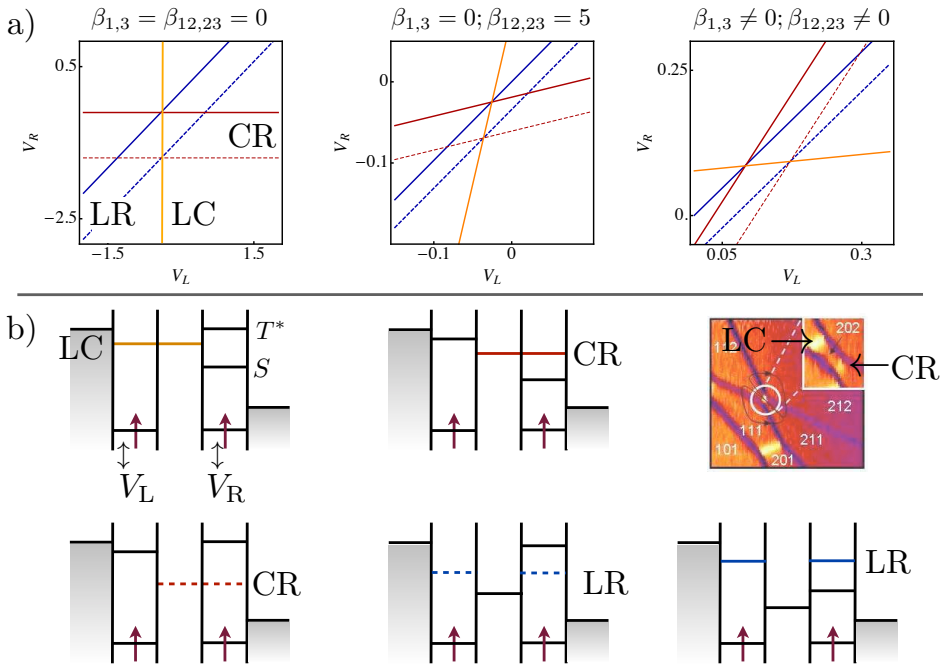

Figure A.1.: **Resonance lines in a linear TQD for the $\{V_L, V_R\}$ parameter space. a)** Calculated resonance lines (see as an example Eq. (A.3)) for three different sets of the conversion parameters $\alpha_{1,3}$, $\beta_{1,3}$, $\beta_{12,23}$. In the left panel, $\beta_{1,3,12,23} = 0$, so that the voltages do not affect any neighboring dot. Middle panel: $\beta_{1,3} = 0$, $\beta_{12,23} = 5$ (meV/V). Both LC and CR lines are tilted, but the slope of the LC line is much bigger than the slope of the CR line. Right panel: $\alpha_1 = 25.6$, $\alpha_3 = 26.4$, $\beta_1 = 13.2$, $\beta_3 = 13.2$, $\beta_{12} = 25.11$, $\beta_{23} = 18.4$. Now the CR lines are steeper than the LC line, see also the experimental stability diagram just below, where the LC and CR lines are indicated by arrows. **b)** Energy level configurations for the different resonance lines. The stability diagram is taken from ref. [113].

The LR resonance line is thus written as a function $V_R(V_L)$ whose slope only depends on the conversion factors, i.e. on the extent to which the voltages affect the energy levels of the dots. It is very helpful for the understanding of the transport triangles to see how much a change in the conversion factors can affect the slope of the resonance lines. We show therefore in Fig. A.1 *resonance line* plots in the $\{V_L, V_R\}$ parameter space for three different sets of the parameters $\alpha_{1,3}$, $\beta_{1,3}$ and $\beta_{12,23}$.

If the voltages applied to the left and right dot did not affect any of their respective neighboring dots, the LC resonance line would be *vertical* (orange solid line), the CR line *horizontal* (red solid and dashed lines), and the LR line perfectly *diagonal* (blue solid and dashed lines), see Fig. A.1 a) (left panel). There are two points where three of the lines cross, namely the red, blue and orange solid lines, and the red dashed, blue dashed and orange solid lines. At the latter crossing, all three dots are on resonance, so that in the right dot the singlet level is aligned with the single level in the center dot and the singlet level in the left dot, and at the former crossing, the excited triplet level is aligned with the single level in the center dot and the singlet level in the left dot. We will henceforth refer

to the LR singlet and the LR triplet, as well as to the CR triplet and CR singlet line. In Fig. A.1 a) (middle panel), we plot the resonance lines for the parameters $\alpha_1 = 25.6$, $\alpha_3 = 26.4$, $\beta_1 = 0$, $\beta_3 = 0$, $\beta_{12,23} = 5$, all in meV/V. The former vertical LC line is now tilted, as are also the former horizontal CR lines, and the LR lines are basically the same. Note that the slope of the CR lines is smaller than the slope of the LC line. This is contrary to what was measured in the experiment, where the CR slope is much steeper than the LC slope (see stability diagram in b). With a bit of playing around with the conversion parameters we have found a set of parameters that reproduces quite well the different slopes. This is shown in Fig. A.1 a) (right panel). See also the current plots in Figs. 5.2, 5.3.

A.2. Eigenvalues at the singlet LR resonance

As has been said, the LR singlet resonance line, where an enhanced current flows through the TQD for zero external magnetic field, goes along with a drop of occupation of the state $|S,0,S\rangle$. In order to understand this transport feature, we analyze the eigenstates of the closed system. We consider the states that contribute to transport: $|S,\sigma,\sigma'\rangle$, $|S,0,S\rangle$, $|\sigma',\sigma,S\rangle$. Let us define the states (without normalizing them):

$$\begin{aligned}
|S_{\mathrm{LC}},S\rangle &= |\uparrow,\downarrow,\uparrow\downarrow\rangle - |\downarrow,\uparrow,\uparrow\downarrow\rangle \\
|S,S_{\mathrm{CR}}\rangle &= |\uparrow\downarrow,\uparrow,\downarrow\rangle - |\uparrow\downarrow,\downarrow,\uparrow\rangle \\
|S,0,S\rangle &= |\uparrow\downarrow,0,\uparrow\downarrow\rangle \\
|T^0_{\mathrm{LC}},S\rangle &= |\uparrow,\downarrow,\uparrow\downarrow\rangle + |\downarrow,\uparrow,\uparrow\downarrow\rangle \\
|T^+_{\mathrm{LC}},S\rangle &= |\uparrow,\uparrow,\uparrow\downarrow\rangle \\
|T^-_{\mathrm{LC}},S\rangle &= |\downarrow,\downarrow,\uparrow\downarrow\rangle \\
|S,T^0_{\mathrm{CR}}\rangle &= |\uparrow\downarrow,\uparrow,\downarrow\rangle + |\uparrow\downarrow,\downarrow,\uparrow\rangle \\
|S,T^+_{\mathrm{CR}}\rangle &= |\uparrow\downarrow,\uparrow,\uparrow\rangle \\
|S,T^-_{\mathrm{CR}}\rangle &= |\uparrow\downarrow,\downarrow,\downarrow\rangle
\end{aligned}$$

The notation S_{ij}, T^{α}_{ij} refers to singlet and triplet superpositions formed by electrons in different quantum dots, respectively. We set ε as the left-right detuning, with the central dot's level being off-resonant with both left and right dots. For simplicity, let us first neglect the contribution of the Overhauser field (i.e. effectively different Zeeman splittings in each dot), which will be considered later in a perturbative way. The eigenstates are then $|T^{\alpha}_{\mathrm{LC}},S\rangle$, $|S,T^{\alpha}_{\mathrm{CR}}\rangle$ and three linear combinations of the three singlets that we denote as $|\Sigma_l\rangle$. All $|\Sigma_l\rangle$ contain a contribution of $|S,0,S\rangle$ which depends on the detuning and the interdot hopping:

$$|\Sigma_1\rangle = \gamma_1|S,S_{\mathrm{CR}}\rangle + \eta_1|S_{\mathrm{LC}},S\rangle + \delta_1|S,0,S\rangle \tag{A.4}$$

$$|\Sigma_2\rangle = \gamma_2|S,S_{\mathrm{CR}}\rangle - \eta_2|S_{\mathrm{LC}},S\rangle + \delta_2|S,0,S\rangle \tag{A.5}$$

$$|\Sigma_3\rangle = \gamma_3|S,S_{\mathrm{CR}}\rangle + \eta_3|S_{\mathrm{LC}},S\rangle + \delta_3|S,0,S\rangle \tag{A.6}$$

Note that spin blockade avoids the overlap of states $|T^{\alpha}_{\mathrm{LC}},S\rangle$, $|S,T^{\alpha}_{\mathrm{CR}}\rangle$. Of special importance is $|\Sigma_2\rangle$ for two reasons: at the LR resonance condition

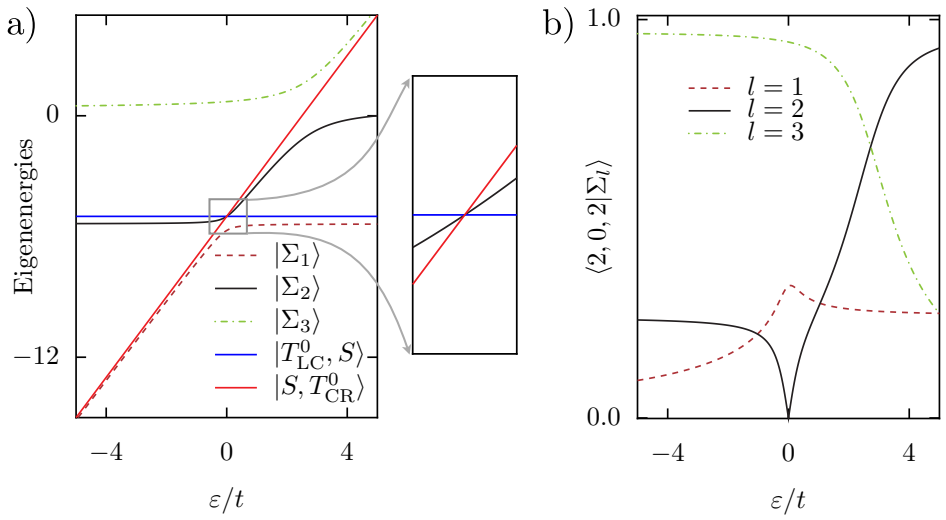

Figure A.2.: **Eigenvalues around the singlet LR resonance for zero Zeeman splittings. a)** Eigenenergies of the closed system as a function of ε (left-right detuning). The eigenenergy of the additional triplet states would coincide with those of $|T^0_{\mathrm{LC}}, S\rangle$ (blue) and $|S, T^0_{\mathrm{CR}}\rangle$ (orange), as defined in the text. The eigenstate $|\Sigma_2\rangle$ (black, Eq. (A.5)) crosses the triplet states $|T^0_{\mathrm{LC}}, S\rangle$ (blue) and $|S, T^0_{\mathrm{CR}}\rangle$ (red), see zoomed region. **b)** The contribution of the state $|S, 0, S\rangle$ to the eigenstates $|\Sigma_l\rangle$ is plotted. The state $|\Sigma_2\rangle$ (black) that crosses the triplet subspace at zero left-right detuning ($\varepsilon = 0$) only contains contributions of states $|2, 1, 1\rangle$ and $|1, 1, 2\rangle$ at that point.

(*i*) it crosses the triplet states (cf. left panel in Fig. A.2),

(*ii*) the contribution of $|S, 0, S\rangle$ to the superposition $|\Sigma_2\rangle$, δ_2, vanishes at this resonance, cf. Fig. A.2 b).

For finite nuclear magnetic field the effective Zeeman splittings in the TQD, Δ_i, will in general be slightly different. In this case singlet and triplet subspaces mix, with the exception of those with parallel spins, $|T^{\pm}_{\mathrm{LC}}, S\rangle$ and $|S, T^{\pm}_{\mathrm{CR}}\rangle$. As a consequence the eigenstates change. In comparison to the homogeneous case we now obtain anticrossings instead of crossings in the energy spectrum around the resonance condition, see Fig. A.3 b). At these anticrossings the former state $|\Sigma_2\rangle$ and the triplet states $|T^0_{\mathrm{LC}}, S\rangle$ and $|S, T^0_{\mathrm{CR}}\rangle$ mix strongly and are not eigenstates of the Hamiltonian any more. For our discussion the most important fact is that, up to leading order in a perturbative expansion, the superposition $|\Sigma_2\rangle$, that is responsible for the spin blockade removal, does not mix with $|S, 0, S\rangle$. It reads now

$$|\Sigma_2'\rangle = |\Sigma_2\rangle + (\Delta_1 - \Delta_2)|S, T^0_{\mathrm{CR}}\rangle + (\Delta_2 - \Delta_3)|T^0_{\mathrm{LC}}, S\rangle + \mathcal{O}(B^2_{\mathrm{nucl}}). \tag{A.7}$$

Close to resonance, this state crosses the states $|S, T^{\pm}_{\mathrm{CR}}\rangle$, which are responsible of spin blockade, as shown in Fig. A.3 in the zoomed region.

Our analysis suggests therefore that the *lifting* of spin blockade occurs via the spin–flip decay of the blocking states, $|S, T^{\pm}_{\mathrm{CR}}\rangle$, into $|\Sigma_2\rangle$. The latter has a finite tunneling rate to the drain contact, thereby opening the system to transport: current will flow from the source to the drain contact until spin

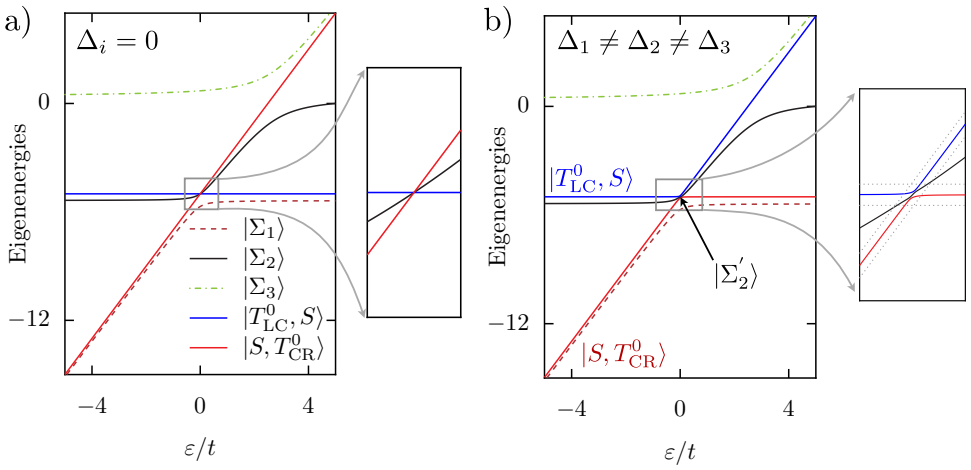

Figure A.3.: **Eigenvalues around the singlet LR resonance for zero and inhomogeneous Zeeman splittings. a)** Eigenenergies of the closed system for zero Zeeman splittings, as also plotted in Fig. A.2. **b)** Eigenenergies of the closed system for Overhauser-induced inhomogeneous splittings. In the zoomed region on the right hand side one can see the anticrossing in the energies due to the nuclear-induced inhomogeneous splittings. At zero left-right detuning, the eigenstate $|\Sigma_2\rangle$ is modified to $|\Sigma_2'\rangle$, cf. Eq. (A.7), with a finite contribution of triplet states $|T^0_{\mathrm{LC}}, S\rangle$ and $|S, T^0_{\mathrm{CR}}\rangle$, but, as in the homogeneous case, the contribution of state $|S, 0, S\rangle$ is zero. The eigenenergies of states $|S, T^{\pm}_{\mathrm{CR}}\rangle$ and $|T^{\pm}_{\mathrm{LC}}, S\rangle$ are represented by the unmixed dotted gray lines.

blockade is restored again. Note that the blockade-lifting transition does not involve the occupation of the intermediate state, $|S, 0, S\rangle$. The sharp dip in $\langle S, 0, S|\Sigma_2\rangle$ (cf. Fig. A.2 b) is therefore consistent with the occupation of $|S, 0, S\rangle$ in the stationary solution of the transport configuration, cf. Fig. 5.4. There the minimum keeps finite due to the contribution of the other current channels in which $|S, 0, S\rangle$ participates.

B. Appendix: Electronic single and many particle properties of graphene irradiated by circularly polarized ac field

B.1. Properties of the Bessel functions of the first kind

For the sake of completeness, we shortly state the properties of the Bessel functions that were used in deriving the matrix elements of the Hamiltonian (7.21). Details can be found e.g. in ref. [242].

$$\begin{aligned}
\frac{2\nu}{z} I_\nu(z) &= I_{\nu-1}(z) - I_{\nu+1}(z) \\
I_\nu(-z) &= (-1)^\nu I_\nu(z) \\
I_{-\nu}(z) &= I_\nu(z), \nu \in \mathbb{Z} \\
I_{\nu'-\nu}(z_1+z_2) &= \sum_{k=-\infty}^{\infty} I_{k-\nu}(z_1) I_{k-\nu'}(z_2) \\
I_\nu(z)^* &= (-1)^\nu I_\nu(z)
\end{aligned} \tag{B.1}$$

B.2. Derivation of the matrix elements of the Hamiltonian Eq. (7.21)

The perturbative part of the Hamiltonian connects the two former disconnected chains abab and abab, so that at site n a and b are connected by $k_x \pm ik_y$. Since the difference between the two chains is the site index n for a(b), which is either odd or even, we can write the solutions $|m\rangle$ as a sum of odd and even sites $|2n\rangle$ and $|2n+1\rangle$:

$$\begin{aligned}
|\psi_l^a\rangle &= \sum_n I_{2n-l} |\phi^{2n,a}\rangle + I_{2n+1-l} |\phi^{2n+1,b}\rangle \\
|\psi_l^b\rangle &= \sum_n I_{2n-l} |\phi^{2n,b}\rangle + I_{2n+1-l} |\phi^{2n+1,a}\rangle
\end{aligned}$$

In the same way, we separate the Hamiltonian $H^{\mathbf{k}}_{\mathrm{F,lin}}$ in a sum of odd and even states:

$$H^{\mathbf{k}}_{\mathrm{F,lin}} = \sum_n (k_x + ik_y) \left(|\phi^{2n,a}\rangle\langle\phi^{2n,b}| + |\phi^{2n+1,a}\rangle\langle\phi^{2n+1,b}| \right) + h.c. \tag{B.2}$$

We get for the matrix element

$$\begin{aligned}\langle\psi^b_{l'}|H^{\mathbf{k}}_{\mathrm{F,lin}}|\psi^a_l\rangle &= \sum_n (-1)^{2n-l'} I_{2n-l} I_{2n-l'}(k_x - ik_y) \\ &+ \sum_n (-1)^{2n+1-l'} I_{2n+1-l} I_{2n+1-l'}(k_x + ik_y) \\ &= k_x \left[\sum_n (-1)^{2n-l'} I_{2n-l} I_{2n-l'} + (-1)^{2n+1-l'} I_{2n+1-l} I_{2n+1-l'}\right] \\ &- ik_y \left[\sum_n (-1)^{2n-l'} I_{2n-l} I_{2n-l'} - (-1)^{2n+1-l'} I_{2n+1-l} I_{2n+1-l'}\right]. \end{aligned} \tag{B.3}$$

We distinguish now between the two cases l' =even/odd, and make successive use of Eq.(B.1):

1. l' even:

$$\begin{aligned}\langle\psi^b_{l'}|H^{\mathbf{k}}_{\mathrm{F,lin}}|\psi^a_l\rangle &= k_x \left[\sum_n I_{n-l}(z) I_{n-l'}(-z)\right] - ik_y \left[\sum_n I_{n-l}(z) I_{n-l'}(z)\right] \\ &= k_x I_{l'-l}(0) - ik_y I_{l'-l}(2z) \\ &= k_x \delta_{l,l'} - ik_y I_{l'-l}(2z) \end{aligned} \tag{B.4}$$

2. l' odd:

$$\begin{aligned}\langle\psi^b_{l'}|H^{\mathbf{k}}_{\mathrm{F,lin}}|\psi^a_l\rangle &= k_x \left[\sum_n I_{n-l}(z) I_{n-l'}(-z)\right] + ik_y \left[\sum_n I_{n-l}(z) I_{n-l'}(z)\right] \\ &= k_x \delta_{l,l'} + ik_y I_{l'-l}(2z) \end{aligned} \tag{B.5}$$

The matrix elements are therefore

$$\langle\psi^b_{l'}|H^{\mathbf{k}}_{\mathrm{F,lin}}|\psi^a_l\rangle = \begin{cases} k_x\delta_{ll'} - ik_y I_{l'-l}(2z), & \text{if } l' \text{ even}, \\ k_x\delta_{ll'} + ik_y I_{l'-l}(2z), & \text{if } l' \text{ odd}. \end{cases} \tag{B.6}$$

$$\langle\psi^a_{l'}|H^{\mathbf{k}}_{\mathrm{F,lin}}|\psi^b_l\rangle = \begin{cases} k_x\delta_{ll'} + ik_y I_{l'-l}(2z), & \text{if } l' \text{ even}, \\ k_x\delta_{ll'} - ik_y I_{l'-l}(2z), & \text{if } l' \text{ odd}. \end{cases} \tag{B.7}$$

B.3. Derivation of the polarizability for circularly polarized field

The derivation of the formula for the dynamical polarizability follows the lines of its counterpart in the 2DEG [230]. The wavefunction for graphene under a periodic driving can be written by use of the Floquet theorem as

$$\psi_{\mathbf{k},\sigma}(\mathbf{r},t) = \frac{1}{\sqrt{2}} e^{i\mathbf{k}\mathbf{r}} e^{-i\epsilon_{\mathbf{k},\sigma}t} \phi_{\mathbf{k},\sigma}(t), \tag{B.8}$$

where $\epsilon_{\mathbf{k},\sigma}$ is the quasienergy and $\phi_{\mathbf{k},\sigma}(t)$ are the Floquet states, which fulfill the time-periodicity of the driving field, and we have chosen the solution corresponding to the First Brillouin zone. After

applying a weak probe potential, these wavefunctions are not any more eigenfunctions of the full Hamiltonian, but we can use them as a basis to write the new wavefunction

$$\Psi_{\mathbf{k},\sigma}(\mathbf{r},t) = \sum_{\mathbf{k}'\sigma'} a_{\mathbf{k}',\sigma'}(t)\psi_{\mathbf{k}',\sigma'}(\mathbf{r},t). \tag{B.9}$$

Inserting this into the Schrödinger equation for the Hamiltonian $H_0(t) + H_1(t)$, where $H_0(t)$ is the Hamiltonian for the periodically driven graphene, and $H_1(t) = V(\mathbf{r},t)$ represents the weak probe potential, we are left with a differential equation for the coefficients $a_{\mathbf{k},\sigma}(t)$

$$i\sum_{\mathbf{k}'\sigma'} \dot{a}_{\mathbf{k}',\sigma'}(t)\psi_{\mathbf{k}',\sigma'}(\mathbf{r},t) = \sum_{\mathbf{k}'\sigma'} a_{\mathbf{k}',\sigma'}(t)V(\mathbf{r},t)\psi_{\mathbf{k}',\sigma'}(\mathbf{r},t). \tag{B.10}$$

We can now project this equation into a state $\psi_{\mathbf{k}'',\sigma''}$, yielding

$$\dot{a}_{\mathbf{k}'',\sigma''}(t) = -i\sum_{\mathbf{k}'\sigma'} a_{\mathbf{k}',\sigma'}(t)e^{i(\epsilon_{\mathbf{k}'',\sigma''}-\epsilon_{\mathbf{k}',\sigma'})t}\phi^*_{\mathbf{k}'',\sigma''}(t)\phi_{\mathbf{k}',\sigma'}(t)V(\mathbf{k}''-\mathbf{k}',t), \tag{B.11}$$

where $V(\mathbf{k}''-\mathbf{k}',t)$ is the projection of the probe potential into the states $\mathbf{k}'$ and $\mathbf{k}''$. Now we can expand this equation in a power series of the external potential, and, keeping only the first order, we are left with

$$\dot{a}^{(1)}_{\mathbf{k}'',\sigma''}(t) = -ie^{i(\epsilon_{\mathbf{k}'',\sigma''}-\epsilon_{\mathbf{k},\sigma})t}\phi^*_{\mathbf{k}'',\sigma''}(t)\phi_{\mathbf{k},\sigma}(t)V(\mathbf{k}''-\mathbf{k},t). \tag{B.12}$$

This equation can be simplified by Fourier transformation, yielding

$$a_{\mathbf{k}'',\sigma''}(t) = \int\frac{d\omega}{2\pi}V(\mathbf{k}''-\mathbf{k},\omega)e^{-i\omega t}e^{i(\epsilon_{\mathbf{k}'',\sigma''}-\epsilon_{\mathbf{k},\sigma})t}e^{\eta t}\sum_{nn'}\frac{e^{i(n'-n)\Omega t}\left[\phi^{n',a*}_{\mathbf{k}'',\sigma''}\phi^{n,a*}_{\mathbf{k},\sigma}+\phi^{n',b*}_{\mathbf{k}'',\sigma''}\phi^{n,b*}_{\mathbf{k},\sigma}\right]}{\omega-(n'-n)\Omega-(\epsilon_{\mathbf{k}'',\sigma''}-\epsilon_{\mathbf{k},\sigma})+i\eta}. \tag{B.13}$$

In order to get the response of the system to the external probe in linear response, we write the expression of the induced charge density as

$$\begin{aligned}\rho^{\text{ind}}_{\mathbf{k},\sigma}(\mathbf{r},t) &= \Psi^*_{\mathbf{k},\sigma}(\mathbf{r},t)\Psi_{\mathbf{k},\sigma}(\mathbf{r},t) - \psi^*_{\mathbf{k},\sigma}(\mathbf{r},t)\psi_{\mathbf{k},\sigma}(\mathbf{r},t)\\ &= \sum_{\mathbf{k}'\sigma'} a^*_{\mathbf{k}',\sigma'}(t)\psi^*_{\mathbf{k}',\sigma'}(\mathbf{r},t)\psi_{\mathbf{k},\sigma}(\mathbf{r},t) + a_{\mathbf{k}',\sigma'}(t)\psi^*_{\mathbf{k},\sigma}(\mathbf{r},t)\psi_{\mathbf{k}',\sigma'}(\mathbf{r},t)\end{aligned} \tag{B.14}$$

and insert the result obtained for $a_{\mathbf{k},\sigma}(t)$. After some algebra we arrive at

$$\rho^{\text{ind}}(\mathbf{r},t) = \sum_{\mathbf{q}}\int\frac{d\omega}{2\pi}V^{\text{ext}}(\mathbf{q},\omega)e^{-i\omega t}e^{i\mathbf{q}\mathbf{r}}\sum_{\sigma\sigma'}\sum_{\mathbf{k}} f_{\mathbf{k},\sigma}\mathcal{F}_{\mathbf{k},\sigma,\sigma'}, \tag{B.15}$$

where we have introduced the short notation

$$\begin{aligned}\mathcal{F}_{\mathbf{k},\sigma,\sigma'} = &\frac{1}{2}\sum_{nn'}\sum_{mm'}\\ &\left[\frac{e^{i(n'-n)\Omega t}e^{i(m'-m)\Omega t}\left(\phi^{n',a*}_{\mathbf{k}+\mathbf{q},\sigma'}\phi^{n,a}_{\mathbf{k},\sigma}+\phi^{n',b*}_{\mathbf{k}+\mathbf{q},\sigma'}\phi^{n,b}_{\mathbf{k},\sigma}\right)\left(\phi^{m',a*}_{\mathbf{k},\sigma}\phi^{m,a}_{\mathbf{k}+\mathbf{q},\sigma'}+\phi^{m',b*}_{\mathbf{k},\sigma}\phi^{m,b}_{\mathbf{k}+\mathbf{q},\sigma'}\right)}{\omega-(n'-n)\Omega-(\epsilon_{\mathbf{k}+\mathbf{q},\sigma'}-\epsilon_{\mathbf{k},\sigma})+i\eta}+\right.\\ &\left.\frac{e^{-i(n'-n)\Omega t}e^{-i(m'-m)\Omega t}\left(\phi^{n',a}_{\mathbf{k}-\mathbf{q},\sigma'}\phi^{n,a*}_{\mathbf{k},\sigma}+\phi^{n',b}_{\mathbf{k}-\mathbf{q},\sigma'}\phi^{n,b*}_{\mathbf{k},\sigma}\right)\left(\phi^{m',a}_{\mathbf{k},\sigma}\phi^{m,a*}_{\mathbf{k}-\mathbf{q},\sigma'}+\phi^{m',b}_{\mathbf{k},\sigma}\phi^{m,b*}_{\mathbf{k}-\mathbf{q},\sigma'}\right)}{-\omega-(n'-n)\Omega-(\epsilon_{\mathbf{k}-\mathbf{q},\sigma'}-\epsilon_{\mathbf{k},\sigma})-i\eta}\right].\end{aligned} \tag{B.16}$$

By comparing with the Poisson equation

$$\rho^{\text{ind}}(\mathbf{r},t) = \sum_{\mathbf{q}} \int \frac{d\omega}{2\pi} V^{\text{ind}}(\mathbf{q},\omega) e^{-i\omega t} e^{i\mathbf{q}\mathbf{r}} \frac{q^2}{4\pi} \tag{B.17}$$

we see that the induced potential must fulfill

$$V^{\text{ind}}(\mathbf{q},\omega) = \frac{4\pi}{q^2} V^{\text{ext}}(\mathbf{q},\omega) \sum_{\sigma\sigma'} \sum_{\mathbf{k}} f_{\mathbf{k},\sigma} \mathcal{F}_{\mathbf{k},\sigma,\sigma'}. \tag{B.18}$$

We sum on both sides $V^{\text{ext}}(\mathbf{q},\omega)$ and get

$$V^{\text{tot}}(\mathbf{q},\omega) = \left(1 + \frac{4\pi}{q^2} \sum_{\sigma\sigma'} \sum_{\mathbf{k}} f_{\mathbf{k},\sigma} \mathcal{F}_{\mathbf{k},\sigma,\sigma'}\right) V^{\text{ext}}(\mathbf{q},\omega), \tag{B.19}$$

where the dielectric function is given by

$$\varepsilon(\mathbf{q},\omega) = \frac{1}{1 + \frac{4\pi}{q^2} \sum_{\sigma\sigma'} \sum_{\mathbf{k}} f_{\mathbf{k},\sigma} \mathcal{F}_{\mathbf{k},\sigma,\sigma'}}. \tag{B.20}$$

In the RPA approximation we obtain therefore

$$\varepsilon(\mathbf{q},\omega)_{\text{RPA}} = 1 - \frac{4\pi}{q^2} \sum_{\sigma\sigma'} \sum_{\mathbf{k}} f_{\mathbf{k},\sigma} \mathcal{F}_{\mathbf{k},\sigma,\sigma'}. \tag{B.21}$$

After substituting the expression for $\mathcal{F}_{\mathbf{k},\sigma,\sigma'}$ and some straightforward manipulations, we arrive at our desired result for the dynamical polarizability:

$$\Pi(\mathbf{q},\omega) = \sum_{\sigma\sigma'} \sum_{\mathbf{k}} \sum_{l} \frac{f_{\mathbf{k},\sigma} - f_{\mathbf{k}+\mathbf{q},\sigma'}}{\omega - \epsilon_{\mathbf{k}+\mathbf{q},\sigma',l} + \epsilon_{\mathbf{k},\sigma,0} + i\eta} \sum_{n} |\phi^{n,a,*}_{\mathbf{k}+\mathbf{q},\sigma',l} \phi^{n,a}_{\mathbf{k},\sigma,0} + \phi^{n,b,*}_{\mathbf{k}+\mathbf{q},\sigma',l} \phi^{n,b}_{\mathbf{k},\sigma,0}|^2 \tag{B.22}$$

Notice that now we have simplified the expression by writing it as the scalar product between different Floquet sidebands by using Eqs. (7.7) and (7.9).

General conclusions

In the first part of this thesis various problems of transport through few-electron triple quantum dots (TQD) have been considered. By making use of the reduced density matrix formalism the current, the occupation probabilities and the coherences between certain states have been analyzed in different scenarios.

In chapter 3 a triangular TQD has been studied in a regime where only one or two electrons can be inside the TQD (Coulomb blockade regime). In the case of two electrons one of them is confined in the dot close to the drain contact, so that transport undergoes spin selection rules and can be blocked due to Pauli's exclusion principle (spin blockade regime). The triangular TQD has been considered as exposed to crossed dc and ac magnetic fields, in such a way that the dc field is perpendicular to the TQD area. This combination of fields is used to induce coherent rotation of the electron spin within a quantum dot (electron spin resonance). In a triangular TQD, in which two dots are coupled to leads, an eigenstate exists that is a coherent superposition of two tunnel-coupled dots, but in which the third one does not participate. If this third dot is connected to the drain, a phenomenon called *coherent population trapping* occurs in transport. This phenomenon depends on the magnetic flux coming from the dc field that penetrates the TQD. For the case of one electron the current shows Aharonov-Bohm oscillations when varying the dc magnetic field. An additional ac magnetic field does not affect the coherent superposition that leads to quenching the current, but induces coherent spin rotations of the single trapped electron. If an additional electron is confined in the drain dot, spin blockade occurs in the current through the TQD. It is demonstrated that with only a dc magnetic field applied to the TQD the current does not show Aharonov-Bohm oscillations as a function of the magnetic flux, since it is either blocked by coherent population trapping or, – for flux values that destroy the coherent superposition –, by spin blockade. For the latter situation an ac magnetic field applied to the TQD induces current by breaking the spin blockade. However, the field does not affect the coherent trapping, and therefore the Aharonov-Bohm oscillations of the current are recovered. Most importantly, it is shown that the ac magnetic field does not only break spin blockade, but *induces* it again at a different frequency (or equivalently at a different dc magnetic field). In this situation a novel spin blockade state is formed, which is induced by the ac field *and* decoupled from it.

In chapter 4 the effect of crossed dc and ac magnetic fields on a double quantum dot (DQD) and a linear TQD in the Coulomb blockade regime, i.e. with only one or two electrons, has been analyzed. Transport through the DQD has been treated in detail in terms of eigenstates of two combined two-level systems, – the two-level system due to tunneling from one electron to the other, and the two-level system of spin-up and spin-down within one dot. The analysis of the different resonance conditions of the ac magnetic field frequency with different Zeeman splittings within the DQD show that the

DQD can work as a spin-polarizer when the Zeeman splitting of the drain dot is off-resonant with the ac field, but the Zeeman splitting of the source dot is on resonance. For this situation a change in the energetic detuning between the two dots provides a way of changing between spin-up and spin-down polarized current. In a similar way it is demonstrated that a TQD can be operated both as a spin-polarizer and a spin-inverter, in which e.g. a spin-up polarized current is inverted to spin-down polarized current.

In chapter 5 the current through a linear TQD has been calculated, and the theoretical results have been compared to results experimentally obtained in the group of Prof. A. Sachrajda (NRC, Canada). In contrast to the foregoing chapters no ac magnetic field has been considered here. Transport through the TQD has been analyzed for an electronic configuration of three, four or five electrons inside the TQD, where two of them are confined in the two lateral dots that are connected to source and drain. By making use of the density matrix formalism the current has been calculated as a function of the left and right gate voltages at constant center voltage, for both zero and finite magnetic dc field. It has been shown that the theoretical results for the current coincide very well with the experimental results by A. Sachrajda *et al.* Both measurements and calculations have shown that the current is blocked both in positive and negative bias direction due to spin blockade, if a finite dc magnetic field is applied to the TQD. This bipolar blockade is, however, lifted at zero field by hyperfine-induced spin-flip processes that are strongly suppressed in a finite magnetic field. By analyzing the density matrix of the TQD system it could be shown that the lifting of spin blockade occurs due to the formation of a particular eigenstate of the TQD in which an electron is delocalized between the resonant left and right dot, but in which the center dot does not participate at all. This kind of states could have important applications in spin-busing schemes and nanospintronics.

In the second part of this thesis, chapter 7, the electronic singleparticle and multiparticle properties of graphene irradiated by ac electric fields have been analyzed. For both circular and linear polarization of the ac field analytic approximations have been derived that are shown to constitute an excellent approximation for the case of weak field intensities, where only up to one-photon processes are important. The analytical approximations have been used to calculate the quasienergy spectrum and the density of states. It has been found that a circularly polarized field induces gaps in the density of states both at the Dirac point and for higher energies, where the absorption of one photon becomes important. It has also been found out that a linearly polarized influences the quasienergy spectrum and density of states in a similar way, although no gap is induced at the Dirac point, and no effect is visible along the polarization axis of the field. The effect of Coulomb interactions has only been considered for the case of a circularly polarized field due to its larger symmetry with respect to the linear case. In order to analyze the excitation spectra for the interacting system a general formula for the dynamical polarizability of irradiated graphene has been derived. The analytic approximations have been applied to evaluate the dynamical polarizability at low field intensities. Thus, within the RPA, a plasmon has been found even for undoped graphene, which is in strong contrast to free graphene where the RPA only predicts a plasmon for doped graphene, and it has also been demonstrated that a circularly polarized ac field changes the plasmon dispersion relation with respect to the one for pristine graphene. However, it also makes the plasmon unstable due to higher order photon

processes, which become important for higher field intensities. In conclusion, it has been analyzed that the presence of time-dependent electric fields can strongly change the electronic properties of graphene and thereby open the way for the discovery of new physics in this outstanding material.

Conclusiones generales

En la primera parte de esta tesis se han considerado diversos problemas de transporte de pocos electrones a través de un triple punto cuántico (TQD). Al hacer uso del formalismo de la matriz densidad reducida, las probabilidades de ocupación y las coherencias entre algunos estados se han analizado en diferentes escenarios.

En el capítulo 3 se ha estudiado un TQD triangular en un régimen donde sólo pueden estar uno o dos electrones dentro del TQD (régimen de bloqueo de Coulomb). En el caso de dos electrones, uno de ellos está confinado en el punto cuántico al lado del contacto de drenaje, por lo que el transporte se somete a las reglas de selección de espín y puede ser bloqueado debido al principio de exclusión de Pauli (régimen de bloqueo de espín). Se ha considerado que el TQD triangular está expuesto a campos cruzados magnéticos dc y ac, de tal manera que el campo dc es perpendicular al área del TQD. Esta combinación de campos se utiliza para inducir la rotación coherente del espín del electrón en un punto cuántico (resonancia de espín electrónica). En un TQD triangular, en el que dos puntos están acoplados a contactos, existe un autoestado que es una superposición coherente de dos puntos acoplados por túnel, pero en el que el tercero no participa. Si este tercer punto está conectado a un contacto de drenaje, un fenómeno llamado *atrapamiento de población coherente* se produce en el transporte. Este fenómeno depende del flujo magnético procedente del campo dc que atraviesa el TQD. Para el caso de un electrón en el interior del TQD la corriente exhibe oscilaciones Aharonov-Bohm cuando se varía el campo magnético dc. Se ha encontrado que un campo ac adicional no afecta a la superposición coherente que lleva a la extinción de la corriente, sino que induce rotaciones coherentes del espín del electrón atrapado en la superposición coherente. Si un electrón adicional se confina en el punto cerca del contacto de drenaje, se produce bloqueo de espín en la corriente a través del TQD. A continuación, se ha analizado que con sólo un campo magnético dc aplicado al TQD la corriente como una función del flujo magnético no muestra oscilaciones Aharonov-Bohm, ya que está bloqueada o bien por el atrapamiento de población coherente o bien, – para valores de flujo que destruyen la superposición coherente –, por el bloqueo de espín. En esta última situación un campo magnético ac aplicado al TQD induce corriente al romper el bloqueo de espín. Sin embargo, el campo ac no afecta al atrapamiento coherente, y por lo tanto las oscilaciones Aharonov-Bohm de la corriente se recuperan. Como resultado principal de este capítulo, se ha mostrado que el campo magnético ac no sólo puede romper el bloqueo de espín, sino que lo *induce* de nuevo al variar su frecuencia (o equivalentemente el campo magnético dc). En esta situación se forma un novedoso estado de bloqueo de espín, inducido por el campo ac y *desacoplado* del mismo.

En el capítulo 4 se ha analizado el efecto de aplicar campos magnéticos dc y ac cruzados a un doble punto cuántico (DQD) y un TQD lineal en el régimen de bloqueo de Coulomb, es decir, con sólo uno o dos electrones. El transporte a través del DQD ha sido tratado en detalle en términos de

autoestados de dos sistemas de dos niveles combinados – el sistema de dos niveles debido al efecto túnel de un electrón de un punto cuántico a otro, y el sistema de dos niveles de espín hacia arriba y espín hacia abajo dentro de un punto cuántico. El análisis de las diferentes condiciones de resonancia de la frecuencia del campo magnético ac con los diferentes desdoblamientos Zeeman dentro del DQD ha demostrado que este sistema puede funcionar como un polarizador de espínes cuando el desdoblamiento Zeeman del punto cerca del drenaje está fuera de resonancia con el campo ac, pero a la vez el desdoblamiento Zeeman del punto más próximo a la fuente se encuentra en resonancia. En esta situación un cambio en la diferencia de energías entre los dos puntos proporciona una manera de alternar entre corrientes polarizadas de espín hacia arriba o abajo. De una manera similar se ha demostrado que un TQD puede ser operado tanto como un polarizador o como un inversor de espines, por ejemplo, cuando una corriente polarizada de espín hacia arriba se invierte a una de espín hacia abajo.

En el capítulo 5, como último tema relacionado con el transporte, se ha calculado la corriente a través de un TQD lineal. Los resultados teóricos han sido comparados con unas medidas experimentales llevadas a cabo en el grupo del Profesor A. Sachrajda (NRC, Canada). En contraste con los capítulos anteriores aquí no se ha considerado un campo magnético ac. El transporte a través del TQD se ha analizado para una configuración electrónica de tres, cuatro o cinco electrones en el interior del TQD, donde dos de ellos están confinados en los dos puntos laterales que están conectados a la fuente y el drenaje. La corriente se ha calculado mediante el formalismo de la matriz de densidad como una función de los voltajes de la puerta izquierda y la derecha manteniendo el voltaje de puerta central constante, para ambos cero y campo magnético dc finito. Los resultados teóricos coinciden muy bien con los resultados experimentales de A. Sachrajda *et al.* Ambas medidas y cálculos muestran que la corriente está bloqueada tanto en la dirección de sesgo positivo como negativo debido al bloqueo de espín, si un campo magnético dc finito se aplica al TQD. Este bloqueo bipolar, sin embargo, se rompe a campo magnético cero debido a procesos de flip-flop de espín inducidos por la interacción híperfina, que son muy improbables en un campo magnético finito. Mediante el análisis de la matriz densidad del TQD se ha podido mostrar que la destrucción del bloqueo de espín se produce debido a la formación de un autoestado particular del TQD en el que un electrón se deslocaliza entre los puntos de la izquierda y de la derecha cuando estos están en resonancia, pero en el que el punto del centro no participa en absoluto. Este tipo de estados podría tener aplicaciones importantes en "spin-busing" y en nanoespintrónica.

En la segunda parte de esta tesis, en el capítulo 7, se han calculado las propiedades electrónicas de grafeno irradiado por campos eléctricos dependientes del tiempo, tanto en presencia como en ausencia de interacciones electrón-electrón. Considerando los dos casos relevantes de polarización del campo ac circular y lineal, se han derivado aproximaciones analíticas que constituyen una excelente aproximación cuando la intensidad del campo es débil, pues en este caso sólo los procesos de hasta un fotón son importantes. Las aproximaciones analíticas se han utilizado para calcular el espectro de cuasienergías y la densidad de estados. Se ha encontrado que un campo circularmente polarizado induce gaps en la densidad de estados tanto en el punto de Dirac como para energías más altas, donde la absorción de uno o más fotones es importante. Para el caso lineal, el efecto del campo es

similar en el espectro de cuasienergías y en la densidad de estados, si bien no se induce ningún gap en el punto de Dirac, y ningún efecto es visible a lo largo del eje de polarización del campo. El efecto de la interacción electrón-electrón sólo se ha considerado para el caso de un campo polarizado circularmente, debido a su mayor simetría con respecto al caso lineal. Con el fin de analizar el espectro de excitaciones se ha derivado una fórmula general para la polarizabilidad dinámica de grafeno irradiado, que es válida para intensidades de campo arbitrarias. Las aproximaciones analíticas se han utilizado para evaluar la polarizabilidad dinámica a intensidades de campo bajas. De esta manera, dentro de la aproximación RPA, se ha encontrado que aparece un plasmón incluso para el grafeno sin dopar, lo cual contrasta con lo que ocurre en el grafeno libre, donde la RPA sólo predice un plasmón para el grafeno dopado. Además, se ha demostrado que un campo ac de polarización circular cambia la relación de dispersión del plasmón respecto al caso del grafeno no irradiado, si bien también hace que el plasmón se vuelva inestable debido a procesos con mayor número de fotones que llegan a ser importantes para intensidades de campo más altas. En conclusión, se ha analizado que la presencia de campos eléctricos dependientes del tiempo cambia las propiedades electrónicas del grafeno en gran medida, abriendo así camino para descubrir nueva física en este material extraordinario.

List of publications

- Maria Busl, Rafael Sánchez and Gloria Platero, *Control of spin blockade by ac magnetic fields in triple quantum dots*, Physical Review B **81**, 121306 (2010).
- Maria Busl and Gloria Platero, *Spin-polarized currents in double and triple quantum dots driven by ac magnetic fields*, Physical Review B **82**, 205304 (2010).
- Maria Busl, Gloria Platero and Antti-Pekka Jauho, *Dynamical polarizability of graphene irradiated by circularly polarized ac electric fields*, Physical Review B **85**, 155449 (2012).
- M. Busl, G. Granger, L. Gaudreau, R. Sánchez, A. Kam, M. Pioro-Ladriére, S. A. Studenikin, P. Zawadzki, Z. R. Wasilewski, A. S. Sachrajda, and G. Platero, *Bipolar spin blockade lifting by coherent state superposition in a triple quantum dot*, in preparation.
- Maria Busl, Carlos López-Monís, Rafael Sánchez, Jesús Iñarrea and Gloria Platero, *Spin dynamics in double quantum dots in the spin blockade regime*, Physica E **42**, 643 (2010).
- Maria Busl, Rafael Sánchez and Gloria Platero, *Electron spin resonance in triple quantum dot interferometers*, Physica E **42**, 830 (2010).
- Maria Busl, Rafael Sánchez and Gloria Platero, *Electron spin resonance in triple quantum dots*, Journal of Physics: Conference Series **245**, 012016 (2010).
- Maria Busl and Gloria Platero, *Triple quantum dots as charge rectifiers*, J. Phys.: Condens. Matter **24**, 154001 (2012).

Bibliography

[1] Marc A. Kastner. Artificial atoms. *Physics Today*, 46(1):24–31, 1993. (cited on p. 3)

[2] R. C. Ashoori. Electrons in artificial atoms. *Nature*, 379(6564):413–419, 02 1996. (cited on p. 3)

[3] L P Kouwenhoven, D G Austing, and S Tarucha. Few-electron quantum dots. *Reports on Progress in Physics*, 64(6):701, 2001. (cited on pages 3, 5, and 6)

[4] L. P. Kouwenhoven, T. H. Oosterkamp, M. W. S. Danoesastro, M. Eto, D. G. Austing, T. Honda, and S. Tarucha. Excitation spectra of circular, few-electron quantum dots. *Science*, 278(5344):1788–1792, 1997. (cited on p. 3)

[5] T. A. Fulton and G. J. Dolan. Observation of single-electron charging effects in small tunnel junctions. *Phys. Rev. Lett.*, 59:109–112, Jul 1987. (cited on p. 3)

[6] J. H. F. Scott-Thomas, Stuart B. Field, M. A. Kastner, Henry I. Smith, and D. A. Antoniadis. Conductance oscillations periodic in the density of a one-dimensional electron gas. *Phys. Rev. Lett.*, 62:583–586, Jan 1989. (cited on p. 3)

[7] C. Stampfer, J. Guttinger, F. Molitor, D. Graf, T. Ihn, and K. Ensslin. Tunable coulomb blockade in nanostructured graphene. *Applied Physics Letters*, 92(1):012102, 2008. (cited on p. 3)

[8] S. Tarucha, D. G. Austing, T. Honda, R. J. van der Hage, and L. P. Kouwenhoven. Shell filling and spin effects in a few electron quantum dot. *Phys. Rev. Lett.*, 77:3613–3616, Oct 1996. (cited on p. 3)

[9] M. Ciorga, A. S. Sachrajda, P. Hawrylak, C. Gould, P. Zawadzki, S. Jullian, Y. Feng, and Z. Wasilewski. Addition spectrum of a lateral dot from coulomb and spin-blockade spectroscopy. *Phys. Rev. B*, 61:R16315–R16318, Jun 2000. (cited on pages 3, 5, 6, 10, and 67)

[10] David L. Klein, Richard Roth, Andrew K. L. Lim, A. Paul Alivisatos, and Paul L. McEuen. A single-electron transistor made from a cadmium selenide nanocrystal. *Nature*, 389(6652):699–701, 10 1997. (cited on p. 3)

[11] J. Seufert, M. Rambach, G. Bacher, A. Forchel, T. Passow, and D. Hommel. Single-electron charging of a self-assembled ii–vi quantum dot. *Applied Physics Letters*, 82(22):3946–3948, 2003. (cited on p. 3)

[12] Jan von Delft, Andrei D. Zaikin, Dmitrii S. Golubev, and Wolfgang Tichy. Parity-affected superconductivity in ultrasmall metallic grains. *Phys. Rev. Lett.*, 77:3189–3192, Oct 1996. (cited on p. 3)

[13] Oded Agam, Ned S. Wingreen, Boris L. Altshuler, D. C. Ralph, and M. Tinkham. Chaos, interactions, and nonequilibrium effects in the tunneling resonance spectra of ultrasmall metallic particles. *Phys. Rev. Lett.*, 78:1956–1959, Mar 1997. (cited on p. 3)

[14] L. Chico, M. P. López Sancho, and M. C. Muñoz. Carbon-nanotube-based quantum dot. *Phys. Rev. Lett.*, 81:1278–1281, Aug 1998. (cited on p. 3)

[15] N. Mason, M. J. Biercuk, and C. M. Marcus. Local gate control of a carbon nanotube double quantum dot. *Science*, 303(5658):655–658, 2004. (cited on pages)

[16] K. Grove-Rasmussen, H. I. JÃÿrgensen, T. Hayashi, P. E. Lindelof, and T. Fujisawa. A triple quantum dot in a single-wall carbon nanotube. *Nano Letters*, 8(4):1055–1060, 2008. PMID: 18314966. (cited on p. 17)

[17] H. Ingerslev Jorgensen, K. Grove-Rasmussen, K. Y. Wang, A. M. Blackburn, K. Flensberg, P. E. Lindelof, and D. A. Williams. Singlet-triplet physics and shell filling in carbon nanotube double quantum dots. *Nat Phys*, 4(7):536–539, 07 2008. (cited on p. 3)

[18] C. Stampfer, E. Schurtenberger, F. Molitor, J. GuÌĹttinger, T. Ihn, and K. Ensslin. Tunable graphene single electron transistor. *Nano Letters*, 8(8):2378–2383, 2008. PMID: 18642958. (cited on p. 3)

[19] L. A. Ponomarenko, F. Schedin, M. I. Katsnelson, R. Yang, E. W. Hill, K. S. Novoselov, and A. K. Geim. Chaotic dirac billiard in graphene quantum dots. *Science*, 320(5874):356–358, 2008. (cited on pages)

[20] Juan Peng, Wei Gao, Bipin Kumar Gupta, Zheng Liu, Rebeca Romero-Aburto, Liehui Ge, Li Song, Lawrence B. Alemany, Xiaobo Zhan, Guanhui Gao, Sajna Antony Vithayathil, Benny Abraham Kaipparettu, Angel A. Marti, Takuya Hayashi, Jun-Jie Zhu, and Pulickel M. Ajayan. Graphene quantum dots derived from carbon fibers. *Nano Letters*, 12(2):844–849, 2012. (cited on p. 3)

[21] Arieh Aviram and Mark A. Ratner. Molecular rectifiers. *Chemical Physics Letters*, 29(2):277 – 283, 1974. (cited on p. 3)

[22] Z. J. Donhauser, B. A. Mantooth, K. F. Kelly, L. A. Bumm, J. D. Monnell, J. J. Stapleton, D. W. Price, A. M. Rawlett, D. L. Allara, J. M. Tour, and P. S. Weiss. Conductance switching in single molecules through conformational changes. *Science*, 292(5525):2303–2307, 2001. (cited on pages)

[23] Christian Joachim and Mark A. Ratner. Molecular electronics: Some views on transport junctions and beyond. *Proceedings of the National Academy of Sciences of the United States of America*, 102(25):8801–8808, 2005. (cited on p. 3)

[24] R. M. Potok, J. A. Folk, C. M. Marcus, V. Umansky, M. Hanson, and A. C. Gossard. Spin and polarized current from coulomb blockaded quantum dots. *Phys. Rev. Lett.*, 91:016802, Jul 2003. (cited on p. 4)

[25] R. Hanson, B. Witkamp, L. M. K. Vandersypen, L. H. Willems van Beveren, J. M. Elzerman, and L. P. Kouwenhoven. Zeeman energy and spin relaxation in a one-electron quantum dot. *Phys. Rev. Lett.*, 91:196802, Nov 2003. (cited on pages 12 and 13)

[26] F. H. L. Koppens, C. Buizert, K. J. Tielrooij, I. T. Vink, K. C. Nowack, T. Meunier, L. P. Kouwenhoven, and L. M. K. Vandersypen. Driven coherent oscillations of a single electron spin in a quantum dot. *Nature*, 442(7104):766, 2006. (cited on pages 4, 13, 14, 15, 39, 55, and 56)

[27] Daniel Loss and David P. DiVincenzo. Quantum computation with quantum dots. *Phys. Rev. A*, 57:120–126, Jan 1998. (cited on pages 4 and 55)

[28] Sigurdur I. Erlingsson, Yuli V. Nazarov, and Vladimir I. Fal'ko. Nucleus-mediated spin-flip transitions in gaas quantum dots. *Phys. Rev. B*, 64:195306, Oct 2001. (cited on p. 4)

[29] Sigurdur I. Erlingsson and Yuli V. Nazarov. Hyperfine-mediated transitions between a zeeman split doublet in gaas quantum dots: The role of the internal field. *Phys. Rev. B*, 66:155327, Oct 2002. (cited on pages)

[30] F. H. L. Koppens, J. A. Folk, J. M. Elzerman, R. Hanson, L. H. Willems van Beveren, I. T. Vink, H. P. Tranitz, W. Wegscheider, L. P. Kouwenhoven, , and L. M. K. Vandersypen. Control and detection of singlet-triplet mixing in a random nuclear field. *Science*, 309(5739):1346, 2005. (cited on pages 11, 12, and 67)

[31] J. R. Petta, A. C. Johnson, J. M. Taylor, E. A. Laird, A. Yacoby, M. D. Lukin, C. M. Marcus, M. P. Hanson, and A. C. Gossard. Coherent manipulation of coupled electron spins in semiconductor quantum dots. *Science*, 309(5744):2180, 2005. (cited on pages 4, 8, 9, 12, 39, and 67)

[32] E. A. Laird, C. Barthel, E. I. Rashba, C. M. Marcus, M. P. Hanson, and A. C. Gossard. Hyperfine-mediated gate-driven electron spin resonance. *Phys. Rev. Lett.*, 99:246601, Dec 2007. (cited on pages 4, 15, 39, and 55)

[33] K. C. Nowack, F. H. L. Koppens, Yu. V. Nazarov, and L. M. K. Vandersypen. Coherent control of a single electron spin with electric fields. *Science*, 318(5855):1430–1433, 2007. (cited on pages 15, 39, and 55)

[34] B. Erbe and J. Schliemann. Swapping and entangling hyperfine coupled nuclear spin baths. *EPL (Europhysics Letters)*, 95(4):47009, 2011. (cited on p. 4)

[35] J. M. Elzerman, R. Hanson, J. S. Greidanus, L. H. Willems van Beveren, S. De Franceschi, L. M. K. Vandersypen, S. Tarucha, and L. P. Kouwenhoven. Few-electron quantum dot circuit with integrated charge read out. *Phys. Rev. B*, 67:161308, Apr 2003. (cited on p. 4)

[36] M. Pioro-Ladrière, M. Ciorga, J. Lapointe, P. Zawadzki, M. Korkusiński, P. Hawrylak, and A. S. Sachrajda. Spin-blockade spectroscopy of a two-level artificial molecule. *Phys. Rev. Lett.*, 91:026803, Jul 2003. (cited on pages)

[37] J. R. Petta, A. C. Johnson, C. M. Marcus, M. P. Hanson, and A. C. Gossard. Manipulation of a single charge in a double quantum dot. *Phys. Rev. Lett.*, 93:186802, Oct 2004. (cited on pages)

[38] M. Pioro-Ladrière, M. R. Abolfath, P. Zawadzki, J. Lapointe, S. A. Studenikin, A. S. Sachrajda, and P. Hawrylak. Charge sensing of an artificial h_2^+ molecule in lateral quantum dots. *Phys. Rev. B*, 72:125307, Sep 2005. (cited on p. 4)

[39] K. Ono, D. G. Austing, Y. Tokura, , and S. Tarucha. Current rectification by pauli exclusion in a weakly coupled double quantum dot system. *Science*, 297(5585):1313–1317, 2002. (cited on pages 4, 10, 39, 46, 67, 69, and 70)

[40] A. C. Johnson, J. R. Petta, C. M. Marcus, M. P. Hanson, and A. C. Gossard. Singlet-triplet spin blockade and charge sensing in a few-electron double quantum dot. *Phys. Rev. B*, 72:165308, Oct 2005. (cited on pages 4, 10, and 70)

[41] H. R. Gray, R. M. Whitley, and Jr. C. R. Stroud. Coherent trapping of atomic populations. *Opt. Lett.*, 3(6):218–220, Dec 1978. (cited on pages 4, 38, and 39)

[42] Andrew D. Greentree, Jared H. Cole, A. R. Hamilton, and Lloyd C. L. Hollenberg. Coherent electronic transfer in quantum dot systems using adiabatic passage. *Phys. Rev. B*, 70:235317, Dec 2004. (cited on p. 4)

[43] Pierre M. Petroff, Axel Lorke, and Atac Imamoglu. Epitaxially self-assembled quantum dots. *Physics Today*, 54(5):46–52, 2001. (cited on p. 5)

[44] R. Hanson, L. P. Kouwenhoven, J. R. Petta, S. Tarucha, and L. M. K. Vandersypen. Spins in few-electron quantum dots. *Rev. Mod. Phys.*, 79:1217–1265, Oct 2007. (cited on pages 5, 8, and 12)

[45] L. P. Kouwenhoven, G. Schön, and L. L. Sohn. Introduction to mesoscopic electron transport. In L. L. Sohn, L. P. Kouwenhoven, and G. Schön, editors, *Mesoscopic Electron Transport*. Kluwer Academic Publishers, Dordrecht, Boston, London, 1997. (cited on pages 5 and 6)

[46] H. Grabert and M. H. Devoret. *Single Charge Tunneling*. Plenum, New York, 1992. (cited on p. 7)

[47] Matveev K. A. Glazman L. I. Coulomb correlations in the tunneling through resonance centers. *JETP*, 48:445, 1988. (cited on pages 6 and 8)

[48] D.V. Averin and A.N. Korotkov. Influence of discrete energy spectrum on correlated single-electron tunneling via a mesoscopically small metal granule. *Sov. Phys. JETP*, 70:937, 1990. (cited on p. 6)

[49] D. V. Averin, A. N. Korotkov, and K. K. Likharev. Theory of single-electron charging of quantum wells and dots. *Phys. Rev. B*, 44:6199–6211, Sep 1991. (cited on p. 6)

[50] C. W. J. Beenakker. Theory of coulomb-blockade oscillations in the conductance of a quantum dot. *Phys. Rev. B*, 44:1646–1656, Jul 1991. (cited on pages 6 and 8)

[51] W. G. van der Wiel, S. De Franceschi, J. M. Elzerman, T. Fujisawa, S. Tarucha, and L. P. Kouwenhoven. Electron transport through double quantum dots. *Rev. Mod. Phys.*, 75:1–22, Dec 2002. (cited on pages 7, 8, 9, and 15)

[52] Alexander W. Holleitner, Robert H. Blick, Andreas K. HâĹŽÂžttel, Karl Eberl, and JâĹŽâĹĆrg P. Kotthaus. Probing and controlling the bonds of an artificial molecule. *Science*, 297(5578):70–72, 2002. (cited on p. 8)

[53] S. A. Gurvitz and Ya. S. Prager. Microscopic derivation of rate equations for quantum transport. *Phys. Rev. B*, 53:15932–15943, Jun 1996. (cited on pages 8 and 29)

[54] S. A. Gurvitz. Rate equations for quantum transport in multidot systems. *Phys. Rev. B*, 57:6602–6611, Mar 1998. (cited on pages)

[55] R. Ziegler, C. Bruder, and Herbert Schoeller. Transport through double quantum dots. *Phys. Rev. B*, 62:1961–1970, Jul 2000. (cited on p. 8)

[56] Dietmar Weinmann, Wolfgang Häusler, and Bernhard Kramer. Spin blockades in linear and nonlinear transport through quantum dots. *Phys. Rev. Lett.*, 74:984–987, Feb 1995. (cited on p. 10)

[57] T. Fujisawa, D. G. Austing, Y. Tokura, Y. Hirayama, and S. Tarucha. Allowed and forbidden transitions in artificial hydrogen and helium atoms. *Nature*, 419(6904):278, 2002. (cited on pages 11 and 12)

[58] Alexander V. Khaetskii and Yuli V. Nazarov. Spin-flip transitions between zeeman sublevels in semiconductor quantum dots. *Phys. Rev. B*, 64:125316, Sep 2001. (cited on p. 11)

[59] R. Hanson, L. M. K. Vandersypen, L. H. Willems van Beveren, J. M. Elzerman, I. T. Vink, and L. P. Kouwenhoven. Semiconductor few-electron quantum dot operated as a bipolar spin filter. *Phys. Rev. B*, 70:241304, Dec 2004. (cited on p. 12)

[60] S. Amasha, K. MacLean, Iuliana Radu, D. M. Zumbuhl, M. A. Kastner, M. P. Hanson, and A. C. Gossard. Measurements of the spin relaxation rate at low magnetic fields in a quantum dot. *arXiv:cond-mat/0607110v1*, 2006. (cited on p. 12)

[61] Oleg N. Jouravlev and Yuli V. Nazarov. Electron transport in a double quantum dot governed by a nuclear magnetic field. *Phys. Rev. Lett.*, 96:176804, May 2006. (cited on p. 12)

[62] M. S. Rudner and L. S. Levitov. Self-polarization and dynamical cooling of nuclear spins in double quantum dots. *Phys. Rev. Lett.*, 99:036602, Jul 2007. (cited on pages 39 and 55)

[63] Jesús Iñarrea, Gloria Platero, and Allan H. MacDonald. Electronic transport through a double quantum dot in the spin-blockade regime: Theoretical models. *Phys. Rev. B*, 76:085329, Aug 2007. (cited on p. 12)

[64] Jeroen Danon and Yuli V. Nazarov. Nuclear tuning and detuning of the electron spin resonance in a quantum dot: Theoretical consideration. *Phys. Rev. Lett.*, 100:056603, Feb 2008. (cited on p. 55)

[65] Fernando Domínguez and Gloria Platero. Hyperfine mediated triplet-singlet transition probability in a double-quantum-dot system: Analogy with the double-slit experiment. *Phys. Rev. B*, 80:201301, Nov 2009. (cited on pages)

[66] F. Qassemi, W. A. Coish, and F. K. Wilhelm. Stationary and transient leakage current in the pauli spin blockade. *Phys. Rev. Lett.*, 102:176806, Apr 2009. (cited on pages)

[67] M. Gullans, J. J. Krich, J. M. Taylor, H. Bluhm, B. I. Halperin, C. M. Marcus, M. Stopa, A. Yacoby, and M. D. Lukin. Dynamic nuclear polarization in double quantum dots. *Phys. Rev. Lett.*, 104:226807, Jun 2010. (cited on pages)

[68] Carlos López-Monís, Jesús I narrea, and Gloria Platero. Dynamical nuclear spin polarization induced by electronic current through double quantum dots. *New Journal of Physics*, 13(5):053010, 2011. (cited on p. 12)

[69] F. H. L. Koppens, C. Buizert, I. T. Vink, K. C. Nowack, T. Meunier, L. P. Kouwenhoven, and L. M. K. Vandersypen. Detection of single electron spin resonance in a double quantum dot. *Journal of Applied Physics*, 101(8):081706, 2007. (cited on p. 13)

[70] F. H. L. Koppens, D. Klauser, W. A. Coish, K. C. Nowack, L. P. Kouwenhoven, D. Loss, and L. M. K. Vandersypen. Universal phase shift and nonexponential decay of driven single-spin oscillations. *Phys. Rev. Lett.*, 99:106803, Sep 2007. (cited on pages 13 and 39)

[71] Rafael Sánchez, Carlos López-Monís, and Gloria Platero. Coherent spin rotations in open driven double quantum dots. *Phys. Rev. B*, 77:165312, Apr 2008. (cited on pages 15, 39, 46, 49, 55, and 57)

[72] M. Pioro-Ladrière, T. Obata, Y. Tokura, Y.-S. Shin, T. Kubo, K. Yoshida, T. Taniyama, and S. Tarucha. Electrically driven single-electron spin resonance in a slanting zeeman field. *Nat Phys*, 4(10):776–779, 2008. (cited on pages 15, 16, 39, 46, and 55)

[73] L. P. Kouwenhoven, S. Jauhar, K. McCormick, D. Dixon, P. L. McEuen, Yu. V. Nazarov, N. C. van der Vaart, and C. T. Foxon. Photon-assisted tunneling through a quantum dot. *Phys. Rev. B*, 50:2019–2022, Jul 1994. (cited on p. 15)

[74] R. H. Blick, R. J. Haug, D. W. van der Weide, K. von Klitzing, and K. Eberl. Photon-assisted tunneling through a quantum dot at high microwave frequencies. *Applied Physics Letters*, 67(26):3924–3926, 1995. (cited on pages)

[75] Gloria Platero and Ramón Aguado. Photon-assisted transport in semiconductor nanostructures. *Physics Reports*, 395(1-2):1 – 157, 2004. (cited on pages 15, 97, and 101)

[76] Y. Kato, R. C. Myers, D. C. Driscoll, A. C. Gossard, J. Levy, and D. D. Awschalom. Gigahertz electron spin manipulation using voltage-controlled g-tensor modulation. *Science*, 299(5610):1201–1204, 2003. (cited on p. 15)

[77] L. Gaudreau, S. A. Studenikin, A. S. Sachrajda, P. Zawadzki, A. Kam, J. Lapointe, M. Korkusinski, and P. Hawrylak. Stability diagram of a few-electron triple dot. *Phys. Rev. Lett.*, 97(3):036807, Jul 2006. (cited on pages 16, 17, 39, 67, and 70)

[78] Daniel S. Saraga and Daniel Loss. Spin-entangled currents created by a triple quantum dot. *Phys. Rev. Lett.*, 90:166803, Apr 2003. (cited on p. 16)

[79] D. Bacon, J. Kempe, D. A. Lidar, and K. B. Whaley. Universal fault-tolerant quantum computation on decoherence-free subspaces. *Phys. Rev. Lett.*, 85:1758–1761, Aug 2000. (cited on p. 16)

[80] Pawel Hawrylak and Marek Korkusinski. Voltage-controlled coded qubit based on electron spin. *Solid State Communications*, 136(9-10):508 – 512, 2005. (cited on p. 16)

[81] M. Stopa. Rectifying behavior in coulomb blockades: Charging rectifiers. *Phys. Rev. Lett.*, 88:146802, Mar 2002. (cited on p. 16)

[82] A. Vidan, R. M. Westervelt, M. Stopa, M. Hanson, and A. C. Gossard. Triple quantum dot charging rectifier. *Applied Physics Letters*, 85:3602, 2004. (cited on p. 16)

[83] Marek Korkusinski, Irene Puerto Gimenez, Pawel Hawrylak, Louis Gaudreau, Sergei A. Studenikin, and Andrew S. Sachrajda. Topological hunds rules and the electronic properties of a triple lateral quantum dot molecule. *Phys. Rev. B*, 75(11):115301, Mar 2007. (cited on p. 16)

[84] F. Delgado, Y.-P. Shim, M. Korkusinski, and P. Hawrylak. Theory of spin, electronic, and transport properties of the lateral triple quantum dot molecule in a magnetic field. *Phys. Rev. B*, 76:115332, Sep 2007. (cited on p. 16)

[85] Bogdan R. Bułka, Tomasz Kostyrko, and Jakub Łuczak. Linear and nonlinear stark effect in a triangular molecule. *Phys. Rev. B*, 83:035301, Jan 2011. (cited on p. 16)

[86] E. Arimondo and G. Orriols. *Nuovo Cim. Lett.*, 17:333, 1976. (cited on pages 16, 38, and 39)

[87] R. M. Whitley and C. R. Stroud. Double optical resonance. *Phys. Rev. A*, 14:1498–1513, Oct 1976. (cited on pages 16, 38, and 39)

[88] B. Michaelis, C. Emary, and C. W. J. Beenakker. All-electronic coherent population trapping in quantum dots. *Europhys. Lett.*, 73(5):677–683, 2006. (cited on pages 16, 38, 39, and 73)

[89] Tomasz Kostyrko and Bogdan R. Bułka. Symmetry-controlled negative differential resistance effect in a triangular molecule. *Phys. Rev. B*, 79:075310, Feb 2009. (cited on pages)

[90] Christina Pöltl, Clive Emary, and Tobias Brandes. Two-particle dark state in the transport through a triple quantum dot. *Phys. Rev. B*, 80:115313, Sep 2009. (cited on p. 39)

[91] Fernando Domínguez, Sigmund Kohler, and Gloria Platero. Phonon-mediated decoherence in triple quantum dot interferometers. *Phys. Rev. B*, 83:235319, Jun 2011. (cited on p. 16)

[92] Clive Emary. Dark states in the magnetotransport through triple quantum dots. *Phys. Rev. B*, 76:245319, Dec 2007. (cited on pages 16, 37, 39, 41, and 46)

[93] Maria Busl, Rafael Sánchez, and Gloria Platero. Control of spin blockade by ac magnetic fields in triple quantum dots. *Phys. Rev. B*, 81:121306, Mar 2010. (cited on pages 16, 17, 49, and 57)

[94] J Villavicencio, I Maldonado, E Cota, and G Platero. Quasienergy spectrum and tunneling current in ac-driven triple quantum dot shuttles. *New Journal of Physics*, 13(2):023032, 2011. (cited on p. 16)

[95] Andrea Donarini, Georg Begemann, and Milena Grifoni. Interference effects in the coulomb blockade regime: Current blocking and spin preparation in symmetric nanojunctions. *Phys. Rev. B*, 82:125451, Sep 2010. (cited on p. 17)

[96] F. Delgado, Y.-P. Shim, M. Korkusinski, L. Gaudreau, S. A. Studenikin, A. S. Sachrajda, and P. Hawrylak. Spin-selective aharonov-bohm oscillations in a lateral triple quantum dot. *Phys. Rev. Lett.*, 101:226810, Nov 2008. (cited on p. 17)

[97] Yun-Pil Shim and Pawel Hawrylak. Gate-controlled spin-spin interactions in lateral quantum dot molecules. *Phys. Rev. B*, 78:165317, Oct 2008. (cited on p. 17)

[98] Beat Röthlisberger, Jörg Lehmann, D. S. Saraga, Philipp Traber, and Daniel Loss. Highly entangled ground states in tripartite qubit systems. *Phys. Rev. Lett.*, 100:100502, Mar 2008. (cited on p. 17)

[99] Anand Sharma and Pawel Hawrylak. Greenberger-horne-zeilinger states in a quantum dot molecule. *Phys. Rev. B*, 83:125311, Mar 2011. (cited on p. 17)

[100] Maria Busl, Rafael Sánchez, and Gloria Platero. Electron spin resonance in triple quantum dot interferometers. *Physica E: Low-dimensional Systems and Nanostructures*, 42(4):830 – 832, 2010. *18th International Conference on Electron Properties of Two-Dimensional Systems*. (cited on pages 17, 39, and 55)

[101] Maria Busl and Gloria Platero. Spin-polarized currents in double and triple quantum dots driven by ac magnetic fields. *Phys. Rev. B*, 82:205304, Nov 2010. (cited on p. 17)

[102] Chang-Yu Hsieh, Yun-Pil Shim, and Pawel Hawrylak. Theory of electronic properties and quantum spin blockade in a gated linear triple quantum dot with one electron spin each. *Phys. Rev. B*, 85:085309, Feb 2012. (cited on p. 17)

[103] R. Žitko, J. Bonča, A. Ramšak, and T. Rejec. Kondo effect in triple quantum dots. *Phys. Rev. B*, 73:153307, Apr 2006. (cited on p. 17)

[104] T. Kuzmenko, K. Kikoin, and Y. Avishai. Magnetically tunable kondo–aharonov-bohm effect in a triangular quantum dot. *Phys. Rev. Lett.*, 96:046601, Feb 2006. (cited on pages)

[105] E. Vernek, C. A. Büsser, G. B. Martins, E. V. Anda, N. Sandler, and S. E. Ulloa. Kondo regime in triangular arrangements of quantum dots: Molecular orbitals, interference, and contact effects. *Phys. Rev. B*, 80:035119, Jul 2009. (cited on pages)

[106] Andrew K. Mitchell and David E. Logan. Two-channel kondo phases and frustration-induced transitions in triple quantum dots. *Phys. Rev. B*, 81:075126, Feb 2010. (cited on p. 17)

[107] F. R. Waugh, M. J. Berry, D. J. Mar, R. M. Westervelt, K. L. Campman, and A. C. Gossard. Single-electron charging in double and triple quantum dots with tunable coupling. *Phys. Rev. Lett.*, 75:705–708, Jul 1995. (cited on p. 17)

[108] F. R. Waugh, M. J. Berry, C. H. Crouch, C. Livermore, D. J. Mar, R. M. Westervelt, K. L. Campman, and A. C. Gossard. Measuring interactions between tunnel-coupled quantum dots. *Phys. Rev. B*, 53:1413–1420, Jan 1996. (cited on p. 17)

[109] D. Schröer, A. D. Greentree, L. Gaudreau, K. Eberl, L. C. L. Hollenberg, J. P. Kotthaus, and S. Ludwig. Electrostatically defined serial triple quantum dot charged with few electrons. *Phys. Rev. B*, 76:075306, Aug 2007. (cited on pages 17, 39, and 67)

[110] M. C. Rogge and R. J. Haug. Two-path transport measurements on a triple quantum dot. *Phys. Rev. B*, 77:193306, May 2008. (cited on pages 39 and 67)

[111] S. Amaha, T. Hatano, T. Kubo, S. Teraoka, Y. Tokura, S. Tarucha, and D. G. Austing. Stability diagrams of laterally coupled triple vertical quantum dots in triangular arrangement. *Applied Physics Letters*, 94:092103, 2009. (cited on p. 17)

[112] M C Rogge and R J Haug. The three dimensionality of triple quantum dot stability diagrams. *New Journal of Physics*, 11(11):113037, 2009. (cited on p. 17)

[113] G. Granger, L. Gaudreau, A. Kam, M. Pioro-Ladrière, S. A. Studenikin, Z. R. Wasilewski, P. Zawadzki, and A. S. Sachrajda. Three-dimensional transport diagram of a triple quantum dot. *Phys. Rev. B*, 82:075304, Aug 2010. (cited on pages 17, 67, 68, and 124)

[114] E. A. Laird, J. M. Taylor, D. P. DiVincenzo, C. M. Marcus, M. P. Hanson, and A. C. Gossard. Coherent spin manipulation in an exchange-only qubit. *Phys. Rev. B*, 82:075403, Aug 2010. (cited on pages 18, 39, and 67)

[115] L. Gaudreau, G. Granger, A. Kam, G. C. Aers, S. A. Studenikin, P. Zawadzki, M. Pioro-Ladriere, Z. R. Wasilewski, and A. S. Sachrajda. Coherent control of three-spin states in a triple quantum dot. *Nat Phys*, 8(1):54–58, 01 2012. (cited on pages 18, 39, and 67)

[116] S.N. Shevchenko, S. Ashhab, and Franco Nori. Landau-zener-stÃijckelberg interferometry. *Physics Reports*, 492(1):1 – 30, 2010. (cited on p. 18)

[117] C. Cohen-Tannoudji and F. Laloë B. Diu. *Quantum Mechanics Vol. 1, second ed.* John Wiley & Sons, New York, London, 1977. (cited on pages 19 and 30)

[118] Karl Blum. *Density Matrix, Theory and Applications, second ed.* Plenum Press, New York, London, 1996. (cited on p. 25)

[119] A. G. Redfield. On the theory of relaxation processes. *IBM J. Res. Dev.*, 1:19, 1957. (cited on p. 25)

[120] D. V. Averin and Yu. V. Nazarov. Virtual electron diffusion during quantum tunneling of the electric charge. *Phys. Rev. Lett.*, 65:2446–2449, Nov 1990. (cited on p. 29)

[121] M. R. Wegewijs and Yu. V. Nazarov. Resonant tunneling through linear arrays of quantum dots. *Phys. Rev. B*, 60:14318–14327, Nov 1999. (cited on p. 35)

[122] T. Brandes and F. Renzoni. Current switch by coherent trapping of electrons in quantum dots. *Phys. Rev. Lett.*, 85:4148–4151, Nov 2000. (cited on pages 38, 39, and 73)

[123] Y. Aharonov and D. Bohm. Significance of electromagnetic potentials in the quantum theory. *Phys. Rev.*, 115:485–491, Aug 1959. (cited on pages 39 and 41)

[124] Rafael Sánchez, Ernesto Cota, Ramón Aguado, and Gloria Platero. Spin-filtering through excited states in double-quantum-dot pumps. *Phys. Rev. B*, 74:035326, Jul 2006. (cited on pages 41, 55, and 70)

[125] S. M. Huang, Y. Tokura, H. Akimoto, K. Kono, J. J. Lin, S. Tarucha, and K. Ono. Spin bottleneck in resonant tunneling through double quantum dots with different zeeman splittings. *Phys. Rev. Lett.*, 104:136801, Apr 2010. (cited on pages 46, 55, 58, and 63)

[126] Tobias Brandes. Coherent and collective quantum optical effects in mesoscopic systems. *Physics Reports*, 408(5âĂŞ6):315 – 474, 2005. (cited on p. 49)

[127] Rafael Sánchez and Gloria Platero. unpublished. (cited on p. 51)

[128] Ernesto Cota, Ramón Aguado, and Gloria Platero. ac-driven double quantum dots as spin pumps and spin filters. *Phys. Rev. Lett.*, 94:107202, Mar 2005. (cited on p. 55)

[129] Hans-Andreas Engel and Daniel Loss. Single-spin dynamics and decoherence in a quantum dot via charge transport. *Phys. Rev. B*, 65:195321, May 2002. (cited on p. 55)

[130] W. A. Coish and Daniel Loss. Exchange-controlled single-electron-spin rotations in quantum dots. *Phys. Rev. B*, 75:161302, Apr 2007. (cited on p. 55)

[131] T. Hayashi, T. Fujisawa, H. D. Cheong, Y. H. Jeong, and Y. Hirayama. Coherent manipulation of electronic states in a double quantum dot. *Phys. Rev. Lett.*, 91:226804, Nov 2003. (cited on p. 67)

[132] Ronald Hanson and Guido Burkard. Universal set of quantum gates for double-dot spin qubits with fixed interdot coupling. *Phys. Rev. Lett.*, 98:050502, Jan 2007. (cited on p. 67)

[133] E. Arimondo. V coherent population trapping in laser spectroscopy. volume 35 of *Progress in Optics*, pages 257 – 354. Elsevier, 1996. (cited on p. 73)

[134] M. A. Ratner. Bridge-assisted electron transfer: effective electronic coupling. *J. Phys. Chem.*, 94:4877, 1990. (cited on p. 73)

[135] K. S. Novoselov, A. K. Geim, S. V. Morozov, D. Jiang, Y. Zhang, S. V. Dubonos, I. V. Grigorieva, and A. A. Firsov. Electric field effect in atomically thin carbon films. *Science*, 306(5696):666–669, 2004. (cited on pages 79, 81, and 85)

[136] Y. Zhang, Y.-W. Tan, H. L. Stormer, and P. Kim. Experimental observation of the quantum hall effect and berry's phase in graphene. *Nature*, 438:201 – 204, 2005. (cited on pages 79, 85, and 95)

[137] P. R. Wallace. The band theory of graphite. *Phys. Rev.*, 71:622–634, May 1947. (cited on pages 79 and 82)

[138] David Derbyshire. The wonder stuff that could change the world: Graphene is so strong a sheet of it as thin as clingfilm could support an elephant, October 2011. (cited on p. 79)

[139] IOP Institute of Physics. Graphene – a new form of carbon with scientific impact and technological promise, 2011. (cited on p. 79)

[140] Alexander A. Balandin, Suchismita Ghosh, Wenzhong Bao, Irene Calizo, Desalegne Teweldebrhan, Feng Miao, and Chun Ning Lau. Superior thermal conductivity of single-layer graphene. *Nano Letters*, 8(3):902–907, 2008. PMID: 18284217. (cited on p. 79)

[141] F. Bonaccorso, Z. Sun, T. Hasan, and A. C. Ferrari. Graphene photonics and optoelectronics. *Nat Photon*, 4(9):611–622, 09 2010. (cited on p. 79)

[142] R. R. Nair, P. Blake, A. N. Grigorenko, K. S. Novoselov, T. J. Booth, T. Stauber, N. M. R. Peres, and A. K. Geim. Fine structure constant defines visual transparency of graphene. *Science*, 320(5881):1308, 2008. (cited on pages 79 and 81)

[143] Sukang Bae, Hyeongkeun Kim, Youngbin Lee, Xiangfan Xu, Jae-Sung Park, Yi Zheng, Jayakumar Balakrishnan, Tian Lei, Hye Ri Kim, Young Il Song, Young-Jin Kim, Kwang S. Kim, Barbaros Ozyilmaz, Jong-Hyun Ahn, Byung Hee Hong, and Sumio Iijima. Roll-to-roll production of 30-inch graphene films for transparent electrodes. *Nat Nano*, 5(8):574–578, 08 2010. (cited on p. 79)

[144] Yanqing Wu, Yu-ming Lin, Ageeth A. Bol, Keith A. Jenkins, Fengnian Xia, Damon B. Farmer, Yu Zhu, and Phaedon Avouris. High-frequency, scaled graphene transistors on diamond-like carbon. *Nature*, 472(7341):74–78, 04 2011. (cited on p. 79)

[145] Leonhard Prechtel, Li Song, Dieter Schuh, Pulickel Ajayan, Werner Wegscheider, and Alexander W. Holleitner. Time-resolved ultrafast photocurrents and terahertz generation in freely suspended graphene. *Nat Commun*, 3, 01 2012. (cited on p. 79)

[146] D. Garcia-Sanchez, A. M. van der Zande, A. San Paulo, B. Lassagne, P. L. McEuen, and A. Bachtold. Imaging mechanical vibrations in suspended graphene sheets. *Nano Letters*, 8(5):1399–1403, 2008. PMID: 18402478. (cited on p. 80)

[147] S.A. Maier. *Plasmonics: fundamentals and applications*. Springer, 2007. (cited on p. 80)

[148] Frank H. L. Koppens, Darrick E. Chang, and F. Javier GarciÌĄa de Abajo. Graphene plasmonics: A platform for strong lightâĂŞmatter interactions. *Nano Letters*, 11(8):3370–3377, 2011. (cited on p. 80)

[149] Kenjiro K. Gomes, Warren Mar, Wonhee Ko, Francisco Guinea, and Hari C. Manoharan. Designer dirac fermions and topological phases in molecular graphene. *Nature*, 483(7389):306–310, 03 2012. (cited on p. 80)

[150] K. S. Novoselov, D. Jiang, F. Schedin, T. J. Booth, V. V. Khotkevich, S. V. Morozov, and A. K. Geim. Two-dimensional atomic crystals. *Proceedings of the National Academy of Sciences of the United States of America*, 102(30):10451–10453, 2005. (cited on p. 80)

[151] Jannik C. Meyer, A. K. Geim, M. I. Katsnelson, K. S. Novoselov, T. J. Booth, and S. Roth. The structure of suspended graphene sheets. *Nature*, 446(7131):60–63, 03 2007. (cited on p. 81)

[152] K.I. Bolotin, K.J. Sikes, Z. Jiang, M. Klima, G. Fudenberg, J. Hone, P. Kim, and H.L. Stormer. Ultrahigh electron mobility in suspended graphene. *Solid State Communications*, 146(9âĂŽĂĎĂň10):351 – 355, 2008. (cited on p. 81)

[153] A. L. Vázquez de Parga, F. Calleja, B. Borca, M. C. G. Passeggi, J. J. Hinarejos, F. Guinea, and R. Miranda. Periodically rippled graphene: Growth and spatially resolved electronic structure. *Phys. Rev. Lett.*, 100:056807, Feb 2008. (cited on p. 81)

[154] I. Forbeaux, J.-M. Themlin, and J.-M. Debever. Heteroepitaxial graphite on $6h-\mathrm{SiC}(0001)$: interface formation through conduction-band electronic structure. *Phys. Rev. B*, 58:16396–16406, Dec 1998. (cited on p. 81)

[155] Claire Berger, Zhimin Song, Tianbo Li, Xuebin Li, Asmerom Y. Ogbazghi, Rui Feng, Zhenting Dai, Alexei N. Marchenkov, Edward H. Conrad, Phillip N. First, and Walt A. de Heer. Ultrathin epitaxial graphite:âĂĽ 2d electron gas properties and a route toward graphene-based nanoelectronics. *The Journal of Physical Chemistry B*, 108(52):19912–19916, 2004. (cited on pages)

[156] Claire Berger, Zhimin Song, Xuebin Li, Xiaosong Wu, Nate Brown, CâĹŽÂľcile Naud, Didier Mayou, Tianbo Li, Joanna Hass, Alexei N. Marchenkov, Edward H. Conrad, Phillip N. First, and Walt A. de Heer. Electronic confinement and coherence in patterned epitaxial graphene. *Science*, 312(5777):1191–1196, 2006. (cited on p. 81)

[157] Aaron Bostwick, Taisuke Ohta, Thomas Seyller, Karsten Horn, and Eli Rotenberg. Quasiparticle dynamics in graphene. *Nat Phys*, 3(1):36–40, 01 2007. (cited on p. 81)

[158] Xiaosong Wu, Yike Hu, Ming Ruan, Nerasoa K Madiomanana, John Hankinson, Mike Sprinkle, Claire Berger, and Walt A. de Heer. Half integer quantum hall effect in high mobility single layer epitaxial graphene. *Applied Physics Letters*, 95(22):223108, 2009. (cited on p. 81)

[159] S. Y. Zhou, G. H. Gweon, A. V. Fedorov, P. N. First, W. A. de Heer, D. H. Lee, F. Guinea, A. H. Castro Neto, and A. Lanzara. Substrate-induced bandgap opening in epitaxial graphene. *Nat Mater*, 6(10):770–775, 10 2007. (cited on p. 81)

[160] Keun Soo Kim, Yue Zhao, Houk Jang, Sang Yoon Lee, Jong Min Kim, Kwang S. Kim, Jong-Hyun Ahn, Philip Kim, Jae-Young Choi, and Byung Hee Hong. Large-scale pattern growth of graphene films for stretchable transparent electrodes. *Nature*, 457(7230):706–710, 02 2009. (cited on p. 82)

[161] Alfonso Reina, Xiaoting Jia, John Ho, Daniel Nezich, Hyungbin Son, Vladimir Bulovic, Mildred S. Dresselhaus, and Jing Kong. Large area, few-layer graphene films on arbitrary substrates by chemical vapor deposition. *Nano Letters*, 9(1):30–35, 2009. (cited on p. 82)

[162] Alexander N. Obraztsov. Chemical vapour deposition: Making graphene on a large scale. *Nat Nano*, 4(4):212–213, 04 2009. (cited on p. 82)

[163] A. H. Castro Neto, F. Guinea, N. M. R. Peres, K. S. Novoselov, and A. K. Geim. The electronic properties of graphene. *Rev. Mod. Phys.*, 81(1):109–162, Jan 2009. (cited on pages 83 and 85)

[164] O. Klein. Die reflexion von elektronen an einem potentialsprung nach der relativistischen dynamik von dirac. *Z. Phys.*, 53:157–165, 1929. (cited on p. 84)

[165] Ru-Keng Su, G G Siu, and Xiu Chou. Barrier penetration and klein paradox. *Journal of Physics A: Mathematical and General*, 26(4):1001, 1993. (cited on p. 84)

[166] M. I. Katsnelson, K. S. Novoselov, and A. K. Geim. Chiral tunnelling and the klein paradox in graphene. *Nat Phys*, 2(9):620–625, 09 2006. (cited on p. 85)

[167] Andrea F. Young and Philip Kim. Quantum interference and klein tunnelling in graphene heterojunctions. *Nat Phys*, 5(3):222–226, 03 2009. (cited on p. 85)

[168] V. P. Gusynin and S. G. Sharapov. Unconventional integer quantum hall effect in graphene. *Phys. Rev. Lett.*, 95:146801, Sep 2005. (cited on p. 85)

[169] N. M. R. Peres, F. Guinea, and A. H. Castro Neto. Electronic properties of disordered two-dimensional carbon. *Phys. Rev. B*, 73:125411, Mar 2006. (cited on p. 85)

[170] K. S. Novoselov, A. K. Geim, S. V. Morozov, D. Jiang, M. I. Katsnelson, I. V. Grigorieva, S. V. Dubonos, and A. A. Firsov. Two-dimensional gas of massless dirac fermions in graphene. *Nature*, 438:197 – 200, 2005. (cited on pages 85, 86, and 95)

[171] V. P. Gusynin and S. G. Sharapov. Magnetic oscillations in planar systems with the dirac-like spectrum of quasiparticle excitations. ii. transport properties. *Phys. Rev. B*, 71:125124, Mar 2005. (cited on p. 85)

[172] K. S. Novoselov, Z. Jiang, Y. Zhang, S. V. Morozov, H. L. Stormer, U. Zeitler, J. C. Maan, G. S. Boebinger, P. Kim, and A. K. Geim. Room-temperature quantum hall effect in graphene. *Science*, 315(5817):1379, 2007. (cited on p. 85)

[173] E. Abrahams, P. W. Anderson, D. C. Licciardello, and T. V. Ramakrishnan. Scaling theory of localization: Absence of quantum diffusion in two dimensions. *Phys. Rev. Lett.*, 42:673–676, Mar 1979. (cited on p. 85)

[174] Eduardo Fradkin. Critical behavior of disordered degenerate semiconductors. ii. spectrum and transport properties in mean-field theory. *Phys. Rev. B*, 33:3263–3268, Mar 1986. (cited on p. 85)

[175] Andreas W. W. Ludwig, Matthew P. A. Fisher, R. Shankar, and G. Grinstein. Integer quantum hall transition: An alternative approach and exact results. *Phys. Rev. B*, 50:7526–7552, Sep 1994. (cited on p. 85)

[176] J. Tworzydło, B. Trauzettel, M. Titov, A. Rycerz, and C. W. J. Beenakker. Sub-poissonian shot noise in graphene. *Phys. Rev. Lett.*, 96:246802, Jun 2006. (cited on p. 85)

[177] R. Peierls. Quelques propriétés typiques des corps solides. *Ann. I. H. Poincaré*, 1935. (cited on p. 85)

[178] L. D. Landau. Zur theorie der phasenumwandlungen. *Phys. Z. Sowjetunion*, 1937. (cited on p. 85)

[179] N. D. Mermin and H. Wagner. Absence of ferromagnetism or antiferromagnetism in one- or two-dimensional isotropic heisenberg models. *Phys. Rev. Lett.*, 17:1133–1136, Nov 1966. (cited on p. 85)

[180] P. C. Hohenberg. Existence of long-range order in one and two dimensions. *Phys. Rev.*, 158:383–386, Jun 1967. (cited on p. 85)

[181] A. K. Geim and K. S. Novoselov. The rise of graphene. *Nat Mater*, 6(3):183–191, 03 2007. (cited on p. 86)

[182] J.C. Meyer, A.K. Geim, M.I. Katsnelson, K.S. Novoselov, D. Obergfell, S. Roth, C. Girit, and A. Zettl. On the roughness of single- and bi-layer graphene membranes. *Solid State Communications*, 143(1âĂŽĂĎÃň2):101 – 109, 2007. <ce:title>Exploring graphene</ce:title> <ce:subtitle>Recent research advances</ce:subtitle>. (cited on p. 86)

[183] A. Fasolino, J. H. Los, and M. I. Katsnelson. Intrinsic ripples in graphene. *Nat Mater*, 6(11):858–861, 11 2007. (cited on p. 86)

[184] L. D. Landau. The theory of the fermi liquid. *Sov Phys. JETP*, 3, 1957. (cited on p. 86)

[185] J. González, F. Guinea, and M.A.H. Vozmediano. Non-fermi liquid behavior of electrons in the half-filled honeycomb lattice (a renormalization group approach). *Nuclear Physics B*, 424(3):595 – 618, 1994. (cited on pages 87, 88, and 112)

[186] S. Gangadharaiah, A. M. Farid, and E. G. Mishchenko. Charge response function and a novel plasmon mode in graphene. *Phys. Rev. Lett.*, 100:166802, Apr 2008. (cited on pages 87, 96, 112, and 114)

[187] J. Martin, N. Akerman, G. Ulbricht, T. Lohmann, J. H. Smet, K. von Klitzing, and A. Yacoby. Observation of electron-hole puddles in graphene using a scanning single-electron transistor. *Nat Phys*, 4(2):144–148, 02 2008. (cited on p. 87)

[188] J. Sabio, C. Seoánez, S. Fratini, F. Guinea, A. H. Castro Neto, and F. Sols. Electrostatic interactions between graphene layers and their environment. *Phys. Rev. B*, 77:195409, May 2008. (cited on p. 87)

[189] V. N. Kotov, B. Uchoa, V. M. Pereira, F. Guinea, and A. H. Castro Neto. Electron-electron interactions in graphene: Current status and perspectives. *Rev. Mod. Phys.*, 2011. accepted. (cited on pages 87, 91, and 113)

[190] J. González, F. Guinea, and M. A. H. Vozmediano. Unconventional quasiparticle lifetime in graphite. *Phys. Rev. Lett.*, 77:3589–3592, Oct 1996. (cited on p. 88)

[191] D. T. Son. Quantum critical point in graphene approached in the limit of infinitely strong coulomb interaction. *Phys. Rev. B*, 75:235423, Jun 2007. (cited on p. 88)

[192] Igor F. Herbut, Vladimir Juričić, and Oskar Vafek. Coulomb interaction, ripples, and the minimal conductivity of graphene. *Phys. Rev. Lett.*, 100:046403, Jan 2008. (cited on pages)

[193] J. Sabio, F. Sols, and F. Guinea. Variational approach to the excitonic phase transition in graphene. *Phys. Rev. B*, 82:121413, Sep 2010. (cited on p. 88)

[194] David Bohm and David Pines. A collective description of electron interactions. i. magnetic interactions. *Phys. Rev.*, 82:625–634, Jun 1951. (cited on p. 88)

[195] David Pines and David Bohm. A collective description of electron interactions: Ii. collective vs individual particle aspects of the interactions. *Phys. Rev.*, 85:338–353, Jan 1952. (cited on pages)

[196] David Bohm and David Pines. A collective description of electron interactions: Iii. coulomb interactions in a degenerate electron gas. *Phys. Rev.*, 92:609–625, Nov 1953. (cited on p. 88)

[197] H. Bruus and K. Flensberg. *Introduction to Many-body quantum theory in condensed matter physics*. Oxford graduate texts in mathematics. Oxford University Press, 2002. (cited on p. 88)

[198] D. Pines and P. Noziéres. *The theory of quantum liquids, Vol. 1*. W. A. Benjamin, INC., New York, Amsterdam, 1966. (cited on pages 88 and 90)

[199] P. Coleman. *Introduction to Many Body Physics*. Cambridge University Press, 2008. (cited on p. 88)

[200] J. Lindhard. *Mat.–Fys. Medd.*, 28, 1954. (cited on p. 88)

[201] H. Nyquist. Thermal agitation of electric charge in conductors. *Phys. Rev.*, 32:110–113, Jul 1928. (cited on p. 89)

[202] Frank Stern. Polarizability of a two-dimensional electron gas. *Phys. Rev. Lett.*, 18:546–548, Apr 1967. (cited on p. 90)

[203] E. G. Mishchenko. Effect of electron-electron interactions on the conductivity of clean graphene. *Phys. Rev. Lett.*, 98:216801, May 2007. (cited on p. 91)

[204] S. Gangadharaiah, A. M. Farid, and E. G. Mishchenko. Charge response function and a novel plasmon mode in graphene. *Phys. Rev. Lett.*, 100:166802, Apr 2008. (cited on p. 91)

[205] B. Wunsch, T. Stauber, F. Sols, and F. Guinea. Dynamical polarization of graphene at finite doping. *New Journal of Physics*, 8(12):318, 2006. (cited on pages 91, 92, 93, 96, and 112)

[206] Kenneth W. K. Shung. Dielectric function and plasmon structure of stage-1 intercalated graphite. *Phys. Rev. B*, 34:979–993, Jul 1986. (cited on pages 92, 96, and 112)

[207] E. H. Hwang and S. Das Sarma. Dielectric function, screening, and plasmons in two-dimensional graphene. *Phys. Rev. B*, 75(20):205418, May 2007. (cited on pages 91, 92, 96, and 112)

[208] Tsuneya Ando. Screening effect and impurity scattering in monolayer graphene. *Journal of the Physical Society of Japan*, 75(7):074716, 2006. (cited on p. 91)

[209] Tsuneya Ando, Alan B. Fowler, and Frank Stern. Electronic properties of two-dimensional systems. *Rev. Mod. Phys.*, 54:437–672, Apr 1982. (cited on p. 92)

[210] Xu Du, Ivan Skachko, Fabian Duerr, Adina Luican, and Eva Y. Andrei. Fractional quantum hall effect and insulating phase of dirac electrons in graphene. *Nature*, 462(7270):192–195, 11 2009. (cited on p. 95)

[211] C. R. Dean, A. F. Young, P. Cadden-Zimansky, L. Wang, H. Ren, K. Watanabe, T. Taniguchi, P. Kim, J. Hone, and K. L. Shepard. Multicomponent fractional quantum hall effect in graphene. *Nat Phys*, 7(9):693–696, 09 2011. (cited on p. 95)

[212] Takashi Oka and Hideo Aoki. Photovoltaic hall effect in graphene. *Phys. Rev. B*, 79(8):081406, Feb 2009. (cited on pages 95, 106, and 108)

[213] O. V. Kibis. Metal-insulator transition in graphene induced by circularly polarized photons. *Phys. Rev. B*, 81:165433, Apr 2010. (cited on p. 95)

[214] D. S. L. Abergel and Tapash Chakraborty. Generation of valley polarized current in bilayer graphene. *Applied Physics Letters*, 95(6):062107, 2009. (cited on p. 95)

[215] D. S. L. Abergel and T. Chakraborty. Irradiated bilayer graphene. *Nanotechnology*, 22(1):015203, 2011. (cited on p. 95)

[216] Takuya Kitagawa, Takashi Oka, Arne Brataas, Liang Fu, and Eugene Demler. Transport properties of nonequilibrium systems under the application of light: Photoinduced quantum hall insulators without landau levels. *Phys. Rev. B*, 84:235108, Dec 2011. (cited on p. 95)

[217] Zhenghao Gu, H. A. Fertig, Daniel P. Arovas, and Assa Auerbach. Floquet spectrum and transport through an irradiated graphene ribbon. *Phys. Rev. Lett.*, 107:216601, Nov 2011. (cited on p. 95)

[218] S. V. Syzranov, M. V. Fistul, and K. B. Efetov. Effect of radiation on transport in graphene. *Phys. Rev. B*, 78:045407, Jul 2008. (cited on p. 95)

[219] Claudia G. Rocha, Luis E. F. Foa Torres, and Gianaurelio Cuniberti. ac transport in graphene-based fabry-pérot devices. *Phys. Rev. B*, 81:115435, Mar 2010. (cited on p. 95)

[220] Pablo San-Jose, Elsa Prada, Sigmund Kohler, and Henning Schomerus. Single-parameter pumping in graphene. *Phys. Rev. B*, 84:155408, Oct 2011. (cited on p. 95)

[221] J. Karch, P. Olbrich, M. Schmalzbauer, C. Zoth, C. Brinsteiner, M. Fehrenbacher, U. Wurstbauer, M. M. Glazov, S. A. Tarasenko, E. L. Ivchenko, D. Weiss, J. Eroms, R. Yakimova, S. Lara-Avila, S. Kubatkin, and S. D. Ganichev. Dynamic hall effect driven by circularly polarized light in a graphene layer. *Phys. Rev. Lett.*, 105(22):227402, Nov 2010. (cited on p. 95)

[222] H. L. Calvo, H. M. Pastawski, S. Roche, and L. E. F. Foa Torres. Tuning laser-induced band gaps in graphene. *Applied Physics Letters*, 98:232103, 2011. (cited on pages 95, 106, and 109)

[223] F. J. López-Rodríguez and G. G. Naumis. Analytic solution for electrons and holes in graphene under electromagnetic waves: Gap appearance and nonlinear effects. *Phys. Rev. B*, 78(20):201406, Nov 2008. (cited on pages)

[224] P. H. Rivera, A. L. C. Pereira, and P. A. Schulz. Quasienergy spectra of graphene dots in intense ac fields: Field anisotropy and photon-dressed quantum rings. *Phys. Rev. B*, 79(20):205406, May 2009. (cited on pages)

[225] Wei Zhang, Ping Zhang, Suqing Duan, and Xian geng Zhao. Quasi-energy spectra of a charged particle in planar honeycomb lattices. *New Journal of Physics*, 11(6):063032, 2009. (cited on p. 95)

[226] Y. Zhou and M. W. Wu. Optical response of graphene under intense terahertz fields. *Phys. Rev. B*, 83(24):245436, Jun 2011. (cited on pages 95, 106, 109, and 111)

[227] J. Sabio, J. Nilsson, and A. H. Castro Neto. f-sum rule and unconventional spectral weight transfer in graphene. *Phys. Rev. B*, 78:075410, Aug 2008. (cited on pages 96 and 113)

[228] T. Stauber. Analytical expressions for the polarizability of the honeycomb lattice. *Phys. Rev. B*, 82:201404, Nov 2010. (cited on pages)

[229] R. Roldán, J.-N. Fuchs, and M. O. Goerbig. Collective modes of doped graphene and a standard two-dimensional electron gas in a strong magnetic field: Linear magnetoplasmons versus magnetoexcitons. *Phys. Rev. B*, 80:085408, Aug 2009. (cited on p. 96)

[230] C. Zhang. Dynamic screening and collective excitation of an electron gas under intense terahertz radiation. *Phys. Rev. B*, 65:153107, Apr 2002. (cited on pages 96, 113, and 130)

[231] Milena Grifoni and Peter Hänggi. Driven quantum tunneling. *Physics Reports*, 304(5-6):229 – 354, 1998. (cited on p. 97)

[232] Sigmund Kohler, Jörg Lehmann, and Peter Hänggi. Driven quantum transport on the nanoscale. *Physics Reports*, 406(6):379 – 443, 2005. (cited on p. 97)

[233] Andreas Wacker. Semiconductor superlattices: a model system for nonlinear transport. *Physics Reports*, 357(1):1 – 111, 2002. (cited on p. 99)

[234] Johannes Hausinger and Milena Grifoni. Dissipative two-level system under strong ac driving: A combination of floquet and van vleck perturbation theory. *Phys. Rev. A*, 81(2):022117, Feb 2010. (cited on p. 101)

[235] A. P. Jauho and K. Johnsen. Dynamical franz-keldysh effect. *Phys. Rev. Lett.*, 76:4576–4579, Jun 1996. (cited on p. 106)

[236] K. B. Nordstrom, K. Johnsen, S. J. Allen, A.-P. Jauho, B. Birnir, J. Kono, T. Noda, H. Akiyama, and H. Sakaki. Excitonic dynamical franz-keldysh effect. *Phys. Rev. Lett.*, 81:457–460, Jul 1998. (cited on p. 106)

[237] J. D. Jackson. *Classical Electrodynamics, third ed.* John Wiley & Sons, New York, London, 1999. (cited on p. 112)

[238] Kristinn Johnsen and Antti-Pekka Jauho. Quasienergy spectroscopy of excitons. *Phys. Rev. Lett.*, 83:1207–1210, Aug 1999. (cited on p. 113)

[239] P. K. Pyatkovskiy. Dynamical polarization, screening, and plasmons in gapped graphene. *Journal of Physics: Condensed Matter*, 21(2):025506, 2009. (cited on pages 114 and 115)

[240] Thomas G. Pedersen, Christian Flindt, Jesper Pedersen, Niels Asger Mortensen, Antti-Pekka Jauho, and Kjeld Pedersen. Graphene antidot lattices: Designed defects and spin qubits. *Phys. Rev. Lett.*, 100:136804, Apr 2008. (cited on p. 116)

[241] M. H. Schultz, A. P. Jauho, and T. G. Pedersen. Screening in graphene antidot lattices. *Phys. Rev. B*, 84:045428, Jul 2011. (cited on p. 116)

[242] M. Abramowitz and I.A. Stegun. *Handbook of Mathematical Functions: With Formulas, Graphs, and Mathematical Tables*. Applied mathematics series. Dover Publications, 1964. (cited on p. 129)